Dissertation
submitted to the
Combined Faculties for the Natural Sciences and for Mathematics
of the Ruperto Carola University of Heidelberg, Germany
for the degree of
Doctor of Natural Sciences

presented by
Dipl. Phys.: Sebastian Kreycy
born in: Bühl

Oral examination: 30.10.2012

Investigation of the Stratospheric Bromine Chemistry by Balloon-Borne Spectroscopic Observations and Photochemical Modelling: A Case Study of J($BrONO_2$) / $k_{[BrO][NO_2]}$

Referees: Prof. Dr. Klaus Pfeilsticker
Dr. Christoph Garbe

Contents

1. Introduction **3**

I. Background 7

2. The Atmosphere **9**
2.1. The Troposphere . . . 9
2.1.1. Atmospheric Dynamics . . . 11
2.2. The Stratosphere . . . 13
2.3. The Mesosphere . . . 14
2.4. The Thermosphere . . . 14
2.5. The Exosphere . . . 15

3. Atmospheric Photochemistry **17**
3.1. Stratospheric Oxygen Photochemistry . . . 18
3.2. Stratospheric Nitrogen Photochemistry . . . 22
3.3. Stratospheric Halogen Photochemistry . . . 25
3.3.1. Stratospheric Bromine Photochemistry . . . 26

4. Atmospheric Radiation Transfer **31**
4.1. Incoming Solar Radiation . . . 31
4.2. Scattering of Radiation in the Atmosphere . . . 33
4.2.1. Rayleigh Scattering . . . 34
4.2.2. Mie Scattering . . . 35
4.2.3. Raman Scattering . . . 36
4.3. Absorption of Radiation in the Atmosphere . . . 36

II. Methods and Tools 41

5. Radiative Transfer Modelling **43**
5.1. DAMF . . . 43
5.2. McArtim . . . 43

6. DOAS Principle **47**
6.1. Shortcomings and Errors . . . 49
6.1.1. Correlations of Retrieval Parameters . . . 49
6.1.2. Solar I_0 Effect . . . 49
6.1.3. Instrumental Stray Light . . . 51
6.1.4. Ring Effect . . . 51
6.2. Langley Plot . . . 51

7. Profile Inversion **53**
7.1. Maximum A Posteriori . . . 54
7.2. Singular Value Decomposition . . . 56
7.3. The L-curve Method . . . 59

8. Photochemical Modelling **61**

9. Instrumentation **65**
9.1. The LPMA/DOAS Balloon Payload . . . 65
9.1.1. The LPMA Fourier Transform Interferometer . . . 65
9.1.2. The DOAS Balloon Instrument for Direct Sunlight Observations . . 67
9.1.3. The miniDOAS Instrument for Limb Observations of Scattered Skylight . . . 70
9.1.4. The STAC Instrument . . . 74

III. Measurements 77

10. StraPolÉté Campaign **79**
10.1. The LPMA/DOAS Flight . . . 80
10.2. State of the Atmosphere . . . 83

11. Direct Sunlight Measurements **87**
11.1. Inferred Slant Column Densities . . . 87
11.1.1. O_3 Spectral Retrieval . . . 87
11.1.2. NO_2 Spectral Retrieval . . . 90
11.1.3. BrO Spectral Retrieval . . . 92
11.2. Profile Retrieval of the Direct Sunlight Measurements . . . 93

12. Limb Measurements of Scattered Skylight **97**
12.1. Inferred Slant Column Densities . . . 97
12.1.1. O_3 Spectral Retrieval . . . 97
12.1.2. NO_2 Spectral Retrieval . . . 100
12.1.3. BrO Spectral Retrieval . . . 102
12.2. Radiances . . . 112
12.2.1. Sensitivity Studies for the Number of Photon Trajectories . . . 112
12.2.2. Aerosol Extinction . . . 116
12.2.3. Field of View . . . 120
12.3. The Balloon Ascent Measurements . . . 132
12.4. Profile Retrieval of the Limb Measurements of Scattered Skylight . . . 134
12.4.1. Impact of the A Priori Error . . . 136
12.4.2. Adaptation of A Priori Ascent Profiles . . . 138
12.4.3. Impact of the Regularisation Parameter . . . 138
12.4.4. Comparison of MAP and SVD Inversion . . . 139
12.4.5. Fraunhofer Offset for Scattered Skylight Limb Measurements . . . 140
12.4.6. Impact of the Retrieval Grid . . . 142
12.4.7. Test of Interfering Trace Gases . . . 143
12.4.8. Retrieved Profiles of the Scattered Skylight Limb Measurements . . 144

IV. Results 153

13. Investigation of the Stratospheric Bromine Chemistry **155**
13.1. Sensitivity Study . . . 156
13.1.1. The $BrONO_2$ Absorption Cross Section . . . 158
13.2. Labmos Model Initialisation . . . 160
13.2.1. Sunrise Initialisation . . . 161
13.3. Comparison between Measured and Modelled Limb Observations of Scattered Skylight . . . 162
13.3.1. J - k Dependence . . . 165

13.3.2. Br_Y Dependence 166
13.4. Comparison between Measured and Modelled Direct Sunlight Observations 166
13.4.1. Sunrise Observations 172
13.5. Discussion of Results 173

14. Satellite Validation **177**
14.1. The SCIAMACHY Instrument 177
14.2. Validation Approach 178
14.2.1. Summary 184

15. Conclusion and Outlook **187**

References **191**

A. J-k Plots **205**

Acknowledgements **217**

Abstract

Besides chlorine, bromine is the second most important halogen when it comes to the destruction of ozone in the stratosphere. Although 150 times more chlorine than bromine is transported into the stratosphere, the higher ozone-depleting efficiency of bromine (by a factor of 45) makes it very important for catalytic cycles.
In this study, balloon-borne DOAS (Differential Optical Absorption Spectroscopy) measurements of direct sunlight and limb measurements of scattered skylight, recorded at high latitudes in fall 2009, were used to analyse the bromine chemistry of the stratosphere. These measurements were compared with data from the 1D photochemical model Labmos, initialised with output from the 3D chemical transport model SLIMCAT. This comparison showed that the ratio of the photolysis rate J_{BrONO2} and the $BrONO_2$ formation rate coefficient $k_{[\mathrm{BrO}][\mathrm{NO2}]}$ deviates from the JPL-2011 recommendations, leading to a larger $BrO/BrONO_2$ ratio. Using the revised $J_{\mathrm{BrONO2}}/k_{[\mathrm{BrO}][\mathrm{NO2}]}$ ratio, the total stratospheric Br_Y is likely to be 1.4 ppt lower than the previously estimated (20.3 $\pm$ 2.5) ppt.
Furthermore, photochemical corrections of the balloon-borne trace gas concentration profiles were applied in order to compare them with observations from the satellite instrument SCIAMACHY (SCanning Imaging Absorption spectroMeter for Atmospheric CHartographY) for validation of the satellite retrievals.

Zusammenfassung

Brom ist in Bezug auf Ozonabbau in der Stratosphäre nach Chlor das zweitwichtigste Halogen. Obwohl 150 mal mehr Chlor als Brom in die Stratosphäre eingebracht wird, ist Brom aufgrund seiner höheren Effizienz (Faktor 45) im katalytischen Ozonabbau von großer Bedeutung.
Zur Untersuchung der stratosphärischen Ozonchemie wurden in dieser Studie ballongestützte DOAS (Differentielle Optische Absorptions Spektroskopie) Messungen von direktem Sonnenlicht und gestreutem Himmelslicht aus hohen Breitengraden von Herbst 2009 verwendet. Diese Messungen wurden mit Daten aus dem photochemischen 1D-Modell Labmos verglichen, welches wiederum mit Daten aus dem chemischen 3D-Transport-Modell SLIMCAT initialisiert wurde. Dieser Vergleich zeigte eine Verschiebung im Verhältnis der Photolyserate J_{BrONO2} zu dem Ratenkoeffizienten $k_{[\mathrm{BrO}][\mathrm{NO2}]}$ der $BrONO_2$ Produktionsreaktion gegenüber den JPL 2011 Empfehlungen, was auf ein höheres $BrO/BrONO_2$-Verhältnis hinweist. Das geänderte $J_{\mathrm{BrONO2}}/k_{[\mathrm{BrO}][\mathrm{NO2}]}$-Verhältnis impliziert eine Verringerung der stratosphärischen Gesamtbrommenge von ursprünglich (20.3 $\pm$ 2.5) ppt um 1.4 ppt.
Darüber hinaus wurden die Konzentrationsprofile der Spurengase aus den Ballonmessungen photochemisch korrigiert und mit Beobachtungen des Satelliteninstruments SCIAMACHY (SCanning Imaging Absorption spectroMeter for Atmospheric CHartographY) verglichen, um die Auswertung der Satellitendaten zu validieren.

1. Introduction

The stratospheric ozone layer has its maximum concentration at an altitude of around 25 km. It influences the atmosphere and life on Earth in many ways. Ozone (O_3) absorbs the ultraviolet (UV) radiation from the Sun and thereby effectively shields the Earth's surface and protects life from high energy UV radiation, which can damage DNA sequences. The molecules can also absorb infra-red radiation coming from the surface. This creates the characteristic temperature gradient of the stratosphere. In contrast with the troposphere, where anthropogenic pollution can create ozone, stratospheric ozone can be diminished through anthropogenic emissions of O_3 depleting substances (ODS).
Nitrogen and halogen compounds act as catalysts in ozone destroying reactions. Although this had already been established in the 1970s (*Crutzen* (1970), *Johnston* (1971), *Molina and Rowland* (1974)), the depletion of almost the entire ozone in the 12 - 25 km altitude range over Antarctica came as a surprise to the scientific community (*Farman et al.* 1985). Soon the anthropogenic emission of halogen compounds, predominantly chlorofluorocarbons and halons, were identified as the cause of the ozone depletion in the polar regions during spring time (*Bishop* 1979). As a result of these findings, the Montreal Protocol was enacted in 1987. The protocol and a number of amendments and adjustments (London, 1990; Copenhagen, 1992; Vienna, 1995; Montreal, 1997; Beijing, 2000) led to the phase-out of many ODS, as already described by *Dorf* (2005).

Despite the reduction of emissions of ODS, the ozone hole still occurs over Antarctica during spring and ozone depletion in the Arctic stratosphere can reach levels classified as an ozone hole. This happened most recently in 2011, shown in Figure 1.1. The statistical transport time through the tropopause into the stratosphere (∼5 years) and the long lifetimes of ODS facilitate this long-lasting effect on the stratosphere. However, recent measurements (update of *Dorf et al.* (2006)) indicate a stagnation or slight decrease in the total Br_Y concentrations in the stratosphere.

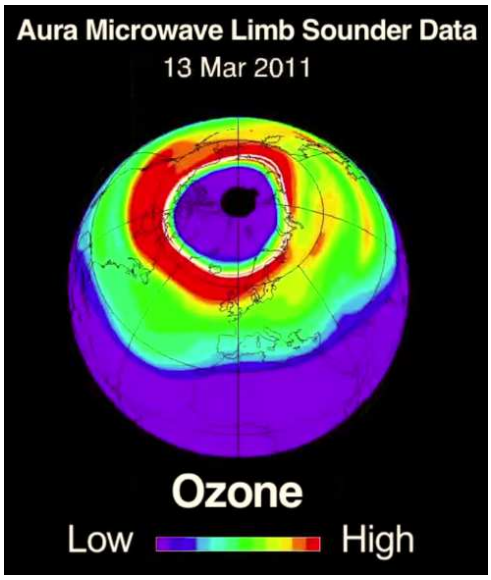

Figure 1.1.: *Ozone Hole over the Arctic in 2011 recorded by the Aura MLS satellite instrument. Adopted from NASA (2012a).*

The winter- and springtime polar stratosphere was the target of extensive atmospheric research after the discovery of the ozone hole. However, little research has been done into the photochemistry of the summertime condition and the turnover of the polar stratosphere.

During daylight the most abundant stratospheric bromine species is BrO, which accounts for approximately 70% of total Br_Y (*Lary* (1996), *Lary et al.* (1996)). In the summer polar stratosphere the second most abundant bromine species is $BrONO_2$, the night-time reservoir of BrO. The ratio between BrO and $BrONO_2$ is determined by considering their transformation reactions: The photolysis of $BrONO_2$ and the three-body association reaction of BrO and NO_2.

$$BrONO_2 + h\nu \rightarrow BrO + NO_2 \qquad \text{depending on } J_{BrONO2} \tag{1.1}$$

$$BrO + NO_2 + M \rightarrow BrONO_2 + M \qquad \text{depending on } k_{[BrO][NO2]} \tag{1.2}$$

Both the photolysis rate J_{BrONO_2} and the rate coefficient $k_{[BrO][NO_2]}$ of the formation process were determined by laboratory measurements (*Sander et al.* 2011). BrO is also the most practical inorganic bromine species to detect, which makes it possible to derive the total stratospheric bromine budget Br_Y from BrO measurements. When taking stratospheric measurements, BrO is measured and the total stratospheric Br_Y is estimated from the BrO/Br_Y ratio (*Harder et al.* (1998), *Harder et al.* (2000), *Dorf et al.* (2006), *Millán et al.* (2012)). The total stratospheric Br_Y is determined by

$$[Br_Y] = [BrO] \cdot (1 + k_{[BrO][NO_2]}\,[NO_2][M] \,/\, J_{BrONO_2} \,\ldots) \tag{1.3}$$

where "..." indicates contributions from minor bromine species in the stratosphere (e.g., HOBr, Br, BrCl, HBr). This approach is referred to as the inorganic method.
A second method for the estimation of the total stratospheric Br_Y are measurements of organic source gases of Br_Y in the troposphere and estimates of their transport into

the stratosphere (*Montzka et al.* (2008), *Hossaini et al.* (2010), *Aschmann et al.* (2011)). However, the estimates of Br_Y derived from the measurements of organic source gases still fall short of the concentrations calculated using the balloon-borne stratospheric BrO measurements (update of *Dorf et al.* (2006) in *WMO* (2011)). So far, this was attributed to contributions of very short-lived brominated source gases (VSLS) or direct upward transport of inorganic bromine across the tropopause (*Liang et al.* (2010), *Schofield et al.* (2011), *Hossaini et al.* (2012), *Brinckmann et al.* (2012)).

To gather more information on the condition of the high-latitude summer stratosphere the StraPolÉté Campaign[1] was conducted between late July and mid-September 2009. With the cooperation of 13 research institutes, a total of seven scientific research balloons were launched by the Centre National d'Études Spatiales (CNES) from the Esrange Space Center near Kiruna, northern Sweden. Two optical spectrometers developed at the Institute of Environmental Physics at the University of Heidelberg were deployed on board the LPMA/DOAS (Limb Profile Monitor of the Atmosphere/Differential Optical Absorption Spectroscopy) balloon gondola (*Camy-Peyret et al.* 1995). The two holographic grating spectrometers use the DOAS technique introduced by *Platt et al.* (1979). One is designed for direct sunlight observations (*Ferlemann et al.* 2000), the other for limb measurements of scattered skylight (*Weidner et al.* 2005). Both instruments have a spectral range covering the UV and the visible (vis) range. This makes it possible to analyse the recorded spectra for absorption features of, among others, ozone (O_3), nitrogen dioxide (NO_2) and bromine monoxide (BrO). With 16 hours of flight time, this was the longest ever balloon flight of the LPMA/DOAS gondola. It made possible the recording of three different datasets regarding the retrieval of trace gas concentration profiles.
The data gathered with the two DOAS spectrometers during the StraPolÉté Campaign is analysed in this thesis. The retrieved O_3, NO_2 and BrO slant column densities are inverted and concentration profiles are inferred for the three species. The measurements are used to test the transformation of BrO and the night-time reservoir gas $BrONO_2$. The comparison between measured concentrations and concentrations calculated from photochemical modelling indicates that the $J_{BrONO_2}/k_{[BrO][NO_2]}$ ratio deviates from the recommendation given by *Sander et al.* (2011). Such a discrepancy has an impact on the steady state ratio of BrO and $BrONO_2$, and thereby on the total bromine load of the stratosphere determined by the inorganic method. Using the revised $J_{(BrONO_2)}/k_{[BrO][NO_2]}$ ratio the previous estimate of the total stratospheric Br_Y of (20.3 ± 2.5) ppt (update of *Dorf et al.* (2006) in *WMO* (2011)) is 1.4 ppt lower. This would bring the estimate of the total stratospheric Br_Y into closer agreement with the estimate based on the organic method. It must be noted that these calculations are only valid in a high NO_X environment, such as that found at high-latitudes during summer.

Widespread observations are necessary if reliable estimates about budgets and temporal trends are to be made. Since balloon observations allow only for point measurements,

[1]The name is a combination of the three French terms describing the scientific background of the campaign: **Stra**tosphérique (stratospheric), **pol**aire (polar), **été** (summer).

satellite instruments are used to analyse the concentration and distribution of atmospheric trace gases on a global scale. The trace gas profiles of O_3, NO_2 and BrO retrieved from the two DOAS instruments are also used to validate the Envisat SCIAMACHY [2] instrument (*Bovensmann et al.* 1999). Satellite instruments are becoming more important and are well suited to global coverage and trend analysis over long periods of time. However, profile retrieval from a satellite-borne, fast moving instrument is fairly complicated. In order to improve retrieval methods, the balloon-borne DOAS profiles are used to validate the returned SCIAMACHY profiles. The balloon-borne profiles are much more accurate, due to the higher information content of the recorded data. During balloon-borne observations, about 50 times more spectra are recorded and can be used to create a single concentration profile.

This thesis is divided into four parts. The first part of this thesis gives an overview of the scientific background regarding the Earths atmosphere with respect to transport and dynamics (Chapter 2). In Chapter 3 a short outline of stratospheric photochemistry is given. There is a focus on oxygen, nitrogen and bromine chemistry, including the most important reactions. The theoretical basics of radiative transfer in the atmosphere are explained in Chapter 4. The second part describes the methods and tools, that are used in the course of this thesis. This includes how the theory of radiative transfer is calculated in mathematical models (Chapter 5), the spectral analysis using the DOAS technique (Chapter 6) and a description of the trace gas profile inversion methods (Chapter 7). The photochemical models, which are used within the framework of the thesis are described in Chapter 8, before an overview of the instruments used in the course of this thesis is given in Chapter 9. The third part of this thesis, called "Measurements", describes in three chapters the StraPolÉté campaign (Chapter 10), followed by the results of the two spectrographs in Chapters 11 and 12. The implications of the measurements are presented in the fourth part of this thesis: Chapters 13 and 14, before conclusions and an outlook are given in Chapter 15.

[2]SCIAMACHY = SCanning Imaging Absorption spectroMeter for Atmospheric CHartographY

Part I.

Background

2. The Atmosphere

Although it only represents $1/10^6$ of the Earth's mass, the atmosphere of our planet plays an important role. It interacts in many ways with the surface and simultaneously shields it from solar and galactic cosmic radiation. The Earth's atmosphere is composed of many different gases, and only the gravitational field keeps them from dissipating into outer space. The layers into which the atmosphere can be divided depends on the parameter chosen, with the most common being temperature. In this chapter a short description of the relevant structural and dynamic features of the atmosphere is given.

Figure 2.1.: *This photograph taken on board the ISS can give an idea how thin the Earth's atmosphere is. Adopted from NASA (2012a).*

2.1. The Troposphere

The different layers of the atmosphere are called -spheres, while the boundaries between them are called -pauses (see Figure 2.2). The first layer above the surface is the troposphere.

All weather effects take place in this turbulent, well-mixed layer. Warm air from the surface ascends and starts cooling down, mostly due to adiabatic expansion. This convection is further driven through the release of latent heat from the condensation of water vapour. These effects cause a continuing vertical mixing in this layer. These processes are

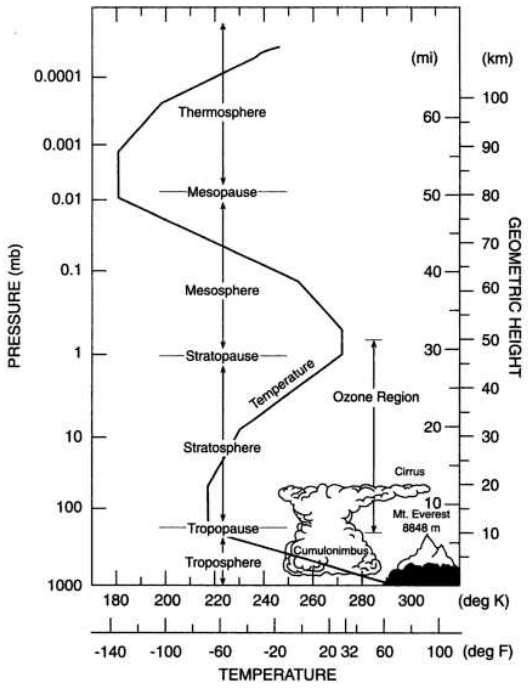

Figure 2.2.: *Layout of the Earth's atmosphere. Shown in the middle is the atmosphere's thermal gradient, used to divide the atmosphere in different layers. Adopted from Brasseur and Solomon (2005).*

also the reason for the temperature decrease from the surface to the upper boundary of the troposphere. The point where the temperature decrease ceases marks the tropopause, the boundary of the stratosphere. The troposphere extends up to approximately 8 to 10 kilometres high at the poles and up to 18 kilometres in the tropics. Despite being the thinnest layer, it contains approximately 80% of total atmospheric mass.
With surface topography posing the only barriers to horizontal transport, the northern and southern troposphere are well mixed within a few months. Mixing between the two hemispheres, on the other hand, can take more than a year (see Figure 2.3).

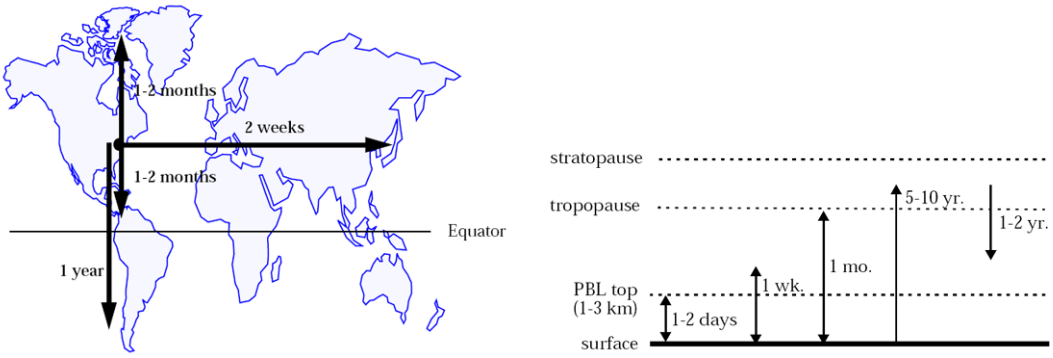

Figure 2.3.: *Transport times for horizontal transport on the left and vertical transport on the right. In the right plot the planetary boundary layer (PBL) is marked. The PBL is the lowest part of the troposphere and its behaviour is directly influenced by its contact with the planetary surface. Above the PBL the free atmosphere begins. Here the wind is approximately geostrophic (parallel to the isobars), while within the PBL the wind is affected by surface drag and turns across the isobars. Adopted from Jacobson (2005).*

2.1.1. Atmospheric Dynamics

Evidently there is no real boundary between the troposphere and the stratosphere. The World Meteorological Organization (WMO) defines the tropopause as the lowest altitude where the temperature gradient decreases to $2\frac{\mathrm{K}}{\mathrm{km}}$ or less and the lapse rate between this level and any level within the next higher 2 km does not exceed $2\frac{\mathrm{K}}{\mathrm{km}}$ (*WMO* 2011). As the temperature gradient declines, the vertical transport also slows, reaching its minimum at the tropopause.
Another concept which is often used when describing the thermal layering of the atmosphere is the potential temperature Θ.

$$\Theta = T \cdot \left(\frac{p_0}{p}\right)^{\frac{R_L}{c_p}} \tag{2.1}$$

Where T is the temperature, p the pressure, p_0 the reference pressure at ground level (standard condition 1013 mbar), R_L the gas constant and c_p the specific heat of air at constant pressure. Potential temperature is the temperature that an air parcel would attain if brought adiabatically to the reference pressure at the ground without heat exchange, such as release of latent heat or absorption of radiation (*Roedel* 2011).
Due to the very low temperatures around the tropopause (∼220 K), almost all water vapour freezes out and condensation becomes negligible at higher levels. Therefore, above the tropopause in the absence of diabatic processes the potential temperature is a very important parameter. An air parcel will always move across a surface of constant potential temperature if no energy is added to the air mass via other effects such as wave breaking or radiative heating. These surfaces are called isentropes.
Regarding horizontal transport problems a concept similar to the potential temperature, is the potential vorticity Z, which is defined as:

$$Z = \frac{f + \vartheta}{\rho} \cdot \frac{d\Theta}{dz} \tag{2.2}$$

$\vartheta = \vec{\nabla} \times \vec{v}$ is the relative vorticity where $\vec{v}$ is the horizontal air flow, ρ is the density of air, z is the vertical coordinate and $f = 2\Omega\, sin(\phi)$ is the Coriolis parameter with latitude ϕ and the absolute value of the angular velocity of the Earth Ω. Potential vorticity is derived from the combination of isentropic flow and stability (*Bergmann* 2001). Potential vorticity is measured in Potential Vorticity Units (PVU)

$$[Z] \;=\; \frac{\text{Temperature} \cdot \text{Space}}{\text{Mass} \cdot \text{Time}} \;=\; 10^{-6}\,\frac{\mathrm{K\,m^2}}{\mathrm{kg\,s}} \;=\; 1\,\mathrm{PVU} \tag{2.3}$$

With these definitions in mind, the tropical tropopause is also defined as the 380 K isentrope or as the 2 PVU surface in the extratropical region (*Gettelman et al.* 2011).
The timescale of diabatic or dissipative processes is often longer than the timescale of the process being studied, such as air mass transport. In these cases potential vorticity is a good tracer for transport modelling. Potential vorticity is conserved for adiabatic

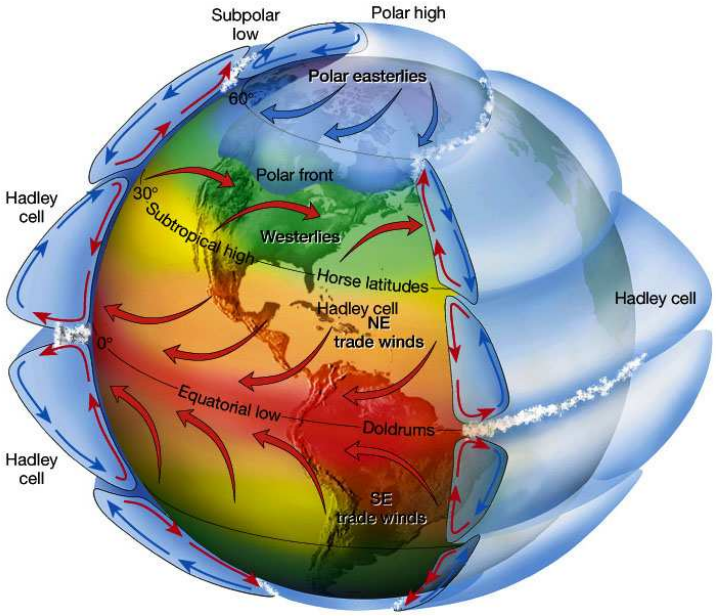

Figure 2.4.: *This figure shows a depiction of the atmospheric circulation and the main circulation cells: the Hadley cell at the equator, the Ferrel cell in the mid-latitudes and the Polar cell at the pole. The trade winds are also shown. Adopted from Short (2010).*

and frictionless flow and air masses move on surfaces of constant potential vorticity for these conditions. These surfaces are normally aligned with the latitude bands. Hence, meridional air mass transport is generally only possible through radiative heating, dissipative transport or turbulence. Compared with horizontal transport of air masses, vertical transport is a more complex process. The greater part of the troposphere-stratosphere exchange is controlled by the global circulation driven by the extratropical pump. The majority of air mass transport from the troposphere to the stratosphere occurs in the tropics (*Holton et al.* 1995, *Fueglistaler et al.* 2009, *Birner and Bönisch* 2011). From there the air starts moving polewards along the major circulation patterns and re-enters the troposphere predominantly in mid- and high-latitudes (*Polvani et al.* 2010), as shown in Figures 2.4 and 2.5.

As indicated in Figure 2.6, the 380 K isentrope is below the tropopause in the extratropical

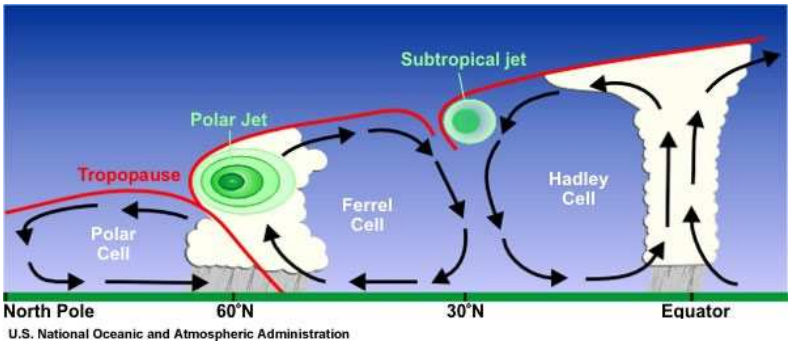

Figure 2.5.: *The plot shows a cross section of the tropospheric circulation in the northern hemisphere. Adopted from NOAA and NWS (2010).*

region and mid-latitudes. Therefore, isentropic transport and exchange between the troposphere and stratosphere is possible. In the extratropical region the tropopause folds and stratospheric intrusions contribute to troposphere-stratosphere exchange, but the detailed mechanisms of exchange between the lowermost stratosphere and the troposphere are very complex and far from being completely understood (*Dessler* 2002, *Fueglistaler et al.* 2009, *Boenisch et al.* 2011).

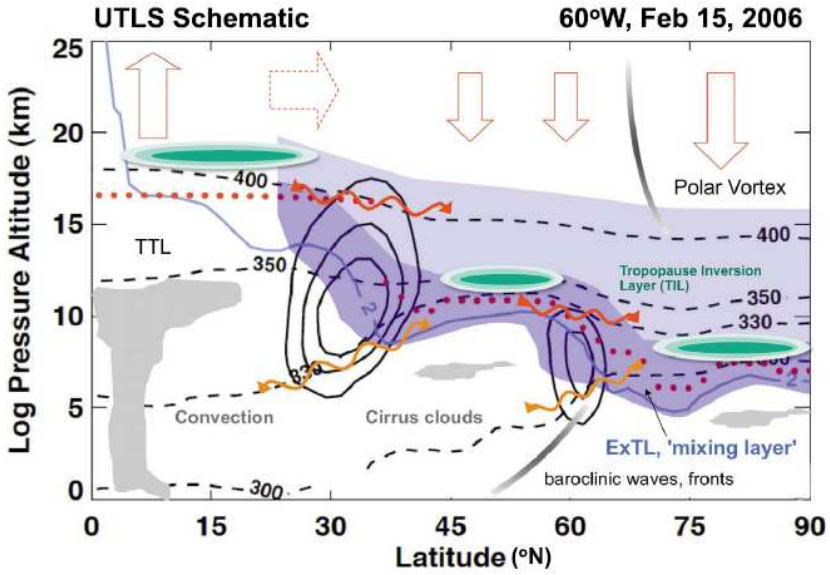

Figure 2.6.: *Schematic of the extratropical UTLS cross section, including wind patterns. Adopted from Gettelman et al. (2011).*

2.2. The Stratosphere

In the lower stratosphere, the sensible temperature starts increasing with altitude. As a result convective transport is negligible, and the energy balance of the stratosphere is dominated by radiation processes. Incoming solar UV radiation is absorbed by O_2 and O_3. At the same time emission of thermal radiation by O_3, carbon dioxide CO_2 and other trace gases cools the stratosphere.

The difference between the solar heating of the ocean and the atmosphere leads to a build up of temperature and pressure gradients and induces planetary waves in the atmosphere (*Shindell et al.* 1997). These waves originate in the troposphere and propagate partly into the stratosphere where they deposit energy and momentum. In this way they contribute to stratospheric transport patterns in the surface zone. They can also transport warm air from the mid-latitudes to polar regions. In contrast to the southern hemisphere, the north pole is not only surrounded by oceans but by landmasses as well. These geographic differences between the two hemispheres mean that planetary waves are more common, of higher magnitude and propagate to higher latitudes in the northern hemisphere.

The overall dynamic of the annual mean stratospheric meridional circulation is well described by the Brewer-Dobson circulation (*Brewer* 1949, *Dobson* 1956). Based on obser-

vations of the global transport of water vapour and ozone Brewer and Dobson suggested a circulation rising in the tropics, and descending at extra-tropical latitudes. This classical picture of the Brewer-Dobson circulation has been refined considerably in recent years (*Polvani et al.* 2010, *WMO* 2011). Stratospheric transport and mixing reveals a number of distinct regions, depicted in Figure 2.6. The stratosphere can be separated into four regions: the summer hemisphere, the tropics, the wintertime mid-latitude "surf zone", and the winter polar vortex. Stratospheric transport is dominated by mean diabatic advection (upwelling in the tropics, downwelling in the surf zone and the vortex) and, especially, by rapid isentropic stirring within the surf zone.
The most important aspects of stratospheric dynamics are illustrated in Figure 2.6 which represents a meridional cross section of the atmosphere.
The stratosphere contains approximately 19% of the total atmospheric mass, so 99% of the total mass is below 50 km.

2.3. The Mesosphere

At the upper boundary of the stratosphere the stratopause marks the layer where the temperature starts decreasing again. Airplanes and research balloons do not reach high enough to perform in situ measurements at this altitude, while the minimum orbit for a spacecraft is above the mesosphere. Only sounding rockets are able to probe the mesosphere for direct measurements. As a result, much remains uncertain about the specifics of red sprites, blue jets (electrical discharges or lightning within the lower mesosphere), noctilucent clouds and density shears within this layer. The decreasing temperature reaches the coldest point in the atmosphere of around 180 K approximately 85 km above ground. This marks the mesopause. Just beyond the mesopause, at approximately 100 km altitude, NASA defines the end of the atmosphere, because 99.9999% of the atmospheric mass can be found below this limit. However, using the thermal layering of the atmosphere there are still two layers left.

2.4. The Thermosphere

This absolute temperature minimum marks the mesopause, the boundary between the mesosphere and the thermosphere. This layer of the Earth's atmosphere is highly influenced by solar radiation with its top varying with the 11 year solar cycle. The temperature increases again with altitude due to the absorption of high energy solar radiation by the small amount of residual oxygen that is still present (*Roedel* 2011). Due to the intense energy level of incoming radiation, the thermosphere is partly ionized and its constituents start to separate based on their mass.

2.5. The Exosphere

The outermost layer of the atmosphere is the exosphere. The density is so low that a molecule is unlikely to collide with another molecule. The main constituents of the Earth's exosphere are the lightest gases: predominantly hydrogen, some helium, carbon dioxide and charged particles (O^+, N^+, N_2^+, etc.) (*Bergmann* 2001). The exosphere is the last layer before outer space. Since there is no clear boundary between outer space and the exosphere, the exosphere is considered a part of outer space. The upper boundary of the exosphere can be defined theoretically by the altitude at which the influence of solar radiation on atomic hydrogen velocities exceeds that of the Earth's gravitational pull. This occurs at around 190,000 km, half the distance to the Moon.

3. Atmospheric Photochemistry

The most abundant constituent of the Earth's atmosphere is the gas nitrogen N_2 (see Figure 3.1). It is distributed throughout the entire atmosphere and comprises 78% of the atmospheric mass. The second most abundant species is oxygen O_2. Together they make up 99% of the Earth's atmosphere. Putting argon (Ar) aside (0.934%), that leaves only 0.036% for a large variety of species. Despite these small percentages, they are still of great importance.
The atmosphere starts separating its different constituents by mass in the heterosphere. Before this, the different species are mixed in the so-called homosphere (*Roedel* 2011). These mixed gases are constantly bombarded with energy by the Sun as they circulate according to the dynamics of the atmosphere. As mentioned in Section 2.1.1, the stratosphere is not mixed as quickly as the troposphere due to the much slower vertical transport. Many species that are important for tropospheric chemistry are washed out or bound in stable compounds before they reach the stratosphere. Therefore, stratospheric chemistry does not contain as many active species as the troposphere and can be described in a more lucid way. The complicated interactions can be arranged more clearly by considering the different timescales on which the chemical reactions occur (*Brasseur and Solomon* 2005). The focus of this thesis is on the chemistry in the lower and middle stratosphere and the photochemistry of oxygen, nitrogen and bromine. While there are a huge number of different compounds containing these elements, only the dominant reactions are discussed here. A more detailed description of stratospheric photochemistry is given by *Finlayson-Pitts and J. N. Pitts* (1999) and *Brasseur and Solomon* (2005).

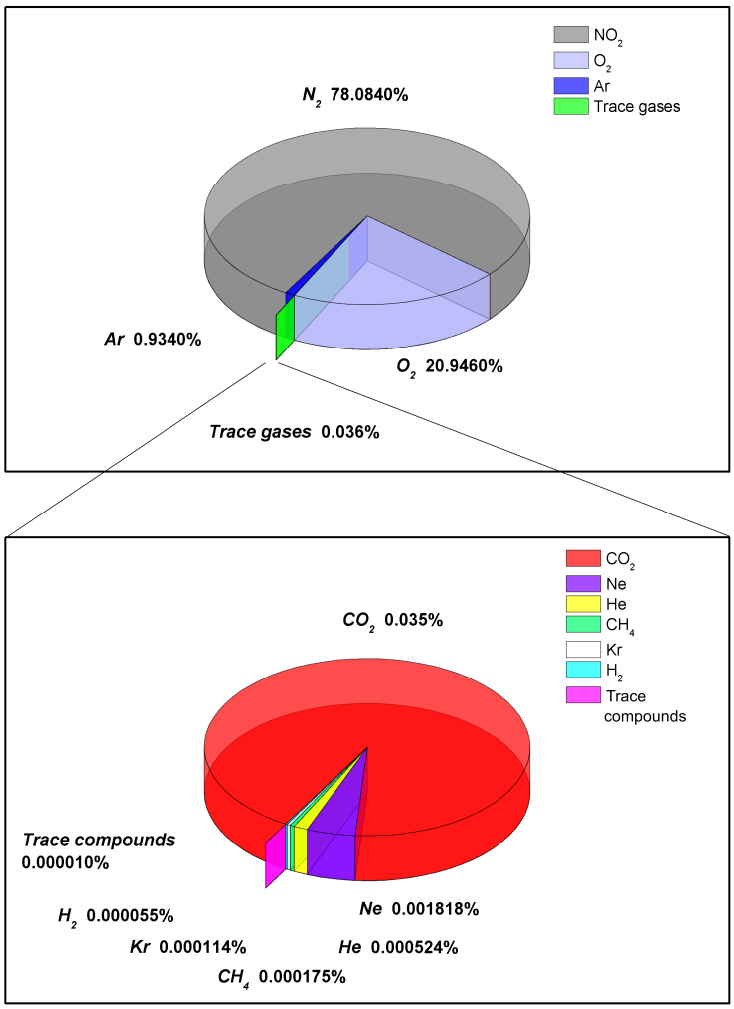

Figure 3.1.: *The upper pie chart shows the chemical composition of Earth's atmosphere. The lower pie chart represents the different trace gases which together comprise 0.036% of the atmosphere. The numbers are mean values from between 1996 and 2000. Data based on Brasseur and Solomon (2005).*

3.1. Stratospheric Oxygen Photochemistry

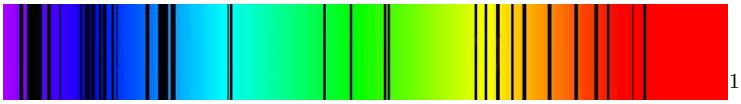 [1]

The majority of oxygen in the atmosphere exists in the form of molecular O_2 (see Figure 3.1). The second largest amount is in the form of ozone (O_3). The formation of the ozone layer in the stratosphere can be explained by a small number of reactions which were discovered by Alan Chapman (*Chapman* 1930). These reactions containing only oxygen species are called the Chapman cycle:

[1]Spectrum (400 - 700nm) with oxygen absorption lines. Based on *Petty* (2012) and *NIST* (2012).

$$O_2 + h\nu \longrightarrow 2\,O \qquad (\lambda \leq 242\,nm) \tag{3.1}$$
$$O + O_2 + M \longrightarrow O_3 + M \tag{3.2}$$
$$O_3 + h\nu \longrightarrow O_2 + O(^1D) \qquad (\lambda \leq 308\,nm) \tag{3.3}$$
$$O_3 + h\nu \longrightarrow O_2 + O(^3P) \qquad (\lambda \leq 1180\,nm) \tag{3.4}$$
$$O(^1D) + M \longrightarrow O + M \tag{3.5}$$
$$O + O + M \longrightarrow O_2 + M \tag{3.6}$$
$$O + O_3 \longrightarrow 2\,O_2 \tag{3.7}$$

While Reactions 3.1 and 3.2 represent processes creating ozone, Reactions 3.3 through 3.7 represent processes destroying so-called odd oxygen (O_X). Molecular oxygen is split up by photolysis according to Reaction 3.1 at wavelengths smaller than 242 nm through absorption of UV radiation in the spectral ranges of the Herzberg continuum. The photolysis generates both ground-state oxygen atoms $O(^3P)$, as well as oxygen atoms in the excited $O(^1D)$ state. As altitude decreases, more UV radiation is absorbed until none is left to photolyse O_2 (see Figure 3.2). Because of this, the photolysis of molecular oxygen and the formation of ozone happens mainly in the upper and middle stratosphere.
On the other hand, the energy necessary to dissolve O_3 is already achieved at wavelengths smaller than 1180 nm.

The net ozone loss occurs only on a larger timescale because many of the single oxygen

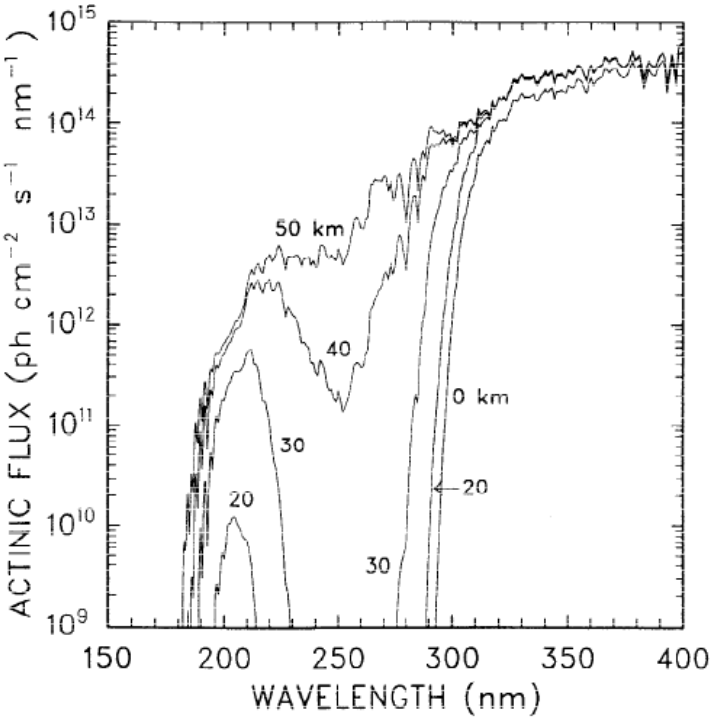

Figure 3.2.: *The penetration depth of UV radiation is dependent on the presence of O_2 and O_3, which act as a shield against UV radiation via absorption. Adopted from DeMore et al. (1997).*

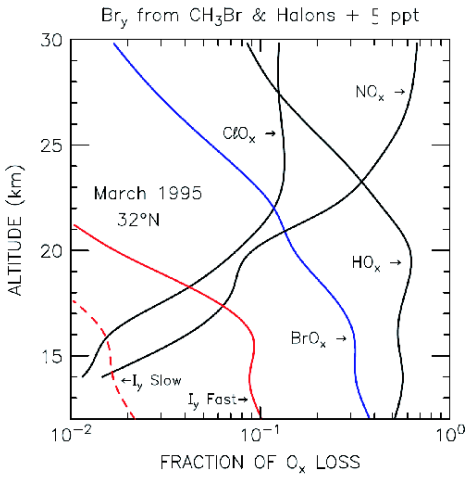

Figure 3.3.: *Calculated fractional contribution O_X loss by catalytic cycles: HO_X, NO_X, ClO_X, BrO_X and IO_X (negligible). In general, the removal of O_X in the stratosphere is driven by BrO_x and HO_x reactions in the low stratosphere, by NO_X reactions between 25-40 km, and by the ClO_X catalytic cycle for higher altitudes. Adopted from WMO (2011).*

atoms produced by the photolysis of O_3 immediately recombine via Reaction 3.2 into O_3. A net loss of O_X only occurs when these single atoms pair up into a O_2 molecule via Reaction 3.6. In addition to these processes, a small proportion of the single oxygen atoms created from O_3 photolysis react with an ozone molecule (Reaction 3.7), resulting in a net loss of O_X to the long-lived reservoir species O_2.
As a result, the lifetimes of the O_X constituents $O(^1D)$ ($\tau = 10^{-8}$ s), $O(^3P)$($\tau = 0.04$ s) and O_3 (τ=30 min at 30 km altitude) are much shorter than the photochemical lifetime of their sum O_X ($\tau \approx$ weeks) (*Finlayson-Pitts and J. N. Pitts* 1999). Since the photochemical lifetime of odd oxygen and the transport timescales in the middle and lower stratosphere are of the same order, the global distribution of ozone depends on latitude and season.
It can easily be derived that the principal part of ozone production and the highest ozone mixing ratios can be found in the equatorial region with a maximum of overhead sun. But even at mid-latitudes and up to 60° latitude the process rate for net O_3 production is still effective. Because of the altitude and latitude distribution of UV radiation that penetrates the atmosphere, ozone production occurs predominantly in the tropics. Ozone is transported polewards via the Brewer-Dobson circulation, where the air masses cool and sink down. This explains why the largest concentrations of ozone per volume can be found at high-latitudes during polar spring.
When measurements of ozone showed the maximum of the measured profiles, along with continuous smaller concentrations, at a lower altitude than expected, it became obvious that some important reactions were missing.
Bates and Nicolet (1950) first suggested that ozone destruction can occur via catalytic cycles involving only two reactions,

$$X + O_3 \longrightarrow XO + O_2 \tag{3.8}$$
$$O + XO \longrightarrow X + O_2 \tag{3.9}$$
$$\text{net}: \quad O + O_3 \longrightarrow 2\,O_2 \tag{3.10}$$

The catalyst is neither destroyed nor absorbed during this process and

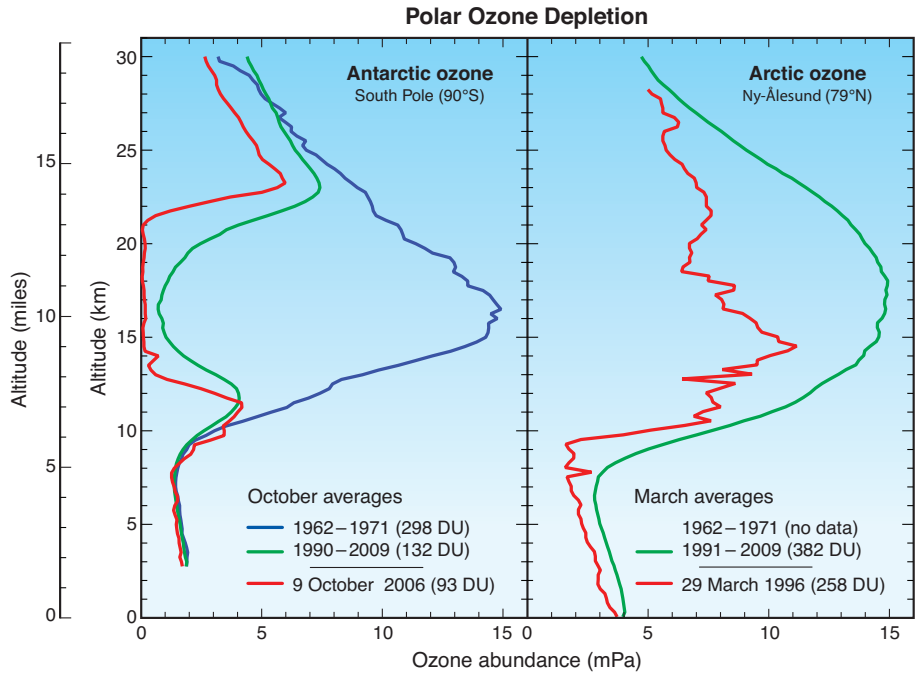

Figure 3.4.: *Vertical distribution of Arctic and Antarctic ozone. Anthropogenic release of catalyst led to a significant depletion of ozone concentrations in polar Ozone concentrations compared to earlier measurements (1962-1971). Adopted from WMO (2011).*

can start a new cycle. Several radicals were identified to be functioning as a catalyst: OH (*Bates and Nicolet* 1950), NO (*Crutzen* 1970, *Johnston* 1971), Cl (*Molina and Rowland* 1974), Br (*Wofsy et al.* 1975) and possibly I (*Solomon et al.* 1994). They all react faster with ozone than molecular oxygen, as shown in Figure 3.3. Each radical can complete a different number of cycles before it is lost in some termination reaction. To assess their overall importance it is important to take into account their concentration, as well as their kinetic and thermodynamic ozone destroying potential.
O_3 destruction can also occur in catalytic cycles which couple different families of catalysts:

$$X + O_3 \longrightarrow XO + O_2 \tag{3.11}$$
$$Y + O_3 \longrightarrow YO + O_2 \tag{3.12}$$
$$XO + YO \longrightarrow X + Y + O_2 \tag{3.13}$$

$$\text{net}: \quad 2\,O_3 \longrightarrow 3\,O_2 \tag{3.14}$$

with X being OH or Br, and Y being Cl, Br or Cl, respectively. The details of the photochemistry of the catalysts NO and Br are described in dedicated sections below (Sections 3.2 and 3.3.1).

3.2. Stratospheric Nitrogen Photochemistry

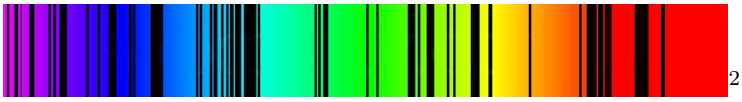

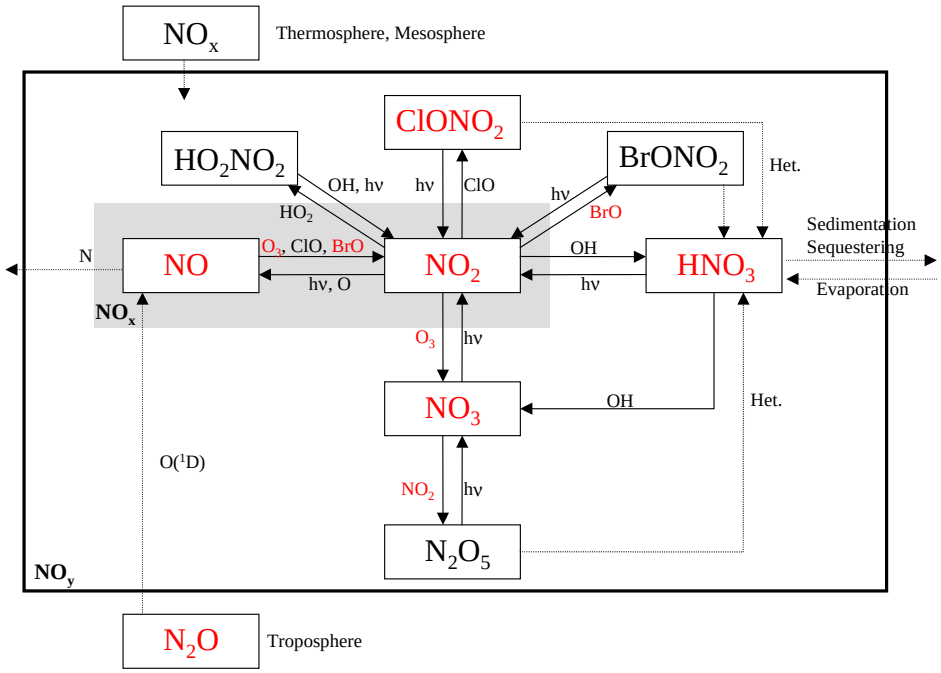

Figure 3.5.: *Principle components, sources, sinks, and pathways of the NO_Y family. The dotted lines indicate heterogeneous pathways. The red marked species can be measured with the instruments on board the LPMA/DOAS balloon gondola. Adopted from Bösch (2002).*

Nitrogen species also play an important role in stratospheric chemistry with respect to ozone. They can destroy ozone via the NO_X cycle and transform active halogen radicals into passive reservoir gases.

The dominant source of stratospheric NO_X (NO, NO_2 and NO_3) is nitrous oxide N_2O. N_2O is predominantly of natural origin, emitted from oceans and forests. However, anthropogenic emissions of N_2O are growing due to intensified biomass burning and increased use of artificial nitrogen fertilizers. They currently comprise a third of total emissions (*WMO* 2011). The N_2O lifetime is estimated at 97-137 years, as no destruction process is

[2]Spectrum (400 - 700 nm) with nitrogen absorption lines. Based on *Petty* (2012) and *NIST* (2012).

known for the inert gas in the lower stratosphere. Photolysis of N_2O, which happens only at wavelengths smaller than 398 nm, currently accounts for 90% of N_2O removal in the stratosphere.

$$N_2O + h\nu \longrightarrow N_2 + O(^1D) \qquad (\lambda \leq 398 \text{ nm}) \tag{3.15}$$

Additional loss of N_2O occurs via the reaction with $O(^1D)$ atoms:

$$O(^1D) + N_2O \longrightarrow 2\,NO \qquad (58\%) \tag{3.16}$$

$$\longrightarrow N_2 + O_2 \tag{3.17}$$

Therefore, only 6% of the destruction processes of N_2O actually create NO_X in the lower stratosphere. Another source beside ascending or upward transported N_2O is descending NO_X from the mesosphere. In the mesosphere or lower thermosphere N_2 can be split apart by high energy particles or cosmic radiation forming a reactive nitrogen species. During winter and early spring, when downward atmospheric transport at mid- and high-latitudes occurs, NO_X rich air masses can descend into the stratosphere. However, this sort of NO_Y production is highly variable, (*Vitt and Jackman* 1996).
During daytime, NO and NO_2 are in a photochemically balanced ratio, mostly via the reactions:

$$NO + O_3 \longrightarrow NO_2 + O_2 \tag{3.18}$$

$$NO_2 + O \longrightarrow NO + O_2 \tag{3.19}$$

which represent a net odd oxygen loss. NO is reproduced through photodissociation of NO_2 to create odd oxygen:

$$NO_2 + h\nu \longrightarrow NO + O \qquad (\lambda \leq 405 \text{ nm}) \tag{3.20}$$

Ozone can be replaced in Reaction 3.18 by a number of species. This could even result in an odd oxygen formation process:

$$NO + HO_2 \longrightarrow NO_2 + OH \tag{3.21}$$

$$NO + RO_2 \longrightarrow NO_2 + RO \tag{3.22}$$

$$NO + ClO \longrightarrow NO_2 + Cl \tag{3.23}$$

$$NO + BrO \longrightarrow NO_2 + Br \tag{3.24}$$

RO_2 in Reaction 3.22 is an organoperoxy radical. The reactions listed above result in a Leighton Ratio $NO/NO_2 \approx 1$, almost constant for altitudes below 40 km during daytime. With increasing numbers of oxygen atoms above 40 km, the abundance of NO rises much faster than that of NO_2 in the middle stratosphere due to Reaction 3.19. At dusk, photolysis of NO_2 fades out and NO is rapidly converted to NO_2. NO_2 then reacts with O_3

and builds NO_3 via:

$$NO_2 + O_3 \longrightarrow NO_3 + O_2 \tag{3.25}$$

During the day, NO_3 is immediately destroyed through photolysis.

$$NO_3 + h\nu \longrightarrow NO + O_2 \qquad (\lambda \leq 7320\,\text{nm}) \tag{3.26}$$
$$\longrightarrow NO_2 + O \qquad (\lambda \leq 574\,\text{nm}) \tag{3.27}$$

In the absence of sunlight, NO_3 then forms N_2O_5, the night-time reservoir gas.

$$NO_2 + NO_3 + M \longrightarrow N_2O_5 + M \tag{3.28}$$

This process can be reversed by a simple collision process

$$N_2O_5 + M \longrightarrow NO_2 + NO_3 + M \tag{3.29}$$

However, this process is rather slow and dominated after dawn by photolysis

$$N_2O_5 + h\nu \longrightarrow NO_2 + NO_3 \qquad (\lambda \leq 1252\,\text{nm}) \tag{3.30}$$

The interactions and transformations of the most important nitrogen compounds are depicted in Figure 3.5.
With sunrise and the onset of NO_2 photolysis, the NO concentration rapidly increases. The photolysis of N_2O_5 is much slower, causing an increase of NO_x during the day. Additional reservoir gases formed during the night are: $ClONO_2$, $BrONO_2$ and to some minor extend HNO_3

$$NO_2 + ClO + M \longrightarrow ClONO_2 + M \tag{3.31}$$
$$NO_2 + BrO + M \longrightarrow BrONO_2 + M \tag{3.32}$$
$$NO_2 + OH + M \longrightarrow HNO_3 + M \tag{3.33}$$

which act as source gases for ClO and BrO via photolysis (See Section 3.3.1).

$$ClONO_2 + h\nu \longrightarrow Cl + NO_3 \qquad (\lambda \leq 735\ \text{nm}) \tag{3.34}$$
$$\longrightarrow ClO + NO_2 \qquad (\lambda \leq 1065\ \text{nm}) \tag{3.35}$$
$$BrONO_2 + h\nu \longrightarrow Br + NO_3 \qquad (\lambda \leq 861\ \text{nm}) \tag{3.36}$$
$$\longrightarrow BrO + NO_2 \qquad (\lambda \leq 1129\ \text{nm}) \tag{3.37}$$
$$HNO_3 + h\nu \longrightarrow OH + NO_2 \tag{3.38}$$

3.3. Stratospheric Halogen Photochemistry

Halogen photochemistry includes fluorine, chlorine, bromine and iodine compounds. Fluorine rapidly reacts with H_2O and CH_4 to form HF which is photochemically very stable. Since fluorine atoms are rapidly scavenged, they are poor catalysts for ozone destruction (*Stolarski and Rundel* 1975). Given the short lifetime of naturally produced iodine-containing species, their direct transport into the stratosphere seems negligible as well. Iodine is highly reactive, but the amount of iodine in the stratosphere is very low. Several studies (*Bösch et al.* 2003, *Butz et al.* 2009, *WMO* 2011) indicate that the abundances of inorganic iodine species in the stratosphere are very low and below the respective detection limits. Currently the tightest upper limit for gaseous inorganic iodine in the mid- and high-latitudinal stratosphere is (0.10 ± 0.02) ppt as inferred by *Bösch et al.* (2003) and *Butz et al.* (2009) from measured upper limits of IO and OIO.

Of the remaining halogens chlorine and bromine, the latter has the higher ozone depleting potential. However, due to the much higher concentrations of chlorine species in the stratosphere, as shown in Figure 3.6, chlorine remains the overall dominant ozone-depleting halogen. The total amount of chlorine entering the stratosphere is 150 times higher than that of total bromine. Furthermore, the bulk of chlorine species transported to the stratosphere is of anthropogenic origin (*WMO* 2011).

Since the focus of this thesis is limited to bromine chemistry, chlorine and iodine chemistry is not described here.

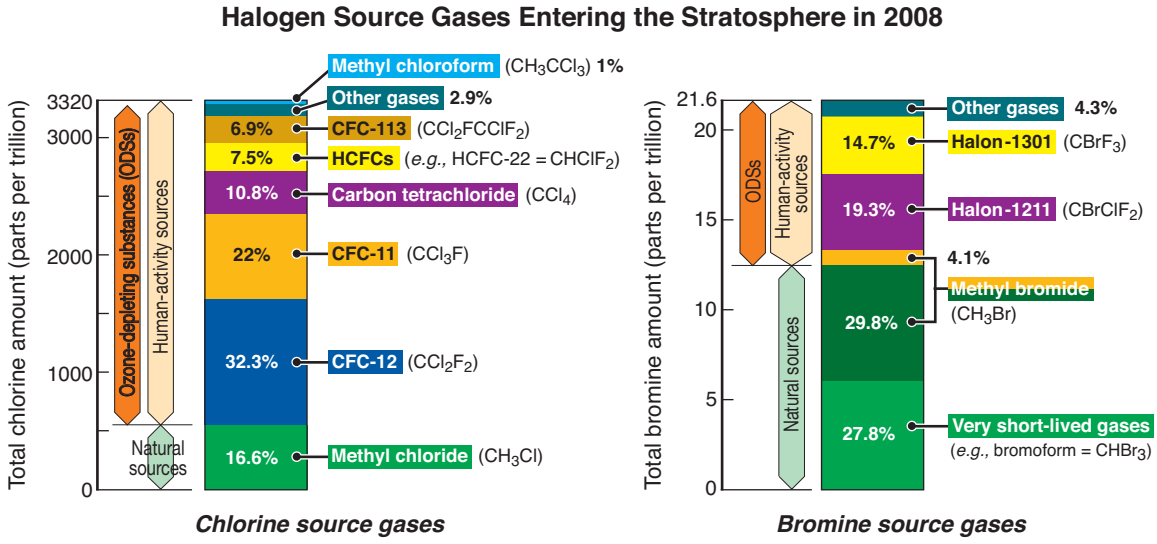

Figure 3.6.: *Depicted are the source gases for chlorine and bromine in the atmosphere that are transported to the stratosphere for the year 2008. Natural and anthropogenic sources are distinguished, as well as the different ozone-depleting substances (ODS). The approximate amounts are derived from tropospheric observations of each gas in 2008. It is important to note the large difference in the vertical scales. Adopted from WMO (2011).*

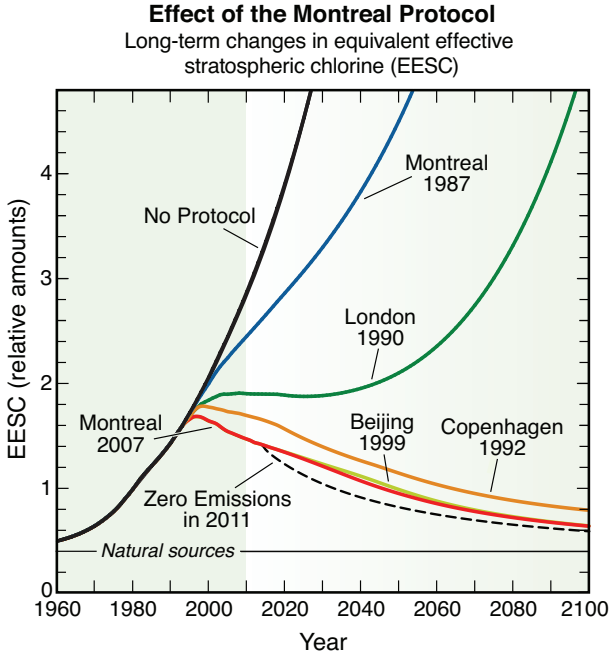

Figure 3.7.: *Effect of the Montreal Protocol. The city names and years indicate where and when changes to the original 1987 Protocol provisions were agreed upon. The zero emission line shows stratospheric abundances if all emissions were reduced to zero beginning in 2003. The Equivalent Effective Stratospheric Chlorine (EESC) (on the y-axis) is used to account for the combined effect of chlorine and bromine gases. Adopted from WMO (2011).*

3.3.1. Stratospheric Bromine Photochemistry

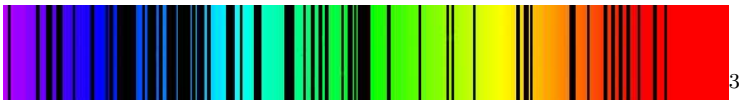 [3]

The largest source of bromine in the atmosphere is methyl bromide (CH_3Br), which is primarily of natural origin (60 - 80%). CH_3Br is predominantly emitted from oceans, saltmarshes and from forests via biomass burning, but there are also anthropogenic sources (*WMO* 2011). Man-made halons, including solvents, pesticides and halogenated hydrocarbons, which are used in fire extinguishers, contribute about 31 - 36% to the global bromine budget. Restricted by the Montreal Protocol, the global emission of halons seems to be stagnant or slightly receding *WMO* (2011).

The tropospheric bromine loading from halons and methyl bromide peaked around 1998 at 16 - 17 ppt and afterwards started to decline by a mean annual rate of (0.25 ± 0.09) $\frac{\text{ppt}}{\text{year}}$ (*WMO* 2011). Recent balloon-borne measurements of BrO by *Dorf et al.* (2006) (update in *WMO* (2011)) indicate a total inorganic bromine burden of the stratosphere of (20.3 ± 2.5) ppt. Consistent with the tropospheric trend, the stratospheric total bromine concentration is staying constant or slightly decreasing. Figure 3.9 illustrates trends in the levels of tropospheric and stratospheric bromine throughout the past 20

[3] Spectrum (400 - 700 nm) with bromine absorption lines. Based on *Petty* (2012) and *NIST* (2012).

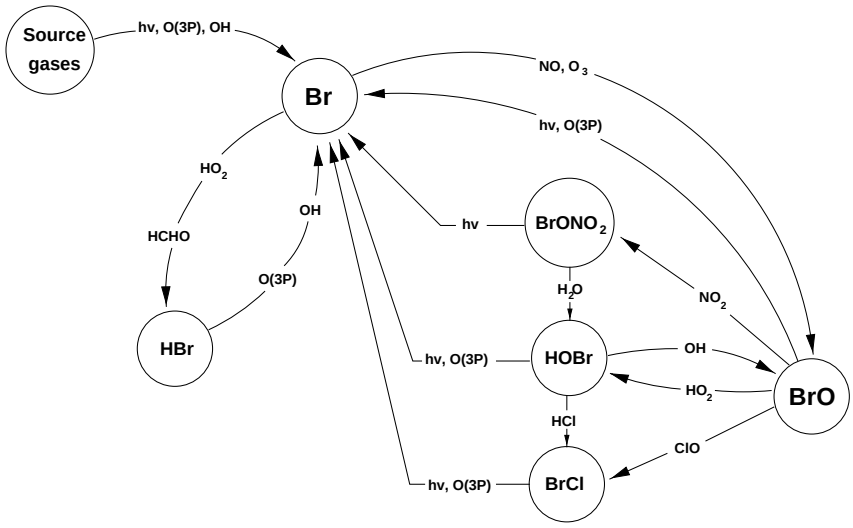

Figure 3.8.: *Stratospheric bromine chemistry scheme. Adopted from Lary (1996).*

years. The total stratospheric bromine load Br_Y (Br_Y includes Br, BrO, $BrONO_2$, HOBr, BrCl, HBr, BrONO, Br_2) can be determined through tropospheric measurements of the organic source gases (CH_3Br, CH_2Br_2, $CHBr_3$, the halons, etc.) (*Montzka et al.* 2003, *Liang et al.* 2010, *Hossaini et al.* 2010) and estimates of transport into the stratosphere (*Montzka et al.* 2008, *Aschmann et al.* 2011). This is referred to as the organic method. Another method are balloon-borne measurements of BrO in the stratosphere and estimates of the concentrations of the other bromine species based on their reciprocal concentration ratios (e.g., *Harder et al.* 2000, *Dorf et al.* 2006, *Millán et al.* 2012)

$$[Br_Y] = [BrO] \cdot (1 + k_{[BrO][NO_2]} [NO_2][M] / J_{BrONO_2} \ ...) \tag{3.39}$$

where "..." indicates contributions from minor bromine species in the stratosphere (e.g., HOBr, Br, BrCl, HBr). This approach is referred to as the inorganic method.
The apparent discrepancy illustrated in Figure 3.9 between total stratospheric bromine Br_Y determined by the two different methods, is believed to be due to very short-lived brominated source gases (VSLS) or direct upward transport of inorganic bromine across the tropopause (*WMO* 2011, *Schofield et al.* 2011, *Hossaini et al.* 2012, *Brinckmann et al.* 2012).
For stratospheric data, the date on the x-axis in Figure 3.9 corresponds to the time when the air mass passed the tropopause, i.e., sampling date minus estimated mean age of the stratospheric air parcel. For tropospheric data, the sampling time is used as a date; no correction is necessary for the transport of air from the Earth's surface to the tropopause on the timescale used here. Pre-industrial levels were (5.8 ± 0.3) ppt for CH_3Br (*Saltzman et al.* 2004), zero for the halons (*Reeves et al.* 2005) and unknown for the VSLS.
Due to their short lifetime, the tropospheric concentrations of bromine species are highly spatially and temporally variable. The highest concentrations can be found near coastal areas in the tropics and subtropics (*Brinckmann et al.* 2012). Oceanic emissions account

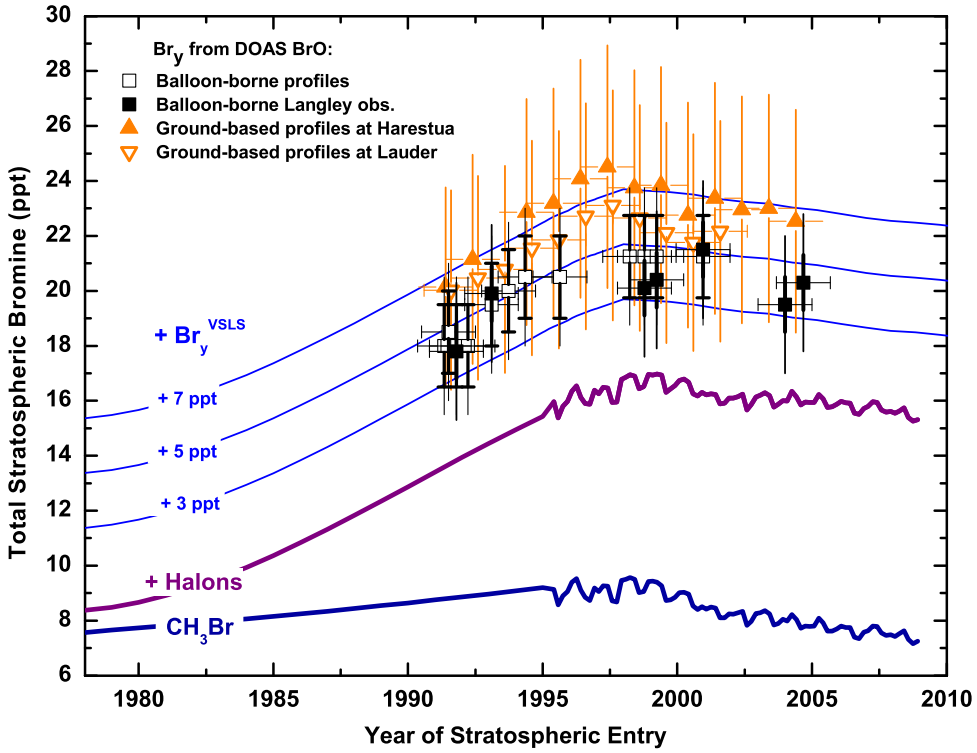

Figure 3.9.: *The figure shows the changes in total stratospheric Br_Y derived from balloon-borne BrO observations (squares) and annual mean mixing ratios calculated from ground-based UV/vis measurements of stratospheric BrO. Squares show total inorganic bromine derived from stratospheric measurements of BrO and photochemical modelling that accounts for BrO/Br_Y partitioning from slopes of Langley BrO observations above balloon float altitude (filled squares) and lowermost stratospheric BrO measurements (open squares). For the balloon-borne observations, bold/faint error bars correspond to the precision/accuracy of the estimates respectively. For the ground-based measurements (triangles), the error bars correspond to the total uncertainties in the Br_Y estimates. Update of Dorf et al. (2006) published in WMO (2011).*

for 90% to 95% of brominated species to the atmosphere. Bromoform ($CHBr_3$) is the most important troposperic VSL bromine species.

Other compounds acting as a source are the naturally released compounds CH_2Br_2, $CHBr_2Cl$ and $CHBrCl_2$. Anthropogenic emissions of most bromine species play only a minor role in the global budget; however, they can be of considerable importance on a regional scale.

The most important reactions involving bromine in the stratosphere are depicted in Figure 3.8. Regarding ozone chemistry, bromine can act as a catalyst in Reaction 3.8:

$$Br + O_3 \longrightarrow BrO + O_2 \tag{3.40}$$

$$BrO + O \longrightarrow Br + O_2 \tag{3.41}$$

$$\text{net}: \quad O + O_3 \longrightarrow 2\,O_2 \tag{3.42}$$

Besides 3.40 and 3.41, the rapid interconversion between the different bromine species is facilitated by several reactions including:

$$BrO + NO \longrightarrow Br + NO_2 \tag{3.43}$$
$$BrO + O \longrightarrow Br + O_2 \tag{3.44}$$
$$BrO + h\nu \longrightarrow Br + O \qquad (\lambda \leq 515\ \text{nm}) \tag{3.45}$$

If a BrO molecule is destroyed by photolysis (or split up in another manner) atomic Br quickly recombines with oxygen. The most important sinks for BrO besides its photolysis are reactions which lead to more stable compounds or reservoir gases:

$$BrO + NO_2 + M \longrightarrow BrONO_2 + M \tag{3.46}$$
$$BrO + HO_2 \longrightarrow HOBr + O_2 \tag{3.47}$$
$$BrO + ClO \longrightarrow BrCl + O_2 \tag{3.48}$$
$$Br + HO_2 \longrightarrow HBr + O_2 \tag{3.49}$$

In the absence of sunlight after dusk, the concentrations of reservoir gases increase and BrO fades out. The most important reservoir species for BrO is $BrONO_2$. According to *Sander et al.* (2011), the rate coefficient $k_{[BrO][NO_2]}$ of Reaction 3.46 is $5.2{\cdot}10^{-31}\,\frac{\text{cm}^6}{\text{molec}^2\,\text{s}}$ at 300 K for low pressure, with an uncertainty factor of 1.2. This reaction in particular is studied in this thesis.
However, there are two conditions under which HOBr, which can make up 30% of the total inorganic bromine during daytime, can become more important: inside the polar vortex under denoxified conditions, or in the presence of elevated concentrations of sulphuric acid background aerosols causing hydrolysis of $BrONO_2$.

$$BrONO_2 + H_2O_{(aq)} \rightarrow HOBr + HNO_3 \tag{3.50}$$

During sunrise the different reservoir gases are photolysed and the concentrations of Br and BrO increase again. The relatively long photolysis wavelength facilitates a very efficient photodissosication throughout the whole stratosphere.

$$BrONO_2 + h\nu \longrightarrow BrO + NO_2 \qquad (\text{see Reaction 3.54 below}) \tag{3.51}$$
$$HOBr + h\nu \longrightarrow Br + OH \qquad (\lambda \leq 578\,\text{nm}) \tag{3.52}$$
$$BrCl + h\nu \longrightarrow Br + Cl \qquad (\lambda \leq 546\,\text{nm}) \tag{3.53}$$

The formation of $BrONO_2$ and photolysis creating BrO and NO_2 are investigated in this work.
These reactions are the reason why, despite the short lifetime of BrO during the day ($\sim$1s), 40 - 70% of the total inorganic bromine budget (Br_Y) exists in the form of BrO.

Sander et al. (2011) lists the following channels for the photolysis of $BrONO_2$:

$$BrONO_2 + h\nu \longrightarrow BrO + NO_2 \qquad (\lambda \leq 1100\,\text{nm}) \tag{3.54}$$

$$\longrightarrow Br + NO_3 \qquad (\lambda \leq 900\,\text{nm}) \tag{3.55}$$

$$\longrightarrow BrO + NO + O \qquad (\lambda \leq 288\,\text{nm}) \tag{3.56}$$

While the second and third channel do not create BrO and NO_2 directly, both species are quickly produced through Reactions 3.26 and 3.18. Hence, the balance is kept between the participants of the first reaction, $BrONO_2$, BrO and NO_2.

4. Atmospheric Radiation Transfer

4.1. Incoming Solar Radiation

The radiation emitted by the Sun spans the electromagnetic spectrum from X-rays, ultraviolet (UV), visible (vis) to infrared (IR) and radio waves. Most solar radiation output is generated in the photosphere, the lowermost layer of a star's atmosphere. As an approximation, the Sun can be regarded as a blackbody radiator with a surface temperature of 5500 K. The amount of incoming solar radiation on Earth is described by the solar constant:

$$S = E \cdot \frac{r_{Sun}^2}{d_{E-S}^2} = 1.361 \left[\frac{\mathrm{kW}}{\mathrm{m}^2}\right] \tag{4.1}$$

as stated by *Kopp and Lean* (2011). E is the energy output of the Sun, r_{Sun} is the radius of the Sun and d_{E-S} is the distance between Earth and the Sun. The temperature and pressure gradient throughout the Sun's photosphere causes a mixing or superposition of emission lines of the different layers, creating a continuous spectrum (see Figure 4.1). The outer layers of the Sun's atmosphere also absorb radiation emitted by the deeper located layers, so only a thin region, called photosphere actually emits the solar spectrum (*Gray* 2008). Absorption lines of gas molecules and atoms in this layer create a unique spectrum that allows chemical elements in our star's atmosphere to be identified. These absorption lines are called Fraunhofer lines.

Definitions At this point several important radiometric quantities must be defined.

$$\begin{aligned}
\text{spectral flux :} \quad & \Phi(\lambda) = \frac{\text{radiation energy}}{\text{wavelength and time}} && \left[\frac{W}{nm}\right] \\
\text{radiance :} \quad & \mathrm{I}(\lambda) = \frac{\text{spectral flux}}{\text{space angle and area}} = \frac{\Phi(\lambda)}{\Omega \cdot A} && \left[\frac{W}{nm\,m^2\,sr}\right] \\
\text{irradiance :} \quad & \mathrm{E}(\lambda) = \int_{\Omega} I(\lambda,\phi,\theta) \cdot cos(\theta)\, d\Omega = \frac{\Phi(\lambda)}{A} && \left[\frac{W}{nm\,m^2}\right] \\
\text{actinic flux :} \quad & \mathrm{F}(\lambda) = \int_{\Omega} I(\lambda,\phi,\theta)\, d\Omega && \left[\frac{W}{nm\,m^2}\right]
\end{aligned}$$

As the radiation travels through the vacuum of space, the solar spectrum does not change and can be recorded by satellites outside our atmosphere or at the Top Of the Atmosphere (TOA). When the solar radiation penetrates the atmosphere, it undergoes several different processes which are described in this chapter. The overall radiative transfer of

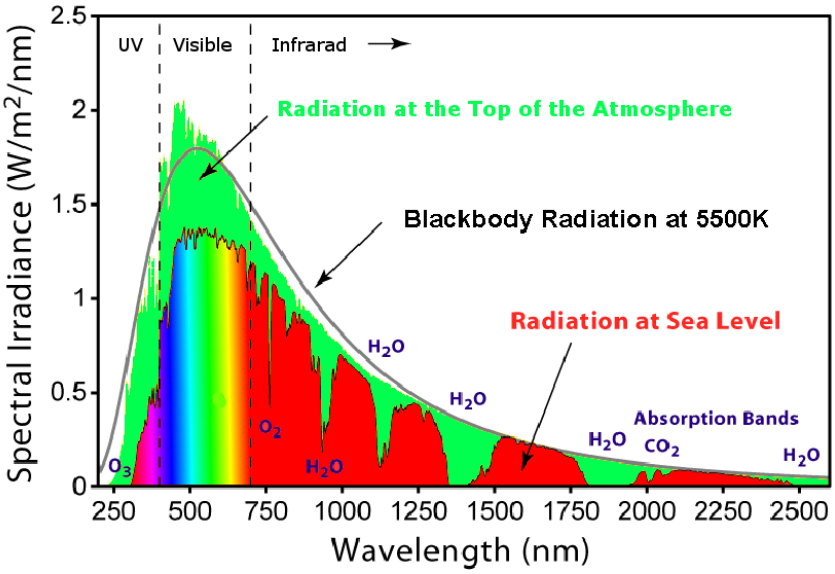

Figure 4.1.: *Sketch of the solar spectrum. Based on a blackbody radiator, the solar radiation can be estimated by using a surface temperature of 5500 K (grey curve). The green area shows the actual solar spectrum recorded outside the Earth's atmosphere (TOA), including the Fraunhofer lines. The red area represents a spectrum recorded at sea level showing several absorption features of atmospheric gases. Based on Finlayson-Pitts and Pitts (1986).*

the atmosphere can be described as a balance between incoming shortwave solar radiation and outgoing longwave terrestrial radiation. A more detailed approach can include latent and sensible heat along with energy transport in the atmosphere and absorption and reemission of radiation. This is indicated in Figure 4.2.

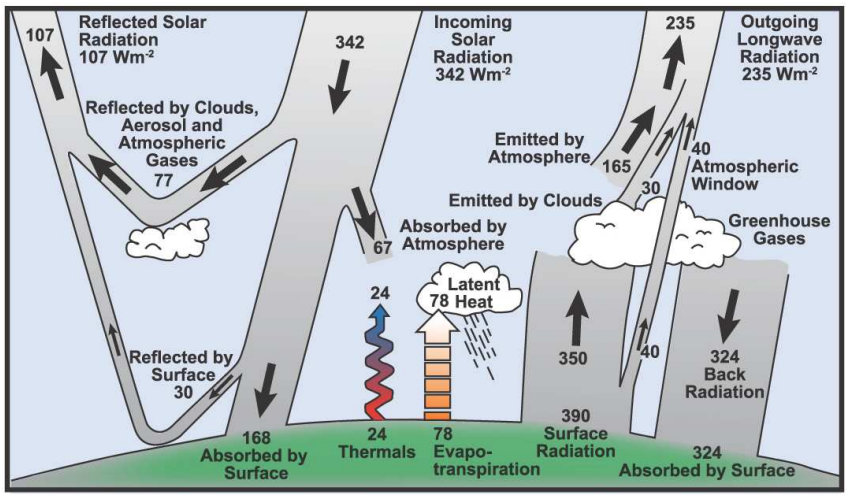

Figure 4.2.: *The Earth's annual and global mean energy balance. Approximately one third of the incoming solar radiation is directly reflected back into space by the atmosphere and the Earth's surface. About 50% is absorbed by the Earth's surface. The absorbed energy is converted to sensible heat, latent heat and thermal infrared radiation, which is reemitted. The atmosphere absorbs solar shortwave and terrestrial longwave radiation and in turn reemits radiation both upwards and downwards. Adopted from Houghton et al. (2001).*

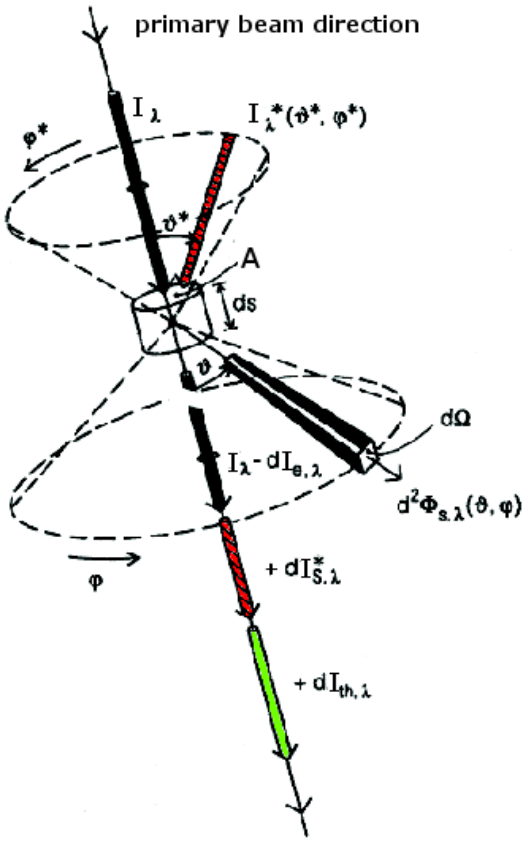

Figure 4.3.: *Contributions to changes of radiance in radiative transmission through a volume A·ds. Indicated in black is transmission minus extinction* I_e*. The shaded arrows (red) denote secondary scattering* I_s^* *and the green arrow is thermal emission* I_{th} *from the volume itself. Based on Roedel (2011).*

4.2. Scattering of Radiation in the Atmosphere

Scattering of radiation occurs when a photon hits an atmospheric particle. The type of scattering depends on the scatterer's shape, composition and its size in relation to the incident electromagnetic wave. Scattering of radiation by matter is already described in the framework of classical electrodynamics. In 1908, Mie described the incident of a plane electromagnetic wave on a spherical dielectric particle (*Mie* 1908). *Van De Hulst* (1980) extended Mie's theory for non-spherical particles. The most common scatterers in the atmosphere are air molecules (N_2, O_2). If the scatterer is small compared to the wavelength of the incident radiation, then the scattering is classified as Rayleigh scattering. This is the case for air molecules with respect to UV/vis radiation. Scattering events involving light with larger particles are referred to as Mie scattering.
Following a scattering event, the incident radiation either continues in the original beam direction or is directed elsewhere, resulting in a loss of intensity. This is indicated in Figure 4.3, which depicts radiative transmission through a volume $A \cdot \mathrm{ds}$. Corresponding to the principle of extinction of intensity (I_e) via scattering away from the original beam direction, radiation coming from an arbitrary direction can be scattered into the original beam direction (I_s^*). In addition to that, thermal emission from the volume itself (I_{th}) into beam direction has to be considered.

4.2.1. Rayleigh Scattering

The scattered light from a target smaller than the wavelength of the incident wave can be treated as radiation from an oscillating dipole. The angular distribution $p(\theta)$ of the scattered radiation peaks in forward and backward direction with respect to the direction of the incident wave, as shown in Figure 4.4. The angular dependence of Rayleigh scattered radiation with angle θ between incident and scattered radiation is described by

$$p(\theta) = \frac{3}{4}\,(\,1 + cos^2\theta\,) \tag{4.2}$$

In the atmosphere it can be assumed that the air molecules are distributed isotropically. According to *Chance and Spurr* (1997), Equation 4.2 can be approximated by

$$p(\theta) = 0.7629\,(\,1 + 0.932\,cos^2\theta\,) \tag{4.3}$$

The Rayleigh cross section is given by

$$\sigma_R(\lambda) = \frac{8\pi^3\alpha^2}{3\epsilon_0^2\lambda^4} \tag{4.4}$$

where the wavelength is taken into account by the power of four, α specifies the polarisability of the scatterer and ϵ_0 is the vacuum permittivity. An empiric formula for atmospheric conditions is given by *Chance and Spurr* (1997):

$$\sigma_R(\lambda) = \frac{3.9993 \cdot 10^{-56}\,\mathrm{m}^6\lambda^{-4}}{1 - 1.069 \cdot 10^{-14}\mathrm{m}^2\lambda^{-2} - 6.681 \cdot 10^{-29}\mathrm{m}^4\lambda^{-4}} \tag{4.5}$$

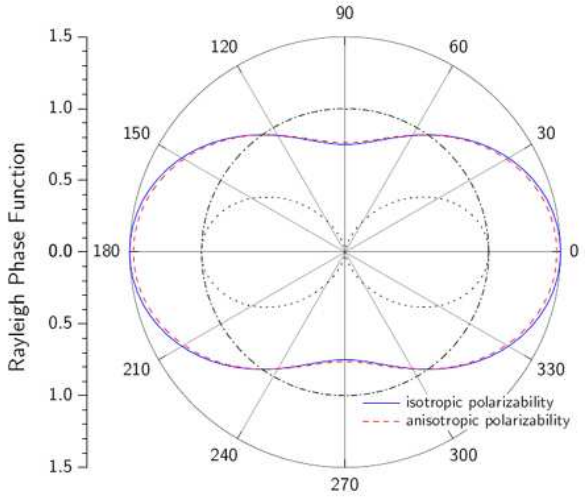

Figure 4.4.: *Rayleigh scattering phase function. Adopted from Prados-Roman (2010).*

4.2.2. Mie Scattering

If the particle size cannot be considered small compared to the wavelength of the incident radiation, then the electromagnetic dipole approximation fails and Rayleigh scattering no longer applies. In such a case, the emission of numerous excited dipoles in the scattering particle has to be considered. The resulting interference based on internal refraction and external diffraction leads to a strong emphasis on the forward direction of the scattered light (see Figure 4.5). This scattering characteristic, called Mie scattering, can be approximated by the Henyey-Greenstein phase function:

$$p(\theta) = \frac{1 - g^2}{4\pi(1 + g^2 - 2g\,cos\theta)^{\frac{3}{2}}} \tag{4.6}$$

with g being the asymmetry factor

$$g = < \cos\theta > = \frac{1}{2} \int_{-1}^{+1} p(\theta) \cdot \cos\theta \; \mathrm{d}(\cos\theta) \tag{4.7}$$

For atmospheric aerosols an asymmetry factor g of approximately 0.65 is usually as-

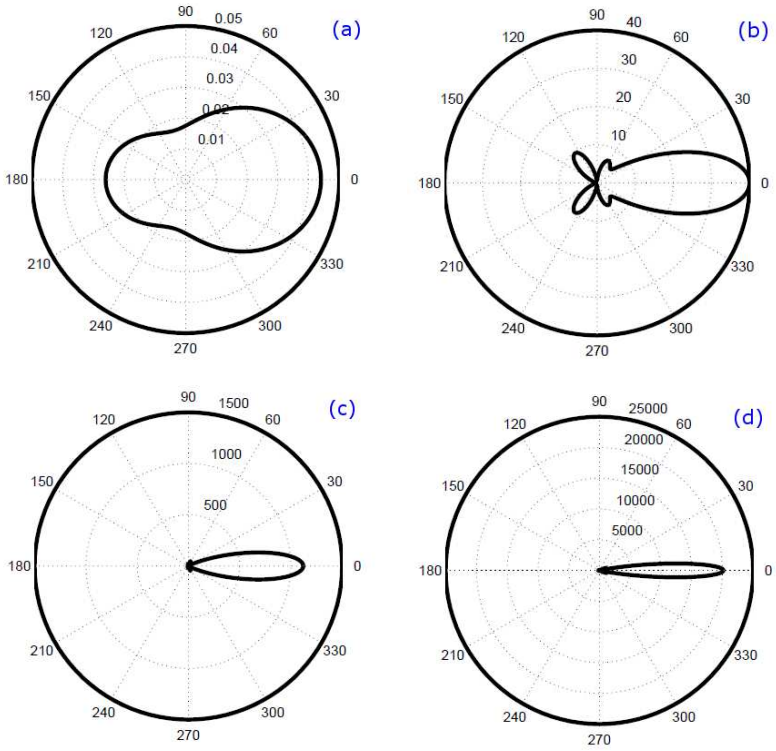

Figure 4.5.: *Mie scattering phase functions for water droplets of different size parameters. Plotted in the polar diagrams is the angular scattering profile for 550 nm. As depicted by the diagrams, the forward direction (0°) of Mie scattering clearly dominates with increasing particle size from (a) to (d). Adopted from Sanghavi (2003).*

sumed, but g can vary depending on the composition and shape of the particle (e.g., soot

or liquid droplet).
While the particles themselves may vary only slightly in form, shape, size or chemical composition, they can still have completely different scattering characteristics. Therefore, instead of the scattering cross section, the macroscopic extinction coefficient is used to describe the particles' optical properties. *Van Hulst* (1957) defined the macroscopic extinction coefficient as the integral over the particle size distribution multiplied with the scattering cross section and the particle surface. The size of a particle is often derived from the size distribution of atmospheric aerosols described by the Junge distribution (*Junge* 1961).
So far, only elastic scattering, where the incoming and the scattered radiation have the same wavelength, has been considered. The scattering molecule can also change its quantum mechanical state during the scattering process and the wavelength of the scattered radiation is shifted with respect to the incident wave. This process is called Raman scattering.

4.2.3. Raman Scattering

Raman scattering occurs when light is scattered inelastically on molecules. In this case energy is absorbed by the scatterer, causing either a change in the rotational or rotational-vibrational quantum state. This changes the wavelength of the incident wave. The scattered light consists of the Rayleigh line accompanied by several closely spaced vibrational Raman bands, each consisting of several rotational Raman lines. The cross section for Raman scattering is much smaller than the one for Rayleigh scattering. As a result, the fraction of scattering events that result in a frequency shift is a factor 10^3 to 10^4 smaller than the unshifted Rayleigh scattering processes.
In absorption spectra, Raman scattering can cause a 'filling in' of high resolution spectral features, e.g. Fraunhofer lines. For direct sunlight measurements this effect is negligible; however, for measurements of scattered sunlight this is an important feature, because strong atmospheric absorption lines can also be affected (*Fish and Jones* 1995). This filling in of lines is referred to as the Ring effect (*Grainger and Ring* 1962), see also Section 6.1.4.

4.3. Absorption of Radiation in the Atmosphere

If a TOA spectrum is compared to a spectrum recorded at the Earth's surface, the difference in intensity will be due to scattering processes as well as absorption of energy in the atmosphere. This is shown in Figure 4.1
An atom or air molecule can be excited to a higher energy state through radiation absorption. The energy of the absorbed photon must equal the energy difference between the two states.
Absorption of UV or vis radiation can induce an electronic transition (transition energy is approximately 1 eV). Absorption of IR radiation can result in a vibrational transition

(transition energy on the order of 0.1 eV) or a change in the rotational-vibrational state of the molecule (see Figure 4.6).
If the two energy states of an atom or molecule are defined by E_i and E_j, the relative population n of the excited state (E_j) at thermal equilibrium follows the Boltzmann distribution:

$$\frac{n_j}{n_i} = \frac{g_j}{g_i} e^{\frac{E_j - E_i}{k_b T}} \tag{4.8}$$

where T is the absolute temperature, $k_B = 8.617 \cdot 10^{-5}$eV/K is the Boltzmann constant and g denotes the degeneracy of the respective level. If the energy conservation is given, the Einstein coefficients describe the probability for such a transition.

$$\left(\frac{dn_1}{dt}\right)_{B_{12}} = \frac{1}{4\pi} B_{12}\, n_1\, I(\nu) \tag{4.9}$$

describes the change in population n_1 regarding absorption with the Einstein coefficient for absorption B_{12},

$$\left(\frac{dn_1}{dt}\right)_{B_{21}} = \frac{1}{4\pi} B_{21}\, n_2\, I(\nu) \tag{4.10}$$

describes the change in population n_1 regarding stimulated or induced emission with the Einstein coefficient for stimulated emission B_{21}.

$$\left(\frac{dn_1}{dt}\right) = \frac{1}{4\pi} A_{21} I(\nu) \tag{4.11}$$

describes the change in population n_1 regarding spontaneous emission with the Einstein coefficient for spontaneous emission A_{21}.
If all coefficients are combined, the change in the occupation number of state n_i is described by

$$\left(\frac{dn_i}{dt}\right) = -n_i \rho_\nu B_{ij} + n_j \rho_\nu B_{ji} + n_j A_{ji}, \tag{4.12}$$

for a given radiation density ρ_ν.
The strength of each process can thereby be calculated. However, not every transition is physically allowed. As well as energy conservation the selection rules for transitions have to be obeyed.
Selection rules are inferred from the symmetry properties of the wave functions of the atomic or molecular states. All absorption characteristics of an atom or molecule are combined in the absorption cross section, which is a description of the probability of absorption at a certain wavelength.
The change in intensity $I(\lambda)$ along a path dl is described by

$$dI(\lambda) = dI_a(\lambda) + dI_{ie}(\lambda) + dI_{se}(\lambda) =$$

$$= \quad -n_i \frac{B_{ij}h}{\lambda} I(\lambda)dl + n_j \frac{B_{ji}h}{\lambda} I(\lambda)dl + n_j \frac{A_{ji}hc}{4\pi\lambda} dl \tag{4.13}$$

The indices in the first line denote absorption (a), induced emission (ie) and stimulated emission (se). The additional factor $\frac{c}{4\pi}$ with the vacuum speed of light c is due to the isotropic character of spontaneous emission. In addition to the electronic transitions avail-

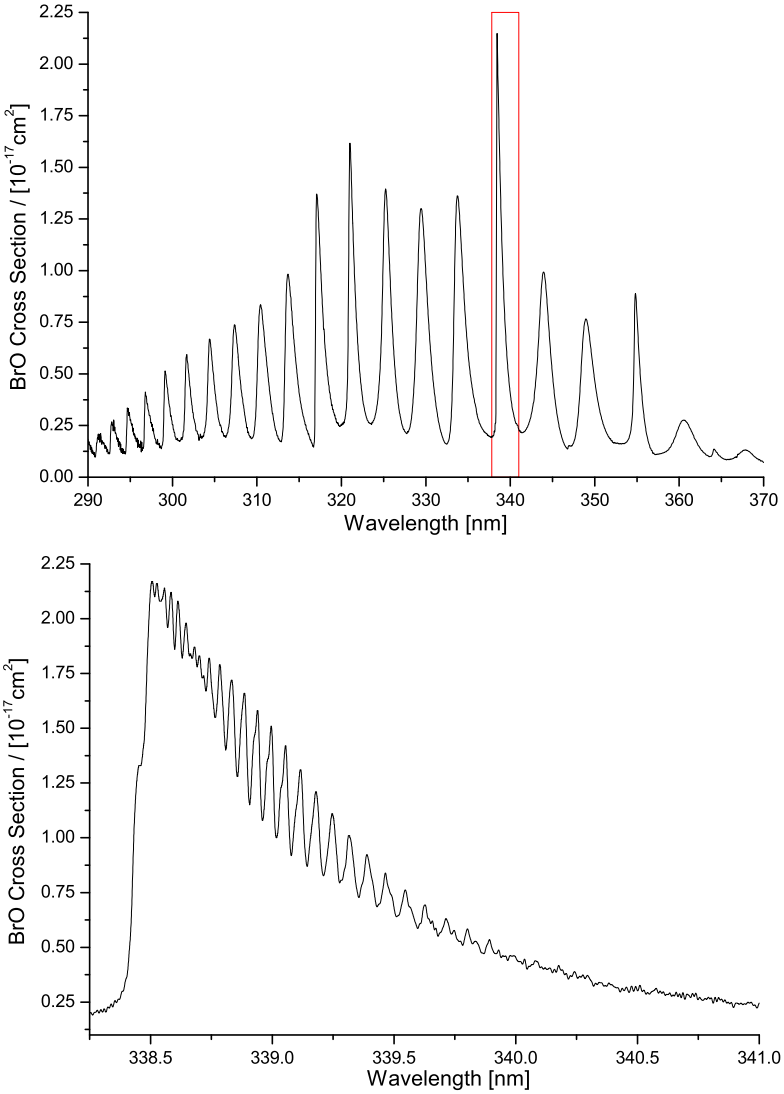

Figure 4.6.: *The BrO absorption cross section recorded at 298 K. The upper plot shows the absorption cross section in the wavelength range from 280 - 380 nm with several vibrational transitions. In the lower plot, a zoom on the line at 339 nm (red box in the upper plot) shows several rotational transitions. Data taken from Wilmouth et al. (1999).*

able to atoms, molecules can also undergo rotational and vibrational transitions. In the spectral range from 300 nm to 700 nm, molecular absorption spectra consist mainly of rotational-vibrational transitions of different electronic states.

These transitions show as spectral lines in an absorption spectrum. The depth or height of such a line is defined by the probability for this specific transition. The natural width of each line is determined by the lifetime of the excited state.

Under atmospheric conditions the thermal motion of atoms and molecules has to be accounted for. Doppler broadening and pressure broadening increase the natural line width. Both broadening effects can be accounted for by a Voigt profile.
Inherently all rotational-vibrational and electronic transitions are strongly dependent on the atom or molecule's mass and the electronic configuration. These characteristic differences between chemical species allow them to be identified using spectroscopic measurements.
Summarizing this chapter, the equation for the Radiative Transfer (RT) accounting for possible extinction and emission events is:

$$dI_\lambda = dI_{\lambda,R-} + dI_{\lambda,R+} + dI_{\lambda,M-} + dI_{\lambda,M+} + dI_{Abs} + dI_{Em} \tag{4.14}$$

including Rayleigh and Mie Scattering out (-) and into beam direction (+) as well as absorption (Abs) and emission (Em) of the observed volume.

Part II.

Methods and Tools

5. Radiative Transfer Modelling

Radiative Transfer Models (RTM) are used to calculate how light propagates through the atmosphere following the descriptions given in the previous chapter. The radiation transfers of the direct sunlight observations are calculated using the programme DAMF (*Schulte* 1996). The calculations for the radiative transfer of limb measurements of scattered skylight are more complicated. The scattering of light in the atmosphere for limb measurements is calculated using the Monte Carlo Atmospheric Radiative Transfer Inversion Model (McArtim) (*Deutschmann et al.* 2010).

5.1. DAMF

Assuming a spherical geometry of the atmosphere and pressure- and temperature-dependent refraction, the ray tracing programme DAMF calculates the light path from the Sun to the balloon. The atmosphere is divided into n spherical layers with constant pressure, temperature and trace gas concentration. The layering can be chosen by the user within reasonable limits. The conditions of the atmosphere are measured using small probes and the various sensors aboard the balloon gondola. The measurements can be completed by model data from sources like the European Centre for Medium-Range Weather Forecasts (ECMWF)[1].
The pressure and temperature are required to calculate the refractive index. The other necessary parameters are the time and location of the measurements and the location of the Sun in the sky. For direct Sun observations the light path does not depend on the trace gas profile to be retrieved and is only given by geometrical considerations.
For each of the n discrete layers in the simulated atmosphere, DAMF calculates the elements of the $\mathbf{K}$ matrix. These elements represent the length of the light path in the respective box. Therefore they are called weighting factors or box air mass factors (BoxAMF). This Weighting Matrix $\mathbf{K}$ is then used in the trace gas profile retrieval (see Chapter 7). The DAMF programme has been used and validated in several studies (e.g., *Harder et al.* 1998, *Ferlemann et al.* 2000, *Dorf et al.* 2006 and *Butz et al.* 2009).

5.2. McArtim

The radiative transfer model used for the calculations of the limb measurements is the RTM McArtim. The programme is designed for simulating radiative transfer in the

[1] European Centre for Medium-Range Weather Forecasts webpage: http://www.ecmwf.int/

UV/vis/NIR spectral range. McArtim simulates the monochromatic radiative transfer equation by modelling the physical processes that a single photon at a given wavelength undergoes in a simulated atmosphere. The simulated light starts at the detector of the instrument not at the Sun (backward RTM). McArtim operates with a statistical Monte Carlo approach, assigning probability distributions to each light extinction and scattering process. Through repeated random sampling in a simulated atmosphere, the derivatives can be modelled for each measured quantity (e.g., SCDs or radiances). Using a backward approach, every simulated photon contributes to the light path distribution, instead of only the tiny fraction which would reach the instrument in a forward approach. The performance of McArtim was successfully compared to other RTMs (*Wagner et al.* 2007, *Wagner et al.* 2009) and validated with measurements (*Deutschmann* 2008, *Deutschmann et al.* 2010).

The main parameters characterising the simulated atmosphere in the RTM are the vertical discretisation grid; the vertical profiles of temperature, pressure, and humidity; the ground albedo; the vertical distribution of the concentrations of trace gases; absorption cross sections associated to those trace gases; optical properties of aerosol and cloud particles, along with their vertical distribution; and, of course, the position of the instrument, its viewing direction and its field of view.

McArtim accounts for the scattering particles, clouds and aerosols in the form of Aerosol Extinction Profiles (AEP). Each scatterer is defined in a class with certain properties like single scattering albedo *ssa* and asymmetry parameter g (see (*Marshak and Davis* 2010)). Then an AEP is defined for the class by the user. The AEP is normally based on data from probes and satellites about cloud coverage and aerosol extinctions. The impact of these parameters and the sensitivity of the model is further discussed in Section 12.2.

Once the user has defined all the atmospheric parameters, the RT in the true 3-D atmosphere is simulated in a 1-D modelled atmosphere divided into concentric spherical cells, defined by the vertical grid. The atmospheric condition in each of these vertical layers is horizontally homogeneous and remains constant for the duration of the measurements.

While the atmosphere remains constant, geometric conditions are defined for each measurement. The viewing geometry of each measurement is defined by: the field of view and altitude of the detector, the solar zenith and solar relative azimuth angle, the latitude and longitude, as well as the elevation angle of the telescope relative to the horizon.

For each of the n discrete layers with a height h_n in the simulated atmosphere, McArtim calculates the elements of the $\mathbf{K}$ matrix. Besides BoxAMF, McArtim is able to calculate other physical quantities such as radiances and SCDs, which can then be compared to the measurements. This is an important tool for calibration and validation of the light path calculations. Details and applications of these quantities are given in (*Deutschmann et al.* 2010).

The calculated BoxAMFs are then used in a Matlab (*Meister and Voemel* 2011) programme to calculate the trace gas concentration profiles of the scattered skylight measurements (see Section 12.4).

Figure 5.1 shows a distribution of scattering events using the PathView routine of McArtim. As an example a viewing geometry of the sunrise limb measurements of scattered

skylight of the balloon flight on September 7^{th} 2009 was chosen. The detector is at an altitude of 31 km and is oriented downward at a 4.88° angle. The solar zenith angle is 80° and the azimuth angle of the instrument is 90°. In this picture the ground scattering events can be seen, because the detector is positioned below the surface looking slightly upwards. The viewing direction of the detector is also indicated by the coordinate system in the upper-right. For this plot the instrument is looking from the left side to the right. Each point in this plot is a scattering event in the atmosphere or on the ground which resulted in the photon reaching the detector. These plots are used to check the field of view of the calculations and overall distribution of scattering events. Figure 5.2 shows the same distribution, rotated 90° around the altitude axis. The detector is now facing the PathView camera.

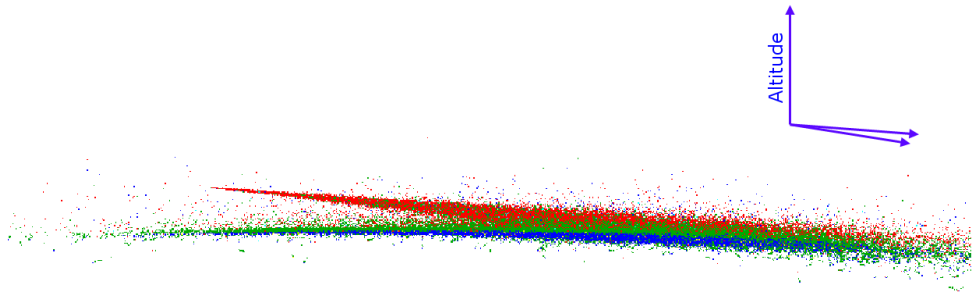

Figure 5.1.: *This plot shows the scattering events of McArtim calculations visualised PathView, a sub-routine of McArtim. The events are colour coded: red for Rayleigh-scattering, green for Mie-scattering and blue for surface scattering events. A coordinate system is indicated in blue.*

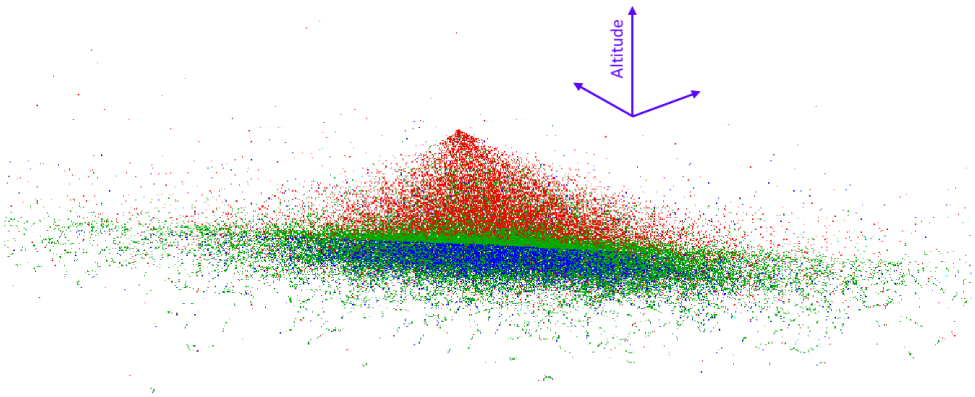

Figure 5.2.: *This plot shows the same distribution of scattering events as Figure 5.1 but from a different viewing point. This plot is rotated 90° around the altitude-axis compared with Figure 5.1. The coordinate system is indicated in the upper-right corner.*

6. DOAS Principle

The Differential Optical Absorption Spectroscopy (DOAS) principle developed by Ulrich Platt in 1979 is extensively described in *Platt and Stutz* (2008). Only a few crucial points are noted here.
As mentioned above, each element and chemical compound has characteristic absorption lines that can be combined in an absorption cross section.
As light passes through a medium, the wavelength-dependent change in intensity is described by the Lambert-Beer law.

$$I(\lambda) = I_0(\lambda)\, e^{(-\tau(\lambda))} \tag{6.1}$$

where I_0 is the initial intensity and $\tau(\lambda)$ is the optical density of the medium. $\tau(\lambda)$ can be described in terms of the absorption and scattering coefficients, $k_A(\lambda)$ and $k_S(\lambda)$.

$$\tau(\lambda) \;=\; \ln \frac{I_0(\lambda)}{I(\lambda)} \;=\; \int\limits_L \left(k_A(\lambda) \;+\; k_S(\lambda)\right)\, dl \tag{6.2}$$

Assuming N types of different absorbing molecules labelled by the index i and the molecular absorption cross sections $\sigma_i(\lambda)$, the first part of the integral can be written as

$$\tau(\lambda) = \int\limits_L k_A(\lambda)\, ds \;=\; \int\limits_L \left(\sum_{i=1}^{N} \sigma_i(\lambda)\, n_i\right)\, dl, \tag{6.3}$$

where n_i represents the number density of absorbers of type i along the light path L.
Both processes - scattering and absorption - cause a decrease in intensity. However, they are distinguished by an important characteristic: their wavelength dependence. Scattering depends strongly on the wavelength (Rayleigh λ^4; Mie λ^2), as described in e.g., Section 4.2. Conversely, many atomic or molecular absorption cross sections exhibit narrow band features. DOAS uses this fact and splits the absorption cross section σ:

$$\sigma_i \;=\; \sigma_{i,b} \;+\; \sigma_i' \tag{6.4}$$

into a broad band component $\sigma_{i,b}$ and a narrow band component σ_i' in the UV/vis spectral range. This means that Equation 6.3 can be divided into broad band and narrow band terms.

$$\tau(\lambda) \;=\; \tau_b(\lambda) \;+\; \tau'(\lambda) = \int_L \left(\sum_{i=1}^{N} \sigma_{i,b}(\lambda)\, n_i \;+\; k_S(\lambda)\right)\, dl \;+\; \int_L \left(\sum_{i=1}^{N} \sigma_i'(\lambda)\, n_i\right)\, dl \tag{6.5}$$

Now that the Lambert-Beer law can be divided, we focus on the second part in Equation

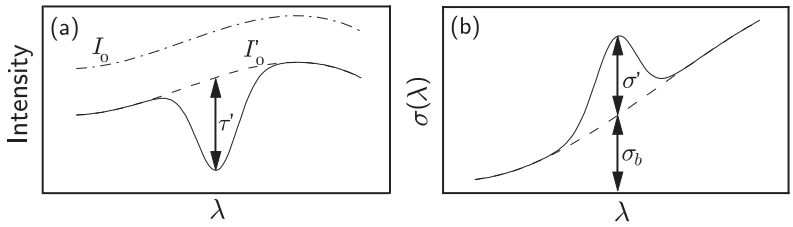

Figure 6.1.: *Illustration of the DOAS principle. The absorption cross section σ can be split into a broad band σ_b and a narrow band component σ'. Adopted from Stutz (1996).*

6.5, containing the relevant trace gas absorption. In a retrieval, broad band structures can be removed either through high pass filtering or by approximating the broad band components $\int_L (k_s + \sigma_b)\, dl$ with a polynomial.
According to these approximations, Equation 6.1 can be written as:

$$I(\lambda) \;=\; I_0(\lambda)\, e^{(-\tau'(\lambda))} \tag{6.6}$$

A requirement for Equation 6.6 above is that the optical density be smaller than 1 ($\tau(\lambda) \ll 1$). The differential optical densities encountered in atmospheric absorption spectra are usually small (10^{-3} to 10^{-1}) and this approximation is justified.
Taking all that into account, Equation 6.2 can be written as

$$\tau(\lambda) = \sum_i \sigma'_i(\lambda) \cdot \int_L n_i \,\mathrm{d}l = \sum_i \sigma'_i(\lambda) \cdot SCD_i \tag{6.7}$$

where the SCD is the Slant Column Density. The SCD is the path integral along the light path over the absorber concentration. Because the SCD is calculated from $\frac{I}{I_0}$, the result is always relative to the reference spectrum I_0. However, these reference spectra I_0 are usually recorded inside the atmosphere and are not a TOA spectrum. As a result, the reference still includes small amounts of the target species. The output of the DOAS retrieval still needs to be corrected for such an offset, which is described in Section 6.2. Unless the SCDs are corrected for this offset, the correct notation would be differential slant column densities (dSCDs).
Two approximations were made in Equation 6.7: that the molecular absorption cross sections are independent of both temperature and pressure. Since the pressure dependence of the cross section is only minor under atmospheric conditions, the second approximation can be justified. Trace gases have the same temperature as the surrounding air, which can vary significantly. This means that the targeted trace gas might have absorption features of different temperatures. To account for these temperature differences, multiple absorption cross sections of the same trace gas recorded at different temperatures are fitted in a retrieval. The fitting routines and their implementation have been described in *Rodgers* (2000), *Bösch et al.* (2001), *Dufour et al.* (2005) and no detailed discussion is given here. The spectral retrievals presented here are calculated using the WinDOAS

software package (*Van Roozendael and Fayt* 2000).

6.1. Shortcomings and Errors

6.1.1. Correlations of Retrieval Parameters

Systematic errors may arise from correlations of retrieval parameters such as the absorption cross sections included in the fit and from correlations of retrieval parameters with the fitting polynomial. In general, these correlations decrease with the number of pixels of the selected fitting range, and increase with the degrees of freedom of the fit, e.g., with the number of absorption cross sections included in the fit and with the polynomial degree.

6.1.2. Solar I_0 Effect

The high-resolution cross sections that are used for the DOAS retrieval are recorded in laboratories using a light source that is almost flat compared to the highly structured solar reference spectrum containing Fraunhofer lines. This difference has to be accounted for.
In DOAS sunlight spectroscopy, the Fraunhofer structures are removed by forming the log ratio of a spectrum to a reference spectrum with minimal absorptions (pseudo-TOA-spectrum). This ensures the absorption features of atmospheric trace gases are retained. Since both spectra forming the ratio are measured using the same instrument and are thus both filtered by the instrument slit function, complete removal of the Fraunhofer structures is not possible. Discarding absorption, a reference spectrum I_{ref} is defined as:

$$I_{ref}(\lambda) = I_0(\lambda) \otimes g(\lambda) = \int I_0(\lambda')\, g(\lambda') \mathrm{d}\lambda' \tag{6.8}$$

where I_0 is a TOA spectrum and g is the normalised instrument function. Accordingly, a measurement spectrum I_{spec}, containing absorption with the optical density τ, is defined:

$$I_{spec}(\lambda) = \int I_0(\lambda') e^{-\tau(\lambda')}\, g(\lambda')\, \mathrm{d}\lambda' \tag{6.9}$$

The logarithm of the ratio of the two spectra $ln(I_{spec}/I_{ref})$ does not completely remove the term I_0 unless the I_{ref} is constant over the integral range $\mathrm{d}\lambda$. While approximate continuity can be assumed for broadly structured absorption cross sections like O_4 and O_3 in the Chappuis bands, this is not the case for NO_2, BrO and O_3 in the Huggins bands. Figure 6.2 shows a comparison between the uncorrected and I_0 corrected cross sections. These restrictions can be avoided by using I_0 corrections for the cross sections in question. The I_0 correction for a cross section can be calculated using the following term:

$$\sigma_{corr}(\lambda) \;=\; -\frac{1}{SCD} \ln\left[\frac{I_{spec}}{I_{ref}}\right]$$

$$= -\frac{1}{SCD} \ln \left[\frac{\left(I_0(\lambda') e^{-\sigma(\lambda) \cdot SCD} \right) \otimes g(\lambda')}{I_0(\lambda) \otimes g(\lambda')} \right] \tag{6.10}$$

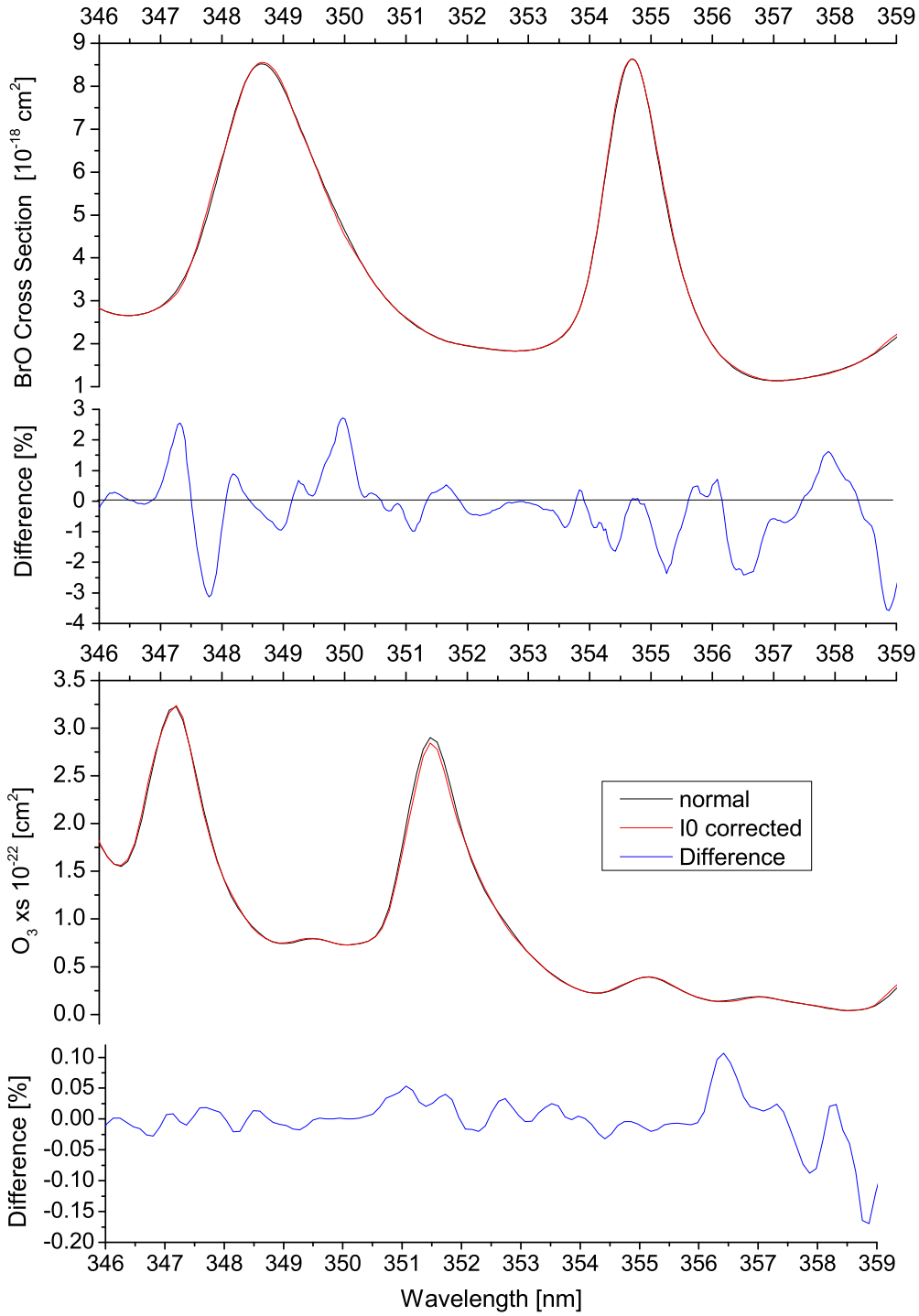

Figure 6.2.: *I_0 correction for the BrO and O_3 cross sections for the BrO retrieval in the 346 - 359 nm wavelength range of the Huggins bands. The normal uncorrected cross section is plotted in black, the I_0 corrected cross section is plotted in red and the difference in percent is plotted in blue.*

6.1.3. Instrumental Stray Light

Spectrometer stray light is caused by light from higher orders reflected by the grating or simply reflections of unblackened material inside the spectrograph. The stray light occurs as an offset added to the measured intensity, an effect which can change the optical densities of the Fraunhofer lines and molecular absorption lines significantly. This stray light can be reduced but not totally suppressed by using optical spectral filters, light traps for higher orders of the grating and by blackening the inside of the spectrograph. By including an additional intensity offset in the spectral analysis, the remaining instrumental stray light can be accounted for in the fitting procedure.

6.1.4. Ring Effect

In addition to elastic scattering processes, inelastic Raman scattering occurs in the Earth's atmosphere, see Section 4.2.3. Raman scattering can be observed in the spectra of scattered skylight as a filling in of Fraunhofer lines. This is the so-called Ring effect. In direct Sun spectra the contribution from inelastically scattered light is negligible (*Bauer* 1997, *Pundt et al.* 1998). Therefore, a correction of the Ring effect is used only for sensitivity tests.
However, for measurements of scattered skylight this effect is important. It is accounted for by including an additional pseudo-Ring-absorber in the DOAS retrieval.
Employing a first order expansion series, the Ring cross section is given by *Chance and Spurr* (1997):

$$\sigma_{Ring} = \frac{I_{Raman}}{I_{Rayleigh}} \approx \frac{I_{Raman}}{I} \tag{6.11}$$

where I_{Raman} is the Raman scattered intensity, $I_{Rayleigh}$ the Rayleigh scattered intensity, and $I = I_{Rayleigh} + I_{Raman}$ the total intensity. The Ring cross section can be calculated using the DOAS tools MFC (*Gomer et al.* 1995), DOASIS (*Kraus* 2006) and WinDOAS. The Ring cross sections used here were calculated with DOASIS and included in WinDOAS for the retrieval. In DOASIS, the Raman spectrum cannot be calculated separately. The Ring tool calculates σ_{Ring} directly from a measured spectrum. This is discussed further in Section 12.1.3.

6.2. Langley Plot

As mentioned above, the values returned by the DOAS retrieval are all relative to the concentration of the reference spectra. The total atmospheric SCD is given by the sum of the dSCD retrieved by the DOAS fit and the amount of absorber in the reference spectrum. This amount is usually obtained for direct sunlight measurements by a Langley Plot. Assuming a constant mixing ratio (VMR) above balloon float altitude, the SCDs obtained for balloon float for SZA $< 90°$ can be written as

$$SCD = AMF \cdot VCD_{Air} \cdot VMR - SCD_{Fraunh} \tag{6.12}$$

with the air mass factor AMF, the vertical column density for air VCD_{Air} and the slant column density in the Fraunhofer spectrum SCD_{Fraunh}. If Equation 6.12 is plotted with the x-axis being the *Air Mass* and the y-axis the target species $dSCD$, the point of interception with the y-axis yields the amount of the absorber in the Fraunhofer reference spectrum, called the *Fraunhofer Offset*.

Figure 6.3 shows a typical Langley plot for the balloon flight at Kiruna on September

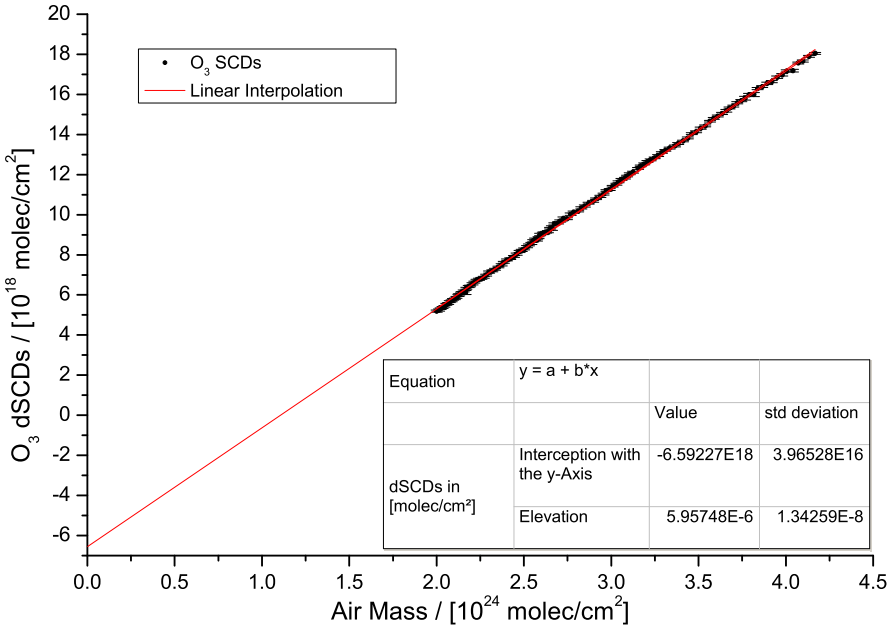

Figure 6.3.: *Langley Plot for Ozone. Plotted for the sunset measurements on September 7^{th} 2009. From the linear interpolation it can be derived that the Fraunhofer offset for these measurements is $6.59{\cdot}10^{18}\ \frac{molec}{cm^2}$. This value is added as an offset to the dSCDs returned by the DOAS retrieval.*

7^{th} 2009. The Langley plot and the corresponding fit is done for each target species and the retrieved values are added as an offset to the dSCDs to get the *true SCDs*.

A necessary prerequisite for a Langley plot is a constant concentration of the trace gas above the balloon float level for the duration of the measurement. Although balloon float altitude was already reached at $SZA = 87.09°$, the first spectra are not used for the Langley plot since they are near the detection limit for all three species and scatter around zero. These values could lead to an unrealistic result in the regression line. The error of the offset is calculated and added according to Gaussian error propagation.

7. Profile Inversion

The previous section discussed the retrieval of slant column densities (SCDs) from the measured spectra. In the next step these measurements are converted into concentration profiles, with concentration as a function of altitude. Only then can they be compared to the measurements and results of other measurements, e.g., Chapter 14.
The profile retrieval is based on a concept from *Rodgers* (2000). The equations given here follow the notation of *Rodgers* (2000), along with the variables used in the inversion script. The inversion is based on three methods of retrieving a trace gas concentration profile:

- Singular Value Decomposition (SVD)
- Maximum A Posteriori (MAP)
- Onion Peeling

While the Singular Value Decomposition and the Maximum A Posteriori approach can be used for a balloon ascent and solar occultation events, the onion peeling method can be used only for an ascent.
If the measurements or SCDs are represented by y and the profile they are based on is x, their transformation can be accounted for by a function $\mathbf{F}$

$$y = \mathbf{F}(x, b) + \epsilon \tag{7.1}$$

There are m measurements and we want to retrieve a profile with n layers of the atmosphere. The model function $\mathbf{F}$ uses the observation geometry and describes the path of the light through the atmosphere for each spectrum. Equation 7.1 can be written in linear form

$$y - \mathbf{F}(x_0) = \frac{\partial \mathbf{F}(x)}{\partial x}(x - x_0) + \epsilon = \mathbf{K}(x - x_0) + \epsilon \tag{7.2}$$

with $\mathbf{K}$ being an $m \times n$ matrix. The radiative transfer and the Weighting Matrix $\mathbf{K}$ of the direct sunlight measurements is calculated using the programme DAMF (see Section 5.1). The radiative transfer calculations for limb measurements of scattered skylight are more complex and can not be calculated by geometrical means only. The RTM McArtim is used to calculate the light paths and the $\mathbf{K}$ Matrix for limb measurements of scattered skylight. This is described in Section 5.2.
Equation 7.2 can be expanded using the covariance matrix:

$$\mathbf{S}_a = \mathbb{1}\left((x - x_a)(x - x_a)^T\right) \tag{7.3}$$

given an a priori x_a. Equation 7.2 can then be rewritten:

$$\hat{x} = x_a + \left(\mathbf{K}^T S_e^{-1}\mathbf{K} + \mathbf{S}_a^{-1}\right)^{-1}\mathbf{K}^T\mathbf{S}_e^{-1}(y - \mathbf{K}x_a) \tag{7.4}$$

$\mathbf{S}_e$ is the measurement error covariance matrix. The term containing the error covariance matrix is also called the Gain Matrix:

$$\mathbf{G} = \left(\mathbf{K}^T\mathbf{S}_e^{-1}\mathbf{K} + \mathbf{S}_a^{-1}\right)^{-1}\mathbf{K}^T\mathbf{S}_e^{-1} \tag{7.5}$$

Using the Gain Matrix, Equation 7.4 can be written as:

$$\hat{x} - x_a = \mathbf{G}(y - \mathbf{K}x_a) = \mathbf{G}[\mathbf{K}(x - x_a) + \epsilon] \tag{7.6}$$

$\mathbf{G}$ is a description of the information content of the measurement. The Gain Matrix is the contribution function matrix which characterises the sensitivity of the retrieval method to the measurement and the measurement error. In other words, it shows whether the information is a priori or comes from a measurement. If $\mathbf{G}$ is multiplied with the $\mathbf{K}$ matrix:

$$\mathbf{A} = \mathbf{G} \cdot \mathbf{K} = \frac{\partial \hat{x}}{\partial x} \tag{7.7}$$

the result is the Averaging Kernel Matrix $\mathbf{A}$.
A single row of the Averaging Kernel Matrix is called the averaging kernel of the corresponding retrieval altitude segment. The averaging kernels are used as diagnostics of the quality of the profile retrieval. To solve Equation 7.3, the user must decide if an a priori is available and should be used.

7.1. Maximum A Posteriori

The Maximum A Posteriori solution (MAP) to Equation 7.1 is based on the Bayesian approach. It relies on the probability density functions of the involved quantities y, x and x_a. Assuming that all the probability density functions are Gaussian, the expectation value $\hat{x}$ of the retrieved profile is given by

$$\hat{x} = x_a + \left(\mathbf{K}^T\mathbf{S}_e^{-1}\mathbf{K} + \mathbf{S}_a^{-1}\right)^{-1}\mathbf{K}^T\mathbf{S}_e^{-1}(y - \mathbf{K}x_a) \tag{7.8}$$

and the Averaging Kernel Matrix is

$$\mathbf{A} = \mathbf{S}_a\mathbf{K}^T\left(\mathbf{K}^T\mathbf{S}_e^{-1}\mathbf{K} + \mathbf{S}_a^{-1}\right)^{-1}\mathbf{K} \tag{7.9}$$

The MAP approach weighs the information from the a priori and the measurement to combine the two. If there is only little or no measurement information, the a priori will dominate the returned profile. The weight of the measurements is characterised by the observation geometry, represented by $\mathbf{K}$, and the measurement error covariance $\mathbf{S}_e$. The

weight of the a priori information is determined by its covariance $\mathbf{S}_a$. If the latter is large, the a priori will only have a minor impact on the retrieved profile. Therefore, it is normal to assume a large error in order to keep the influence of the a priori as small as possible. In the case of an occultation event, the downward boundary of the measurement is the tangent point (∼12 km) and the upward boundary is the float altitude above which no profile information can be retrieved. In this case the weighting functions are unfavourable for retrieving profile information and the a priori has significant impact on the retrieved profile.
In addition to the previous definitions, $\mathbf{G}_y = \frac{\partial \mathbf{R}}{\partial y}$ is the sensitivity of the retrieval to the measurement and $\mathbf{A} = \mathbf{G}_y\ \mathbf{K}_x = \frac{\partial \hat{x}}{\partial x}$ is the sensitivity of the retrieval to the true state.

$$\begin{aligned} \hat{x} - x_a = \quad & \mathbf{R}(\mathbf{F}(x_a, \hat{b}), \hat{b}, x_a, c) - x_a && \text{... bias} \\ & + \mathbf{A}(x - x_a) && \text{... smoothing} \\ & + \mathbf{G}_y \epsilon_y && \text{... retrieval error} \end{aligned} \tag{7.10}$$

By rearranging the components this can be rewritten as

$$\begin{aligned} \hat{x} - x \ = \quad & (\mathbf{A} - 1)(x - x_a) && \text{... smoothing error} \\ & + \mathbf{G}_y \mathbf{K}_b (b - \hat{b}) && \text{... model paramter error} \\ & + \mathbf{G}_y \Delta \mathbf{F}(x, b) && \text{... forward model error} \\ & + \mathbf{G}_y \epsilon && \text{... retrieval noise} \end{aligned} \tag{7.11}$$

For our purposes, only retrieval noise and smoothing error are important. These are the dominant error sources. The accuracy of the measurements means that the error of the auxiliary parameters, measurement location, temperature and pressure can all be ignored. The measurement location and time are recorded by two GPS modules. The pressure and temperature data which is required for the calculation of the refractive index of the altitude layer is recorded with an accuracy of ± 0.2 mbar and ± 0.2 K. The resulting errors are an order of magnitude smaller than the retrieval noise.
The first term on the right side in Equation 7.10 represents the smoothing error. In analogy to Equation 7.3, it can be quantified by the smoothing error covariance matrix $\mathbf{S}_s = (\mathbf{A}\text{-}\mathbb{1})\ \mathbf{S}_a\ (\mathbf{A}\ \text{-}\ \mathbb{1})^T$. $\mathbf{S}_a$ is the a priori covariance matrix which, in our case, is chosen diagonal such that the elements are the variances of the a priori trace gas concentrations. The second and third terms are neglected. The last term in Equation 7.11 is a result of measurement error and can be represented by the retrieval noise covariance $\mathbf{S}_m = \mathbf{G}_y\ \mathbf{S}_e\ \mathbf{G}_y^T$, where $\mathbf{S}_e$ is the measurement error covariance. Assuming that the measurements are independent, $\mathbf{S}_e$ is a diagonal matrix with the squares of the SCD errors as elements. The total covariance of the retrieved profile $\hat{\mathbf{S}}$ is the sum of $\mathbf{S}_s$ and $\mathbf{S}_m$:

$$\hat{\mathbf{S}} = \mathbf{S}_s + \mathbf{S}_m \tag{7.12}$$

As noted above, the MAP solution represents a weighted average between the measurements and an a priori profile. The weight of the measurements in the returned profile is

defined by the observation geometry $\mathbf{K}$ and the correlation between the measurements, defined by the measurement error covariance matrix $\mathbf{S}_e$. The weight of the a priori information is also defined by the covariance of the profile $\mathbf{S}_a$. To keep the influence of the a priori as small as possible, the value of $\mathbf{S}_a$ should be large. The goal in an a priori approach should always be a retrieved profile unaffected by the a priori information in the core altitude range between the lowest tangent heights covered and balloon float altitude. At the boundaries of this range, where only information from the measurements can contribute, the a priori has significant impact on the retrieved profile. The error of the retrieved profile

$$\hat{\mathbf{S}} = (\mathbf{K}^T \mathbf{S}_e^{-1} \mathbf{K} + \mathbf{S}_a^{-1})^{-1} \tag{7.13}$$

includes the smoothing error and the measurement error. The error attributed to the retrieved profile values is given by the square roots of the diagonal elements of $\hat{S}$.

7.2. Singular Value Decomposition

The second method used for retrieving a profile is the Singular Value Decomposition (SVD). Any matrix $\mathbf{K}$ with the dimensions $m \times n$ can be written as the product of an orthogonal $m \times n$ matrix $\mathbf{U}$, a diagonal $m \times n$ matrix Λ and an orthogonal $n \otimes n$ matrix $\mathbf{V}^T$,

$$\mathbf{K} = \mathbf{U}\,\Lambda\,\mathbf{V}^T \tag{7.14}$$

Λ is the diagonal matrix with the singular values λ_i of the matrix $\mathbf{K}$. The matrices $\mathbf{U}$ and $\mathbf{V}^T$ are constructed from the singular vectors of $\mathbf{K}$. By utilising the following conditions

$$(\mathbf{V}\,\Lambda^{-1}\,\mathbf{U}^T)(\mathbf{U}\,\Lambda\,\mathbf{V}^T) = 1 \tag{7.15}$$

$$\mathbf{K}^* = \mathbf{V}\,\Lambda^{-1}\,\mathbf{U}^T \tag{7.16}$$

Equation 7.4 can be rewritten using the pseudo-inverse of K

$$\hat{x} = \mathbf{K}^* y = \mathbf{V}\,\Lambda^{-1}\,\mathbf{U}^T y \tag{7.17}$$

Unfortunately this very direct approach will often return an unsatisfying result.
Typically what happens is that noise induced high-frequency components belonging to small singular values obscure the solution. To suppress these contributions, a smoothness requirement on the reconstruction is introduced. This is referred to as regularisation, because the obtained solutions are regularised. Here the two methods used in this study are presented:

- The truncated SVD method (tSVD)
- The Tikhonov regularisation

Both work by having the user select a regularisation parameter that controls a trade-off between fidelity to the data and smoothness of the returned profile. The effect of the

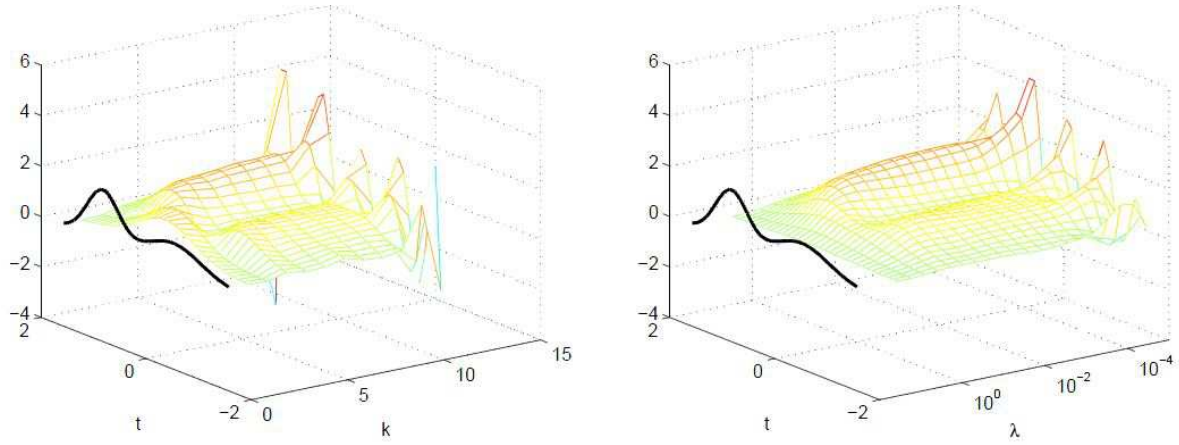

Figure 7.1.: *These are the two regularisation approaches. The left panel shows the truncated SVD approach and the right panel shows a Tickhonov approach. k and λ are the regularisation parameters for the two methods respectively. The picture shows how choosing the correct regularisation parameter can have a large impact on the retrieved profile. Adopted from Jørgensen (2009).*

implementation of a regularisation can be seen in Figure 7.1.
For the tSVD method, Equation 7.17 can be written as

$$\hat{x} = \mathbf{K}_t^* y = \mathbf{V}_t \Lambda_t^{-1} \mathbf{U}_t^T y \tag{7.18}$$

The subscript t indicates truncation. Only the largest singular values and their corresponding vectors are retained. Values which are equal to zero or smaller than a threshold are discarded. The threshold is chosen in terms of a maximum condition number, which is the ratio of the largest to the smallest non-zero singular value. If y is replaced with $(\mathbf{Kx}+\epsilon)$ in Equation 7.18, the result is:

$$\hat{x} = \mathbf{V_t \Lambda_t}^{-1} \mathbf{U_t}^T (\mathbf{K\,x} + \epsilon) = \mathbf{V_t\, V_t}^T \mathbf{x} + \mathbf{V_t \Lambda_t}^{-1} \mathbf{U_t}^T \epsilon \tag{7.19}$$

This approach is used when retrieving a profile of the direct sunlight measurements. The maximum condition number k can be allocated as a parameter in the programme DAMF by the user. The Averaging Kernel Matrix reads

$$\mathbf{A} = \mathbf{V}_t \mathbf{V}_t^T \tag{7.20}$$

which is not the Identity Matrix after truncation. This demonstrates an important point; truncation is a trade-off between reducing the contributions from measurement error and adjusting the altitude resolution of the retrieval to the resolution of the actual observation. Otherwise small singular values produce large contributions to the retrieved state from measurement error and render the retrieved profile unrealistic. For truncation, the inverse of those singular values should be set to zero, since they contribute more to the error than to the actual profile (*Rodgers* 2000).
For the limb measurements of scattered skylight the distinction between smaller and larger

eigenvalues of the **K** matrix is more complicated. Therefore, the Tikhonov regularisation method is used (*Tikhonov et al.* 1977).
In this approach λ is the regularisation parameter that determines the relative importance of the two terms: the fidelity to the data $\|Ax - y\|_2$ and the solution smoothness $\|x\|_2$ (*Hansen* 1994, *Calvetti et al.* 2000). Equation 7.5 is expanded by a term $\lambda\mathbf{H}$:

$$\hat{x} = (\mathbf{K}^T\mathbf{S}_e^{-1}\mathbf{K} + \lambda\mathbf{H})^{-1}\mathbf{K}^T\mathbf{S}_e^{-1}y \tag{7.21}$$

The term $\mathbf{H} = \mathbf{L}^T\ \mathbf{L}$ is the smoothing constraint and λ is the weighting factor. **H** is calculated from the second derivative operator and takes the form shown in Table 7.1.
The Averaging Kernel Matrix derived from Equation 7.21 reads

$$\mathbf{A} = (\mathbf{K}^T\mathbf{S}_e^{-1}\mathbf{K} + \lambda\mathbf{H})^{-1}\mathbf{K}^T\,\mathbf{S}_e^{-1}\mathbf{K} \tag{7.22}$$

Table 7.1.: *The smoothing constraint **H** for a ten point grid.*

1	-2	1	0	0	0	0	0	0	0
-2	5	-4	1	0	0	0	0	0	0
1	-4	6	-4	1	0	0	0	0	0
0	1	-4	6	-4	1	0	0	0	0
0	0	1	-4	6	-4	1	0	0	0
0	0	0	1	-4	6	-4	1	0	0
0	0	0	0	1	-4	6	-4	1	0
0	0	0	0	0	1	-4	6	-4	1
0	0	0	0	0	0	1	-4	5	-2
0	0	0	0	0	0	0	1	-2	1

The SVD approach does not use a priori information and is constrained only by the measurements, their covariance and the smoothing constraints. These constraints are imposed in the form of a truncation or a regularisation. This lack of a priori information means that the SVD can be used to check the influence of a priori information in a MAP approach. According to Equation 7.12, the error of the retrieved profile is equal to the contribution of the retrieval noise.

$$\hat{\mathbf{S}} = (\mathbf{V}^T\mathbf{\Lambda}^{-1}\mathbf{U}^T)\mathbf{S}_e^{-1}(\mathbf{V}\mathbf{\Lambda}^{-1}\mathbf{U}^T) \tag{7.23}$$

However, the choice of the truncation threshold has to be considered as a kind of a priori information that also impacts the SVD retrieval method. The lack of additional information at the boundaries of the altitude grid can lead to artificial oscillations on the profile, while at the same time an overzealous regularisation can obscure the true state of the profile.
Neither tSVD nor the Tikhonov regularisation address the problem of how to choose the

right regularisation parameter. While the discrepancy principle is a good start, we cannot hope to solve $Kx = y$ exactly, because the measurement contains an error. The goal is to achieve a residual error of $\|Kx - y\|_2 \approx \|x\|_2$. The *L-curve* method is a more reliable approach than the discrepancy principle (*Hansen* 1992, *Hanke* 1996).

7.3. The L-curve Method

This approach does not require a priori knowledge of the error. We are looking for a retrieval that sticks to the fidelity of the data while being smoother than the naive SVD approach. Given a reconstruction for $\hat{x}$, we can choose to measure the fidelity to the data by the residual norm $\|Kx - y\|_2$ and the smoothness by the solution norm $\|x\|_2$.
Those two quantities, plotted for a series of regularisation parameters, produce the L-curve. In a double logarithmic plot the graph tends to be shaped like a capital L, hence the name. Figure 7.2 shows the L-curve calculated for the O_3 sunrise measurements. Both values should be as small as possible, so the optimal regularisation parameter is in the corner of the L, the value closest to zero.

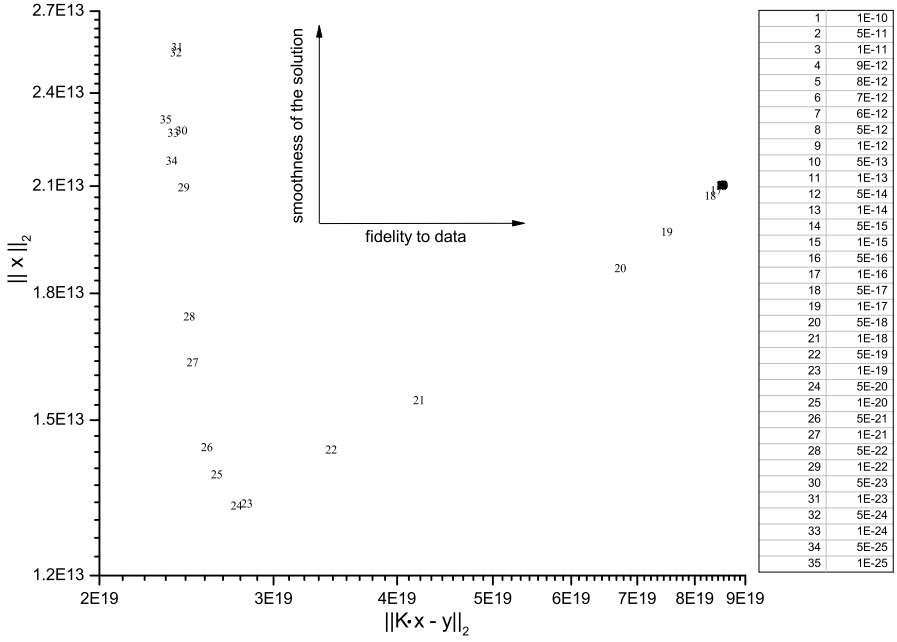

Figure 7.2.: *L-curve plot. The minimum indicates the regularisation parameter that offers a smooth profile using the measurement data while discarding only values with little influence, which would otherwise obscure a clear signal. The regularisation parameters are listed in the table on the right. In this case the best value for the regularisation of the profile is parameter number 24: $5{\cdot}10^{-20}$.*

8. Photochemical Modelling

In this chapter the basics of the photochemical model used in this study are listed, following the description given by *Butz* (2006).
The accuracy of chemical models used to calculate the evolution of trace gases over time is a very good benchmark for checking if our knowledge is sufficient to describe processes in the atmosphere. The model output will only coincide with the measurements if all abundances and rate coefficients for the important reactions are correctly determined. Here all the knowledge about atmospheric composition and the interactions and transformations between the different species is combined. Reliable predictions for future scenarios are only possible if every process is understood and correctly implemented.
Mathematical models of the atmosphere can be divided into different types according to the products they calculate and the range in which they operate. In this work the three-dimensional (3-D) chemical transport model (CTM) SLIMCAT (*Chipperfield et al.* 2005; *Chipperfield* 2006) and the chemical box model Labmos are used to interpret the observations and to test model formulations.
SLIMCAT is a 3-D off-line chemical transport model. It uses wind and temperature data from the European Centre for Medium-Range Weather Forecasts (ECMWF) to calculate the atmospheric transport and the concentration changes of different species in both the troposphere and the stratosphere (*Uppala* 2005). SLIMCAT includes all relevant photochemical and dynamical processes and the model range extends from the ground up to an altitude of approximately 55 km on 32 potential temperature levels. In the horizontal direction SLIMCAT uses a $1^\circ \times 1^\circ$ (latitude $\times$ longitude) grid.
SLIMCAT's and Labmos' chemical schemata have been updated and correspond to the recommendations given by the JPL-2011 report on Chemical Kinetics and Photochemical Data (*Sander et al.* 2011).
Labmos is a 1-D chemistry model, designed for studies of stratospheric photochemistry. It comprises a comprehensive set of gas phase and heterogeneous reactions. However, Labmos does not include dynamical processes per se, although it may be combined with air mass trajectories for a full 3-D formulation. Typically, Labmos is initialised with SLIMCAT output that can be refined using higher accuracy measurements. The version used here is an update of the model used in (*Bösch et al.* 2003), (*Butz* 2006) and (*Kritten* 2009). The stratospheric photochemistry is modelled on 19 potential temperature levels between Θ = 336 K ($\simeq$10 km) and Θ = 1520 K ($\simeq$42 km). The photochemistry is modelled along pre-calculated air mass trajectories in steps of 150 seconds.
The notation used here follows *Finlayson-Pitts and Pitts* (1986), *Finlayson-Pitts and J. N. Pitts* (1999) and (*Sander et al.* 2011).

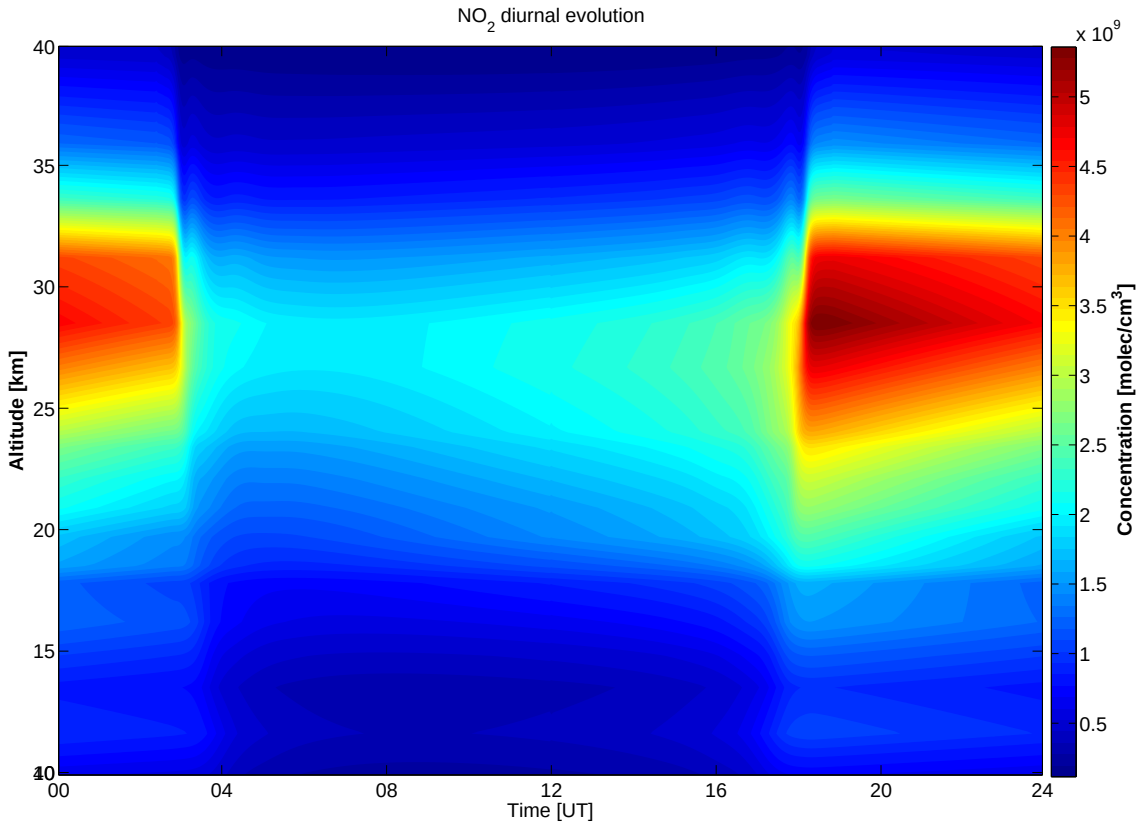

Figure 8.1.: *Model output for the diurnal variation of NO_2 for the atmospheric conditions in Kiruna for the time around the balloon flight for a 24 hour window. The colour coding described in the colour map on the right side represents the concentration of NO_2.*

Rate coefficients are used to calculate the concentration changes for the different species modelled. Reactions involving two educts and two products

$$\mathrm{B} + \mathrm{C} \quad \longrightarrow \quad \mathrm{D} + \mathrm{E} \tag{8.1}$$

are called bimolecular reactions. The corresponding rate coefficient k_{B+C} is defined through

$$k_{B+C}\,[\mathrm{B}]\,[\mathrm{C}] \;=\; -\frac{\mathrm{d}[\mathrm{B}]}{\mathrm{dt}} = -\frac{\mathrm{d}[\mathrm{C}]}{\mathrm{dt}} = \frac{\mathrm{d}[\mathrm{D}]}{\mathrm{dt}} = \frac{\mathrm{d}[\mathrm{E}]}{\mathrm{dt}} \tag{8.2}$$

where [B] represents the concentration of a species B. According to the definition of k_{B+C}, the temporal evolution of the concentration of species B is given by

$$[B](t) = [B]_0\, e^{-k_{B+C}\,[C]\,t}, \tag{8.3}$$

provided a constant concentration of C can be assumed. The index zero in Equation 8.3 denotes the initial or starting concentration of species B. If the rate coefficient k is changing with the surrounding temperature, a temperature dependence can be considered by Arrhenius' law

$$k(T) \;=\; A(T)\, e^{\frac{-E/R}{T}}, \tag{8.4}$$

where T is the temperature, E/R defines the activation temperature, and $A(T)$ is the Arrhenius factor (see *Sander et al.* (2011)).
For termolecular reactions the rate coefficients can be calculated from tabulated low- and high-pressure limits and correction terms for temperature dependencies. In contrast to Reaction 8.1, three-body-collision reactions are pressure dependent, because the third body (M) is most likely an ambient N_2 or O_2 molecule. They involve three steps:

$$\begin{array}{rcll} \mathrm{B + C} & \longrightarrow & \mathrm{(BC)^*} & \text{association with } \mathrm{k_f} \\ \mathrm{(BC)^* + M} & \longrightarrow & \mathrm{B + C} & \text{unimolecular decay with } \mathrm{k_r} \\ \mathrm{(BC)^* + M} & \longrightarrow & \mathrm{(BC) + M^*} & \text{stabilisation with } \mathrm{k_s} \end{array} \tag{8.5}$$

The actual rate coefficient k_3 of the three-body-collision reactions is only the fraction of the process which results in a stable (BC). This is according to Troe's formula (*Troe* 1979):

$$k_3 = \mathrm{k_f} \,/\, 1 + \frac{\mathrm{k_r}}{\mathrm{k_s\,[M]}} \tag{8.6}$$

For low pressure ($k_r \gg k_s[M]$), this means that $k_3 = (k_f \cdot k_s/k_r) \cdot [M]$ and the reaction rate depends on the presence of a third body (M) (*Troe* 1977, *Gilbert et al.* 1983). For high pressure, when $k_r \ll k_s[M]$, the following can be deduced: $k_3 = k_f = k_\infty$ (*Cobos and Troe* 1985). Therefore, the temperature dependent low-pressure rate coefficient is described by:

$$k_0(T) \;=\; k_0^{300} \left(\frac{T}{300}\right)^{-n} \qquad \left[\frac{\mathrm{cm^6}}{\mathrm{molec^2\,s}}\right] \tag{8.7}$$

The temperature dependent high-pressure rate coefficient is described by:

$$k_\infty(T) \;=\; k_\infty^{300} \left(\frac{T}{300}\right)^{-m} \qquad \left[\frac{\mathrm{cm^3}}{\mathrm{molec\,s}}\right] \tag{8.8}$$

The rate coefficients k_0^{300} and k_∞^{300} for all reactions that have been measured and their corresponding parameters n and m are listed in the JPL compilations, which are updated on a regular basis. The most recent version is *Sander et al.* (2011).
For reactions like the $BrONO_2$ photolysis (Reaction 3.54), which depend on the presence of electro-magnetic radiation:

$$\mathrm{B + h\nu \longrightarrow C + D} \tag{8.9}$$

the photolysis frequency J can be calculated from the solar zenith angle (SZA) and atmospheric conditions by integration over the product of the actinic flux $F(\lambda)$, the absorption cross section $\sigma(\lambda)$ and the quantum yield $q(\lambda)$ with respect to the wavelength.

$$J_B = \int F(\lambda) \cdot \sigma(\lambda) \cdot q(\lambda)\, d\lambda \tag{8.10}$$

Besides termolecular reactions and photolysis, Labmos can also calculate heterogeneous reactions between gaseous and condensed materials. Such reactions imply adsorption of gaseous species on the surface of liquid or solid particles into the liquid particles. Heterogeneous reactions can be described in the same manner as gas phase reactions, using a the rate coefficient k_{het}. The rate coefficient k_{het} is proportional to the uptake coefficient γ, the aerosol surface area density A and the mean thermal velocity $\vec{v}$ of the reactants (*Finlayson-Pitts and Pitts* 1986). The uptake coefficient γ is the fraction of surface collisions that lead to an irreversible chemical change in the gaseous educt (*Zellner et al.* 2001).

$$k_{het} = \frac{\gamma \cdot A \cdot \vec{v}}{4} \tag{8.11}$$

An example for a heterogeneous reaction is the hydrolysis of $BrONO_2$ (Reaction 3.50).

9. Instrumentation

In this chapter a short overview is given of the instruments used in the course of this thesis based on the more detailed description given by *Bauer* (1997), *Dorf* (2005) and *Simmes* (2007).
High flying research balloons are the main method used to directly probe the stratosphere and perform in situ measurements. Planes can only reach up to a maximum altitude of 20 km while sounding rockets can only measure within a very short time frame in the stratosphere. Depending on wind patterns and other constraints, a research balloon can carry a gondola to an altitude of 30 to 40 km and remain there for several hours performing measurements.
Two instruments are used to take measurements for the present thesis, both based on the DOAS measuring technique. They have different specifications, advantages and disadvantages, however:

- The DOAS balloon instrument (BigDOAS) was designed for direct sun observations
- The miniDOAS instrument is a smaller, lighter and more compact version of the direct sunlight instrument. It is used for measuring scattered skylight in limb direction

The DOAS balloon instrument is only operated on board the LPMA/DOAS gondola, as described in Section 9.1. The miniDOAS instrument can be used on different, azimuth stabilised balloon platforms (see Figure 9.9).

9.1. The LPMA/DOAS Balloon Payload

LPMA stands for Limb Profile Monitor of the Atmosphere. The technology is based on a gondola for astronomical observations operated by the Observatoire de Genéve. The LPMA/DOAS gondola was modified and optimized for atmospheric measurements by Camy-Peyret in 1993 (*Camy-Peyret et al.* 1993). Its task is to carry the LPMA Fourier transform Interferometer (FTIR) and the DOAS balloon instrument into the stratosphere and perform direct sunlight observations. The schematics of the gondola are shown in Figure 9.1. The gondola has a mass of approximately 500 kg. Depending on the maximum altitude level, the gondola is carried by a helium balloon with a volume between 100,000 m^3 and 400,000 m^3.

9.1.1. The LPMA Fourier Transform Interferometer

This French instrument is based on a commercial BOMEM DA2.01 Michelson type interferometer and is optimised for balloon measurements (*Camy-Peyret et al.* 1995). The setup allows for the recording of interferograms in the infrared spectral range every 50 s. The spectral resolution of 0.02 cm^{-1} is restricted by the maximum path difference of the movable mirror of 50 cm. The commercial detector optics have been replaced by a lab-built optical setup that allows two detectors to be used at the same time. This enables the instrument to record in different spectral ranges simultaneously. The detectors are placed in Dewar containers which are cooled by liquid nitrogen.
Depending on the exact configuration of spectral filters, beamsplitters and detectors used during a flight the instrument can measure a large variety of trace gases, which all absorb in the infrared spectrum, such as O_3, NO_2, NO, HNO_3, N_2O_5, N_2O, CH_4, $ClONO_2$, HCl, H_2O, CO, CO_2, COF_2, HF, CF_2Cl_2 and C_2H_6 (*Camy-Peyret et al.* 1995, *Jeseck* 1995, *Butz* 2006).
A pivot system is used to keep the gondola's front facing the Sun. In addition, a sun-tracker with a moveable mirror allows for optimal light intake. The light collected by the sun-tracker is pointed directly at the interferometer. BigDOAS's two telescopes are mounted between the sun-tracker's folding mirror and the entrance window of the interferometer, as shown in Figure 9.1. This ensures that the two instruments probe the same air masses and prevents the need for an additional tracker.

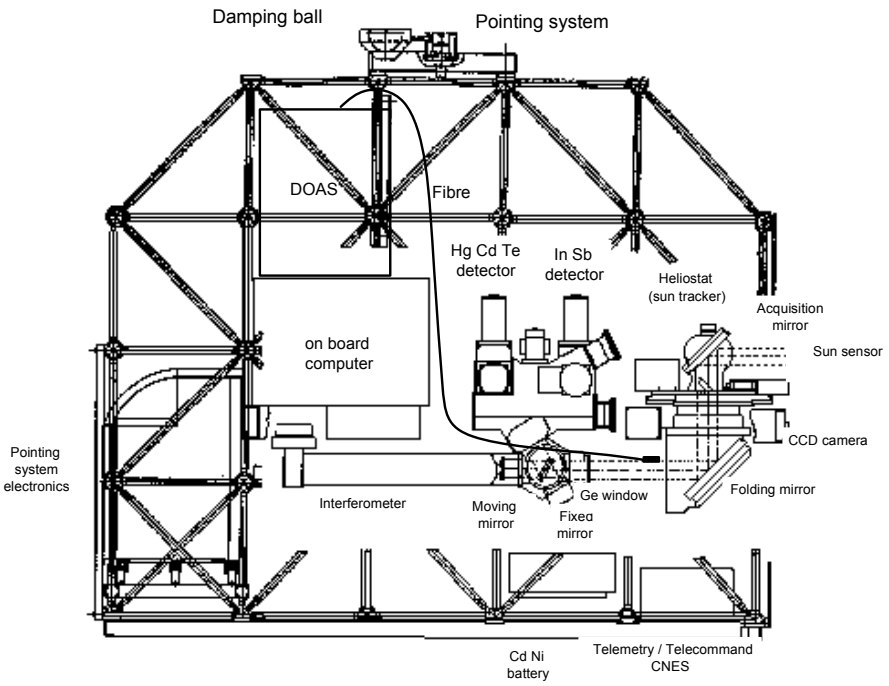

Figure 9.1.: *Schematic drawing of the LPMA/DOAS balloon gondola. Sunlight is directed into the gondola by a sun-tracker and is subsequently analysed by the FTIR and the DOAS instrument. Adopted from Ferlemann et al. (2000).*

9.1.2. The DOAS Balloon Instrument for Direct Sunlight Observations

The DOAS balloon instrument (BigDOAS) was developed at the Institute of Environmental Physics at the University of Heidelberg (*Ferlemann et al.* 2000). It is designed for measuring atmospheric trace gases using direct sunlight spectroscopy. Two holographic grating spectrometers are combined to cover both the UV and the visible spectral range. The entire instrument is configured for balloon-borne observations requiring the following specifications:

- Low mass ($\sim$ 45 kg)
- Low power consumption ($\sim$ 6 W)
- Insensitivity to changes in ambient temperature and pressure, preventing a drift in the optical setup
- High structural integrity

The direct sunlight collected by the sun-tracker is aimed at the two telescopes for separate light uptake into the system. The space availability inside the gondola was one of the main specifications for the telescopes, as well as:

- Signal maximisation in the stratosphere with respect to the minimum readout time of the detector to guarantee a high signal-to-noise ratio
- Minimisation of atmospheric stray light and the necessity of observing the entire Sun disk, to prevent effects of centre-to-limb darkening
- Compliance with the holographic grating's f-number

The two telescopes were redesigned to better withstand changing atmospheric conditions and corrosion. At the same time, the spectrograph's light intake was maximised to optimise the signal to noise ratio (*Kreycy* 2007). Both telescopes hold a number of optical elements to ensure that all photons from the observed spectral range reach the detector while all other radiation is minimised (see Figure 9.2). Just as with the spectrograph itself, the telescopes need to be unaffected by thermal expansion or contraction to prevent damage to the glass lenses or filters. The telescopes are blackened on the inside to prevent light scattering. Quartz fibre bundles are attached to the telescopes to guide the light into the spectrographs.
A metal housing 536 mm deep and 290 mm in diameter contains all the remaining parts: the gratings of the two spectrograph setups, as well as the detectors and the corresponding electronics. From a rectangular slit at the end of the fibre bundle the light falls onto a holographic grating and is reflected to a photodiode.
The width of the entrance slits is chosen to fulfil the empirical sampling criteria given by e.g., *Roscoe et al.* (1996). Both spectrometers use a 1024 pixel diode. The UV spectrometer has a FWHM of 0.55 nm or 5.5 pixel, covering the spectral range from 316.5 - 417 nm.

The vis spectrometer has a FWHM of 1.47 nm or 5.7 pixel and covers a spectral range from 400 - 653 nm.

The aluminium housing is evacuated and thermally stabilised by a surrounding carbon

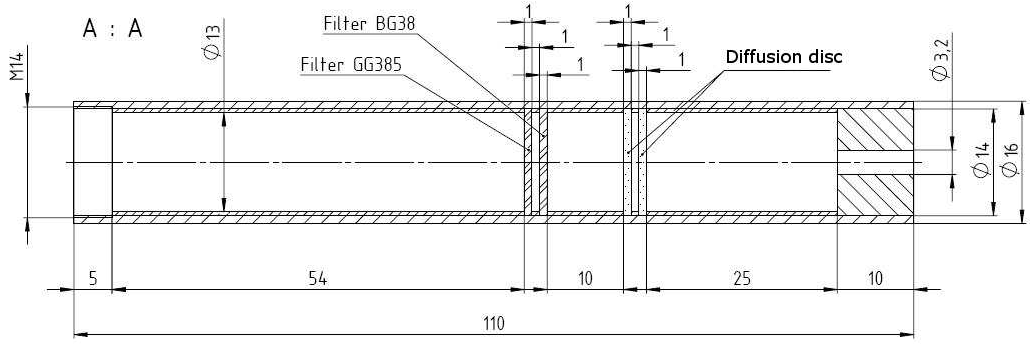

Figure 9.2.: *Schematic of the vis telescope. The telescope holds several optical elements: two filters (BG38, GG385) and two diffusion discs. All measurements are given in mm.*

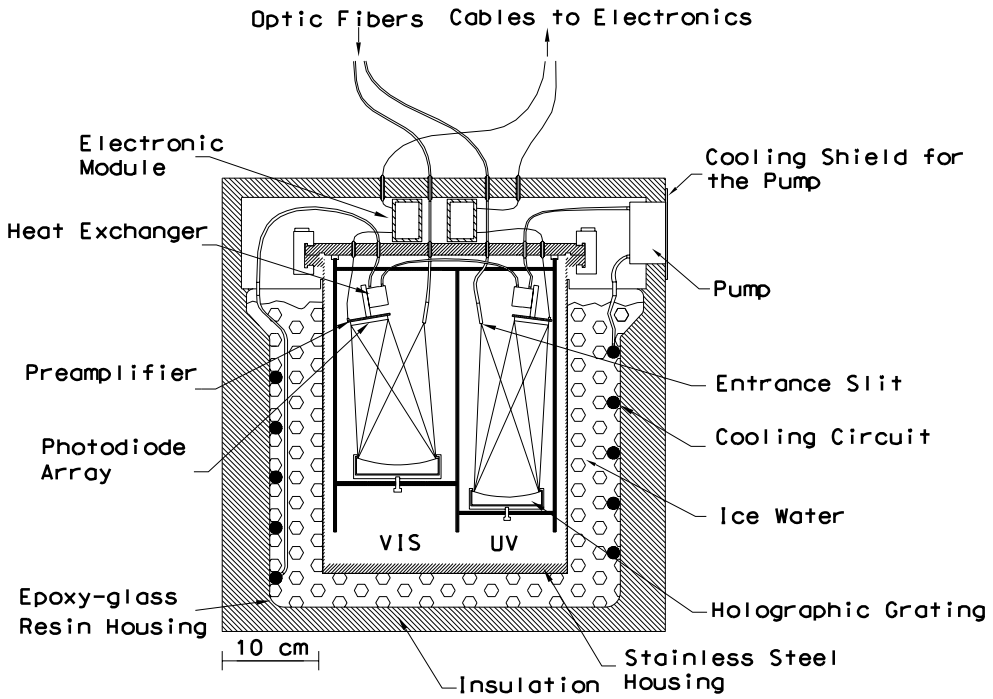

Figure 9.3.: *Schematic drawing of the BigDOAS instrument. Two holographic grating spectrometers (UV and vis) are integrated into a vacuum-sealed housing, placed in an ice-water mixture for temperature stabilisation. Adopted from Ferlemann et al. (2000).*

fibre vessel filled with an ice water mixture. This means an additional weight, but it keeps the entire setup stable at 0°C. This is essential since the temperature gradient of the atmosphere could cause a shift in the optical system during a balloon ascent or descent. Evacuating the spectrometer prevents water vapour from condensing inside the instrument.

The photodiodes themselves are cooled by Peltier elements. They are kept stable at (-10°C) to minimise the dark current and enhance the signal-to-noise ratio. A cooling circle

keeps all the optical parts, the electronics and the warm side of the Peltiers temperature-stable by transporting the produced heat outwards. The inside of the spectrometer housing is blackened to minimise spectrometer stray light. In addition to that, light traps are installed to prevent maxima of zero, second and higher orders from reaching the detector. A schematic of the spectrograph housing is shown in Figure 9.3.
A separate computer unit holds the electronics for controlling the spectrometers and storing the measured spectra to allow for easier excess and handling. This is connected via multiple cables that control the instrument as well as the cooling pumps and temperature sensors.
A more detailed description of the spectrograph can be found in *Ferlemann et al.* (2000) and *Bauer* (1997). The original setup has since been modified for improvement or repairs. Major adjustments include:

- Replacement of the original steel housing with an aluminium housing, reducing the weight by 6 kg
- Replacement of a contaminated holographic UV grating (Jobin Yvon 52300080)
- Readjustment of the vis grating to cover the spectral range from 400 - 653 nm (previously 417 - 671 nm) to include the OClO absorption band
- Replacement of damaged fibre bundles with 150 μm fibres for better sampling
- Reconfiguration of the telescopes for signal optimisation

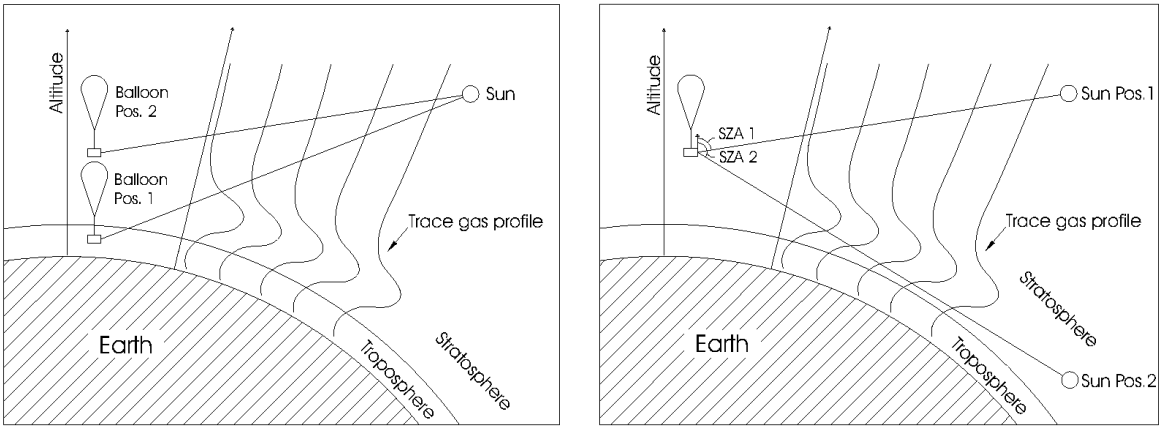

Figure 9.4.: *Observation geometry of the LPMA/DOAS balloon payload. Direct sunlight is measured during balloon ascent (left panel), balloon float and solar occultation (right panel). Adopted from Ferlemann et al. (2000).*

With the sun-tracker system the instrument has two different observation geometries, shown in Figure 9.4. The first is the balloon ascent. The position of the Sun changes marginally as the balloon ascends through the atmosphere. Since the light pathes traverse different parts of the atmosphere, a trace gas concentration profile can be retrieved

(see Figure 9.4). The gondola is normally launched in the early afternoon and ascends to a float altitude of between 30 - 40 km. This takes around 2.5 hours, and the balloon then remains at float altitude until sunset. The solar occultation is the second observation geometry. Now the balloon position changes marginally and the position of the Sun changes to a great extent. Based on the different light paths indicated in the right plot in Figure 9.4, an additional profile can be retrieved. Given this possibility, the balloon remains afloat during the night and an additional profile can be recorded during sunrise. The DOAS balloon instrument is capable of measuring in a spectral range from 320 - 650 nm where species such as O_3, BrO, NO_2, OClO, HONO, HCHO and O_4 in the UV and O_3, NO_2, H_2O, O_4, NO_3, OClO, IO and OIO in the visual range have absorption features (see *Ferlemann et al.* 1998, *Harder et al.* 1998, *Harder et al.* 2000, *Fitzenberger et al.* 2000, *Pfeilsticker et al.* 2000, *Bösch et al.* 2003, *Butz et al.* 2006, *Dorf et al.* 2006, *Dorf et al.* 2008 and *Butz et al.* 2009).

9.1.3. The miniDOAS Instrument for Limb Observations of Scattered Skylight

The miniDOAS instrument is a miniaturised version of the BigDOAS instrument, hence the name. The miniDOAS instrument is designed for measuring scattered skylight in limb direction, instead of observing direct sunlight. The limb observation enables measurements of profiles during the entire day and not just during balloon ascent and solar occultation events. Omitting the sun-tracker makes the miniDOAS very compact and light compared

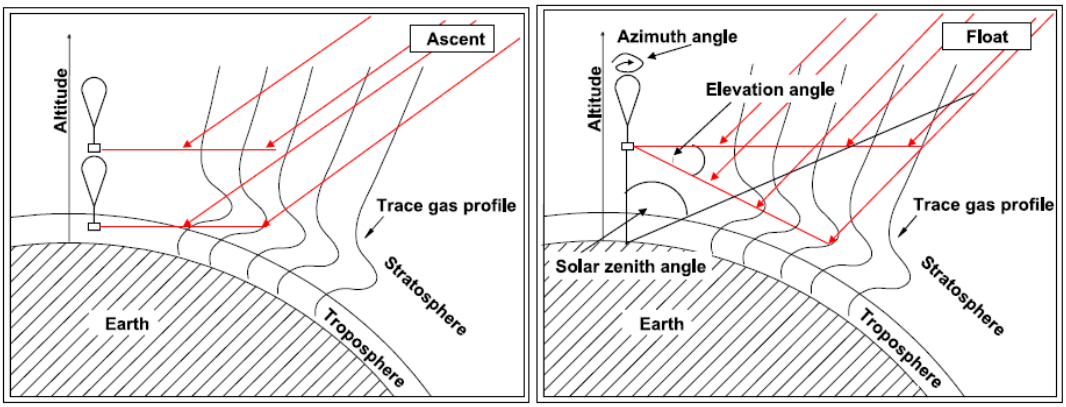

Figure 9.5.: *Viewing geometry of balloon-borne limb scattered skylight measurements during balloon ascent (left panel) and during float (right panel). Adopted from Kritten (2009).*

to the direct sunlight instrument. The instrument has its own battery power supply and needs no information or command module connection to the gondola. It is set up to be a completely autonomous unit. Before each flight, a measurement routine is developed for given flight parameters such as: ascent time, float altitude, time at float level and SZA (see Figure 9.5). This allows the instrument to fly piggyback on several different azimuth stabilised balloon gondolas. Most stratospheric balloon payloads are specifically designed to carry certain instruments, e.g., the LPMA/DOAS gondola (Section 9.1), but are able

to carry additional small and light instruments. A list of recent deployments is given in Figure 9.9.
As mentioned above, the miniDOAS instruments are independent from solar occultation events. However, since they are looking to the horizon instead of the Sun, scattered skylight instruments observe much lower intensities. Accordingly, more time is required to record a single spectrum. Observations of scattered skylight also involve more complex radiative transfer calculations and offer a lower overall sensitivity. However, due to the limb observation geometry longer light paths at each altitude level are observed compared with the direct sunlight observations of the BigDOAS instrument.
Currently two miniDOAS instruments are in use for balloon-borne measurements:

- One built and deployed by Frank Weidner (*Weidner et al.* 2005)
- One described in *Simmes* (2007) and used in this study. It is referred to as miniDOAS (*Oscar*).

Originally the miniDOAS (*Oscar*) instrument was designed for aircraft deployments, but the high versatility of the miniDOAS instruments also allows for its use on board azimuth stabilised balloon gondolas. The instrument has the same components as the BigDOAS instrument:

- Two telescopes mounted on stepper-motors to allow for vertical scanning of the atmosphere once the balloon float level is reached
- Fibre bundles for light intake
- Spectrograph unit
- Computer controlling unit

These parts can all be identified in Figure 9.8. Each part can be replaced or adapted for a specific application. While the spectrometers of the BigDOAS instrument were specifically designed and assembled in the laboratory, the miniDOAS instruments use commercial parts. Oscar has an Ocean Optics USB2000 spectrometer (USB) covering the 408 - 532 nm visible range and an Ocean Optics QE65000 (QE) covering the 320 - 398 nm UV spectral range. The USB and QE are comprised of the same parts as the BigDOAS instrument. Schematic of the Ocean optics spectrometers are shown in Figure 9.6.

Figure 9.6.: *Sketch of the two commercial miniDOAS spectrometers from Ocean Optics. The USB2000 is on the left and the QE65000 is on the right. (1) SMA 905 connector, (2) entrance slit, (3) longpass absorbing filter (optional), (4) collimating mirror, (5) grating, (6) focusing mirror, (7) collection lenses, (8) detector, (9) longpass orders-sorting filter (optional), (10) UV2 or UV4 detector upgrades (optional). Adopted from OceanOptics (2012).*

Table 9.1.: *Summary of the most important characteristics of the miniDOAS instrument.*

	USB2000 *vis channel*	QE65000 *UV channel*
Wavelength range (nm)	408-532	320-398
Detector type	Sony ILX511 1-D array	Hamamatsu S7031 2-D array
Num. pixels	2048	1024
Well-depth (e^-)	$62.5{\cdot}10^3$ /pixel	$1.5{\cdot}10^6$ /column
A/D resolution (bit)	12	16
Num. counts (fall sat.)	4096	65000
photo-e^- count	15.3	23.1
Quantum effiency (at 400nm)	0.1	0.5
Total num. photons	$625{\cdot}10^3$ 150 /pixel	$3{\cdot}10^6$ 46 /column
Slit entrance (width, μm)	50	100
Dispersion (nm/pixel)	0.105	0.08
FWHM	6.2 pixels	4.75 pixels

Just as with the BigDOAS, both spectrometers are kept in an aluminium housing. This metal case is surrounded by a resin housing allowing ice water to keep the setup temperature stable at 0°C. Like the BigDOAS, the spectrograph is evacuated. The entire setup in the configuration for the flight on September 7^{th} 2009 can be seen in Figure 9.8. The integration of the instrument into the gondola depends on the space available. The LPMA/DOAS gondola is designed for direct Sun observations and is oriented towards the Sun. The telescopes of the miniDOAS instrument are aligned to scan 90° to the side of the direct Sun instruments, as shown in Figure 9.7.

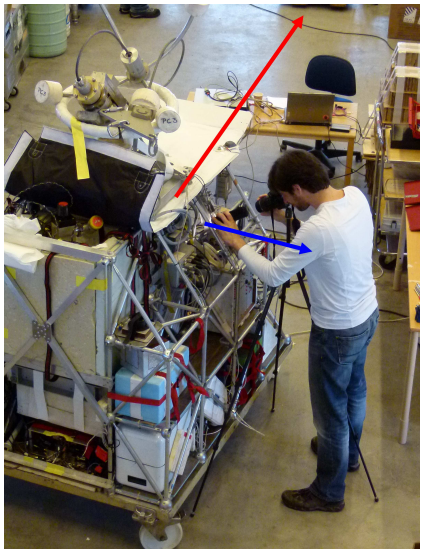

Figure 9.7.: *Picture showing the rear of the LPMA/DOAS gondola, while the miniDOAS telescopes are being calibrated. The LPMA and BigDOAS instruments look toward the Sun (red arrow), while the miniDOAS instrument Oscar looks 90° to the side (blue arrow).*

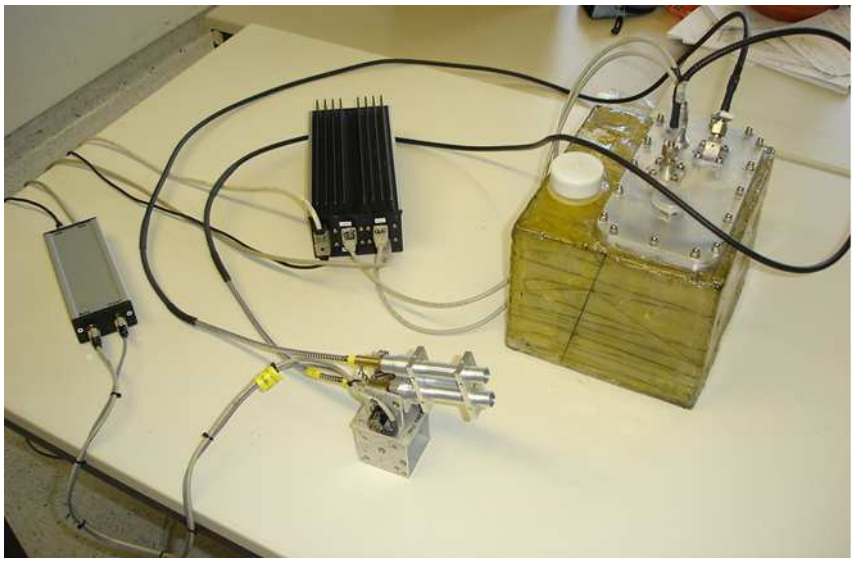

Figure 9.8.: *Complete setup of the Oscar miniDOAS instrument before integration on board the LPMA/DOAS gondola. On the left is the stepper-motor controlling unit (grey) for the telescopes. The computer unit (black) is in the middle. The spectrograph housing is on the right. The two telescopes with the stepper-motor can be seen in the front. Adopted from Werner (2009).*

Date	Time	Location		Geological condition	SZA	Payload
13.June 2008	08:45 - 13:50	Teresina / Brasil	5.1°S, 42.8°W	tropical winter	91°- 32°	LPMA/IASI
27.June 2008	05:22 - 21:18	Teresina / Brasil	5.1°S, 42.8°W	tropical winter	60°- 95°	LPMA/DOAS
10.Mar. 2009	03:34 - 05:10	Kiruna / Sweden	67.9°N, 21.1°E	high latitude, winter	98°- 90°	MIPAS
07./08. Sep 2009	14:53 - 06:05	Kiruna / Sweden	67.9°N, 21.1°E	high latitude, summer	70°- 94°	LPMA/DOAS
31. March 2011	03:01 - 07:05	Kiruna / Sweden	67.9°N, 21.1°E	high latitude, spring	94°-71°	MIPAS
24. April 2011	03:01 - 07:03	Kiruna / Sweden	67.9°N, 21.1°E	high latitude, spring	87°-66°	LPMA/DOAS
28. April 2011	02:35 - 05:03	Kiruna / Sweden	67.9°N, 21.1°E	high latitude, spring	85°- 76°	SALOMON-N2

Figure 9.9.: *Deployment list of the Oscar instrument on board balloon payloads.*

9.1.4. The STAC Instrument

The STAC (Stratospheric and Tropospheric Aerosols Counter) is an aerosol particle counter for in situ measurements (*Renard* 2008). It was developed for taking aerosol size distribution measurements from the middle troposphere up to the middle stratosphere. Initially developed by the Laboratoire de Météorologie Dynamique (LMD), Paris, STAC has been kept under the technical and scientific responsibility of the Laboratoire de Physique et Chimie de l'Environnement et de l'Espace (LPC2E), Orléans since 2005. STAC provides concentration profiles of liquid particles for diameters greater than 0.35 μm and of solid particles for diameters greater than 1 μm. It is commonly implemented on board various gondolas, in particular ELHYSA, SPIRALE, SALOMON-N2 and the LPMA/DOAS gondola.

A nozzle is used to collect ambient air and create an airflow through a measurement chamber. A laser diode illuminates the air flowing through the chamber. Aerosols in the collected air scatter light from the original beam direction onto a photodiode. The amount of aerosols is then calculated based on the intensity of the scattered light. A schematic of the instrument is shown in Figure 9.11. A more detailed description of the principle is given by *Renard et al.* (2010).

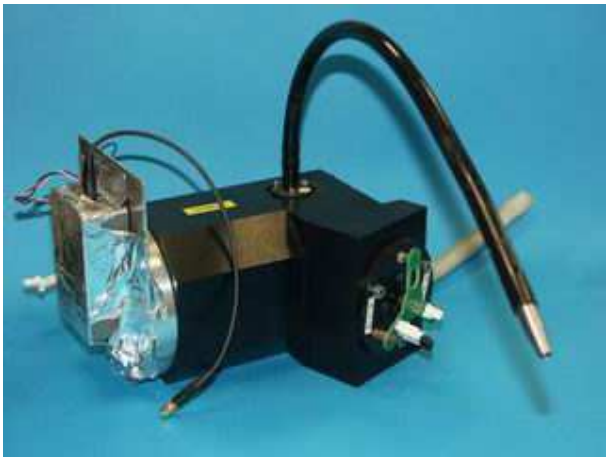

Figure 9.10.: *Photograph of the STAC instrument. The picture clearly shows the nozzle used to pump air through the measurement chamber. The small lightweight instrument was designed to be operated on multiple balloon gondolas without much integration effort. Adopted from Drouin (2012).*

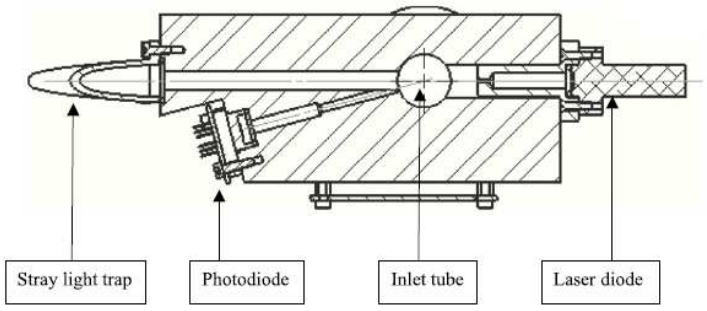

Figure 9.11.: *Schematic drawing of the STAC instrument. Aerosols dragged into the instrument through the inlet scatter light from the laser diode. Concentrations are received based on the intensity of the light measured by the photodiode at the characteristic angle of 15°. Adopted from Renard et al. (2010).*

Part III.

Measurements

10. StraPolÉté Campaign

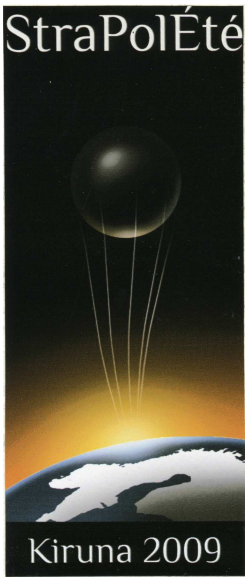

Figure 10.1.: *StraPolÉté Campaign Logo.*

The StraPolÉté Campaign took place in Kiruna, Sweden in late summer 2009. The name is a combination of three French terms that describe the scientific background of the campaign: **Stra**tosphérique (stratospheric), **pol**aire (polar), **été** (summer). Over the last two decades extensive research has been carried out into ozone depletion during winter months. As a result it is quite well understood. In contrast, scientific understanding of the dynamics and chemistry of the stratosphere during summer months still has several unresolved issues. For this reason the StraPolÉté campaign was launched. The overall goals of the campaign were:

- Research into the dynamical state of the stratosphere and its development
- Tests of photochemical and transport models to discover whether they can simulate these mechanisms properly

The French space agency CNES (Centre National d'Études Spatiales) set up the campaign from the Esrange space center near Kiruna in northern Sweden (67.9°N, 22.1°E). From July to September 2009 several research balloons were launched to probe the high latitude stratosphere. This campaign demonstrates the effort and value of creating integrated measurement campaigns, where modelers are part of a campaign to validate their work, in this case the annual evolution of the polar stratosphere, e.g., (*Thieblemont et al.* 2010). More than 30 scientists from seven different research institutes and the CNES "Nacelles pointées" team were on site during the campaign to prepare and operate the payloads. The campaign goals were divided according to the different work packages

1. Dynamical investigations
2. Stratospheric aerosol characterisation
3. Bromine budget investigations
4. Reference state of the polar summer atmosphere

The ELHYSA, SPIRALE, SWIR, SALOMON-N2 and LPMA gondolas measure long-lived species relevant for climate change. For the first time, several measurements of BrO from various instruments (SALOMON-N2, BigDOAS, miniDOAS) were taken in order to determine the bromine content of the stratosphere.
A primary goal of the campaign was to establish the first reference state of the polar summer stratosphere from 9 km to 37 km in terms of reactive chemistry, tracer fields and aerosols.
Model calculations for dynamical and chemical evolution of the polar stratosphere were begun in January 2009, while the scientific measurement campaign started in August 2^{nd} 2009 with the launch of the ELHYSA balloon payload. Six more research balloons were launched in August. The last of the eight flights was the LPMA/DOAS flight on September 7^{th}.

10.1. The LPMA/DOAS Flight

The launch of the LPMA/DOAS payload was originally planned for August 26^{th}, but was delayed due to bad weather conditions on the ground and unfavourable wind patterns in the lower stratosphere. The ground winds finally calmed, however, and on September 7^{th} at 14:51 UT the payload was launched. The balloon ascended to float altitude very quickly. Two hours after the launch, at 16:45 UT, an altitude of 33.9 km was reached, at which the balloon remained during the sunset. Solar occultation was completed at 18:20 UT. The balloon descended slowly to approximately 29 km as the helium cooled down during the night. After the sunrise on September 8^{th} at 02:25 UT the balloon expanded due to the warming of the helium and slowly ascended to an altitude of 31 km. At 06:01 UT, three and a half hours after sunrise and after a total flight time of 16 hours, the payload was separated from the balloon and landed close to the Finnish-Russian border. This relatively short trajectory for a flight duration of 16 hours was possible due to the very low wind speeds at float altitude. The trajectory is superimposed on a map for a better visualisation in Figure fig:BallonFlugStrapolt. Figure 10.3 shows the altitude profile for the flight. The last Figure in this section (Figure 10.4) shows the azimuth orientation of the gondola for the ascent and the sunset. Unfortunately, the LPMA/DOAS gondola does not have an absolute position transducer. Therefore, the stability of the gondola has to be deduced by other means. The azimuth orientation is the first indication for the stability of the gondola. This is discussed further in Section 12.2. While the balloon flight covered the afternoon and evening of September 7^{th} 2009 and the morning of September 8^{th}, it is only referred to as the flight on September 7^{th} 2009 unless specifically the measurements during sunrise are discussed.

Figure 10.2.: *The balloon trajectory (red) after the launch from Esrange Space Station in northern Sweden until the payload landed in Finland 16 hours later. This was the longest recorded flight for the LPMA/DOAS payload and direct sunlight measurements to retrieve three trace gas profile sets (ascent, sunset and sunrise), not including the miniDOAS measurements, were recorded.*

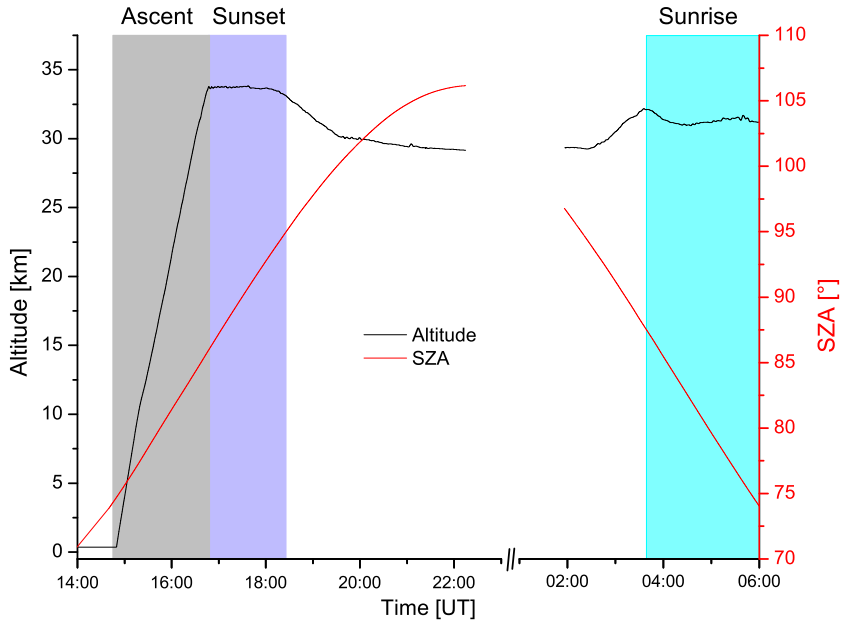

Figure 10.3.: *The altitude profile of the LPMA/DOAS flight is plotted in black. Indicated are the time frames for the ascent (grey), the sunset (blue) and sunrise (light blue) measurements of the miniDOAS instrument. The red line indicates the SZA for a given time. Note that the timeline is interrupted during the night.*

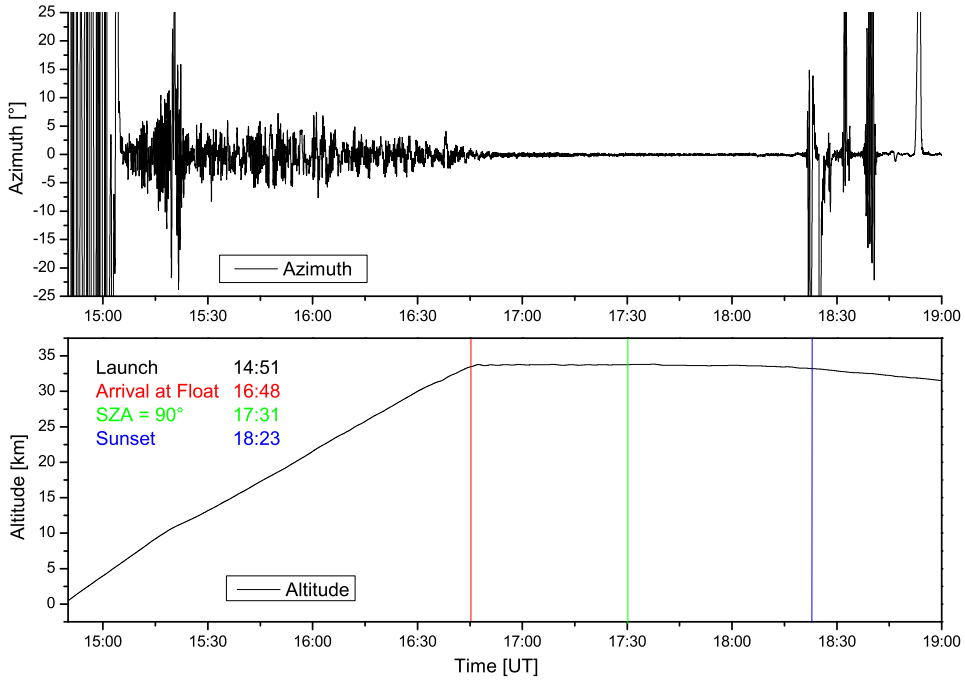

Figure 10.4.: *The upper plot shows the azimuth orientation of the gondola during the ascent and sunset. The oscillation and shaking of the gondola during the ascent can be derived from this data. Once the balloon reached float altitude, the gondola oscillation faded due to low wind activity at this altitude. This is very important, because persistent gondola movement can broaden the field of view of the telescopes. The lower plot contains the altitude plotted for that time, along with the time of arrival at float altitude (red), the SZA = 90° (green) and the final disappearance of the Sun behind the horizon at 18:23 UT (blue).*

10.2. State of the Atmosphere

Several computer models (e.g., FLEXPART (*Stohl et al.* 2005), MIMOSA (*Hauchecorne et al.* 2002)) were used to predict and analyse the atmospheric conditions before, during and after the balloon measurements of the StraPolÉté Campaign. In Section 2.1.1, it is noted that during the summer to winter circulation transition stratospheric winds at high latitudes are very weak ($\sim$ some $\frac{\mathrm{m}}{\mathrm{s}}$). However, on September 7^{th}, remnants of such an intrusion could be detected over eastern Scandinavia. The MIMOSA potential vorticity (PV) maps show a mid-latitude airmass intrusion before the LPMA/DOAS flight (see Figure 10.5). A detailed description of the MIMOSA model is given in *Hauchecorne et al.* (2002).

Besides the satellite coverage, the Esrange team launches small probes on a daily basis and additional ones prior to each balloon flight to get an accurate picture of the atmospheric conditions. These are used in combination with the various sensors on board the gondola to ascertain the complete condition of the atmosphere before and during the balloon flight. Pressure and temperature data from the gondola, the balloon, the ozone soundings and the European Centre for Medium-Range Weather Forecasts (ECMWF) are compared and put together with humidity levels and cloud coverage. This information is very important for the trace gas retrievals and radiative transfer, e.g., the cross sections of the different trace gases are temperature dependant and the temperature and pressure data is necessary to calculate the refractive index of the atmosphere (see Sections 5.2 and 11.1). The combined analysis of the atmosphere during the balloon ascent is plotted in Figure 10.7.

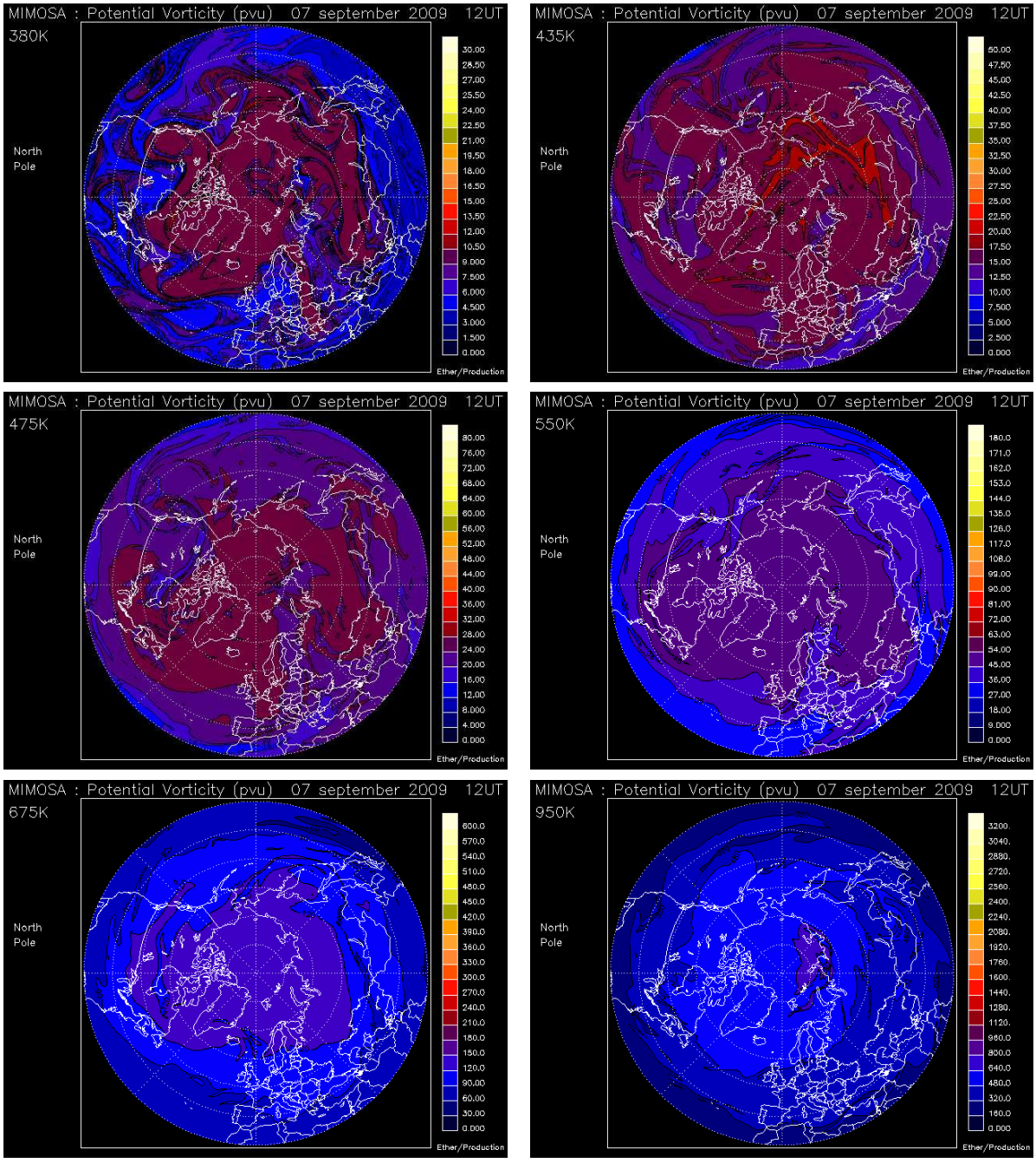

Figure 10.5.: *MIMOSA model output for the PV over the northern hemisphere on September 7th 2009 at 12:00 UT at different potential temperature levels. A mid-latitude air mass intrusion can be seen at 475 K and 550 K over eastern Scandinavia. Such events are rare, since the PV surfaces are normally aligned with the latitude bands, like at 675 K and 950 K. Adopted from (Poulet and Huret 2011).*

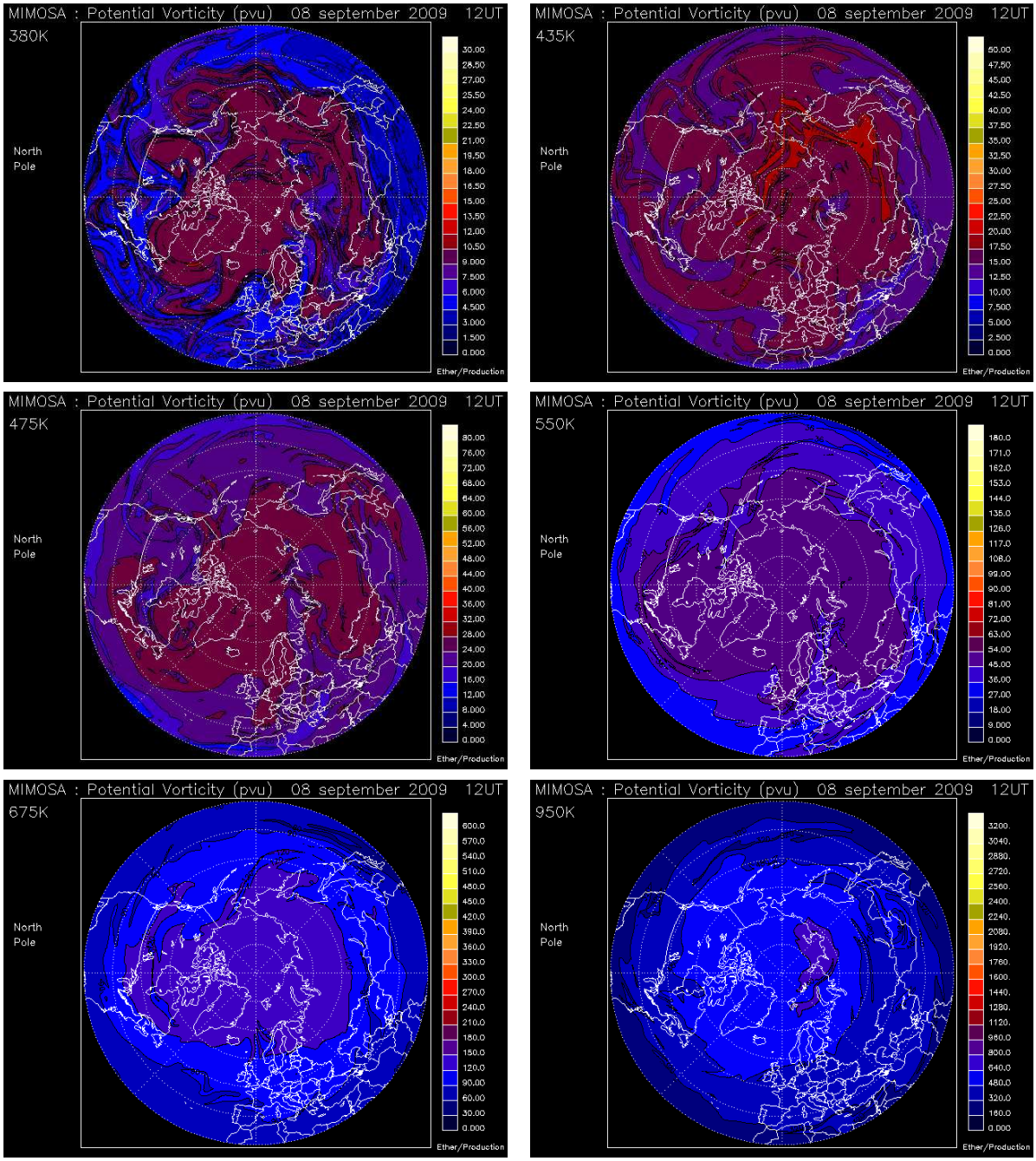

Figure 10.6.: *Same plots as in Figure 10.5 for September 8^{th} 2009 at 12:00 UT. The remnants of the mid-latitude air mass intrusion at 475 K and 550 K moves eastwards towards Russia and starts to dissipate. Adopted from (Poulet and Huret 2011).*

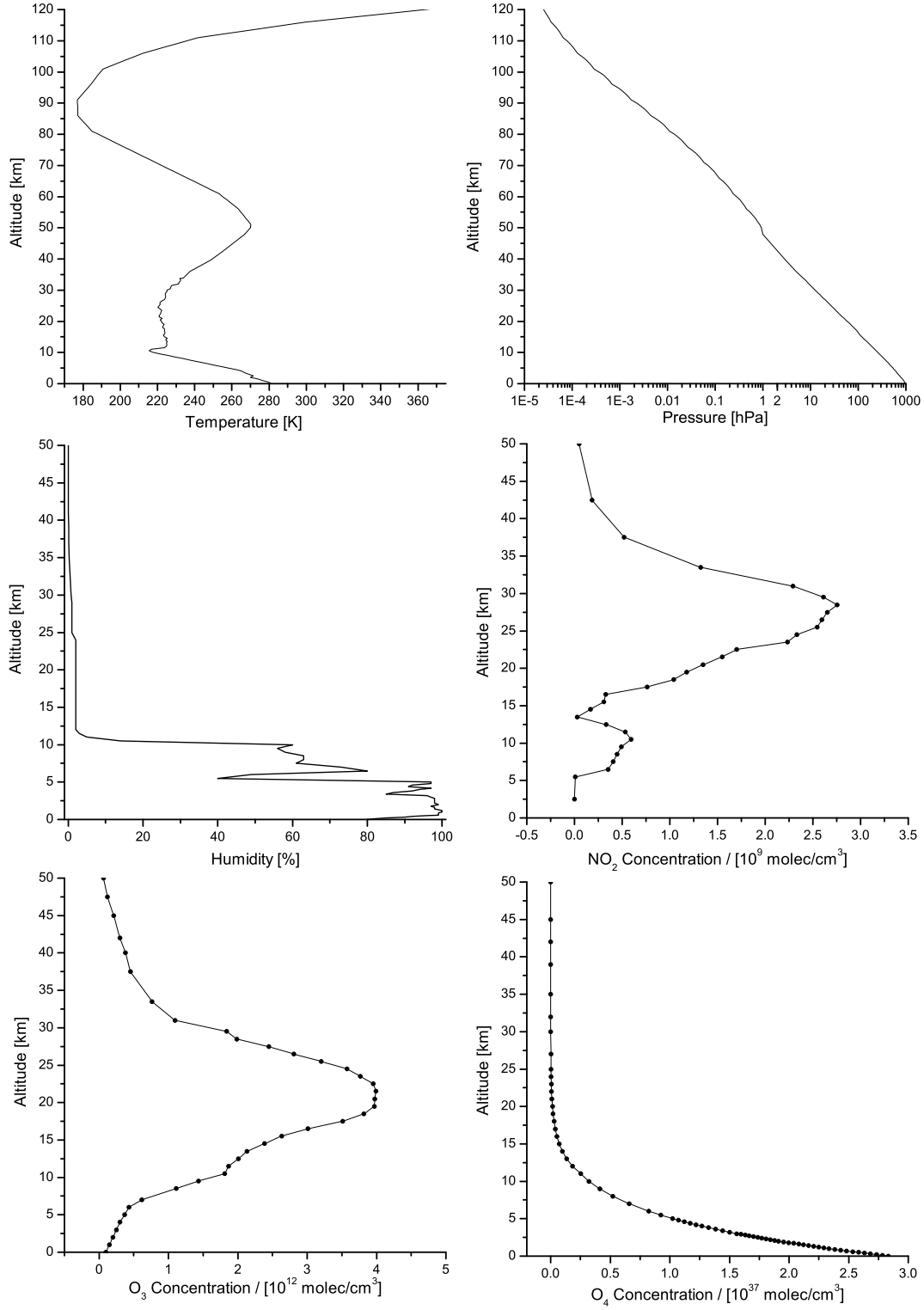

Figure 10.7.: *State of the atmosphere for the balloon ascent of the LPMA/DOAS balloon gondola. The data is compiled from two probes launched during the flight, as well as the various on board sensors and satellites.*

11. Direct Sunlight Measurements

11.1. Inferred Slant Column Densities

The recorded direct sunlight measurements from the flight on September 7^{th} 2009 can be divided into three datasets: ascent, sunset and sunrise. For all three datasets slant column densities (SCDs) are calculated according to the details given in Sections 11.1.1 - 11.1.3. The miniDOAS instrument for limb observations of scattered skylight covers a slightly smaller wavelength range and uses different fitting windows for the DOAS analysis in the visible range. Therefore, the O_3 and NO_2 retrieval are discussed in both the direct sunlight and scattered skylight limb measurement chapters. However, both instruments use the same wavelength range for the spectral retrieval of BrO, so a detailed discussion is given only for the miniDOAS instrument in Section 12.1.3.
The first dataset, the ascent, starts with the tracking of the Sun at 15:05 UT and ends at 16:34 UT on September 7^{th} 2009. Since an in-flight sun-tracker test was performed when the balloon reached the float altitude, the ascent data is evaluated against a Fraunhofer reference spectrum recorded before this sun-tracker test.
The second dataset is from the sunset, which is evaluated against a Fraunhofer reference spectrum recorded after the sun-tracker test. This dataset starts at 17:03 UT and ends at 18:21 UT with the complete occultation of the Sun.
The final dataset is the sunrise. The Sun was first tracked at 02:26 UT on September 8^{th} 2009, and at 04:39 UT a sun-tracker test was performed. A Fraunhofer reference spectrum recorded before this test is used to evaluate the sunrise spectra.
The retrieval of O_3 and NO_2 dSCDs from the spectra from the direct sunlight observations is based on the studies of *Bösch* (2002) and *Butz* (2006). Only slight changes are made in order to account for changing atmospheric conditions. All high resolution absorption cross sections used here are from the Mainzer Spektral Atlas [1] and are corrected for the solar I_0 effect, see Section 6.1.2.

11.1.1. O_3 Spectral Retrieval

The O_3 spectral retrieval is performed in the Chappuis band (545 - 615 nm). The absorption cross section was measured in the laboratory at 221 K (*Kreycy* 2007) and subsequently wavelength aligned with respect to the convolved absorption cross sections from *Voigt et al.* (2001) measured at 223 K.
Interfering differential absorption from NO_2 is handled by simultaneously fitting two ab-

[1] http://www.atmosphere.mpg.de

Table 11.1.: *Characteristics of the BigDOAS retrieval of O_3 and NO_2 direct sunlight measurements.*

Species:	O_3	NO_2
Instrument:	vis	vis
Wavelength range:	545 nm to 615 nm	435 nm to 485 nm
Cross section:	Lab, fitted to *Voigt et al.* (2001)	Lab, fitted to *Voigt et al.* (2002)
Interfering species:	NO_2 at T = 223 K (*Voigt et al.* 2002) NO_2 at T = 246 K (*Voigt et al.* 2002) O_4 (*Herman et al.* 1999) H_2O (Hitran database)	O_3 at T = 223 K (*Voigt et al.* 2001) O_4 (*Herman et al.* 1999) H_2O (Hitran database)
Broad band polynomial:	3rd order	3rd order
Stray light correction:	1st order	1st order

sorption cross sections corresponding to T = 223 K and T = 246 K, which were measured in the laboratory (*Kreycy* 2007) and subsequently wavelength aligned with respect to convolved cross sections from *Voigt et al.* (2002). The two NO_2 cross sections were orthogonalised with respect to each other. Even though the temperatures are stable, two absorption cross sections are used to minimise remnants of NO_2 features in the residual spectrum. Despite this effort there are still NO_2 features in the residual. However, due to their very low optical density (0.01 of the ozone feature) and narrow band nature compared to the O_3 cross section, they do not influence the retrieval. The absorption of O_4 is accounted for by the absorption cross section measured by *Herman et al.* (1999). The H_2O cross section is taken from the Hitran database[2] and convolved with a mercury line at 546 nm. A 3^{rd} order polynomial is used to account for the broad band extinction processes and a 1^{st} order additive polynomial for instrumental stray light. For the spectrum a 1^{st} shift and 1^{st} degree stretch is allowed to account for changes in atmospheric conditions. As recommended in the work of *Stutz and Platt* (1996) and *Butz* (2006), in order to account for systematic residual features the errors of the retrieved O_3 dSCDs given by the fitting routine are multiplied by three. Polynomials of different degrees (up to 5^{th}) are tested for the retrieval to account for broad band features and no polynomial larger than 3^{rd} order should be used due to possible correlations with the O_3 cross section. The Fraunhofer offset, which is added to the dSCDs, and its respective error were treated through Gaussian error propagation. An exemplary DOAS fit for O_3 is shown in Figure 11.1.

[2]http://www.cfa.harvard.edu/hitran/ Version of Fall 2009 was used for all spectral fits.

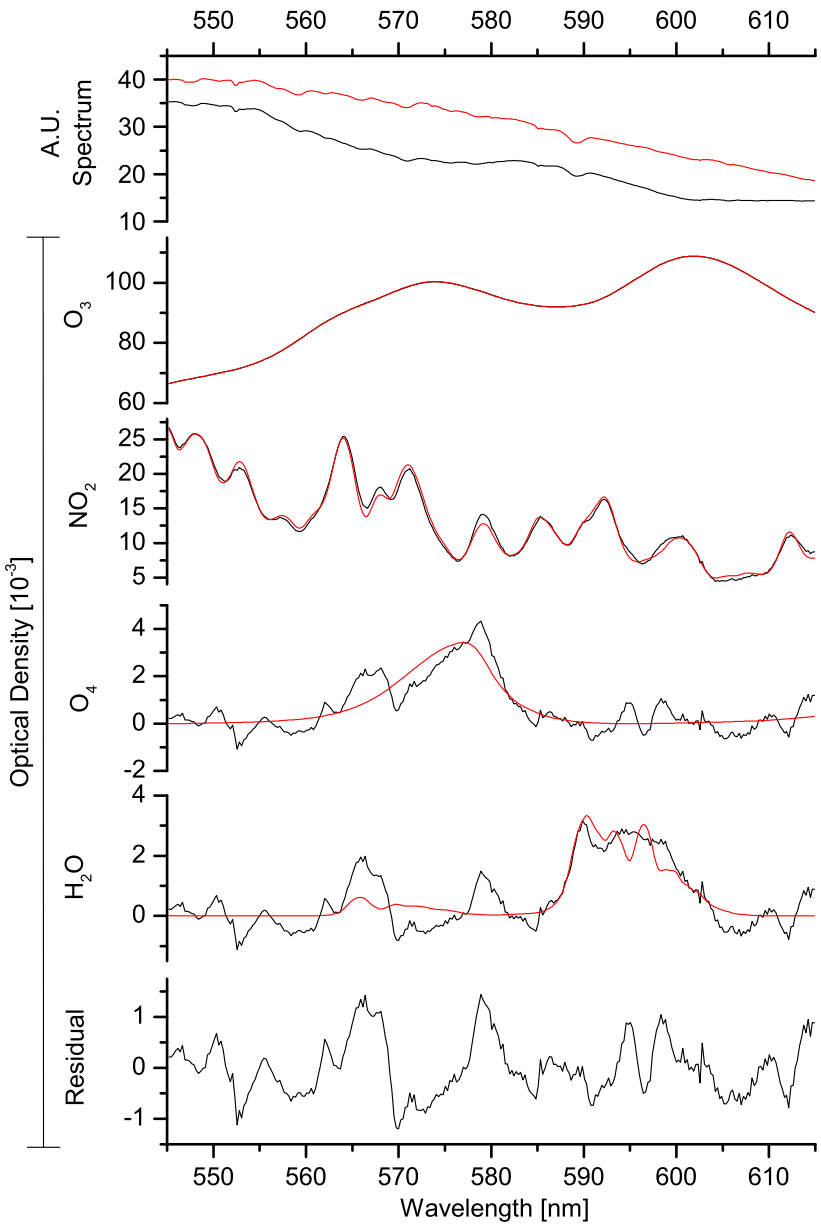

Figure 11.1.: *O_3 DOAS evaluation of a visible spectrum recorded during sunrise at 02:46 UT (SZA=93.1°) September 8^{th} 2009. The upper panel shows the normalised reference (black line) and measured spectrum (red line). In the panels below, the retrieved trace gas absorptions of O_3, NO_2, O_4 and H_2O are shown. The red lines indicate the differential spectral absorption and the black lines the sum of the spectral absorption and the residual. The lowest panel shows the remaining residual of the spectral fitting procedure.*

11.1.2. NO_2 Spectral Retrieval

The NO_2 dSCDs are retrieved in the 435 - 485 nm spectral range to avoid the prominent center-to-limb (CLD) structures at 434 nm and 486 nm. This means that the correction term for the CLD effect described in (*Bösch* 2002) can be neglected.

The NO_2 absorption cross section was measured in the laboratory for temperatures ranging between 200 K and 280 K (*Kreycy* 2007). Subsequently, the lab-measured absorption cross section measured at T = 226 K, which is inherently convolved by the instrument function, was wavelength aligned to the data of *Voigt et al.* (2002) recorded at 223 K. In the 435 - 485 nm range interferences from O_3, O_4 and H_2O must be considered. O_3 is accounted for by including a absorption cross section recorded in the laboratory at T = 223 K with the direct sunlight instrument. The cross section is wavelength aligned to the convolved reference of *Voigt et al.* (2001). The cross section of the O_4 oxygen collision complex is taken from *Herman et al.* (1999). Broad band extinction and instrumental stray light is considered via a 3^{rd} order multiplicative and a 1^{st} order additive polynomial in the spectral fitting routine. For the spectrum a 1^{st} degree shift and a 1^{st} degree stretch is allowed.

The errors given by the fitting routine are multiplied by a factor of two as recommended in the study of *Butz* (2006). An exemplary DOAS fit for NO_2 is shown in Figure 11.2.

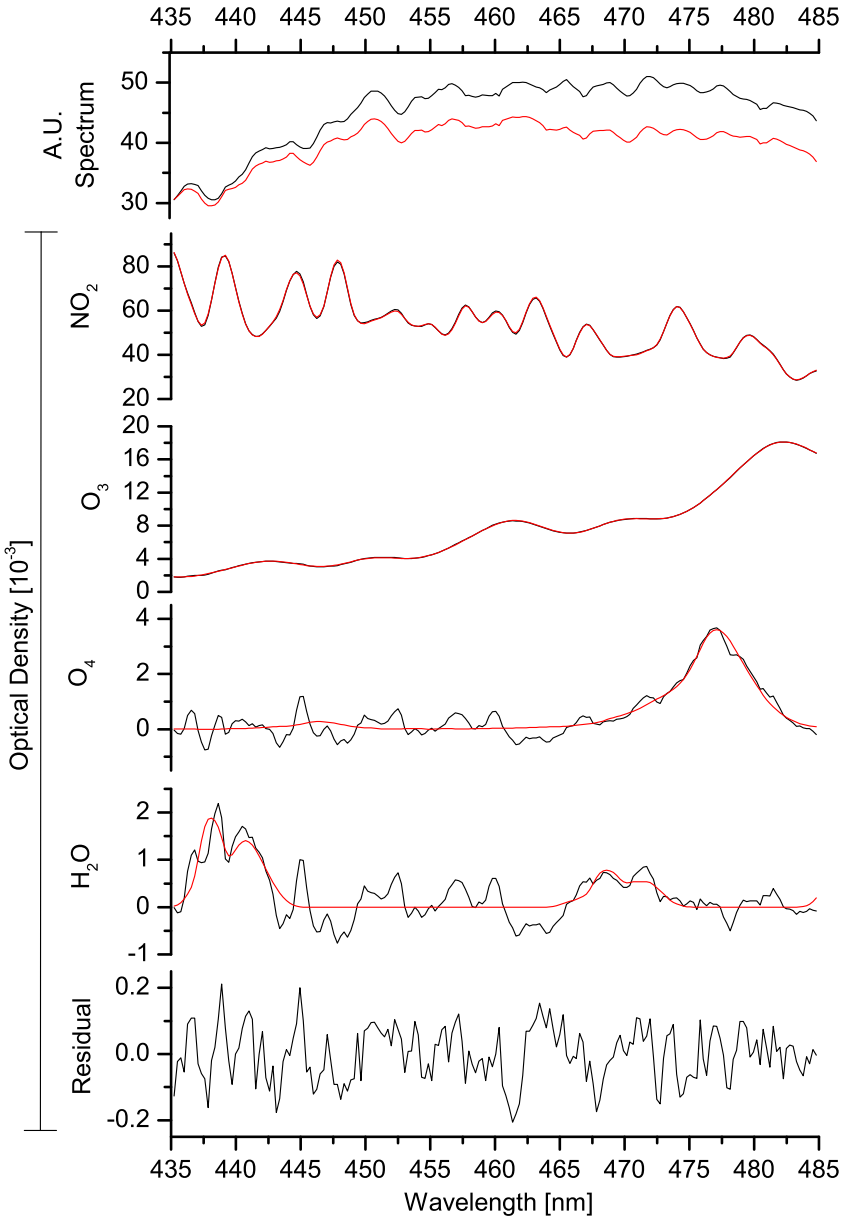

Figure 11.2.: *NO_2 DOAS evaluation in the visible spectral range for a spectrum measured at sunrise at 02:46 UT (SZA=93.1°) September 8^{th} 2009. The upper panel shows the normalised reference (black line) and measured spectrum (red line). In the panels below, the retrieved trace gas absorptions of NO_2, O_3, O_4 and H_2O are shown. The red lines indicate the differential spectral absorption and the black lines the sum of the differential spectral absorption and the residual. The lowest panel shows the remaining residual of the spectral fitting procedure.*

11.1.3. BrO Spectral Retrieval

The DOAS retrieval for BrO is more complicated than for O_3 and NO_2. The lower concentrations result in smaller optical densities. Another problem is that the absorption lines of the different species are closer together compared to the O_3 and NO_2 retrieval in the visible range. Hence, it is more difficult to separate them. Figure 11.3 shows the absorption cross sections for the spectral retrieval of BrO. An incorrectly calculated SCD for O_3 or NO_2 would lead to an incorrect SCD of BrO. This effect would not necessarily show up in the residual.

The BrO DOAS retrieval is based on the work of *Dorf* (2005) and follows the recommendations of *Aliwell et al.* (2002), who did a comprehensive comparison study of the parameters of a DOAS BrO retrieval. Several parameters are analysed: fitting window, high resolution cross sections employed and other parameters such as the shift of the different cross sections.

The fitting range is 346 - 359 nm. The BrO absorption cross section is taken from

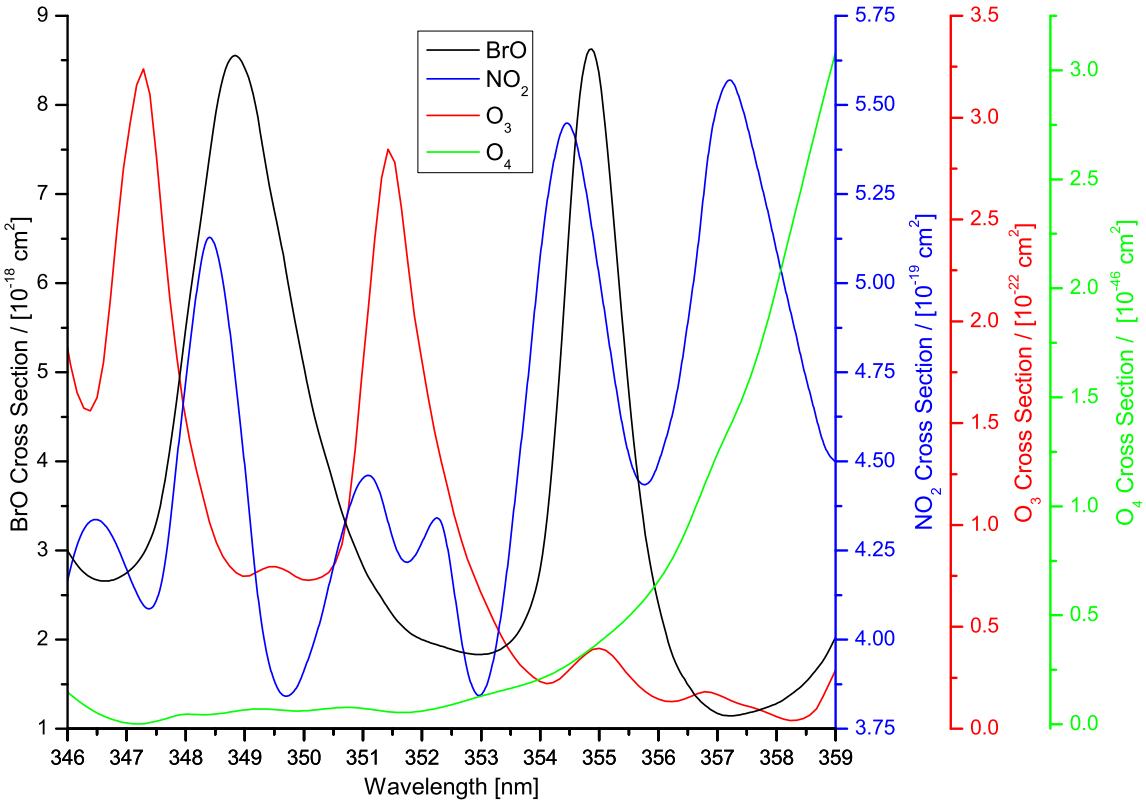

Figure 11.3.: *The absorption cross sections for the BrO retrieval.*

Wahner et al. (1988), measured at 228 K and convolved with the instrument function. Two O_3 absorption cross sections, measured at T = 250 K and T = 210 K using the direct sunlight instrument by *Dorf* (2005), are included to account for absorption features of O_3. Because the cross sections were recorded with the instrument, they are inherently convolved with the instrument function.

The NO_2 absorption cross section was also measured with the instrument by *Dorf* (2005)

Table 11.2.: *Characteristics of the DOAS retrieval of BrO.*

Species:	BrO
Instrument:	UV
Wavelength range:	346 nm to 359 nm
Cross section:	(*Wahner et al.* 1988)
Interfering species:	O_3 at T = 210 K (*Dorf* 2005) O_3 at T = 250 K (*Dorf* 2005) NO_2 at T = 230 K (*Harder et al.* 1997) O_4 (*Herman et al.* 1999) H_2O Hitran
Broad band polynomial:	2nd order
Stray light correction:	2nd order

and adapted to fit the cross section measured by *Harder et al.* (1997). The absorption cross section for O_4 is taken from *Herman et al.* (1999) and convolved with the instrument function. The broad band structures are accounted for by a 2^{nd} order multiplicative polynomial and an additional 2^{nd} order additive polynomial for the stray light correction. For the spectrum a 1^{st} degree shift and a 1^{st} degree stretch is allowed.
The BrO DOAS evaluation follows the same recommendations for the direct sunlight and the miniDOAS instruments for limb measurements of scattered skylight and is discussed further in Section 12.1.3.

11.2. Profile Retrieval of the Direct Sunlight Measurements

The profile retrieval is based on the work of (*Rodgers* 2000). The altitude-based concentration profiles are retrieved because only then can the inferred concentrations be compared to other measurements and results.
The retrieved profiles of the direct sunlight measurements are used for different purposes. A major aim of the StraPolÉté campaign was to get a comprehensive survey of the stratospheric polar summer stratosphere in order to establish a detailed reference state as stated above.
Beyond that, there are several important uses for these measurements. The BrO measurements are important for studying the trend of Br_y species in the stratosphere. Based on the development of the Br_Y trend, predictions are made regarding the recovery of the ozone hole (*WMO* 2011).
The retrieval of concentration profiles from direct sunlight measurements is more basic than retrieval of scattered skylight measurements from the miniDOAS instrument due to the simpler radiative transfer. This is because only geometric calculations for the raytracing including refraction have to be considered in the profile retrieval. Furthermore, the signal-to-noise ratio is much higher for direct sunlight measurements than limb scans of scattered skylight. The DAMF software calculates the Weighting Matrix $\mathbf{K}$ for the given

retrieval grid and returns a profile using a given retrieval approach. The error of the returned profile is dominated by the noise error of the measured dSCDs and uncertainty of the Fraunhofer offset. The SVD approach is used for the retrieval of direct sunlight measurements, with a MAP approach being used only to check the results. Figure 11.4 shows a comparison between the two approaches for the NO_2 balloon ascent measurements. The Averaging Kernel Matrix of the MAP profiles is plotted in the right panel of Figure 11.4 The Averaging Kernel Matrices of Figures 11.4 and 11.5 show that in both cases the

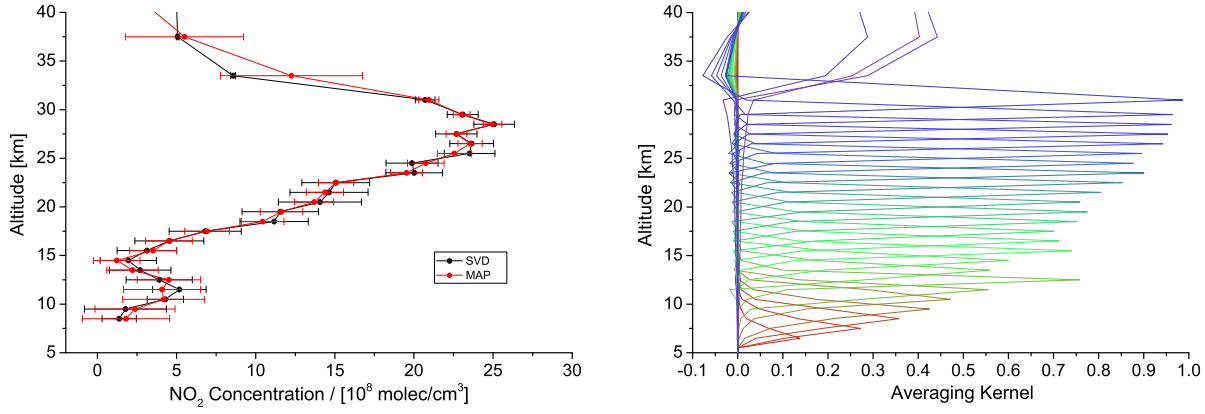

Figure 11.4.: *Comparison of profiles retrieved, with the SVD and the MAP approach to the NO_2 balloon ascent measurements in the left plot. The right panel shows the corresponding Averaging Kernel Matrix of the SVD retrieval.*

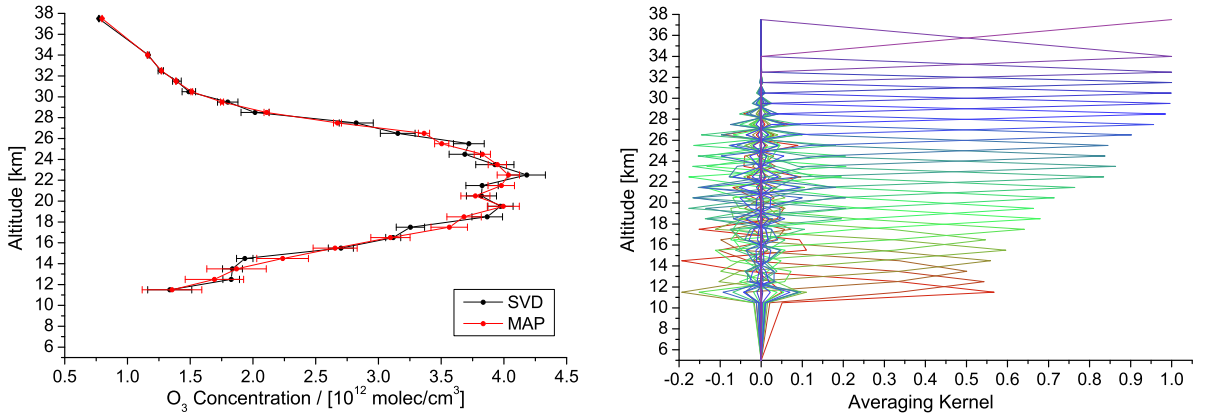

Figure 11.5.: *Comparison of profiles retrieved with the SVD and the MAP approach for the O_3 sunset measurements. The right panel shows the corresponding Averaging Kernel Matrix of the SVD retrieval.*

retrieved profile between 12 and 32 km is based predominantly on information obtained from measurements of the respective altitude segment. The retrieved high accuracy profiles of the direct sunlight measurements are important for the miniDOAS profile retrieval, because they can be used as a priori information for the inversion of the scattered skylight measurements. Figure 11.6 compiles the profiles retrieved from the direct sunlight O_3 and

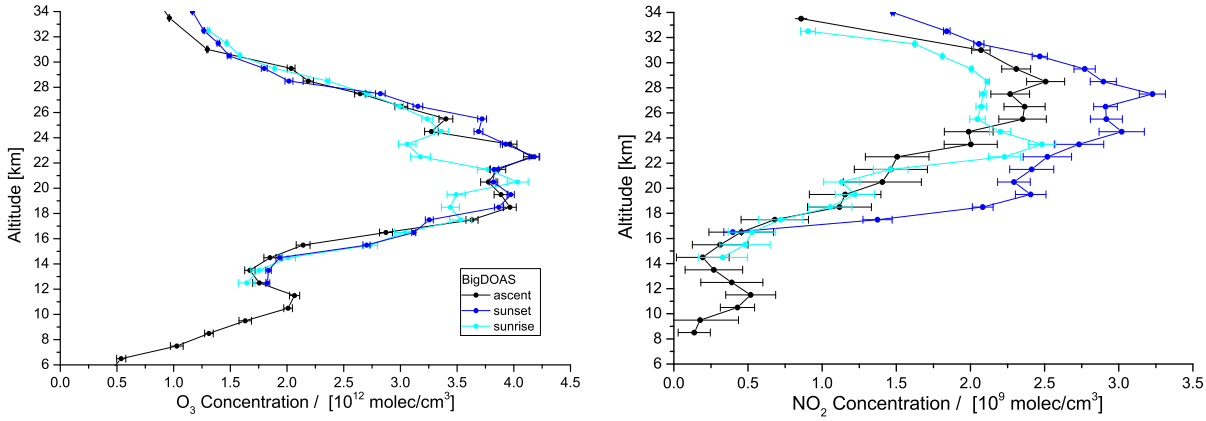

Figure 11.6.: *Concentration profiles retrieved from the three datasets: ascent, sunset and sunrise. The left panels shows the retrieved O_3 profiles and the right panel the NO_2 profiles. The colour coding is the same for both plots.*

NO_2 measurements.

The retrieved profiles are also important for satellite validation, which is discussed in Chapter 14.

12. Limb Measurements of Scattered Skylight

12.1. Inferred Slant Column Densities

Like the direct sunlight measurements recorded during the StraPolÉté balloon flight, the retrieved data of the miniDOAS instrument comprises the three parts marked in Figure 10.3: the balloon ascent, the sunset and the sunrise. The evaluation of the different trace gases follows the details given in Sections 12.1.1 - 12.1.3. The sunset limb scans started at 17:00 UT at float altitude and lasted until the sunset at 18:23 UT September 7^{th} 2009. Due to the faster decrease of the observed radiance in the UV compared to the visible wavelength, only three limb scans can be used to evaluate BrO during sunset. For evaluating O_3 and NO_2, which are analysed in the visible wavelength range, four limb scans are used.
The sunrise on September 8^{th} occurred at 02:26 UT. However, due to the very low temperatures during the night, the stepper-motor mechanics apparently froze and did not start the scanning sequence. The recorded data does not allow to deduce where the telescopes were pointing. Therefore, these early measurements are discarded.
The first measurements are from a limb scan starting at 03:53 UT. At this point the stepper-motor started moving again. Seven limb scans were performed before the gondola was separated from the balloon at 06:04 UT. Because no cross sections were recorded with the miniDOAS instrument itself, high resolution absorption cross sections taken from the Mainzer Spektral Atlas[1] are convolved with a spectral line recorded with the miniDOAS instrument.

12.1.1. O_3 Spectral Retrieval

The miniDOAS instrument covers a smaller wavelength range then the direct sunlight instrument (see Section 9.1.3). Hence, a different fitting window is used in the O_3 analysis. The ozone retrieval is based on the analysis developed by *Weidner* (2005). An important difference is the expansion of the fitting window from 490 - 520 nm to 475 - 515 nm (see Figure 12.1). Expanding the fitting window for the O_3 retrieval minimises the interference between the O_3 absorption cross section and the offset polynomial.
An O_3 absorption cross section measured at 223 K from *Voigt et al.* (2001) is chosen for the retrieval. An NO_2 absorption cross section from *Voigt et al.* (2002) recorded at 223 K

[1] http://www.atmosphere.mpg.de

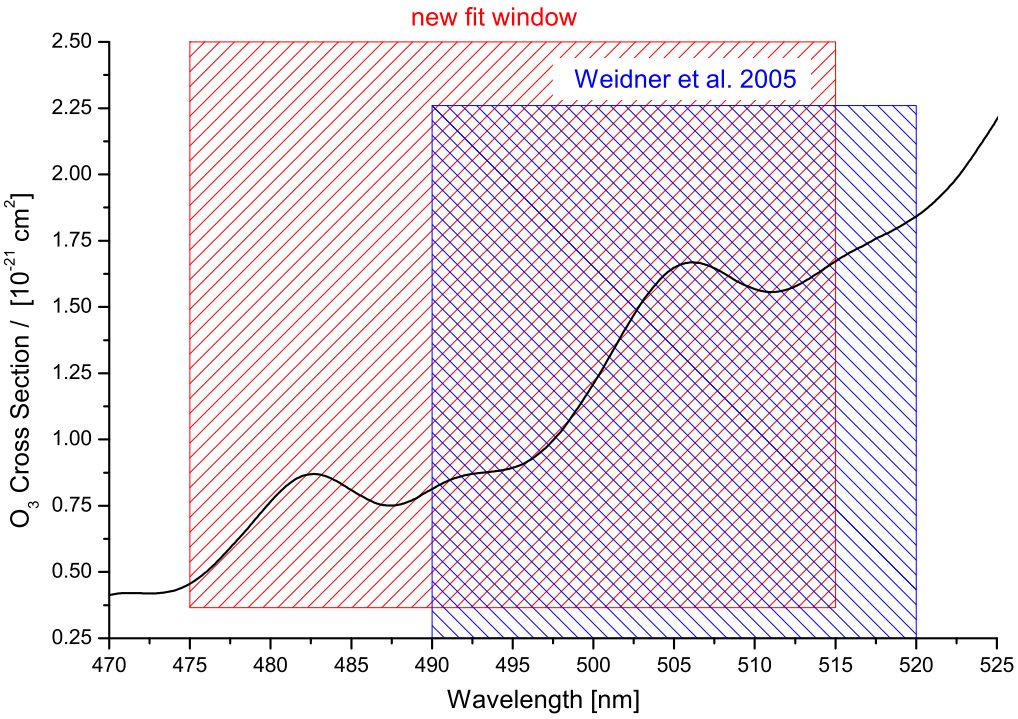

Figure 12.1.: *New fitting window for the DOAS O_3 retrieval compared to the recommendation of Weidner (2005). The window was expanded to a second absorption band as this retrieval proved to be more stable.*

is included in the fit to account for NO_2 and the absorption cross section measured by *Herman et al.* (1999) for O_4. The H_2O absorption cross section is taken from the Hitran Database (*Rothman et al.* 2003 version of October 2009).
All high resolution cross sections were convolved with a cadmium emission line at 467 nm recorded prior to the balloon flight. A pseudo-Ring-absorber calculated with DOASIS is included in the retrieval to account for the Ring effect (see Section 6.1.4). A 2^{nd} degree polynomial is used to account for broad band structures and an additive 1^{st} degree polynomial for stray light. An example for a typical DOAS fit of O_3 is shown in Figure 12.2.

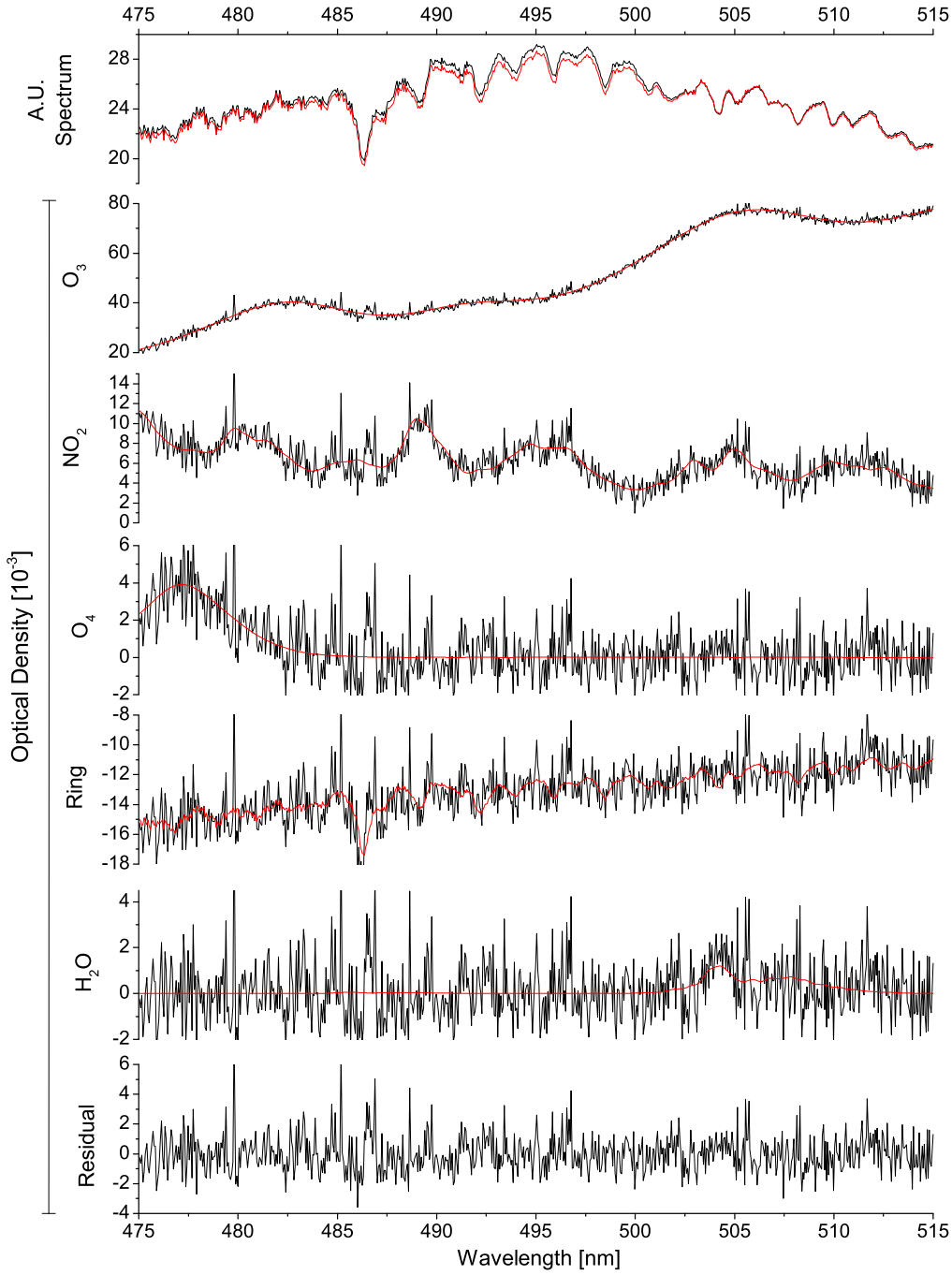

Figure 12.2.: *O_3 DOAS retrieval for a visible spectrum recorded during the ascent of the gondola at 16:10 UT (SZA = 82.4°) September 7^{th} 2009. The upper panel shows the normalised reference spectra (red line) and the measured spectrum (black line). In the panels below, the retrieved trace gas absorptions of O_3, NO_2, O_4, the pseudo-Ring-absorber and H_2O are shown. The red lines indicate the differential spectral absorption and the black lines show the sum of the spectral absorption and the residual. The lowest panel shows the remaining residual of the fitting procedure.*

12.1.2. NO_2 Spectral Retrieval

The NO_2 evaluation is also based on the recommendations of *Weidner* (2005). It is performed in the wavelength range of 435 - 460 nm. An NO_2 absorption cross section from *Voigt et al.* (2002), recorded at 223 K is used for the spectral fit.
An O_3 absorption cross section measured at 223 K also taken from *Voigt et al.* (2001) is included in the fit to account for the ozone absorption features. The O_4 cross section is taken form *Herman et al.* (1999). The H_2O cross section is taken from the Hitran database ((*Rothman et al.* 2003) version of October 2009). As in the O_3 retrieval, a pseudo-Ring-absorber calculated with DOASIS is included to account for the Ring effect.
A 2^{nd} degree polynomial was used to account for broad band structures and an additive 1^{st} degree polynomial for stray light. A DOAS spectral fit for NO_2 is shown in Figure 12.3.

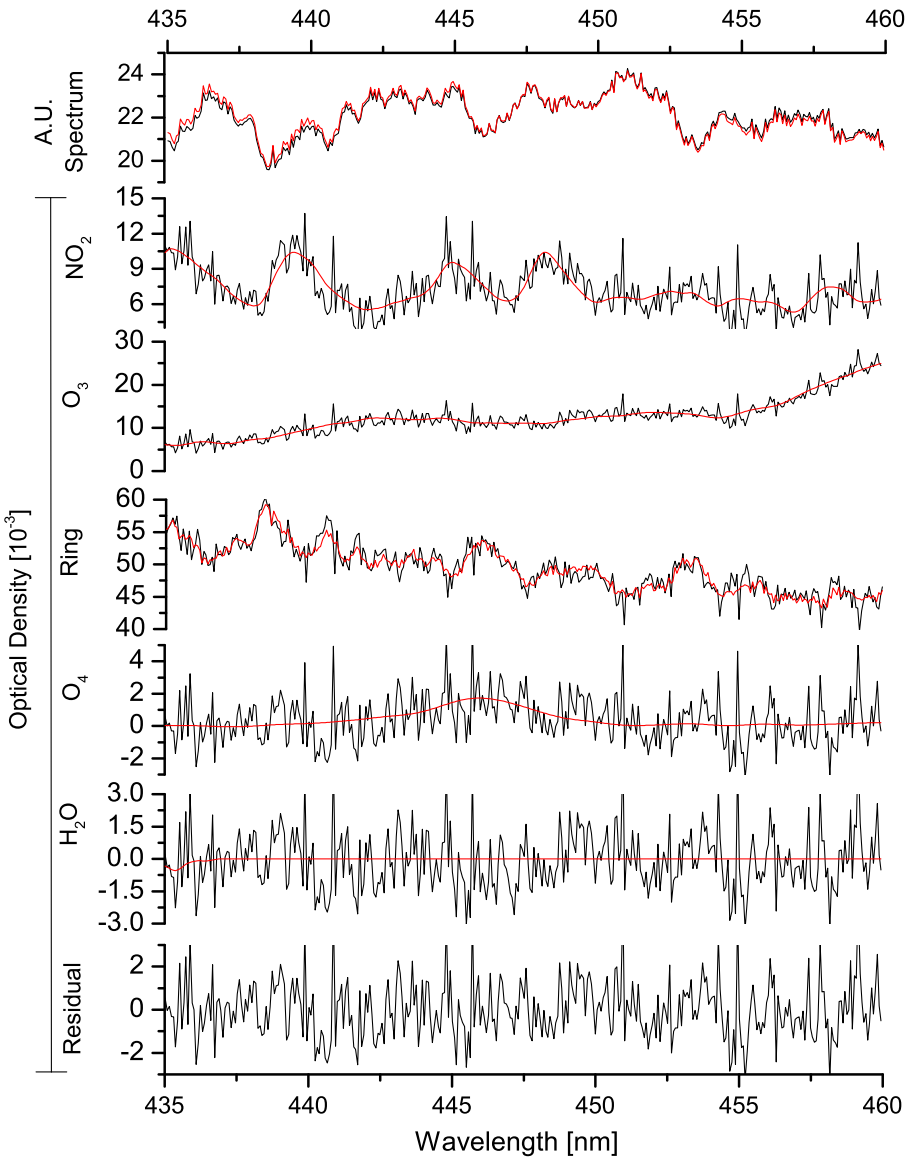

Figure 12.3.: *NO_2 DOAS retrieval for a visible spectrum recorded during the ascent of the gondola at 16:10 UT (SZA = 82.4°). The upper panel shows the normalised reference (red line) and the measured spectrum (black line). In the panels below, the retrieved trace gas absorptions of NO_2, O_3, the pseudo-Ring-absorber, O_4 and H_2O are shown. The absorption of water in this wavelength range is only important at the beginning of the ascent and by this point has faded out. The red lines indicate the differential spectral absorption and the black lines the sum of the spectral absorption and the residual. The lowermost panel shows the remaining residual of the fitting procedure.*

12.1.3. BrO Spectral Retrieval

As mentioned in Section 11.1.3, the retrieval of BrO is more difficult due to the lower optical density of BrO and the fact that the BrO signal in a DOAS retrieval has to be separated from much stronger O_3, NO_2 and Ring features. The retrieval follows the recommendations of *Aliwell et al.* (2002).
The BrO cross section is taken from *Wahner et al.* (1988) and wavelength shifted by +0.17 nm according to *Aliwell et al.* (2002). The O_3 cross section is taken from *Burrows et al.* (1999) and shifted by +0.03 nm. Interference NO_2 absorption features are accounted for via an absorption cross section measured by *Vandaele et al.* (1998). The O_4 cross section is taken from *Herman et al.* (1999). All cross section are convolved with a cadmium emission line at 340 nm recorded with the miniDOAS instrument prior to the balloon flight.
Unfortunately, as can be seen in Figure 12.4, a strong signal remained in the residual spectrum, rendering a BrO DOAS evaluation impossible.
The retrieval for the scattered skylight measurements from the balloon flight on September 7^{th} and 8^{th} 2009 posed a challenge. The fibre bundles were not mounted in an optimal configuration on the spectrograph resulting in an asymmetric instrument function. Figure 12.5 shows a comparison between the cadmium emission line recorded during the StraPolÉté campaign 2009 and a cadmium emission line recorded during the ENRICHED[2] campaign in 2011 with an optimised mounting. Asymmetry can cause difficulties not only for the convolution of the high resolution absorption cross sections, but also for the spectral retrieval. In DOASIS the convolution kernel is defined by the user and a Gauss fit is applied. In the WinDOAS software the centre of the convolution kernel is defined by the user. The DOASIS approach can lead to a shift in wavelength of the convolved cross section (see Figure 12.6). While a simple shift in intensity such as in the 353 - 359 nm range of the *Harder et al.* (1997) absorption cross section poses no problem for the DOAS retrieval, a distortion like the one in the 349 - 352 nm range can lead to false NO_2 and BrO concentrations (see Figure 12.7). *Aliwell et al.* (2002) recommends using the absorption cross section of *Vandaele et al.* (1998) instead of the NO_2 absorption cross section recorded by *Harder et al.* (1997). For a symmetric instrument function neither should cause problems, but for an asymmetric instrument function the lower signal-to-noise ratio of the *Harder et al.* (1997) absorption cross section can lead to a distortion in the convolution.
However, even with these corrections the strong residual features shown in Figure 12.4 cannot be removed. A similar residual feature is found in the BrO retrieval of the preliminary analysis of the 2011 ENRICHED data (see Figure 12.8). The observation parameters of the later balloon campaign are similar to the measurements of the StraPolÉté balloon flight. This indicates a systematic problem in the BrO analysis.
The structure is identified as being a remnant of an incorrectly removed Ring feature (see Section 6.1.4).

[2]The European collaboratioN for Research on stratospherIc CHEmistry and Dynamcis (ENRICHED) campaign took place in Kiruna in spring 2011.

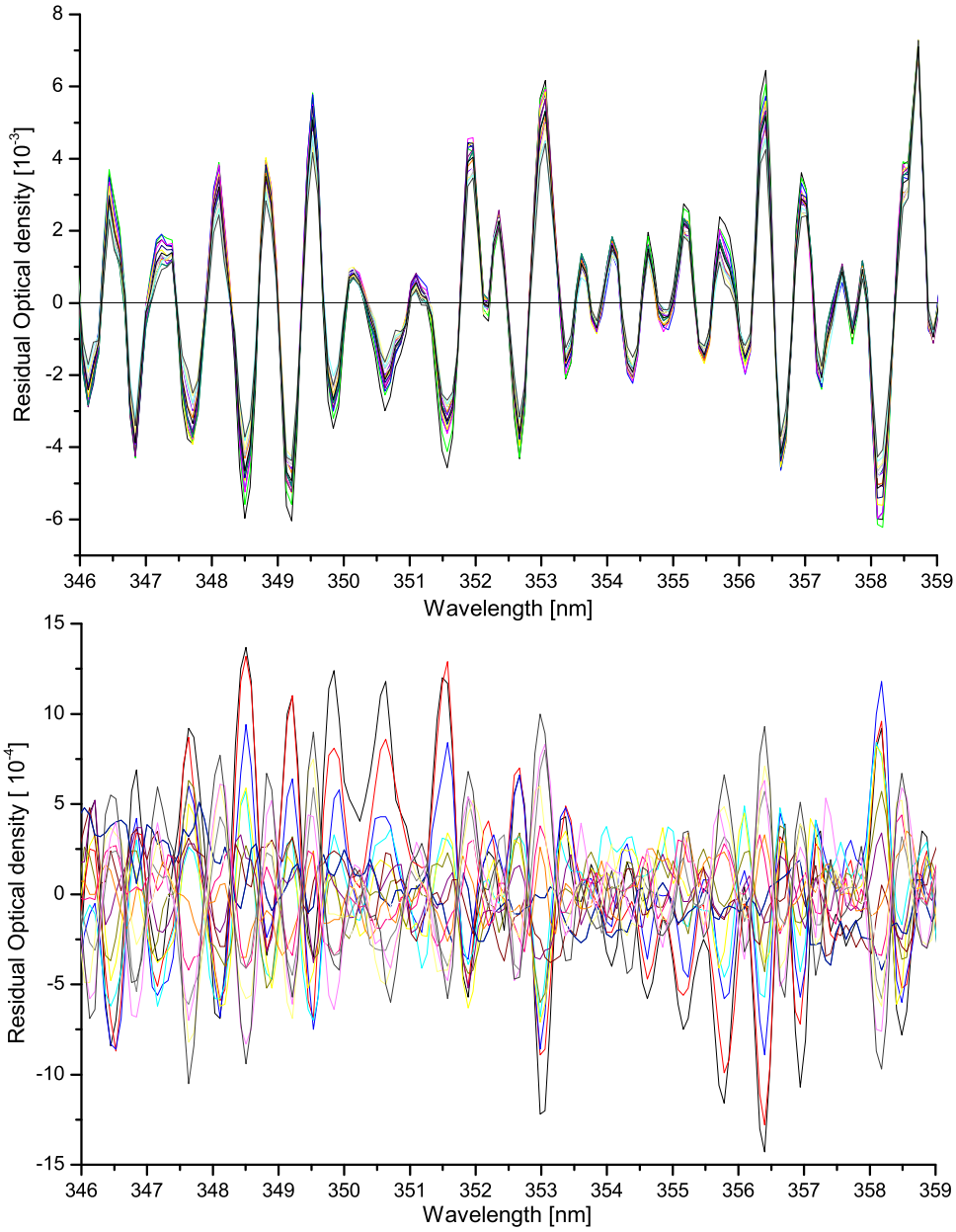

Figure 12.4.: *Residual of 20 consecutive spectra recorded during the ascent of the gondola for a BrO DOAS fit following the recommendations of Aliwell et al. (2002) in the 346 - 359 nm retrieval window. A remaining structure clearly dominates the residual and the expected random noise can only be seen as a small oscillation on top of the signal. The mean values for the 20 spectra are plotted in black. In the lower plot this mean value is subtracted from the individual spectra and the random noise remains. The colour coding is the same for both plots.*

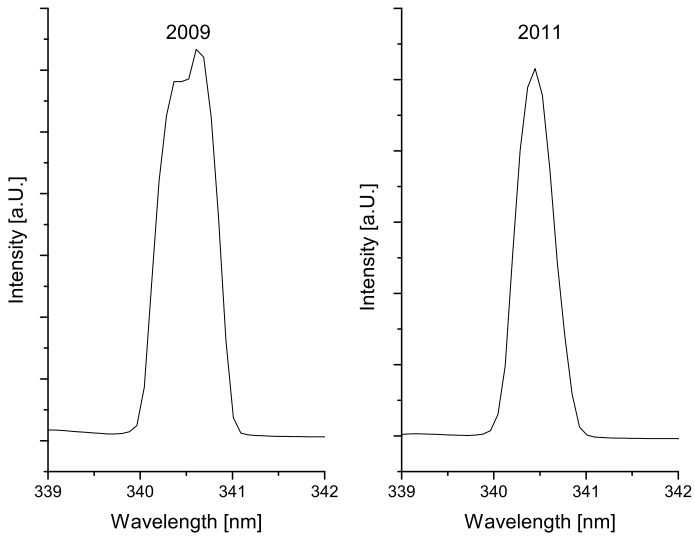

Figure 12.5.: *Instrument function of the QE65000 (UV). The cadmium line in the left panel was recorded during the 2009 campaign and the one in the right panel during the 2011 ENRICHED campaign with an optimal fibre bundle configuration.*

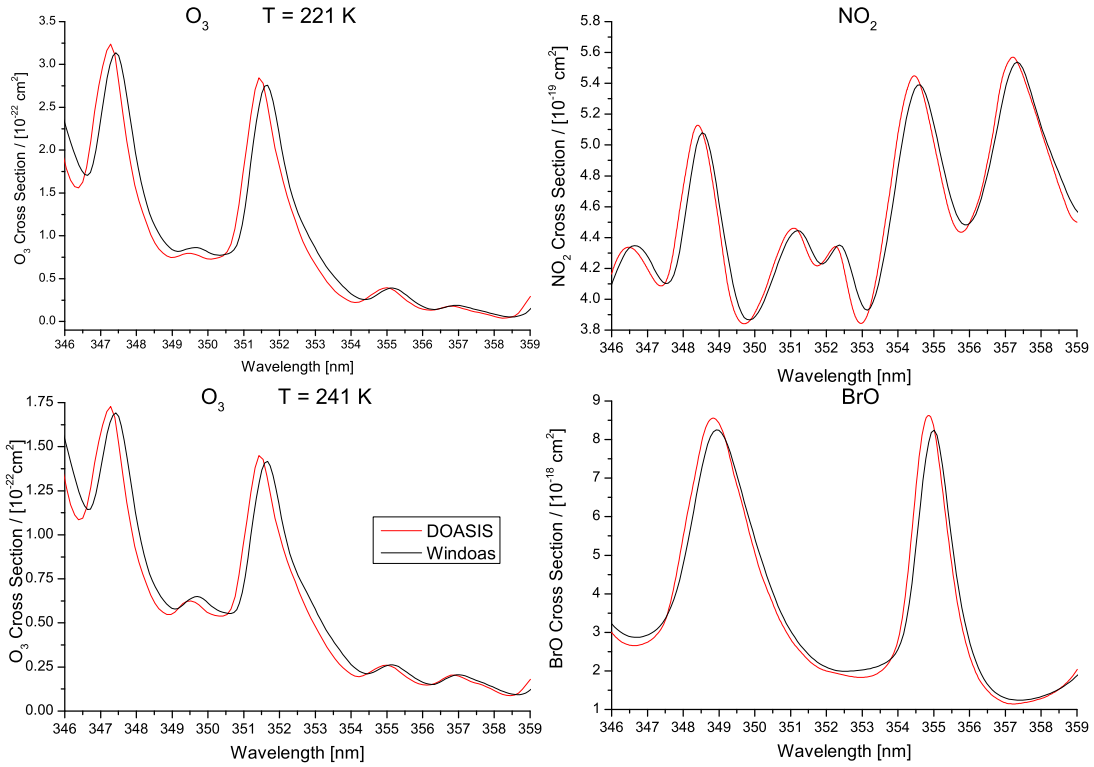

Figure 12.6.: *Convolution of the high resolution cross sections used for the BrO retrieval calculated using DOASIS and WinDOAS. The comparison of the two BrO cross sections shows small differences due to the different convolution kernels. The colour coding holds for all 4 panels.*

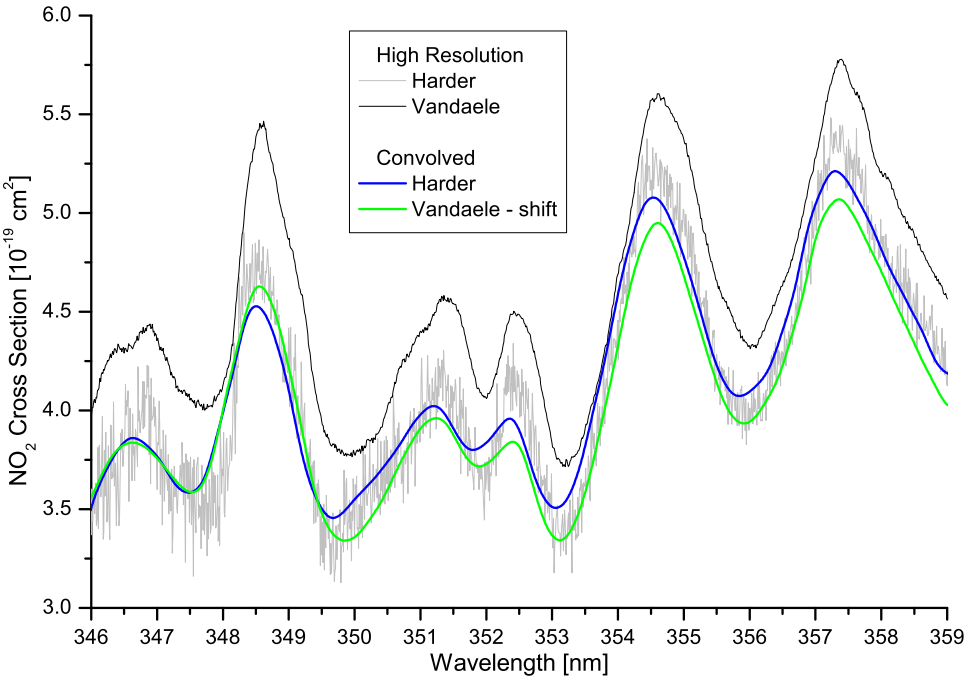

Figure 12.7.: *Comparison of the high resolution and convolved cross sections of Harder et al. (1997) and Vandaele et al. (1998). For a better comparison a factor of $0.5{\cdot}10^{-19}$ was subtracted from the convolved Vandaele cross section to achieve an overlay with the cross section measured by Harder.*

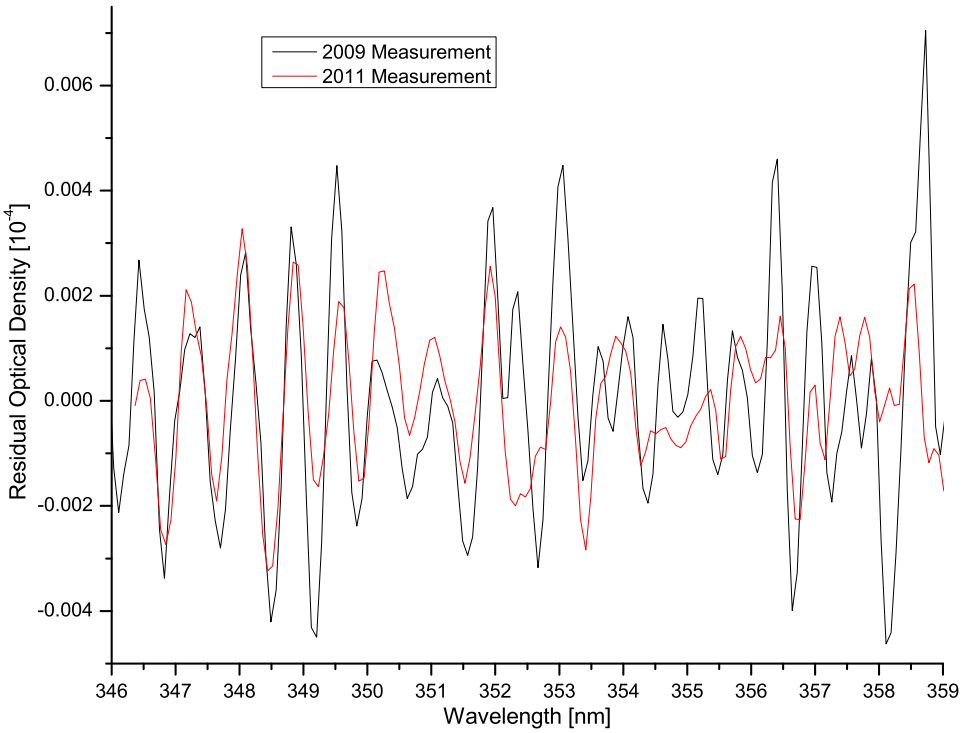

Figure 12.8.: *Comparison of residual structures from the 2009 StraPolÉté and 2011 ENRICHED campaign.*

A detailed analysis of the UV data shows that, for a balloon ascent from the ground up to an altitude of approximately 35 km, a single pseudo-Ring-absorber cannot effectively account for the Ring features in the spectra. Due to the pressure and temperature gradients, the ratio between Rayleigh and Raman scattering changes during a balloon ascent and there is a relative increase in the Ring Effect (see Figure 12.9). The residual struc-

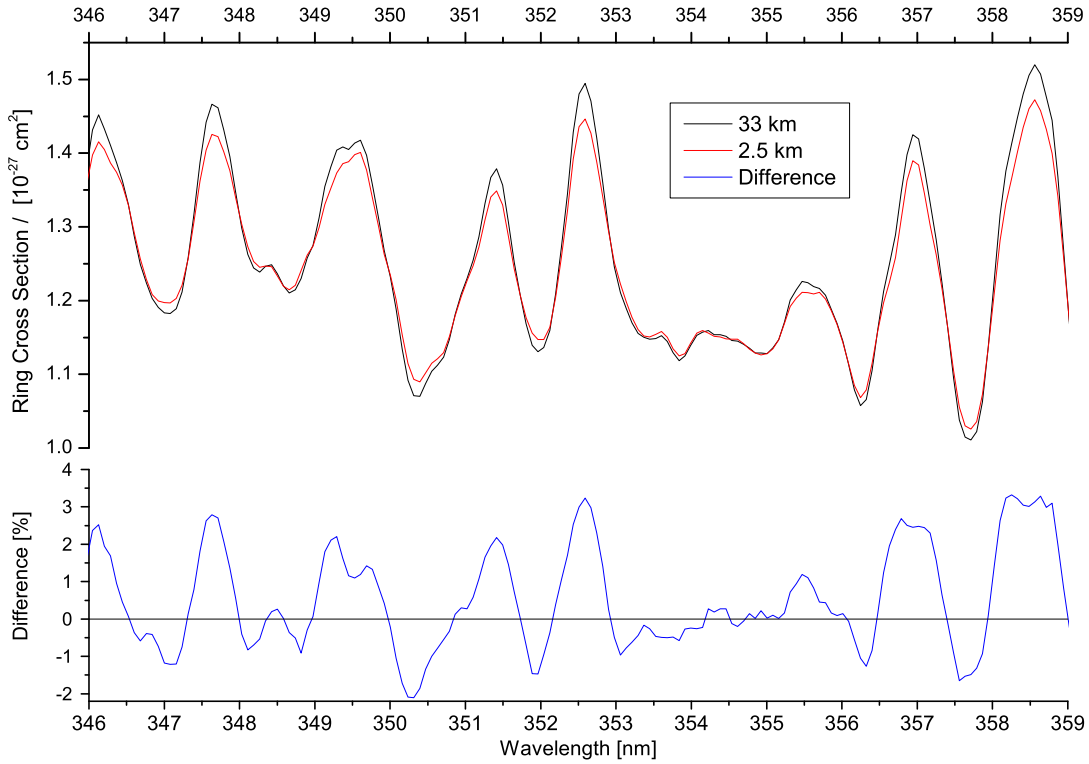

Figure 12.9.: *Absorption cross sections for the pseudo-Ring-absorber in the wavelength range of the BrO retrieval. They are are calculated from spectra recorded at an altitude of 2.5 km (red) during the ascent and at 33km (black), the difference is shown in percent (blue).*

ture can only be completely removed by using the two separate pseudo-Ring-absorber cross sections. As noted in Section 6.1.4, the pseudo-Ring-absorber is calculated directly from the recorded spectra. Hence, only spectra with little or no absorber features may be used for the calculations of the pseudo-Ring-absorber, otherwise the calculated pseudo-Ring-absorber may contain absorption features of the trace gases. In a DOAS fit this pseudo-Ring-absorber would then account for trace gas concentration features resulting in wrongly inferred dSCDs for these respective trace gases. Therefore, a spectrum recorded directly after the launch (2.5 km altitude) and one at the top of the ascent (33 km altitude) are chosen to calculate the pseudo-Ring-absorber. At this altitude the absorption of trace gases is minimal during the balloon ascent.

It is only necessary to use two different pseudo-Ring-absorbers for the spectral analysis of the balloon ascent data. Only one pseudo-Ring-absorber is used for the DOAS retrieval of the limb scans at float altitude.

In previous evaluations, the Ring spectrum for limb scans was calculated from the Fraun-

hofer reference spectra of the analysis (*Weidner et al.* 2005, *Kritten et al.* 2010). The Fraunhofer reference spectrum is typically the spectrum with the highest elevation angle of the telescopes and the smallest absorption features. Analyses showed that the pseudo-Ring-absorber calculated from the spectrum recorded at 2.5 km altitude can better account for the Ring effect. This can be seen in Figure 12.10. It shows a DOAS fit using a pseudo-Ring-absorber calculated from the reference spectrum. Since the Ring effect is not correctly removed, the other absorber dSCDs can also not be retrieved correctly. This is most obvious for O_4, where the fit returns negative SCDs. On the right side of Figure 12.10, a BrO DOAS retrieval using the pseudo-Ring-absorber calculated from the spectrum recorded at 2.5 km altitude is shown. As a consequence of the incorrect Ring fit, BrO is overestimated.

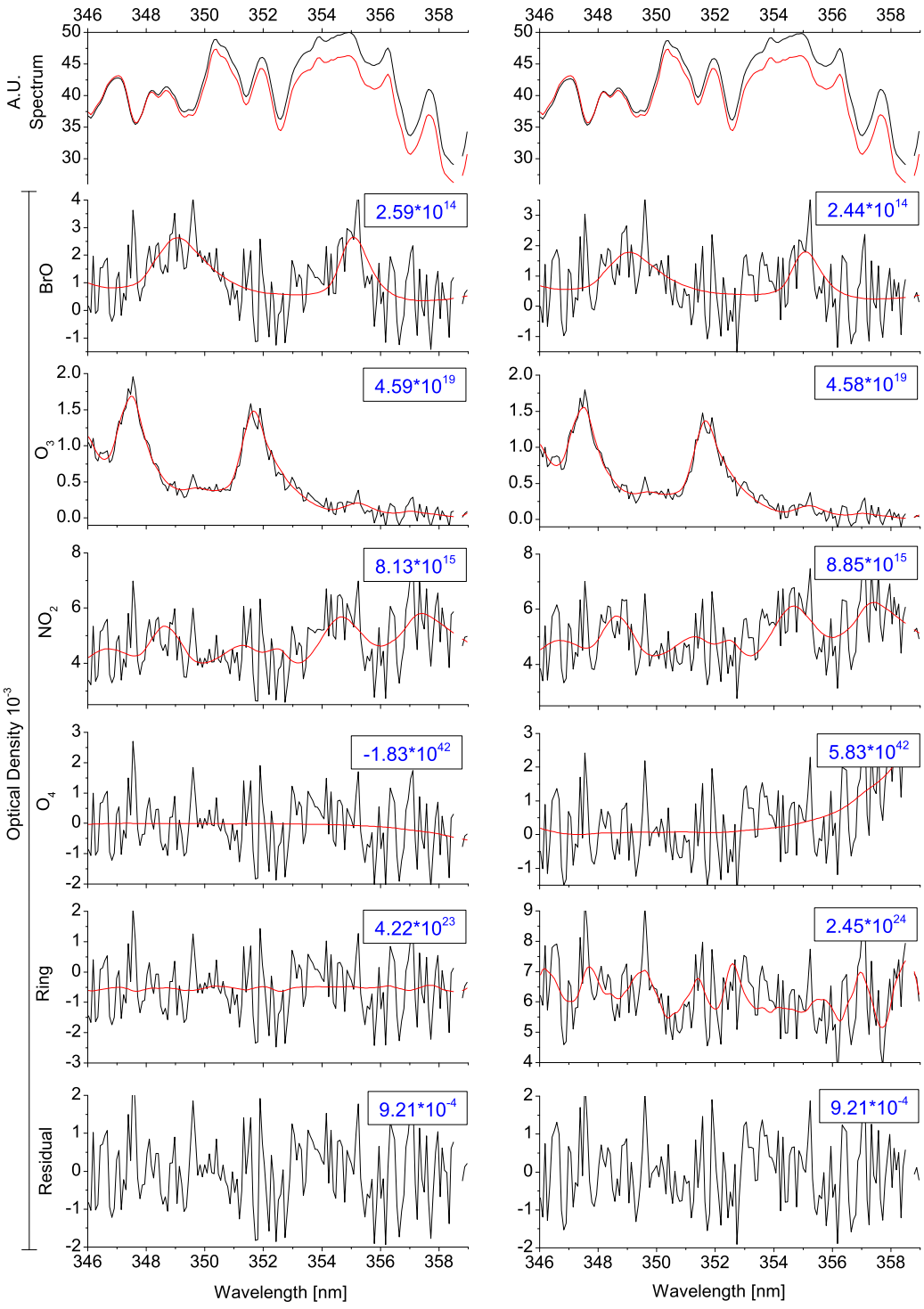

Figure 12.10.: *DOAS fit of a limb spectrum recorded during sunrise at 04:55 UT (SZA=79.8°). On the left side a pseudo-Ring-absorber calculated from the Fraunhofer reference spectra is used while on the right side one from an atmospheric spectrum recorded at the beginning of the ascent of the balloon is used. The inferred dSCDs are shown in blue for each absorber and the residual.*

Application of Shift and Stretch

An important detail of the DOAS analysis is correct wavelength alignment of the absorption cross sections. The convolution of the high resolution absorption cross sections can lead to a shift in wavelength, as shown in Figure 12.6. As stated by *Platt and Stutz* (2008), a shift and stretch might be necessary due to optical instabilities induced by changing ambient conditions (temperature and pressure) during the measurement, particularly during the balloon ascent. Therefore, the absorption cross sections are allowed to shift in a preliminary DOAS evaluation. The resulting shifts are analysed and fixed values for a shift are implemented in the final DOAS evaluation. The shifts for an evaluation are oriented on the strongest absorbers, namely O_3 and NO_2.
This procedure of checking and implementing shift and stretch values is performed for all trace gas analyses and all datasets.
For the optical densities of O_3 and NO_2 the application of a shift might be necessary, but has only minor influence on the resulting dSCDs. For BrO and other trace gases with lower optical densities, the correct choice becomes more important. An incorrectly applied shift or stretch for the different cross sections can significantly change the BrO dSCDs. Figure 12.11 shows the inferred wavelength shift of the NO_2 and O_3 absorption cross section for the balloon ascent measurements. The NO_2 and O_3 absorption cross sections are only allowed to shift together in the preliminary DOAS analysis. The first points are slightly higher, but the measurements in the troposphere returned very low optical densities for NO_2 and O_3. Hence, the wavelength shift can vary. After 16:30 UT, when the concentration maxima of both O_3 and NO_2 are passed, the optical densities decrease again and the shift starts to scatter. For this dataset the shift is fixed to 2.80 pixels (0.24 nm). This result fits very well to the observations of the wavelength shift in the convolution of all high resolution absorption cross sections (see Figure 12.6).

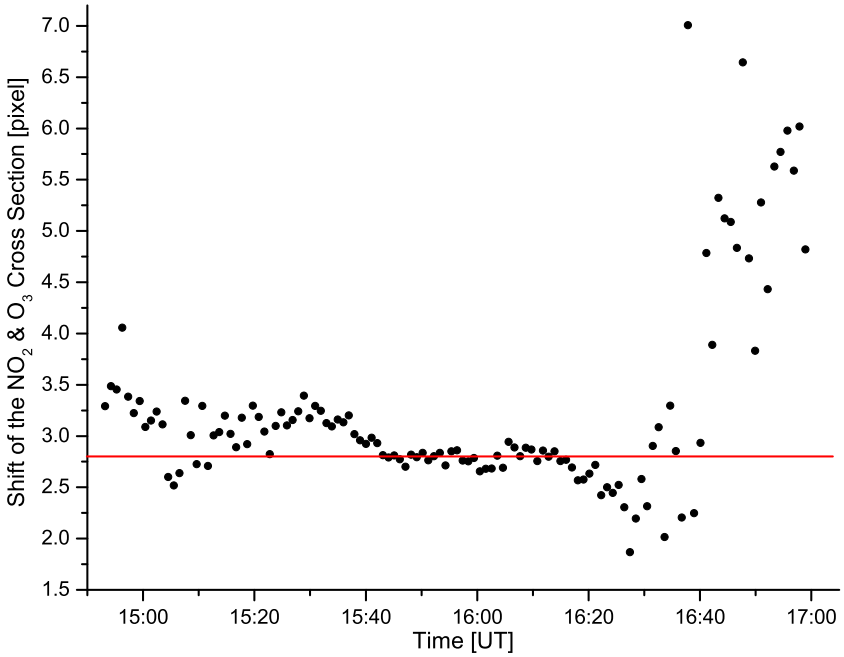

Figure 12.11.: *Shift of the NO_2 and O_3 cross section for the balloon ascent measurement. The red line indicates the shift, which is used in the final DOAS evaluation.*

As an example of how the wavelength shift propagates into the spectral retrieval, Figure 12.12 shows the wavelength shift analysed for the sunrise limb measurements. Because the telescopes look upwards, the optical densities are very low, meaning the wavelength shift is ill-defined. As soon as the elevation angles decrease, the optical densities increase and the shift returns to the expected value found for the ascent measurements. This ascertained shift was adapted for all other trace gas cross sections in the DOAS analysis. The lower panel in Figure 12.12 shows the difference between the two DOAS retrievals with and without wavelength shift correction.

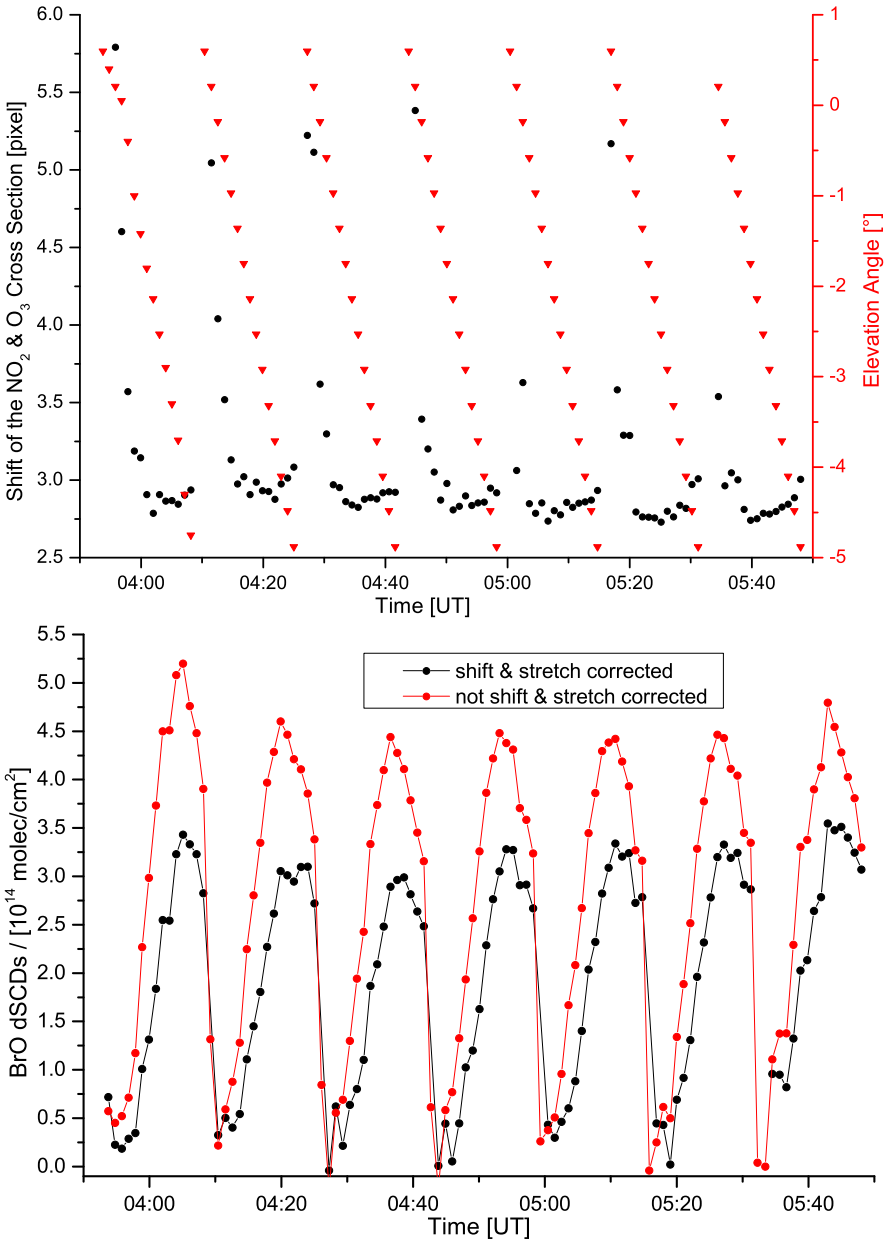

Figure 12.12.: *The shift for the NO_2 and O_3 cross section for the sunrise limb measurements is plotted (black dots) in the upper panel. The elevation angle of the telescopes is indicated by red triangles. The lower panel shows inferred BrO dSCDs.*

12.2. Radiances

The first step towards retrieving a concentration profile is to compare the measured and modelled relative radiances. This is done in order to test the exact elevation angles of the telescopes. The telescopes are fixed to the balloon gondola structure and calibrated for a zero elevation angle. This calibration is done just before the launch when all instruments were integrated into the gondola and the final balancing has been done.
If a constant roll or pitch was not recognised during the balancing of the gondola, then this offset must be accounted for. An offset due to a constant roll can be determined by comparing the measured and modelled radiances after a flight.
The radiance of skylight in the UV/vis spectral range near the horizon is very sensitive to tangent height and shows a wavelength dependent maximum in the lowermost stratosphere (*Sioris et al.* 2004, *Weidner* 2005). Figure 12.13 shows modelled radiance gradients for scattered skylight observations. The gradient was calculated at each altitude level for 450, 559 and 569 nm. Using the radiance gradient of the horizon, the absolute elevation angle of the viewing geometry can be determined.
Section 5.2 describes how the McArtim RT model calculates photon trajectories in the atmosphere. For a given viewing geometry and a certain number of photons, McArtim calculates BoxAMFs and radiances. The number of simulated photons is defined by the parameter *number of quadrature trajectories* (NQT) which is specified by the user. Usually, 5,000 to 15,000 photon trajectories are calculated for each given viewing geometry (*Kritten* 2009). However, a present application study revealed that this number might be too low (see Section 12.2.1). Formerly, the modelled radiances of a single limb scan sequence, calculated by McArtim, were compared with the measured radiances of that particular scan sequence. However, during the analysis of the radiance data it was found that, for an NQT below 10,000, a good agreement between the measured and the modelled radiances of a single scan can be achieved by coincidence. This should be avoided.

12.2.1. Sensitivity Studies for the Number of Photon Trajectories

The calculations of the programme McArtim's are based on random sampling. The accuracy is based on the NQT. A sensitivity study is performed to determine the variability of the calculated radiances.
For the atmospheric conditions of the LPMA/DOAS flight on September 8^{th} 2009, a viewing geometry is chosen and repeatedly calculated while increasing the NQT. The resulting radiances of this test are shown in Figures 12.14 and 12.15.
It was found that the NQT should be increased to 30,000 to reduce the variance of the model (see Figure 12.16) while keeping the computational time acceptable. In addition to the increased NQT, the radiances of several different scans should be compared with respect to their measured and modelled values.
Until now the measured radiances of a single limb scan have been compared with the radiances modelled using McArtim. The difference in the radiance gradient originating from an incorrect elevation angle calibration could then be accounted for by an elevation

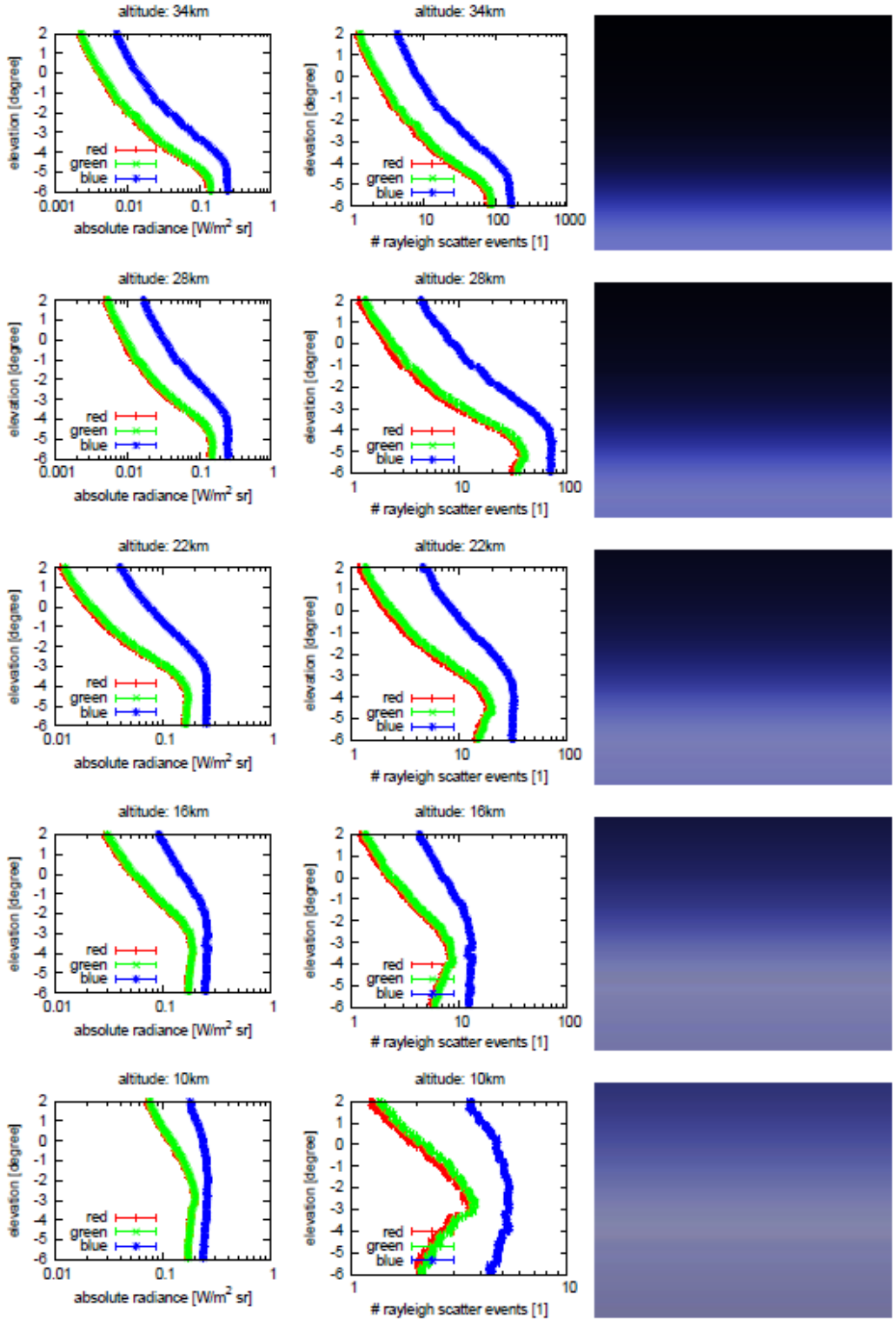

Figure 12.13.: *Modelled radiance gradients of the horizon for scattered skylight measurements at different altitude levels. The panels on the left side show absolute radiances for three different wavelengths. The panels in the middle show the simulated radiance distribution for all wavelengths. The panels on the right side show a simulated webcam picture representing how the human eye would see the overall radiance distribution. Adopted from Deutschman (2011).*

offset, as noted above. However, a simple offset could not correct the differences in the measured radiances and the model output for the balloon flight on September 7^{th} 2009. The McArtim output for the modelled radiances are normalised with respect to the solar irradiance. In order to compare the measured and the modelled radiances relative values are calculated:

- For the balloon ascent, all the radiances are determined relative to the final radiance measured.
- For the limb scans, each value is calculated relative to the largest elevation angle of that particular scan.

Figure 12.17 shows a comparison between the measured and modelled radiances of the sunrise scans at 450 nm.
From Figure 12.17 it can be deduced that, in order to achieve a good agreement in the gradient of the measured radiances, an elevation offset larger than 0.5° is required. However, for an offset larger than 0.5° the total increase in radiance from the largest elevation angle to the most downward elevation angle is too large.

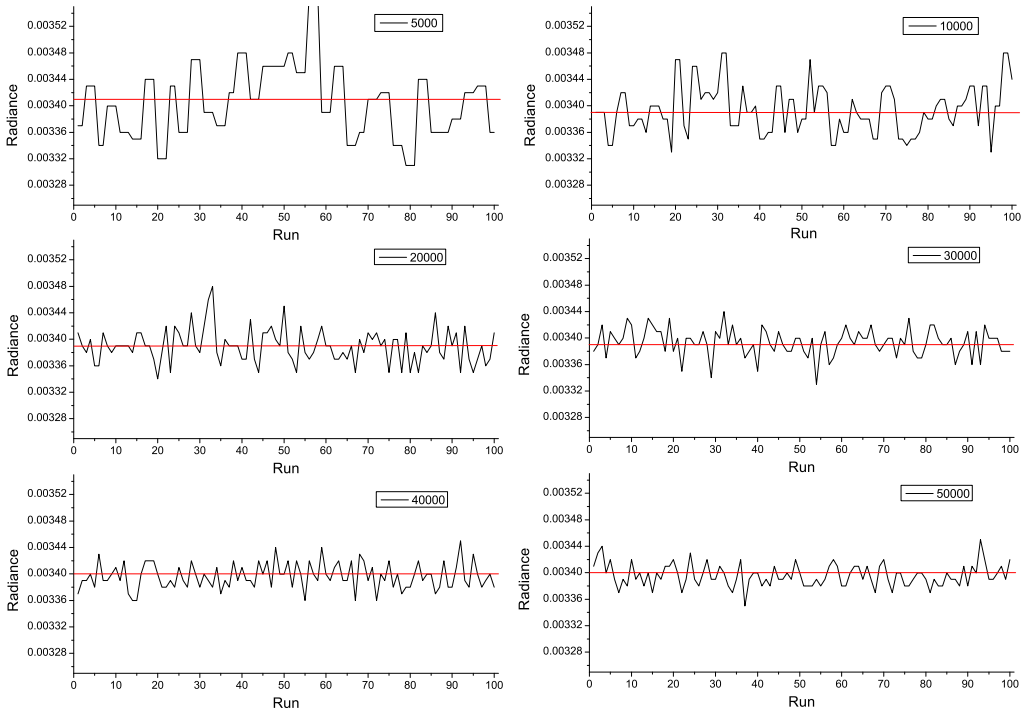

Figure 12.14.: *Modelled radiances at 495 nm using McArtim for six model runs with varying NQT. The number of calculated trajectories is noted in each diagram. The red lines represent the mean value of the model run. The radiances are normalised with respect to the solar irradiance.*

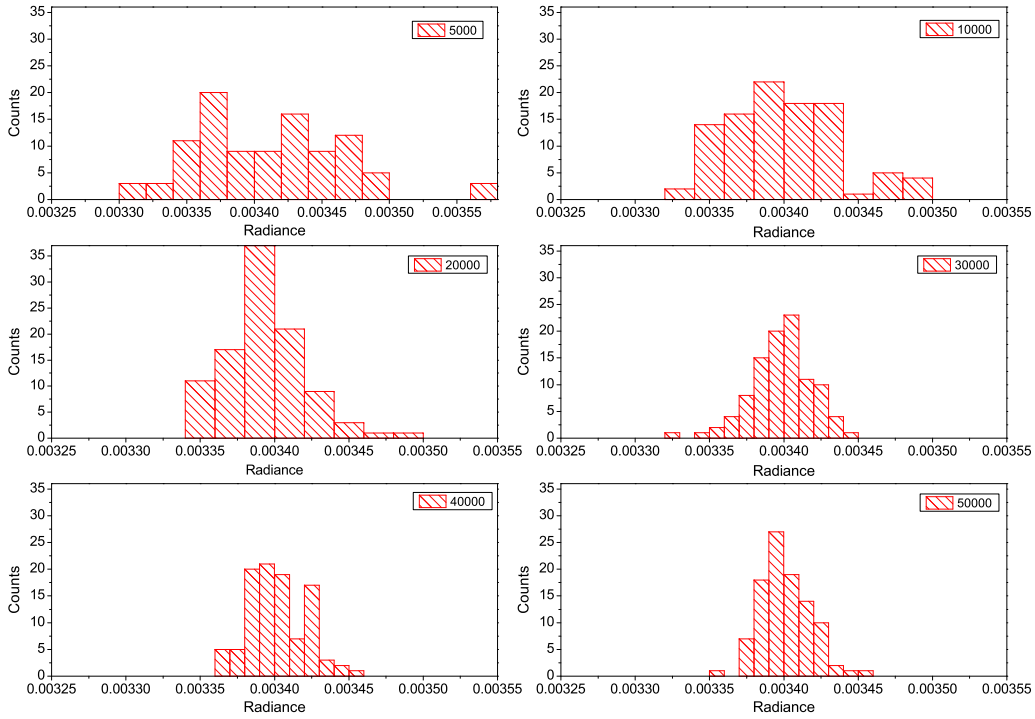

Figure 12.15.: *The statistical distribution for each of the six model runs. The accuracy significantly improves for increasing trajectory numbers, as seen in Figure 12.16. The radiances are normalised with respect to the solar irradiance.*

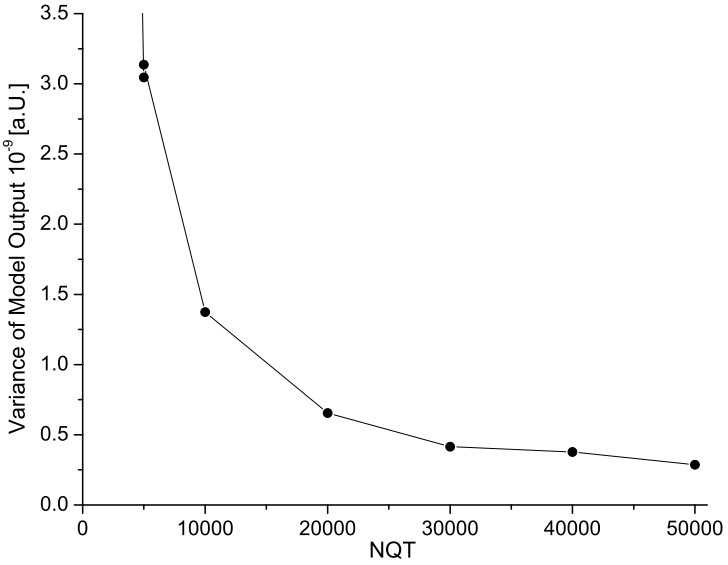

Figure 12.16.: *Variance of the six model runs from Figure 12.14. The variance decreases exponentially, while the computing time increases linearly. Based on these findings, an NQT of 30,000 is recommended to ensure a reasonable duration for radiative transfer calculations.*

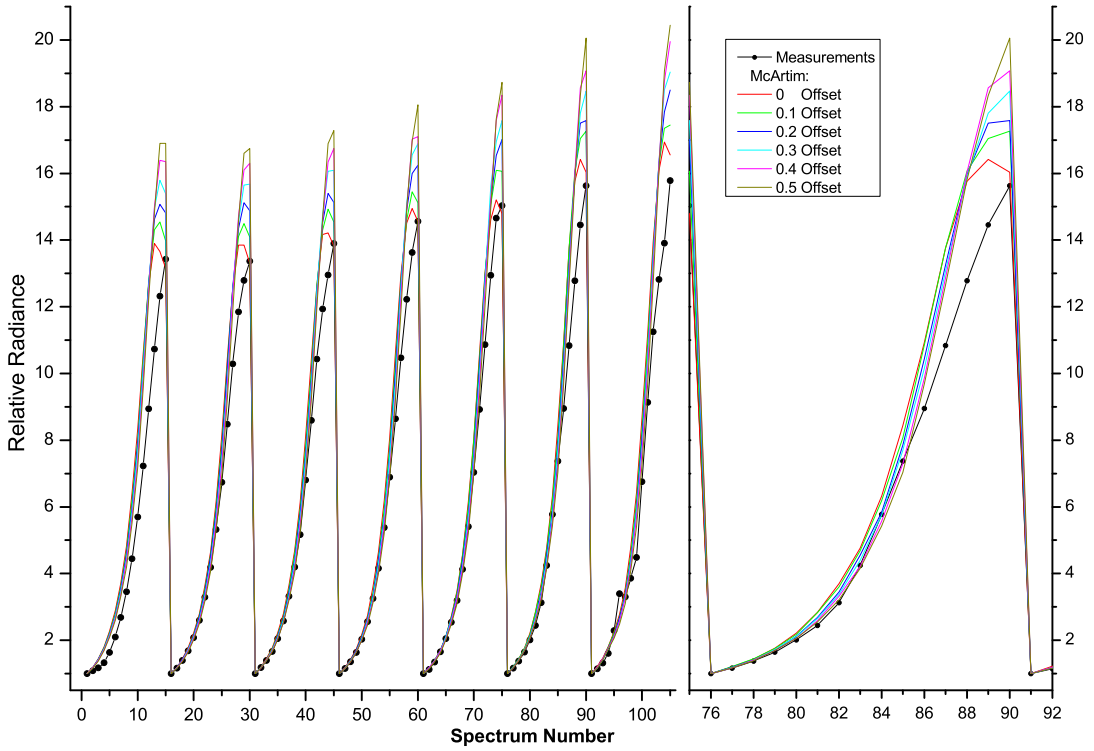

Figure 12.17.: *Comparison of relative radiances for the sunrise limb scans at 450 nm. The 105 radiance measurements from the seven scans are plotted as connected black dots. The radiance of each spectrum is relative to the first value of the corresponding scan. The McArtim model output is plotted in different colours for several elevation angle offsets. Again, the radiances are relative to the first value of each scan. In the right plot a zoom into the sixth scan is shown for better visualisation of the differences between the measured and modelled values.*

Two possible explanations for this discrepancy are considered. A smoother radiance gradient for a scan over the horizon can be achieved by introducing a dimming effect or by using a larger field of view for the telescopes. A dimming effect can arise from optical constituents such as aerosols and clouds. These are very important for tropospheric measurements, but barely influence the radiance distribution in the stratosphere. Large volcanic eruptions are an exception; these can penetrate the stratosphere and deposit large amounts of soot and other aerosol particles in higher altitude ranges.

12.2.2. Aerosol Extinction

On June 12^{th} 2009 the Sarychev Peak, a stratovolcano covering almost the entirety of Matua Island in the Kuril Islands, Russia, erupted and injected large amounts of soot and SO_2 into the atmosphere. The extent of its influence on the radiance measurements can be derived from the measurements of the STAC instrument. Preliminary results from the STAC instrument indicated an additional aerosol load at the float altitude of the balloon from 29 to 34 km.
Unfortunately, the STAC instrument only counts particle numbers and does not measure aerosol optical properties. Based on the first reports of the eruption, a combination of soot

Figure 12.18.: *Photograph of the Sarychev Peak eruption on June 12th 2009, three months prior to the LPMA/DOAS balloon flight. Adopted from NASA (2012a).*

and sulphuric acid droplets are assumed for particle composition. Measurements from the SAGE III satellite instrument are used to initialise a sensitivity analysis of the impact of aerosol dimming on the modelled radiances.
The SAGE III instrument provides altitude-based aerosol extinction profiles (AEP) for different wavelengths (*Thomason and Taha* 2003). For the UV/vis measurements of the miniDOAS instrument, three channels of the SAGE III measurement range are of interest: 384 nm, 448 nm and 520 nm. Unfortunately, the SAGE III instrument was not operative in September 2009. Hence, data for similar atmospheric conditions was identified and used as a starting point.These AEPs were selected based on the following parameters: location, season, temperature and pressure profile. For all three channels, several AEP were chosen and averaged (see Figure 12.21). In order to consolidate the initial AEP of the SAGE III

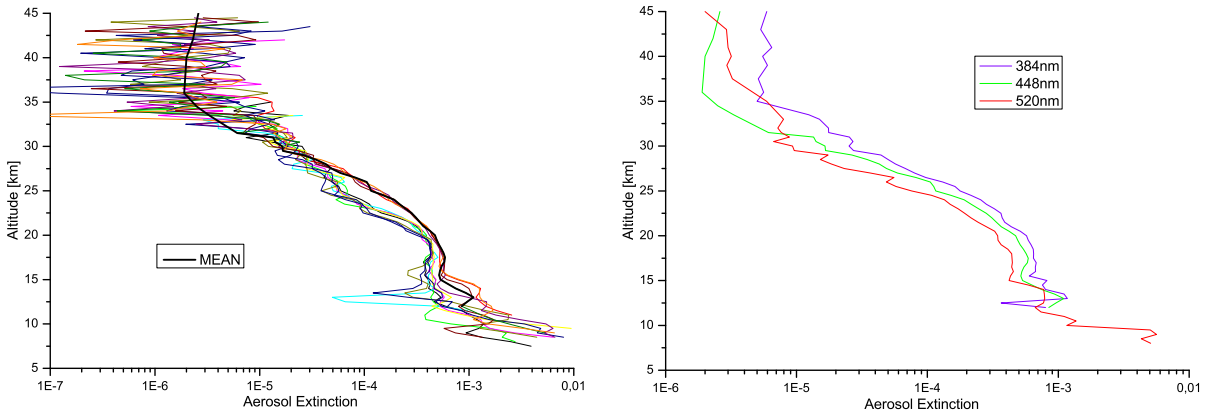

Figure 12.19.: *SAGE III aerosol optical density profiles. Multiple profiles which matched the atmospheric conditions of the 2009 campaign atmosphere were used to create mean values for a profile. An example for the 448 nm channel is shown in the left plot. In the right plot the mean values for all three channels are shown. Data was taken from the SAGE III Data site (NASA 2012b).*

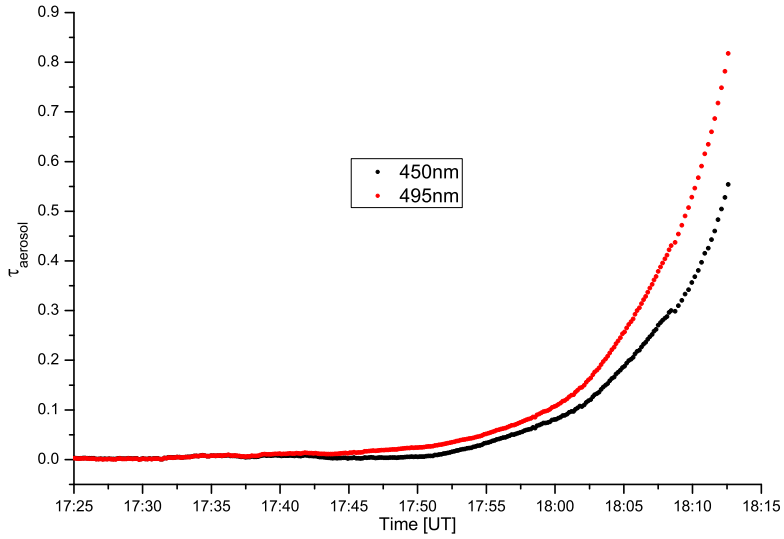

Figure 12.20.: *SCDs for $\tau_{aerosol}$ for the sunset direct sunlight measurements for two different wavelengths (450 nm and 495 nm).*

instrument, the direct sunlight data was consulted. *Gurlit et al.* (2005) and *Butz* (2006) developed a method by which the direct sunlight instrument can retrieve aerosol optical density information from the direct sunlight spectra. The measured intensity of a spectrum is compared to the intensity of the reference spectrum at a certain wavelength. Based on the Lambert-Beer law:

$$I = I_0\, e^{(-\tau)} = I_0\, e^{(-\tau_{absorber} - \tau_{Rayleigh} - \tau_{aerosol})} \tag{12.1}$$

the decrease in intensity is described by trace gas absorption, Rayleigh scattering and an aerosol component. With

$$ln\left(\frac{I}{I_0}\right) + \tau_{absorber} + \tau_{Rayleigh} = -\,\tau_{aerosol} \tag{12.2}$$

a parameter $\tau_{aerosol}$ is calculated for different wavelengths. Following the retrieved dSCDs of the different trace gases for the spectrum, the decrease in intensity due to absorption is calculated. The decrease due to Rayleigh scattering is approximated by Equation 4.5 as explained in Section 4.2.1. The remaining difference is then attributed to the $\tau_{aerosol}$ component. These calculated $\tau_{aerosol}$ values are then treated as normal trace gas dSCDs in a DAMF inversion. The calculated profile is the AEP shown in Figure 12.21. The intensity of the initial AEP is increased stepwise to create a radiance gradient for the atmosphere similar to the measured data. In addition, a combination of several different classes of scatterers is tested to account for the different properties of soot and other aerosol types. Soot particles mainly absorb radiation, while SO_2 particles will predominantly scatter radiation leading to different results regarding radiance distribution. Table 12.1 shows several of the different scattering classes used in this study and their properties.

The analysis of the aerosol extinction profiles showed that only an AEP with highly un-

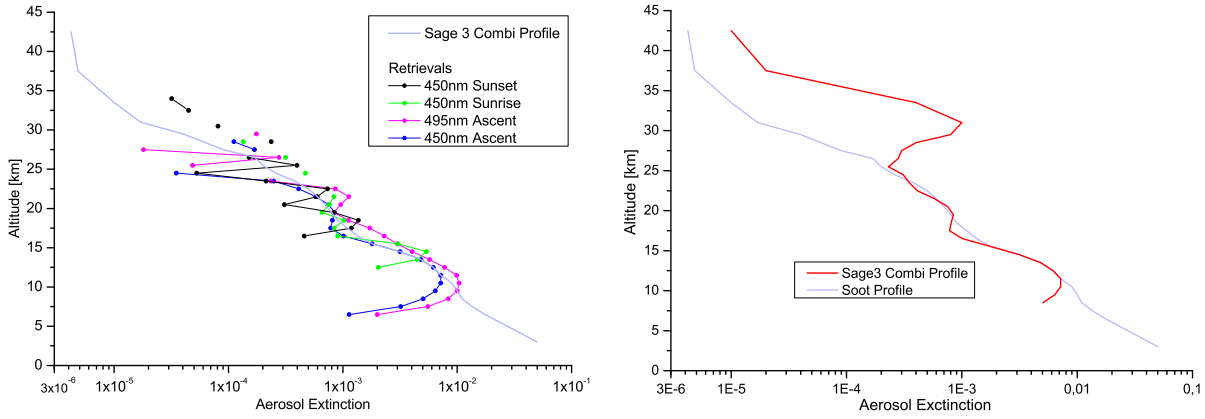

Figure 12.21.: *In the left panel aerosol extinction profiles are combined from the three channels of the SAGE III instrument (blue) and several aerosol extinction profiles retrieved from the direct sunlight measurements. While these profiles cannot be assumed to be of high accuracy, they confirm the expected order of magnitude and shape of the profile. In the right plot the same profile from the SAGE III data (blue) is shown, along with a profile (red) that shows an attempt to achieve the dimmed atmosphere to explain the miniDOAS radiances.*

Table 12.1.: *Different classes of scatterers used in the McArtim simulations, characterised by the single scattering albedo (ssa) and the asymmetry parameter g.*

	urban	soot	aerosol	cloud
ssa	0.99	0.2	0.9982	1.0
g	0.85	0.35	0.68	0.82

realistic extinction values could produce the desired atmospheric dimming effect. Further analysis of the preliminary STAC instrument data proved that the signal around float altitude is a result of a contaminated measurement chamber. Using transport model calculations and measurements from the SPIRALE instrument, *Krysztofiak* (2011) showed that only traces of the additional aerosol load of the Sarychev eruption were present during the measurements in Kiruna in September 2009. These concentrations were too low to create significant changes in the radiative transfer.
Due to these results, the SAGE III profile, confirmed by the direct sunlight retrieval, is used in the McArtim calculations.

Restrictions on the AEP

The comparison of the modelled and measured radiances shows that the miniDOAS limb measurements can also be used to retrieve an AEP (see Figure 12.22). However, without an initial estimation of the AEP the inversion is rather difficult. Unfortunately, the AEP does not allow for conclusions about the specific type of aerosol, only its general properties. The miniDOAS measurements are generally sensitive to extinction values larger than $2{\cdot}10^{-4}$.

The sensitivity is highly dependant on the observed altitude, balloon float level and field of view of the instrument. For this flight, the AEP can be restricted by using the miniDOAS measurements to the uncertainty given by the grey colour in Figure 12.22. Above float level the uncertainty quickly increases as there are no measurements to determine limitations. A more comprehensive study into using miniDOAS instruments for the retrieval of AEP in the troposphere was performed by *Yilmaz* (2011). Another investigation by *Vogel* (2011) tested early detection abilities of DOAS instruments regarding volcanic plumes and ash clouds.

The second possible reason for a decreased overall radiance gradient during a limb scan is that the size of the field of view might be wider than initially calculated. Even a slight misalignment of the telescopes and the fibre bundles has a large impact on the field of view of the miniDOAS instrument.

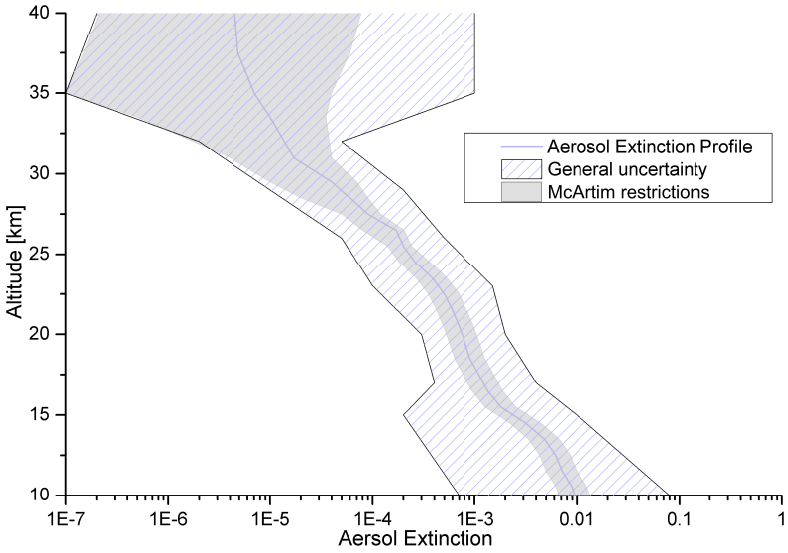

Figure 12.22.: *AEP used for the radiative transfer calculations in the McArtim simulations and the two corresponding uncertainties. The blue area indicates the uncertainty estimated from the SAGE III observations and the grey shaded area the restrictions resulting from the miniDOAS measurements.*

12.2.3. Field of View

The theoretical Field Of View (FOV) of the miniDOAS instrument is derived from the size of the entrance slit and the focal length of the lens used in the telescope:

$$FOV = tan\left(\frac{\text{slitwidth}}{\text{focal length}}\right) = tan\left(\frac{100\,\mu m}{30\,mm}\right) = 0.19° \tag{12.3}$$

for the USB spectrograph in the visual range. This theoretical FOV can be achieved by a perfectly fixed telescope. The QE spectrograph (UV spectral range) has a FOV of 0.382°. However, analysis showed that if the fibre bundle is not exactly at the focal point of the

lens in the telescope, the FOV broadens immediately and takes a Gaussian shape.
The FOV of the miniDOAS instrument is reexamined in light of these findings. In the laboratory, the telescopes scan over a lamp behind a slit and the resulting intensity distribution is compared to the theoretical values. This procedure is repeated for different fibre bundle positions, with respect to the focal distance of the lens in the telescope. The FOV of the configuration of the flight on September 7^{th} is then used as input for McArtim.
For the configuration of the balloon flight on September 7^{th}, it is necessary to use a simple Gaussian shape for the FOV. The FOV of the vis telescope can be seen in Figure 12.23.
This broadening of the FOV naturally leads to a loss in altitude resolution for the limb

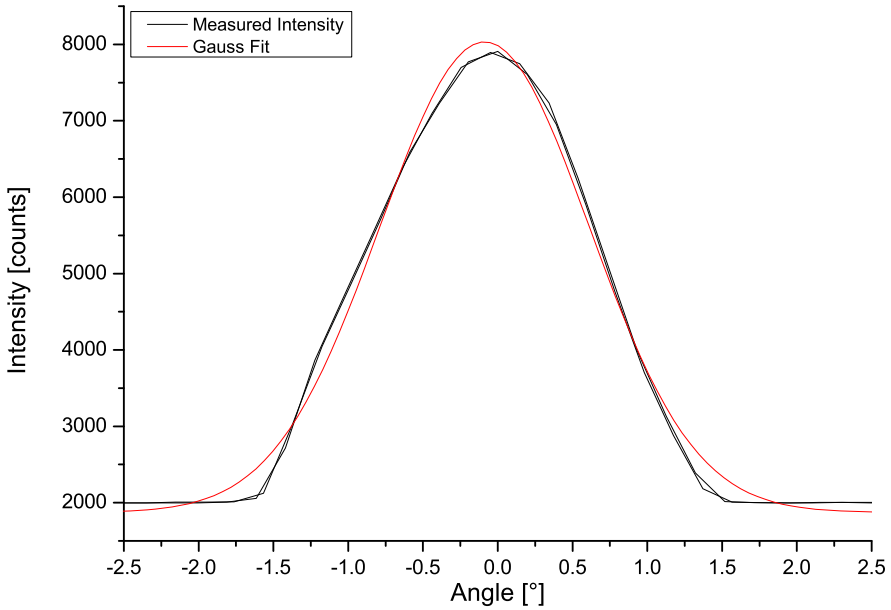

Figure 12.23.: *Experimentally inferred FOV of the vis telescope with the angular sensitivity of the spectrometer in black and a Gaussian fit for this distribution in red.*

measurements. The balloon ascent measurements are less affected by a change in the FOV (see Figure 12.24). The BoxAMFs of the theoretical and actual FOV are shown in the panels on the left side of Figure 12.25.
The loss in sensitivity for the limb measurements is about 50% between 17 and 30 km for elevation angles smaller than -0.97° for the QE. At the same time, the broadening of the FOV increases sensitivity in other altitude regions, because more light is collected. This is shown in the lower right panel of Figure 12.25. Figures 12.26 and 12.27 show the same comparison for $\lambda = 450$ nm and $\lambda = 495$ nm of the USB spectrometer.
Formerly a single elevation scan was used to determine the elevation offset of the gondola during a flight. However, to increase the certainty of an accurate fit, the entire dataset of radiances for all evaluated wavelengths (350 nm for the BrO retrieval; 450 nm for the NO_2 retrieval and 495 nm for the O_3 retrieval) is compared to the modelled values for a certain configuration.
The result of the analysis is shown in Figure 12.28. The comparison between the measured radiances and the modelled radiances resulting from this new FOV show a very

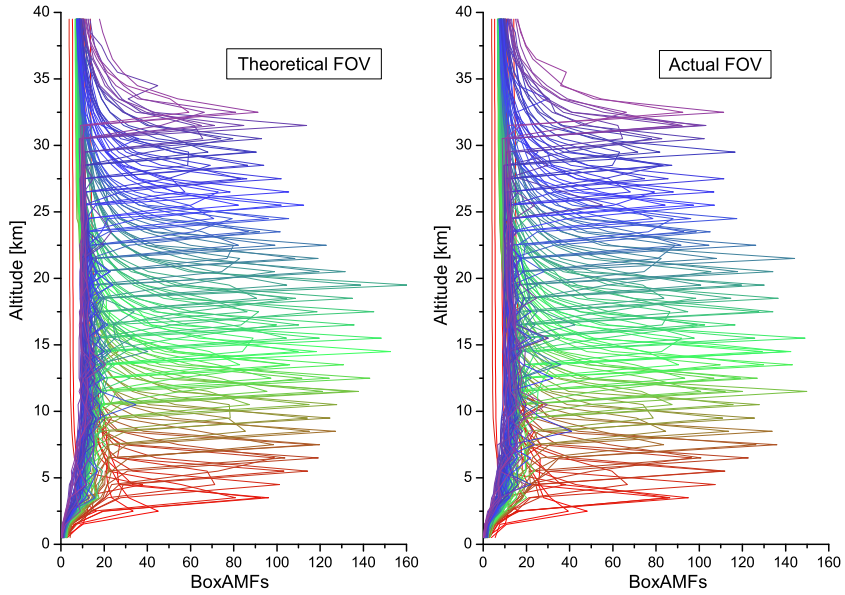

Figure 12.24.: *Comparison of BoxAMFS of the O_3 retrieval with the theoretical rectangular FOV and a comparison of the actual FOV with a Gaussian shape. The colour coding is only used to make the lines distinguishable.*

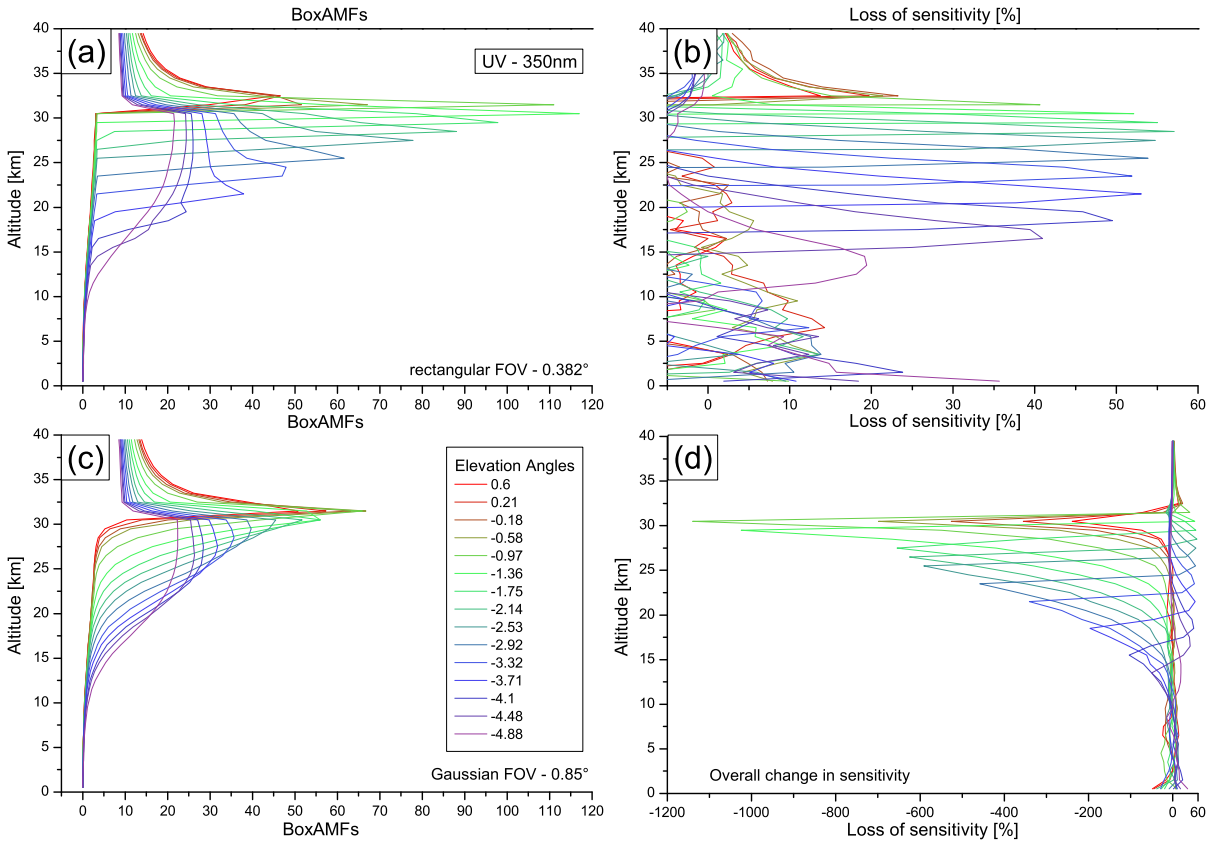

Figure 12.25.: *Effect of FOV broadening on the sensitivity of the QE spectrograph at 350 nm. The panels on the left side show the BoxAMFs: panel (a) for the theoretical FOV and panel (c) for the actual FOV. Panel (b) shows the loss in sensitivity in percent based on the BoxAMFs of the theoretical and actual FOV. Panel (d) shows the overall change in sensitivity. The colour coding given in panel (c) holds for all four panels.*

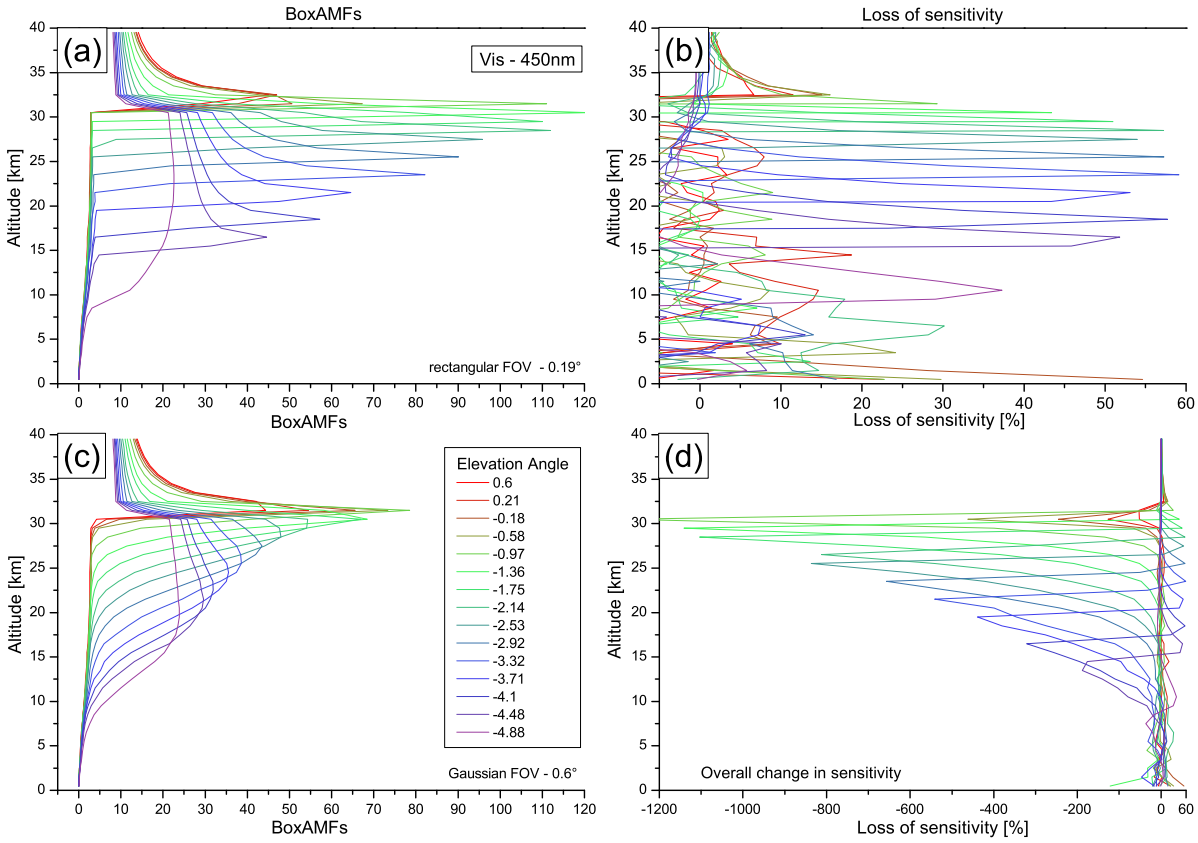

Figure 12.26.: *Effect of FOV broadening on the sensitivity of the USB spectrograph at 450 nm. The panels on the left side show the BoxAMFs: panel (a) for the theoretical FOV and panel (c) for the actual FOV. Panel (b) shows the loss in sensitivity in percent based on the BoxAMFs of the theoretical and actual FOV. Panel (d) the overall change in sensitivity. The colour coding given in panel (c) holds for all four panels.*

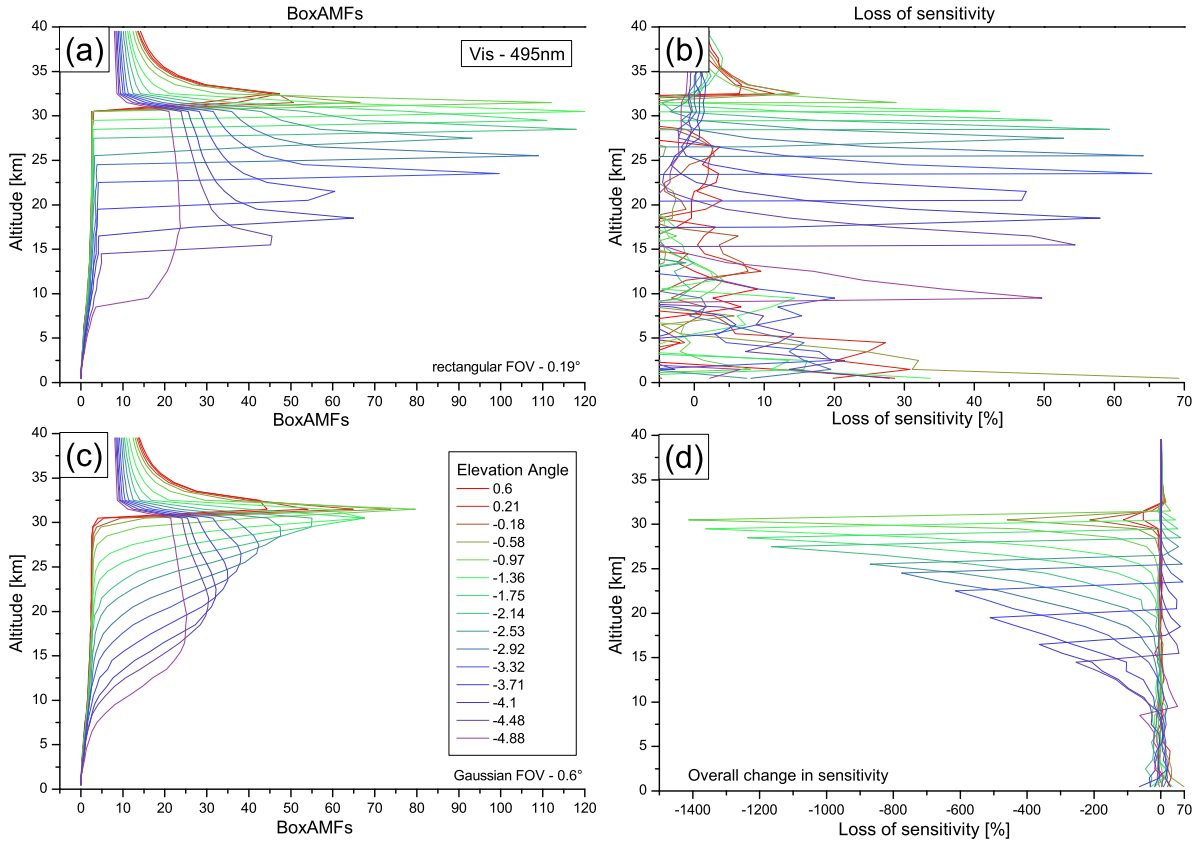

Figure 12.27.: *Effect of FOV broadening on the sensitivity of the USB spectrograph at 495 nm. The panels on the left side show the BoxAMFs: panel (a) for the theoretical FOV and panel (c) for the actual FOV. Panel (b) shows the loss in sensitivity in percent based on the BoxAMFs of the theoretical and actual FOV. Panel (d) the overall change in sensitivity. The colour coding given in panel (c) holds for all four panels.*

good agreement. The offset with the smallest difference from the actual measurement is

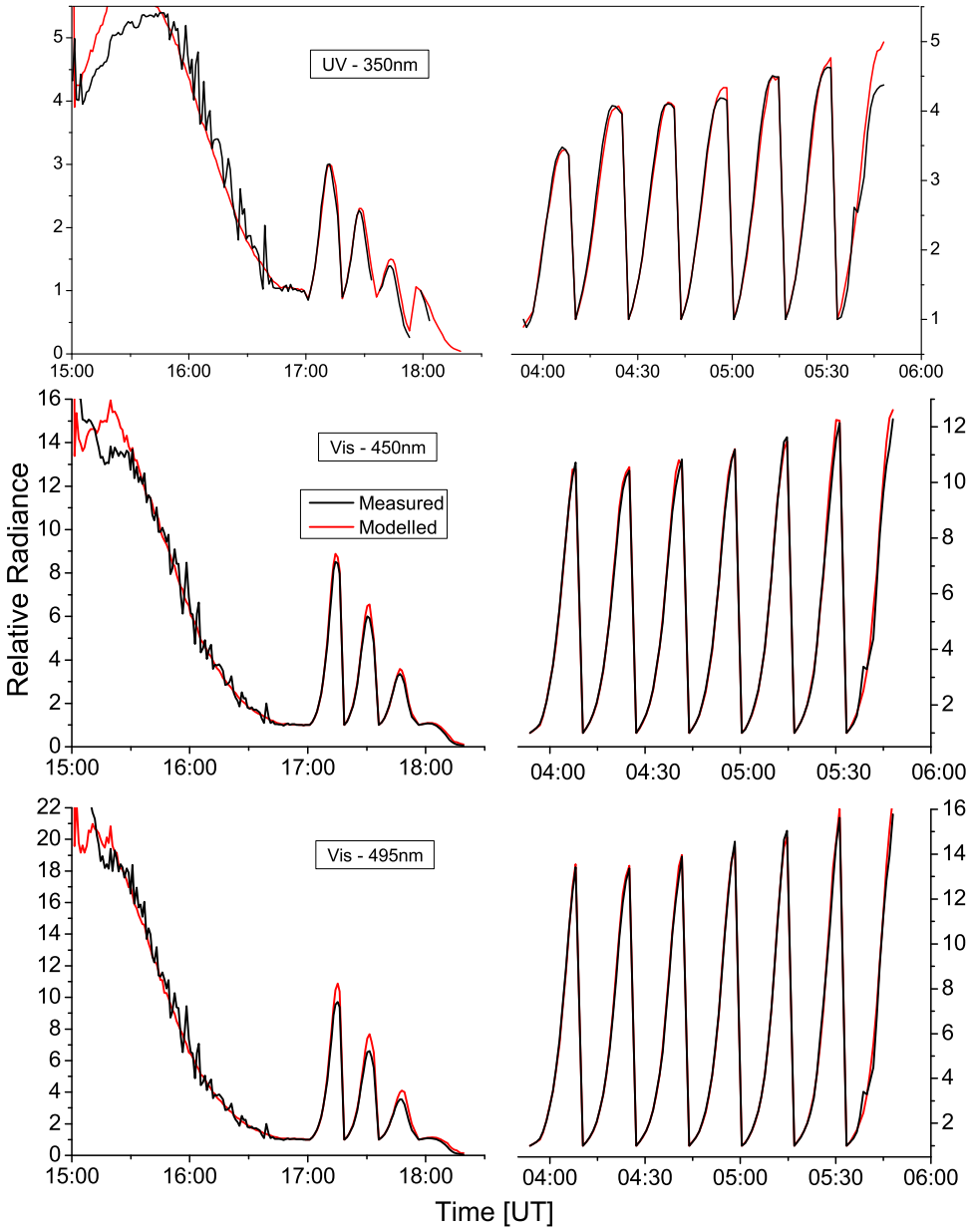

Figure 12.28.: *Comparison between the measured and modelled radiances for different wavelengths for balloon ascent, sunset and sunrise limb profiling mode. The upper panel is for $\lambda = 350$ nm, the middle panel is for $\lambda = 450$ nm and the lower panel is for $\lambda = 495$ nm. The measurements are plotted in black and the modelled radiances in red.*

then added to the elevation sequence and the resulting viewing geometry is used as final input for the radiative transfer calculations.

The first limb scan sequence during sunrise at 03:53 UT is examined further. As mentioned above, the stepper-motor was frozen during the night and only started the scanning sequence after warming by solar heating. Therefore, it cannot be assumed that all the elevation angles were reached correctly during the first scanning sequence. Because of this

uncertainty, the measurements of the first limb scan were calibrated against the calculated radiance gradient (Figure 12.29).

This is only possible because the gondola did not oscillate during the sunrise measure-

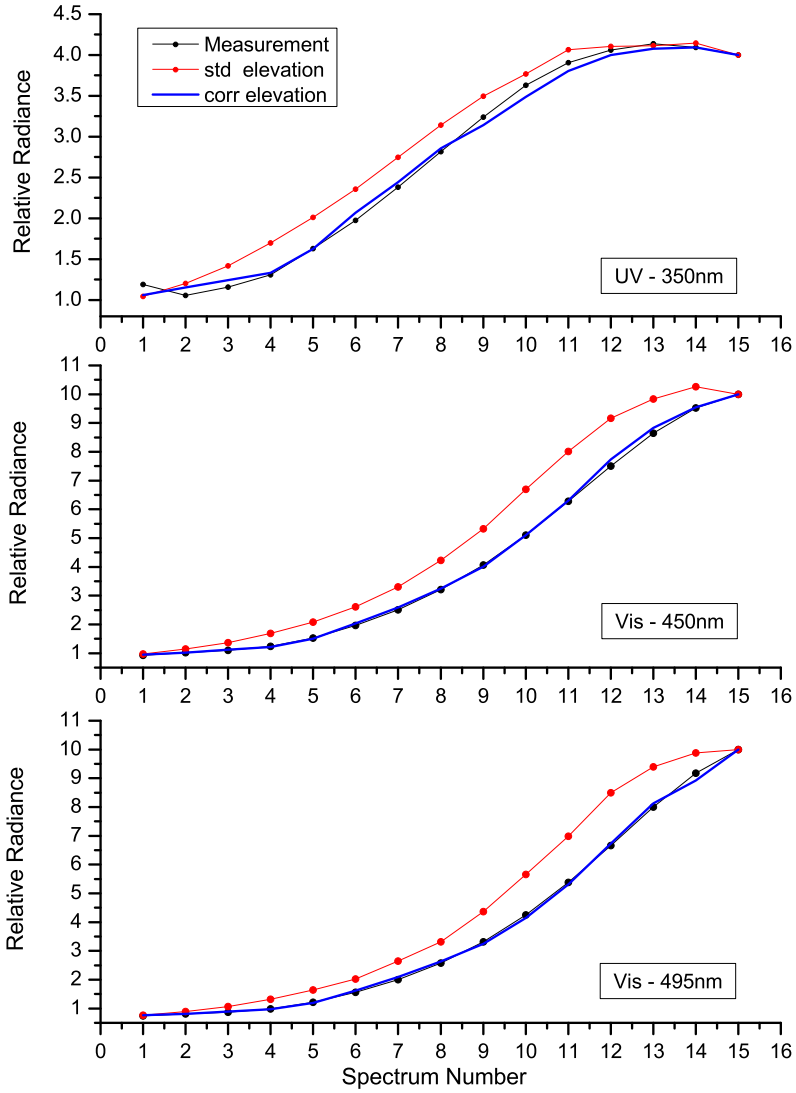

Figure 12.29.: *Radiance calibration for the first limb scan at sunrise. The modelled radiances are calculated for the corrected offset angles and then simultaneously compared to the measured radiances for all three wavelengths. Measured values are plotted in black, values using the original elevation angles in red and values for the newly calibrated elevation angles for the 15 spectra of the first limb scan are in blue.*

ments. Due to very low wind speeds at float level, the balloon gondola was almost completely stable during this time and the azimuth angle fluctuation of the gondola did not exceed 0.3°. The oscillations of the gondola during the ascent were much stronger and higher frequencies occurred. Therefore, the radiance values from the ascent cannot be calibrated using the radiance gradient method. Figure 12.30 shows the azimuth alignment of the gondola. While there are still oscillations during the ascent, the sunset and sunrise are free of perturbations. Only after sunset at 18:25 UT did the gondola start turning when the automated azimuth stabiliser was turned off.

Still, the sensitivity to changes in the azimuth alignment have to be evaluated, if the radiance distribution is to be used to calibrate the elevation. Figure 12.30 shows a test of an azimuth based sensitivity analysis. For positive angles, the radiance does not change considerably turning away from the sun. Scattering becomes more intermittent, however, which can be seen in the wider spread of the retrieved radiances. It must be noted that an azimuth variation exceeding 8° occurred only at 15:12 UT, when the tropopause was passed. For the sunset and sunrise measurements, the azimuth variance is smaller than 0.3° due to the very low wind speeds. Major azimuth variations can only be seen during the balloon ascent in the troposphere and after sunset when the automated azimuth stabiliser was turned off.

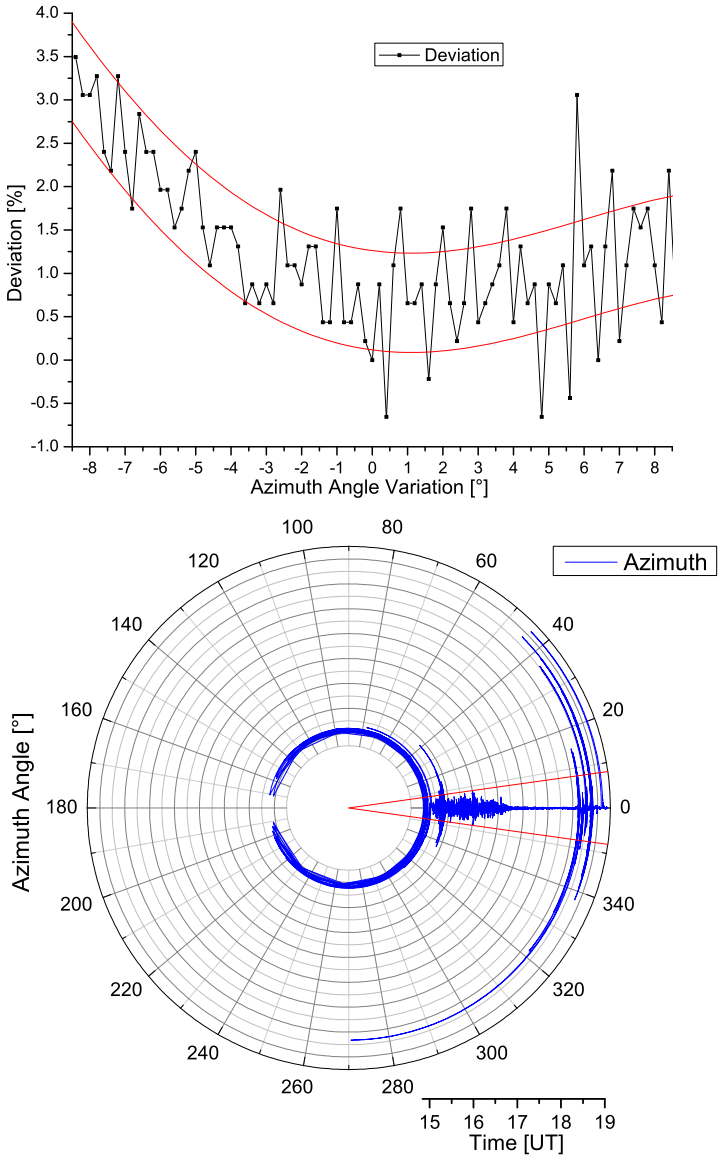

Figure 12.30.: *Radiance variation as a function of change in the azimuth alignment. The x-axis shows the change of the azimuth angle, zero being a viewing direction of 90° to the Sun. Negative values indicate an angle smaller than 90°. At these angles the radiances start to rapidly increase. The 1-σ envelope is indicated in red. In the lower plot the azimuth is shown for the balloon ascent and the sunset. The 8° limits are indicated in red.*

An important fact was discovered during the analysis of the radiance data of the 2009 flight. For the 2009 StraPolÉté campaign, the miniDOAS instrument was operated for the first time with the MS-DOAS software (*Frieß* 2009). MS-DOAS was specially developed as a control software for instruments containing several spectrometers.
A single spectrum normally comprises several readouts or scans during a predetermined integration time. In the spectrometers' normal measurement mode, either a total integration time or a specific number of scans is given by the measurement protocol. The operating software, DOASIS or in this case MS-DOAS, automatically calculates the exposure time of the scans or the number of scans being added to a single spectrum to achieve an 80% saturation for each spectrum. Based on the achieved saturation of a spectrum, exposure time or number of scans per spectrum should be adjusted for the subsequent spectrum. However, it was found that small changes in the saturation level were not accounted for and the required changes in exposure time or number of scans were not calculated. In the MS-DOAS software a user defined variable for the percentage difference in saturation of two consecutive spectra controls if the exposure time or number of scans per spectrum is changed. Figure 12.31 shows the change in exposure time (TExp) and the number of scans (NumScans) per spectrum for the sunrise measurements. For the USB (450 nm, 495 nm), the adjustment for a change in intensity levels or radiance is handled correctly as shown in the visible wavelength range. For the QE (350 nm) the radiance only changes by a small amount for the last spectra of each scan and the number of scans is no longer adjusted.
During the ENRICHED campaign in 2011, a similar effect was observed. However, for this flight the adjustment of the QE performed as expected, while the adjustment of the USB showed the same characteristics as the QE in 2009.
To account for this, the adjustment parameter has been lowered to a 2% change in intensity for both spectrometers.

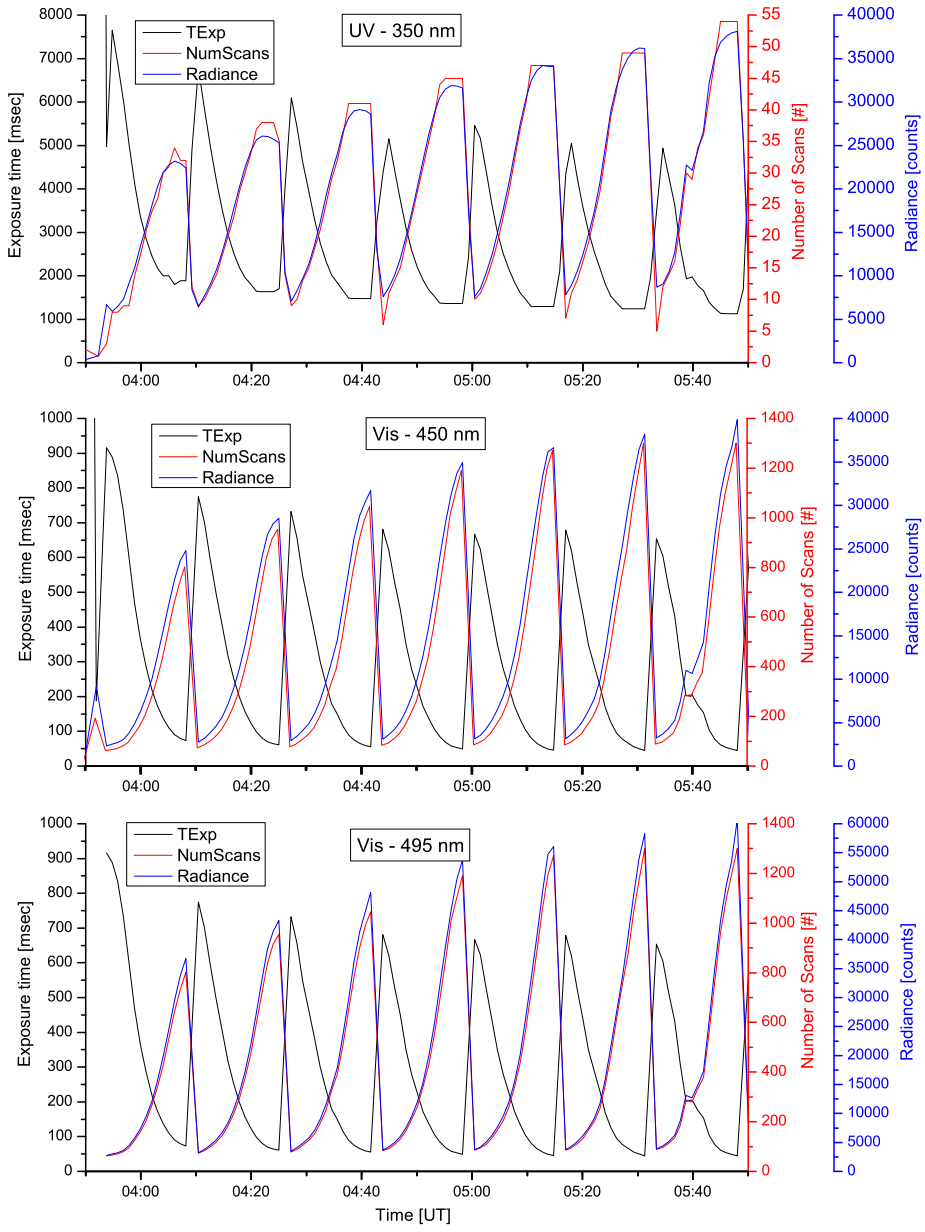

Figure 12.31.: *The three graphs show the exposure time (TExp) in black, the number of scans (NumScans) in red and the measured radiance in blue for the sunrise measurements on September the 8th 2009. Though the radiance still increased, in the UV the number of scans was not automatically adjusted for the last four spectra during an elevation scan sequence.*

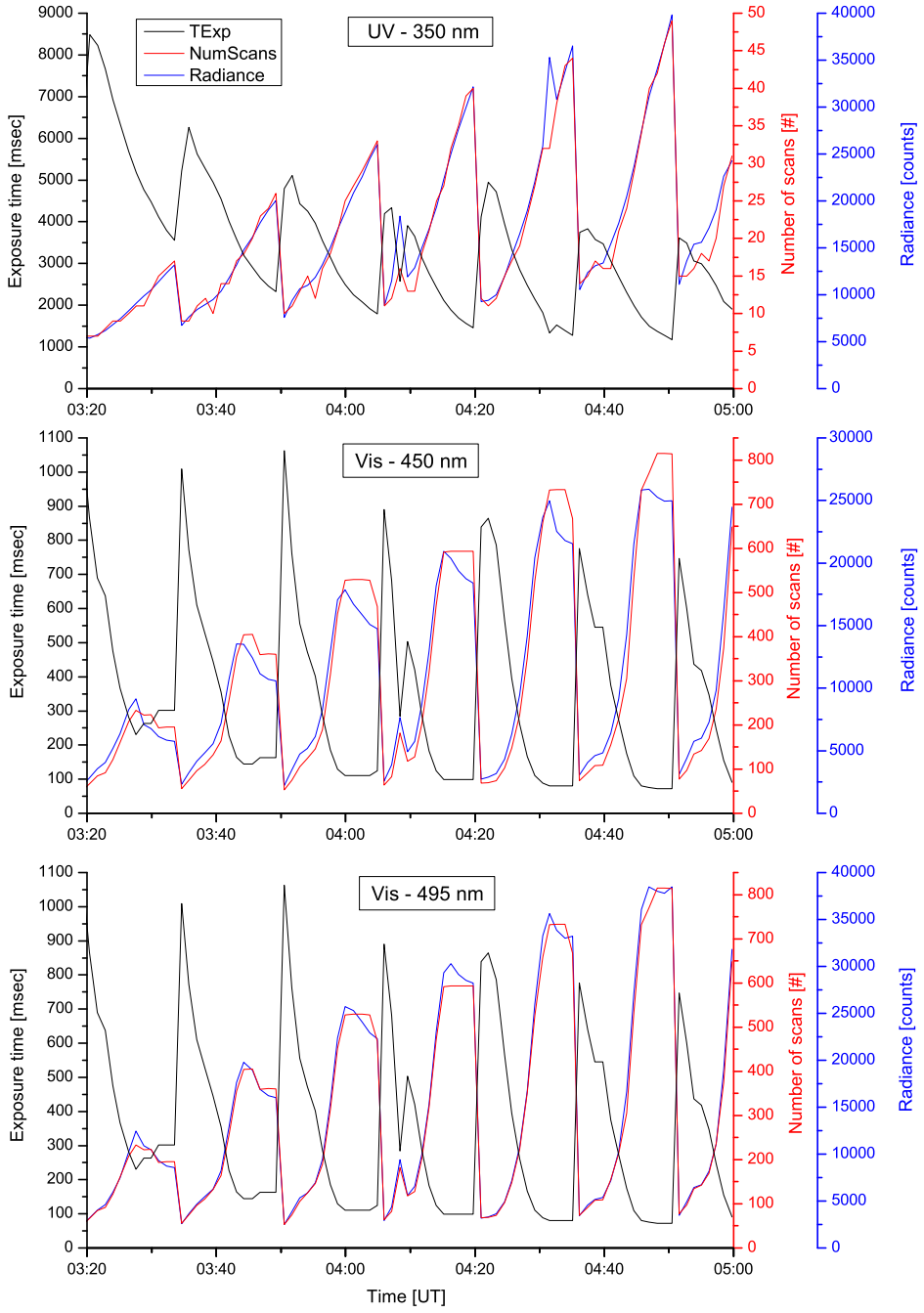

Figure 12.32.: *The three graphs show the exposure time (Texp) in black, the number of scans (NumScans) in red and the measured radiance in blue for the sunrise measurements on March, 31st 2011 during the ENRICHED Campaign. During this flight the automated adjustment worked correctly in the UV but not in the vis range. Though the radiance changed, the number of scans was not automatically adapted for the last spectra in an elevation scan sequence.*

12.3. The Balloon Ascent Measurements

All dSCDs measured during the balloon ascent still show an oscillation from 15:50 UT to 16:20 UT (see Figures 12.33 - 12.35). This is probably due to the gondola oscillations or a pendulum movement of the gondola. These oscillations caused the otherwise fixed telescopes to scan over the horizon. The LPMA gondola has no absolute position recording which would allow the tilt of the gondola to be inferred.
The oscillations of the measured radiance can only show the undulation of the gondola for time frames longer than one minute. Since the radiances are integrated over 60 seconds, they do not account for higher frequencies. Therefore, the exact direction faced cannot be determined. In a spectral retrieval these scattered observations cause severe perturbations and have to be discarded. In order to consolidate the data, the measured and modelled radiances are compared and only values within the 1σ deviation are used for the profile inversion. The radiances in Figures 12.33 - 12.35 are taken from the centre of the respective DOAS fit windows i.e. 495 nm for O_3, 450 nm for NO_2 and 350 nm for BrO. The oscillations faded out once the balloon reached the float altitude. This is due to reduced wind shears at this altitudes.

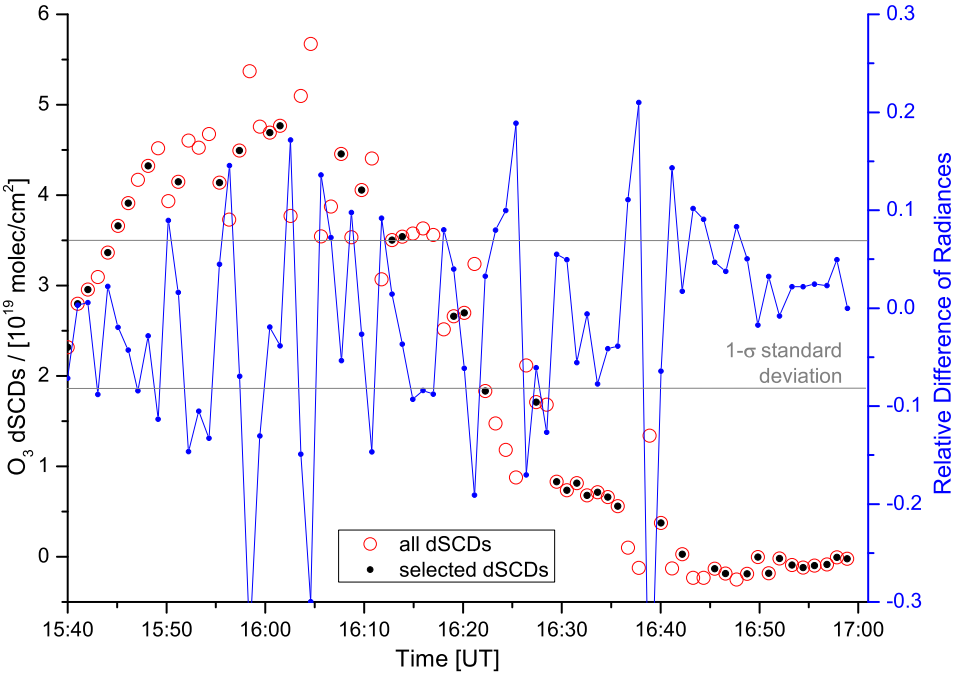

Figure 12.33.: *The O_3 dSCDs are plotted as red circles. The blue line shows the relative difference between the measured and modelled radiances at 495 nm (see also Section 12.2). All values within the 1σ range (grey line) are used for the profile retrieval (black dots). The other values are discarded.*

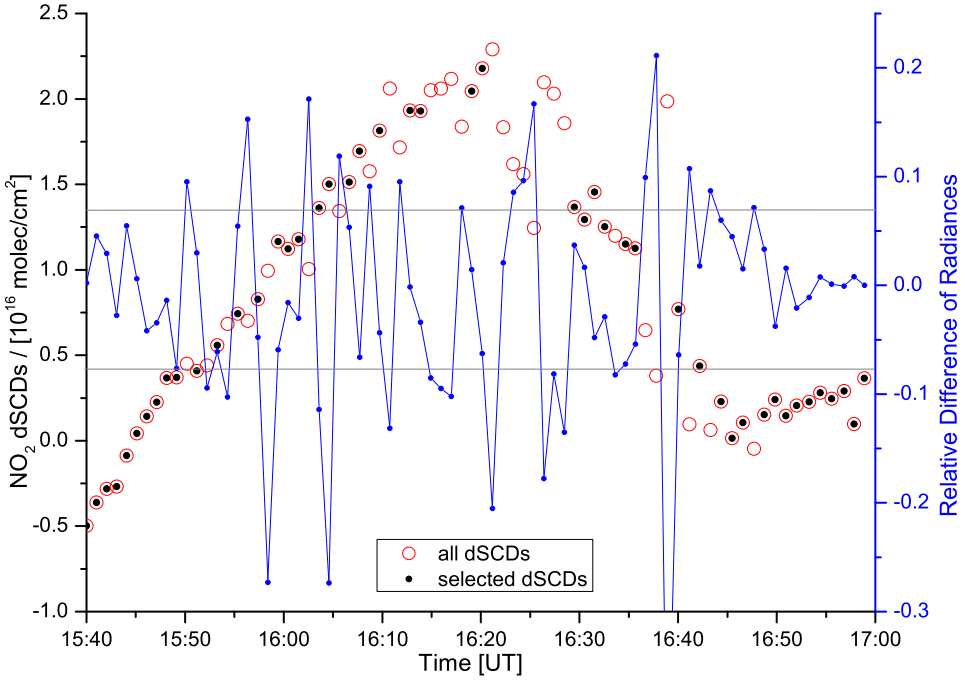

Figure 12.34.: *The NO_2 dSCDs are plotted as red circles. The blue line shows the relative difference between the measured and modelled radiances at 450 nm. All values within the 1σ range (grey line) are used for the profile retrieval (black dots). The other values are discarded.*

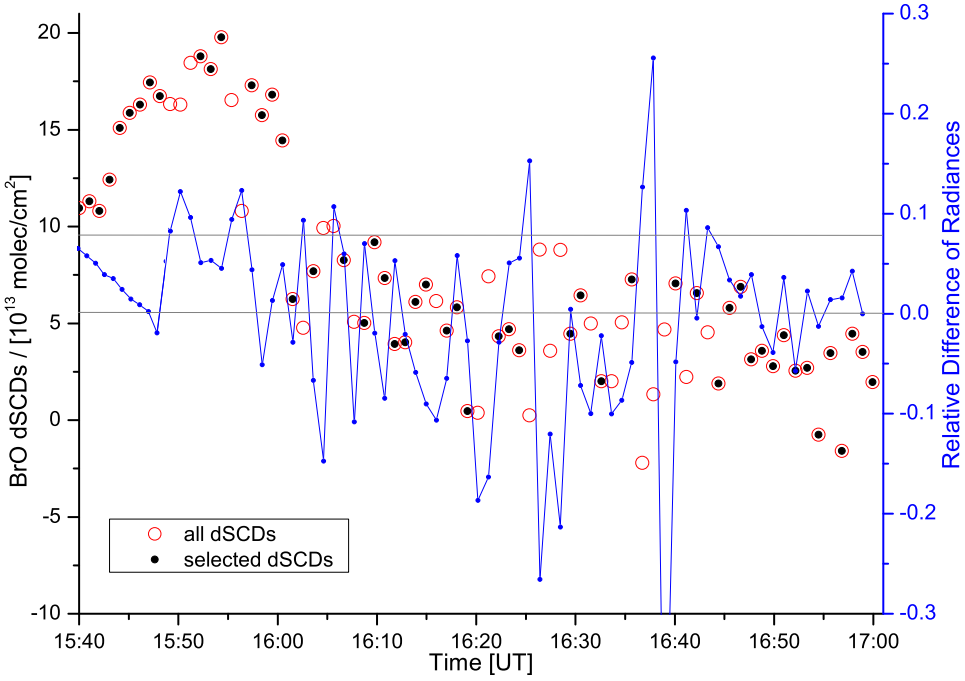

Figure 12.35.: *The BrO dSCDs are plotted as red circles. All values within the 1σ range (grey line) are used for the profile retrieval (black dots). The other values are discarded. The radiances are evaluated at 350 nm.*

12.4. Profile Retrieval of the Limb Measurements of Scattered Skylight

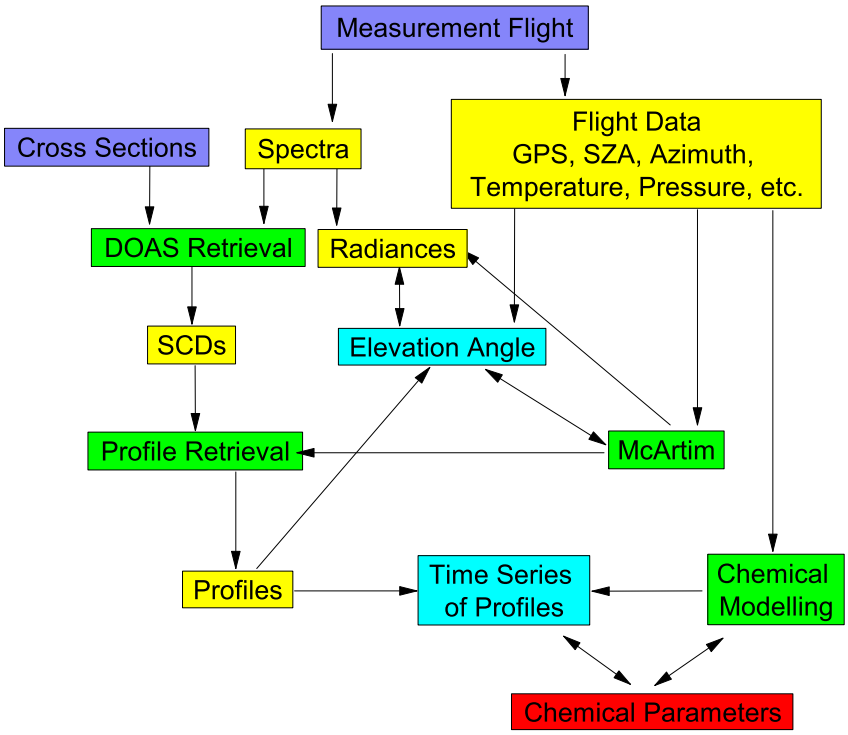

Figure 12.36.: *Schematic of the profile retrieval of the scattered skylight limb observations. Figure based on Kritten (2009).*

The profile retrieval of the miniDOAS data follows the description given in Section 7. Several important points are discussed for one trace gas, but the process is the same for all targeted species.

The scattered skylight measurements observe lower radiances than the direct Sun measurements. Less light reaches the detector and it takes more time to record a spectrum of equal saturation. For the retrieval of the direct sunlight ascent profile 480 spectra are used. For the miniDOAS retrieval only 80 spectra can be used. In addition, the light path for scattered skylight limb measurements is more complex and cannot be determined through geometrical calculations alone. Unlike the retrieval of the direct sunlight measurements, the Weighting Matrix $\mathbf{K}$ is not calculated using the inversion programme. Instead, the BoxAMFs are calculated by McArtim and implemented in a Matlab programme. Figure 12.37 shows the BoxAMFs calculated for the O_3 ascent limb measurements.

The lower information content and the reduced accuracy regarding the light path makes the profile inversion of scattered skylight limb measurements more susceptible to viewing direction perturbations than the solar occultation measurements. Because of this, some parameters such as altitude retrieval grid selection and a priori information influence must be critically tested. These same parameters are of minor importance for direct sunlight measurements.

As well as creating altitude-based trace gas concentration profiles, the profile inversion

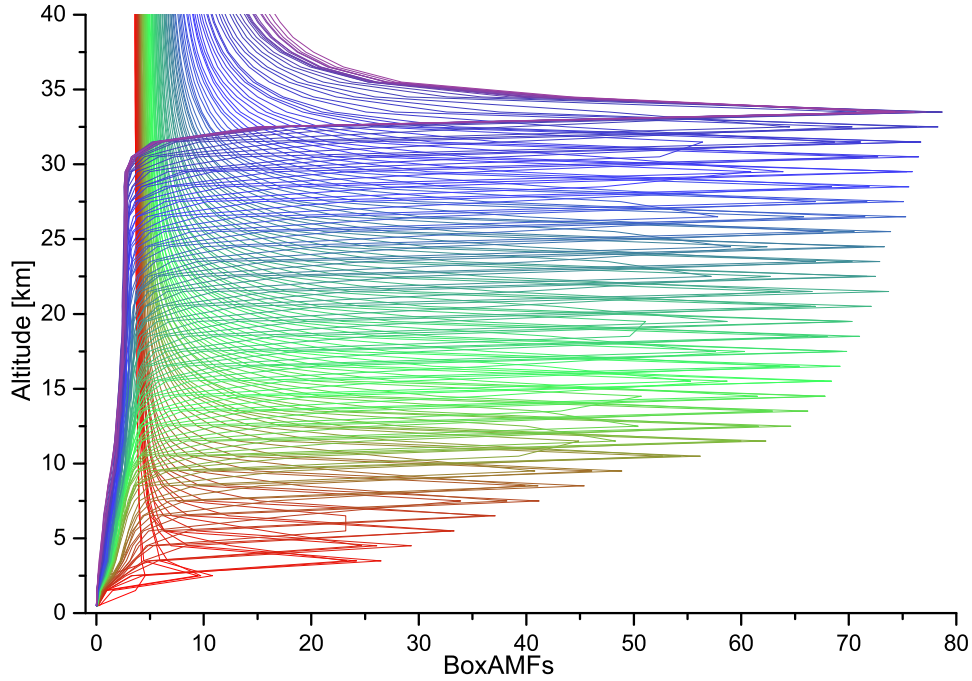

Figure 12.37.: *BoxAMFs for the O_3 ascent measurements at 495 nm. They are calculated for the centre wavelength of the DOAS evaluation of the respective trace gas (475 - 515 nm for O_3). The colour coding is only used to make the lines distinguishable.*

can also be reversed to calculate SCDs from the a priori concentration profiles. These modelled SCDs can be compared to the measured SCDs of the spectral retrieval to check for differences. An example of this is shown in Figure 12.44. A comparison between measured and modelled SCDs has a smaller uncertainty than compared concentration profiles, because the modelled SCDs omit the uncertainty arising from the profile inversion. Instead, the uncertainty of the modelled SCD is based solely on **K** and the a priori profile. The retrieval of direct sunlight measurements is based on the SVD approach and uses the MAP inversion to check the results.

Both inversion methods are used for the scattered skylight measurements of the miniDOAS instrument. The results of the two approaches are then compared to each other and combined into a single profile.

First, a MAP approach is used. The use of an a priori profile prevents unrealistic values in the part of the altitude retrieval grid where little or no information is available. It also suppresses oscillations resulting from this lack of information. The MAP approach ensures that a reasonable profile for the entire retrieval grid is returned. However, because a priori information is used, the shape of the resulting profile will certainly be influenced. Therefore, the second approach is used: SVD. As described in Equation 7.5, the Gain Matrix **G** can clarify where the a priori influences the retrieval. The Averaging Kernel Matrix **A** shows how much the information gained from the measurements contributes to the result. However, only a comparison with a retrieval performed without a priori information can exactly illustrate how the retrieval is influenced by the a priori profile. An SVD retrieval can be compared with the profile retrieved through a MAP approach

to check for differences (see Section 12.4.4).

12.4.1. Impact of the A Priori Error

The measurements from the direct sunlight instrument are used as a priori information. The a priori profile in Figure 12.38 is from the ascent measurements from the direct sunlight instrument. The error is increased so that the miniDOAS measurements are not restricted by the a priori profile in the inversion (see Figure 12.38).

Figure 12.38 illustrates an important point of the retrieval: the influence of the a priori error. While the error should not constrain the measurement, an overestimation of the error can introduce artificial oscillations into the profile. The profile retrieval was initialised with the error of the direct sunlight profile and then stepwise increased to check for changes in the solution. The maximum error at a certain altitude is limited to the concentration value in that respective altitude segment. This is necessary to prevent negative solutions of the inversion. The final error should not restrain the measurement, but should minimise artificial perturbations. However, the ability to identify artificial remnants in the solution would imply knowledge of the true state of the solution. In order to do that, the SVD approach can be used (see Section 12.4.4).

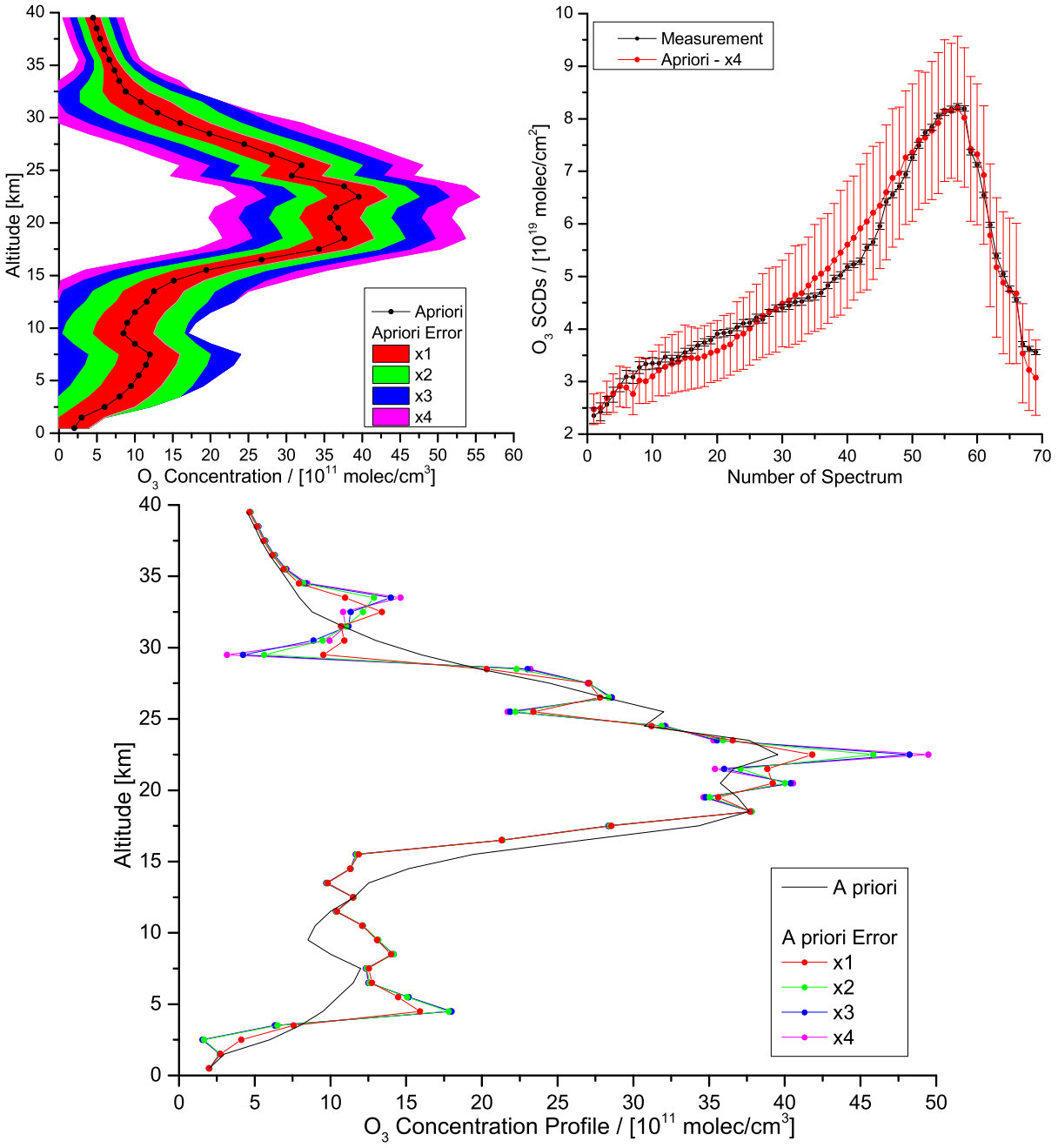

Figure 12.38.: *Influence of the a priori error. The upper left panel shows the a priori in black and a stepwise increased error. The original error (red) was increased by a factor of two (green), thee (blue) and four (magenta). The error is limited to the a priori value itself to prevent negative values. In the upper right plot the measured SCDs and SCDs modelled from the a priori are shown. The a priori error in this plot is taken from the factor four expansion. The lower plot shows the retrieved profiles using the MAP approach for the different a priori errors. It can be seen that the expansion of the error enhances oscillations. The focus is on the shape of the profile and no errors are plotted.*

12.4.2. Adaptation of A Priori Ascent Profiles

The ascent of the balloon gondola up to float altitude takes almost two hours. During that time the concentration of BrO changes with increasing SZA. Figure 12.39 shows the modelled decrease of the BrO concentrations over the time of the ascent, calculated with Labmos. For the miniDOAS ascent measurements, the majority of the information for a single given spectrum is derived from the current balloon altitude (see Figure 12.37). For this reason, the a priori profile is divided into six parts. The concentration in each of these parts is corrected for the time or SZA during which the balloon was passing through that altitude range. The resulting a priori profile and the corresponding uncertainty is shown in the right panel of Figure 12.39. This a priori profile is used in the inversion of the BrO ascent profile shown in Figure 12.45.

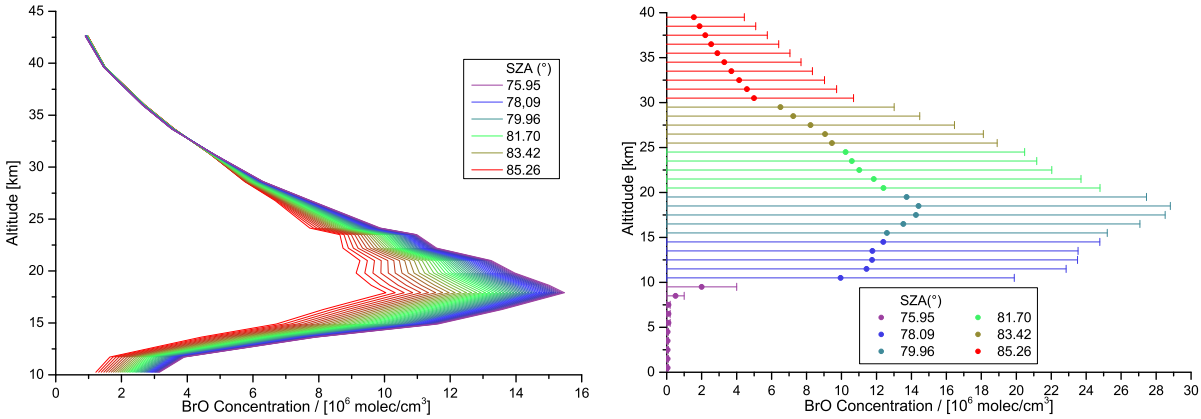

Figure 12.39.: *Adaptation of ascent a priori profile. The left panel shows the modelled evolution of the BrO concentration for the duration of the ascent, indicated by the SZA. The a priori profile in the right panel is divided into six parts, each of which is then corrected for the corresponding SZA during which the balloon crossed that altitude segment.*

12.4.3. Impact of the Regularisation Parameter

The SVD is independent of a priori information and can be used as a reference to check for artificial remnants in the MAP approach's returned profile. It must still be remembered that, when using a regularisation, a strong regularisation parameter can obscure true irregularities or oscillations of a profile. Section 7.3 describes the L-curve method, which is used to determine the regularisation parameter λ. The parameter λ is used for the regularisation of the SVD retrieval. It is slightly varied to check the impact of the regularisation on the retrieved profile (see Figure 12.40). The L-curve is calculated for 50 different values. The plot shows a zoom into the values 39 - 49 at the edge of the L-curve. A larger λ would lead to a smoother solution at the cost of reduced fidelity to the measurements. A smaller λ would mean increased confidence in the measurements but also the possibility of stronger artificial perturbations. The best value according to the L-curve method is between $1{\cdot}10^{-23}$ and $5{\cdot}10^{-24}$. The profiles are shown in Figure

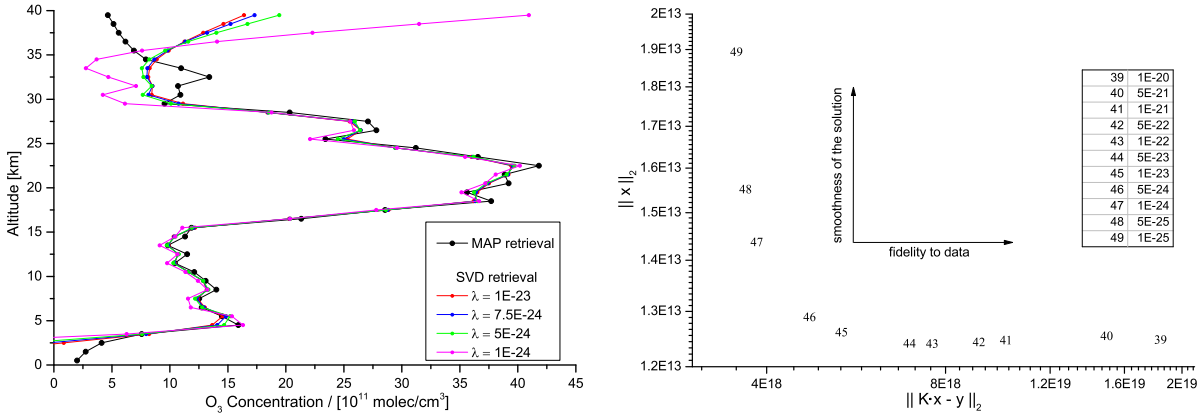

Figure 12.40.: *In the upper plot the retrieved profiles for different regularisation parameters λ are shown. As a reference, the profile returned by the MAP approach is plotted in black. The L-curve for the O_3 ascent measurements is shown in the lower plot. The error for the different profiles is not plotted here for reasons of clarity. Comparison with the MAP inversion shows that the remaining bends in the profile derive from the measurements and not from artificial perturbations. The focus is on the changes in the shape of the profile and no errors are plotted.*

12.40. In addition, a profile using λ=1·10^{-24} is shown. For this value the oscillations increase starting at the lowest and highest altitudes, where only scant information from the measurements is available.

12.4.4. Comparison of MAP and SVD Inversion

Figure 12.41 shows the NO_2 ascent profiles returned by the MAP and SVD inversion. As in Figure 12.40, the returned SVD profile becomes erratic and diverges at the edges of the retrieval grid. However, in the altitude range between 12 and 35 km the two retrieval methods agree very well within the returned error values.
Both retrieval methods can be used to check each other in the core of the retrieval grid. At the edges of the grid only the values of the MAP retrieval should be used. Nevertheless, it is important to keep in mind that these values depend primarily on the a priori profile and only to a small degree on the information gained from the measurements.

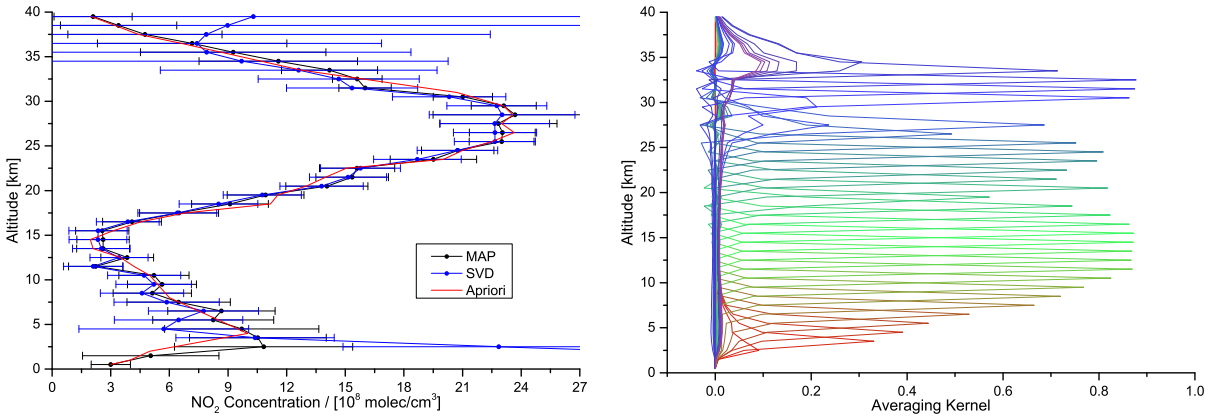

Figure 12.41.: *The left panel shows the NO_2 ascent profiles for the two retrieval methods MAP (in black) and SVD (in blue). At the edges of the retrieval grid, where only scant information is available, the profile returned by the SVD method starts to deviate and the errors increase significantly. This is also shown in the Averaging Kernel (AK) plotted in the right panel, which starts to broaden below the tropopause and around float altitude. Therefore, the grid points of the SVD retrieval below 7 km and above 34 km are discarded. The colour coding in the AK Matrix plot is used only to make the lines distinguishable.*

12.4.5. Fraunhofer Offset for Scattered Skylight Limb Measurements

As mentioned in Section 6, the dSCDs returned by the DOAS retrieval of the miniDOAS instrument are all relative to the reference spectrum. Unlike the direct sunlight measurements, a Langley plot cannot be performed for the scattered skylight measurements. The remaining trace gas concentration in the reference spectrum, or Fraunhofer offset, has to be obtained by other means.

For the scattered skylight measurements the Fraunhofer offset is determined by multiplying the BoxAMF of the reference spectrum with the a priori concentration profile (see Figure 12.42). Unfortunately, this approach is problematic, because it requires an a priori profile representing the true state. Without this, the MAP inversion cannot return a correct profile. The miniDOAS reference spectrum is taken at an altitude of approximately 33 km with a slightly upwards looking viewing geometry. This causes another problem, because at this altitude only a small amount of information from the direct sunlight measurements can be used to deduce an accurate a priori profile. This is why information from the satellite measurements and chemical models are combined to obtain as much information as possible.

Luckily the target trace gases, O_3 and especially BrO, have very low concentrations at this altitude and the Fraunhofer offset is most likely small compared to the measured dSCDs. Only NO_2 has significant concentrations for the Fraunhofer offset calculations in the altitude range from 30 up to 40 km (see Figure 12.42).

The ascent spectra are evaluated against the last spectrum of the ascent and the calculated dSCDs converge towards zero. Therefore, the last of the measured and modelled SCDs should overlap. An incorrect Fraunhofer offset would show as a general offset between measured and modelled SCDs in the retrieval programme (see Figure 12.44).

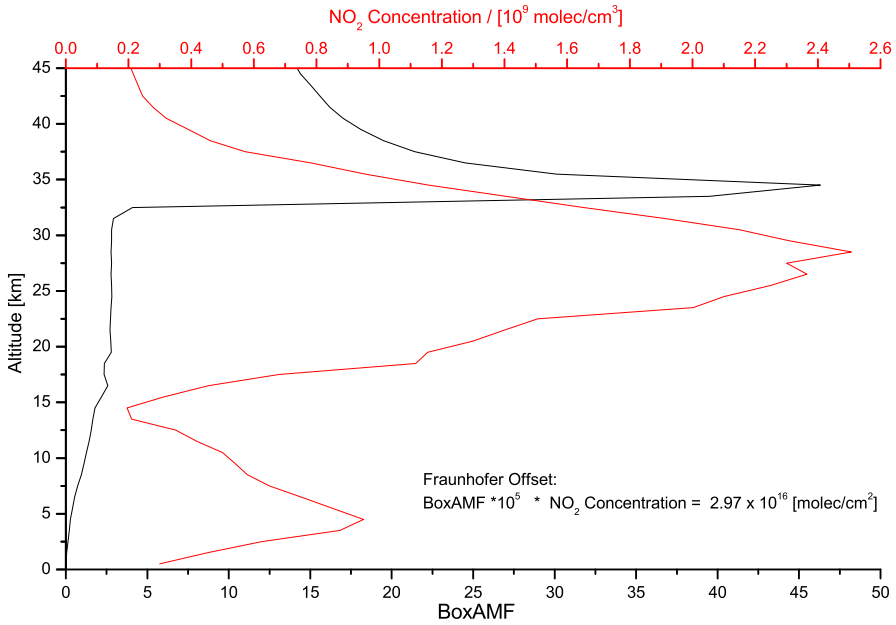

Figure 12.42.: *Fraunhofer offset for the NO_2 ascent measurements. The BoxAMFs, plotted in black, are calculated at a wavelength of 450 nm. They are multiplied by a factor of 10^5. This value corresponds to the light path in centimetres. The product of the NO_2 concentration, plotted in red, and the light path is the amount of NO_2 that should be seen for a given viewing geometry. Both BoxAMFs and concentration are discretely distributed on a 1 km altitude grid, meaning no integral is necessary.*

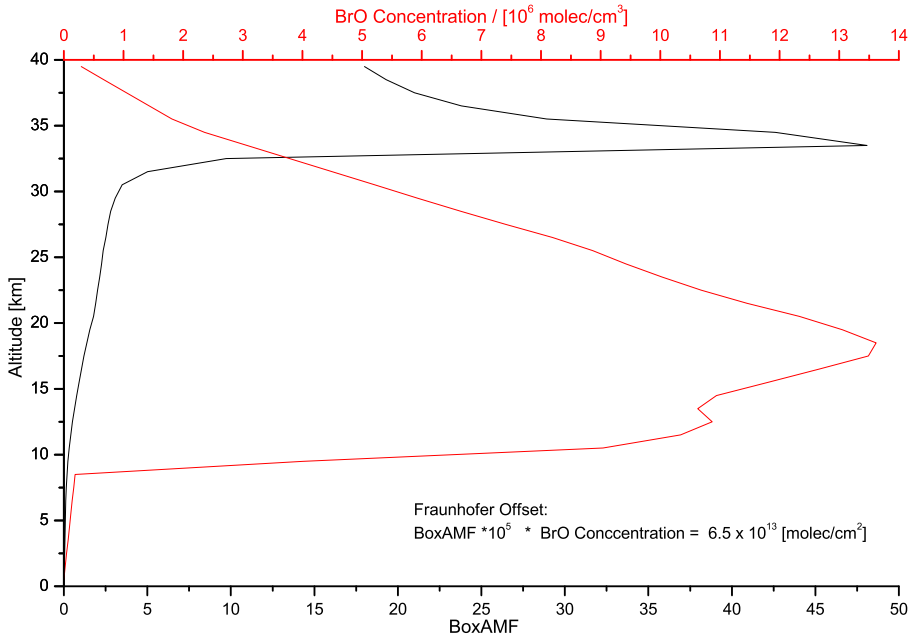

Figure 12.43.: *Fraunhofer offset for the BrO ascent measurements. The product of the BrO concentration, plotted in red, and the light path is the amount of BrO that should be seen for a given viewing geometry. The BrO concentration is already rather low in the altitude range with the highest BoxAMFs values.*

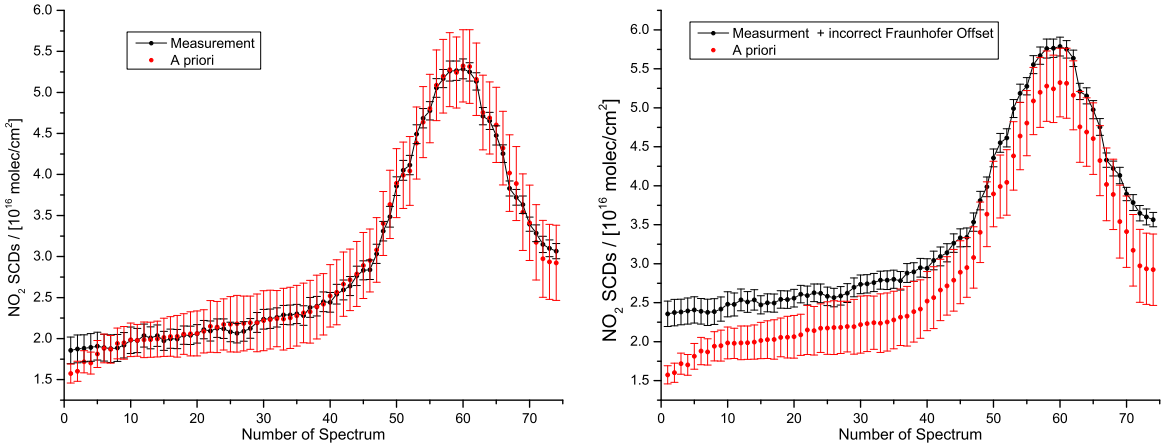

Figure 12.44.: *Comparison of measured NO_2 SCDs and backward modelled SCDs from the a priori profile. The SCDs returned by the DOAS retrieval are plotted in black and the SCDs calculated from the viewing geometry of the respective spectrum are in red. The right panel shows the same plot for an incorrect estimate of the Fraunhofer offset.*

12.4.6. Impact of the Retrieval Grid

The next important point concerning profile retrieval is the choice of the retrieval grid. As stated in Section 7, the regularisation is introduced to suppress oscillations from parts of the retrieval grid with little information. This could also be done by using an adaptive retrieval grid with boxes of different sizes. However, if an adaptive grid is chosen, it might be necessary to interpolate from one grid to the next in order to compare the evolution of the targeted trace gas at a certain altitude. All profile inversions shown so far are calculated using a 1 km altitude grid for the inversion. Given the decreased altitude resolution of the measurements, the grid can be changed to a 2 km or even 3 km grid. The effect of such a change is shown in Figure 12.45. While the profile itself does not change at altitudes above 10 km, the error of each profile point decreases, because more information is available for each altitude segment. This is illustrated by the increased averaging kernels. Below 10 km, little information is available in both cases and the returned values for the profile are negative. They are therefore discarded.

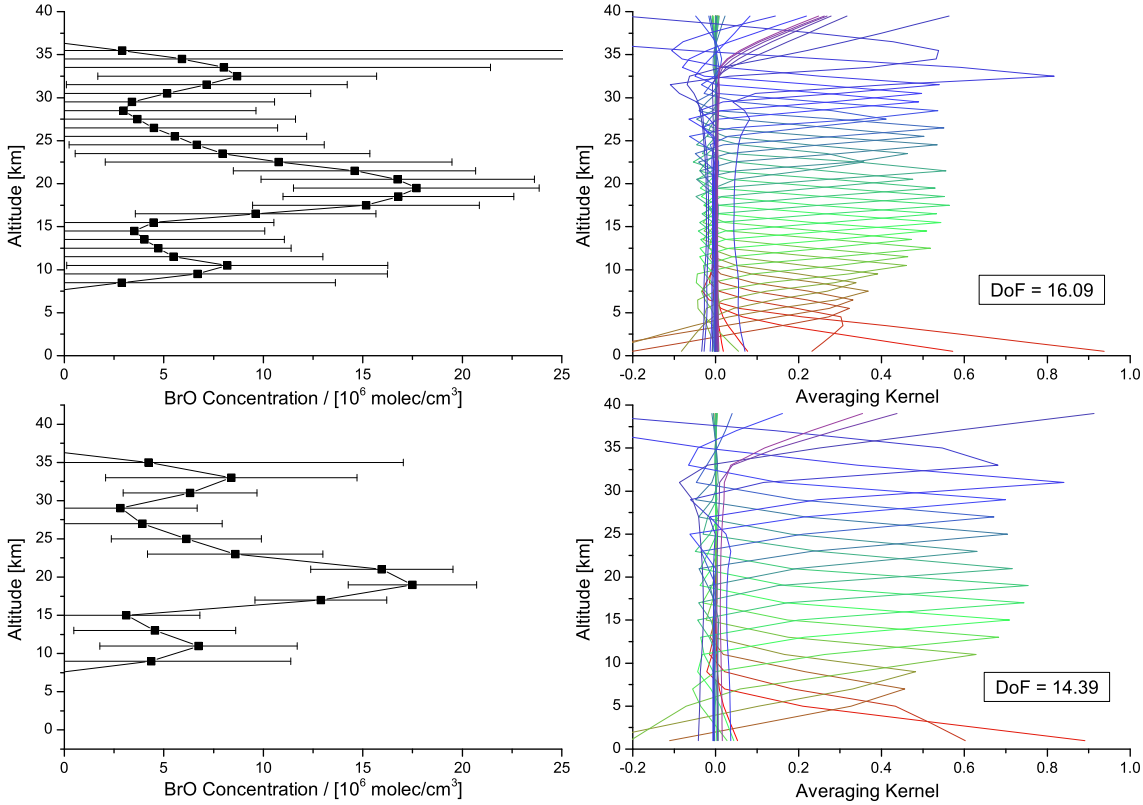

Figure 12.45.: *Comparison between the BrO ascent profile retrievals on a 1 km and a 2 km retrieval grid. In the panels on the right side the respective AK Matrices are plotted and the number of independent elements (Degrees of Freedom = DoF) indicated. The colour coding of the AK Matrices is used only to make the lines distinguishable.*

12.4.7. Test of Interfering Trace Gases

An additional method for affirming the retrieved BrO SCDs is to check if the returned interfering SCDs, in particular O_3 and NO_2, are of the expected magnitude. The light paths in the UV are different from those in the visible wavelength range. Therefore, the SCDs calculated by the DOAS fit cannot be compared directly to the results in Section 12.1.1 and 12.1.2. Nevertheless, the SCDs can be used in an inversion to check the returned profile against the results in the visible wavelength range. Figure 12.46 shows that the calculated SCDs for O_3 and NO_2 are in the expected range.

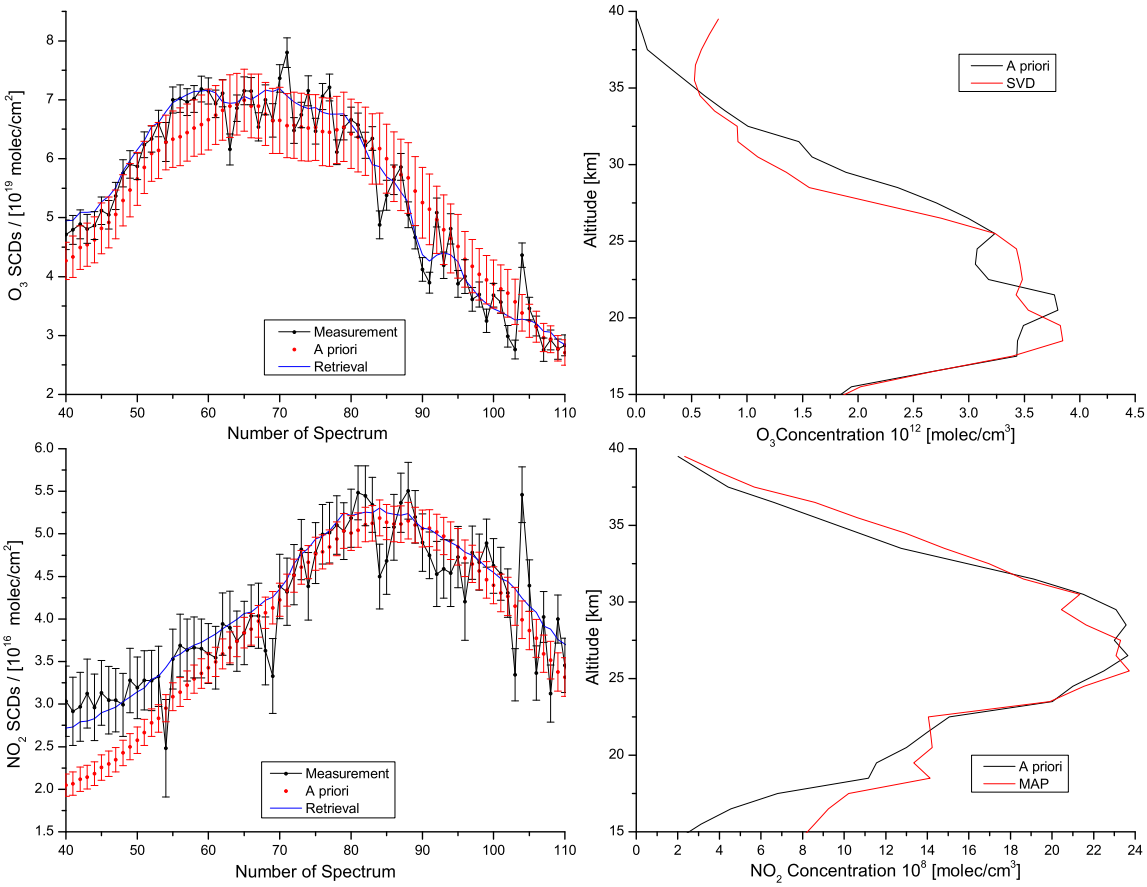

Figure 12.46.: *Test of the dSCDs returned by the BrO DOAS fit. The left-hand panels contain a comparison of the measured SCDs and the SCDs modelled from the profile retrieved in the visible range. The panels on the right show a comparison between the profile retrieved in the vis range and the returned profile of the UV data. As examples, an SVD inversion is shown for O_3 and a MAP profile for NO_2.*

12.4.8. Retrieved Profiles of the Scattered Skylight Limb Measurements

The final inversions for O_3, NO_2 and BrO are initialised, using the configurations derived in the previous sections. For the retrieval of the balloon ascent profiles of O_3 and NO_2 a 1 km grid was chosen. A 2 km grid was chosen for the retrieval of the BrO ascent measurements, due to their reduced information content. The retrieval of all limb measurements is also calculated on a 2 km grid for all three species. For each data set an exemplary AK matrix of the retrieval is plotted. Figures 12.48 - 12.49 show the retrieved ascent profiles for O_3 and NO_2. The retrieved ascent profile for BrO has been shown already in the lower panel of Figure 12.45. Figures 12.50 and 12.52 show the results of the inversion for the O_3 limb measurements for both sunset and sunrise the next morning. Figures 12.50 - 12.53 show the results of the inversion for the NO_2 limb measurements at sunset and sunrise the next morning.

The O_3 and NO_2 measurements are in good agreement with the a priori profiles. However, the BrO SCDs calculated from the photochemically modelled a priori profiles for the limb

scans are too low compared to the measurements (see Figure 12.47). The uppermost panel in Figure 12.47 shows a comparison between the measured and modelled BrO SCDs of the sunset limb measurements of scattered skylight. The second panel shows the comparison between the measured and modelled BrO SCDs of the sunrise limb measurements of scattered skylight. The two last panels show as an example the good agreement of O_3 and NO_2 SCDs of the sunrise limb measurements of scattered skylight. The Fraunhofer offset of the BrO limb measurements of scattered skylight was apparently calculated correctly, because the first measurements of each scan are in agreement. These differences between the measured and modelled BrO SCDs are discussed in Chapter 13.
However, the BrO concentration profiles that are retrieved following the analysis of the discrepancy between measured and modelled SCDs are already shown here with the other retrieved profiles for comparability.

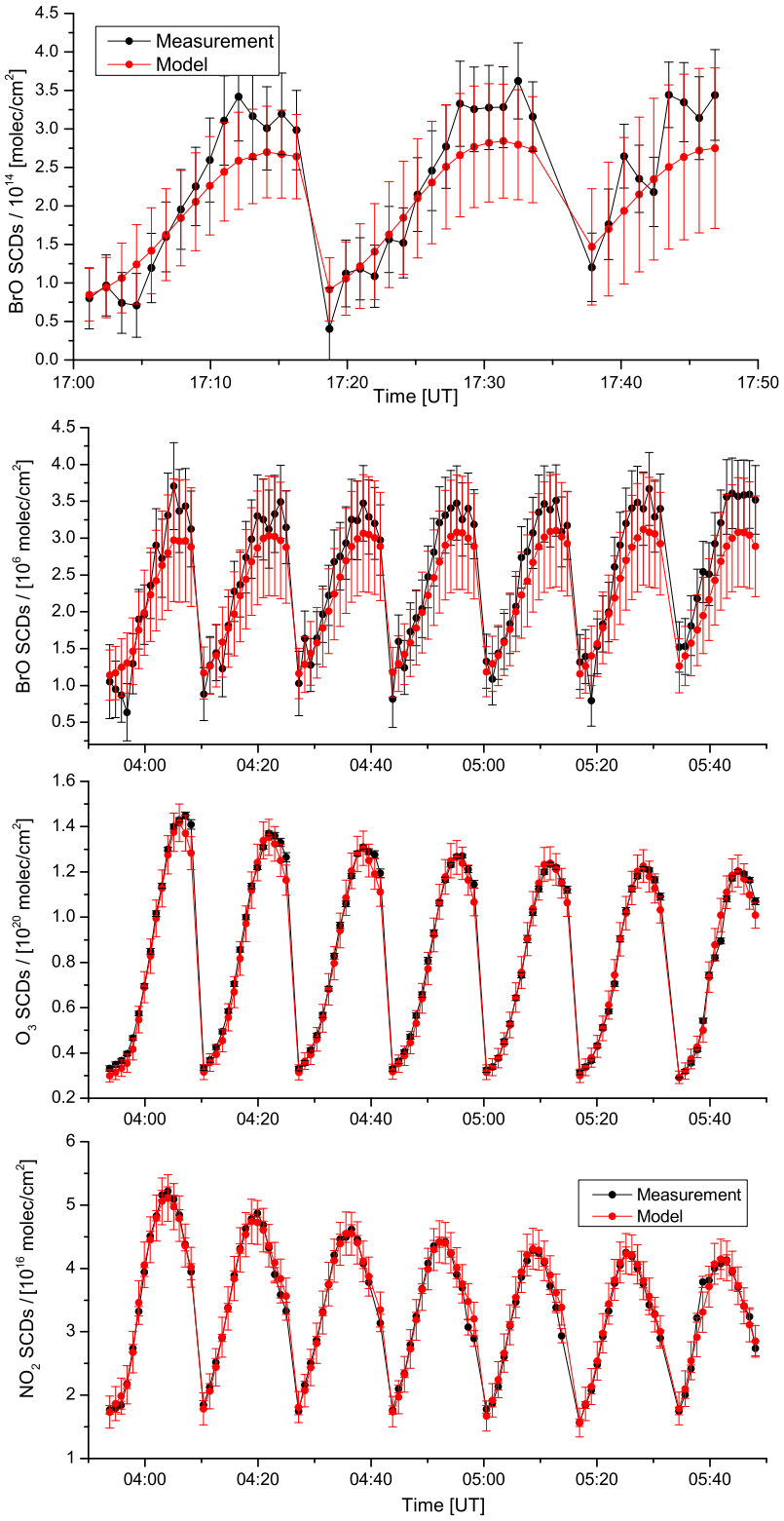

Figure 12.47.: *The uppermost panel shows a comparison of the BrO SCDs measured during sunset and modelled SCDs. The three panels below show the comparison between measured and modelled SCDs for BrO, O_3 and NO_2. Comparison of the measured SCDs during sunrise and the modelled SCDs from the Labmos model. While O_3 and NO_2 measurements are in good agreement with the model data, the measured BrO SCDs are higher than the modelled SCDs for each scan, which means the photochemical model estimates for BrO concentrations are too low.*

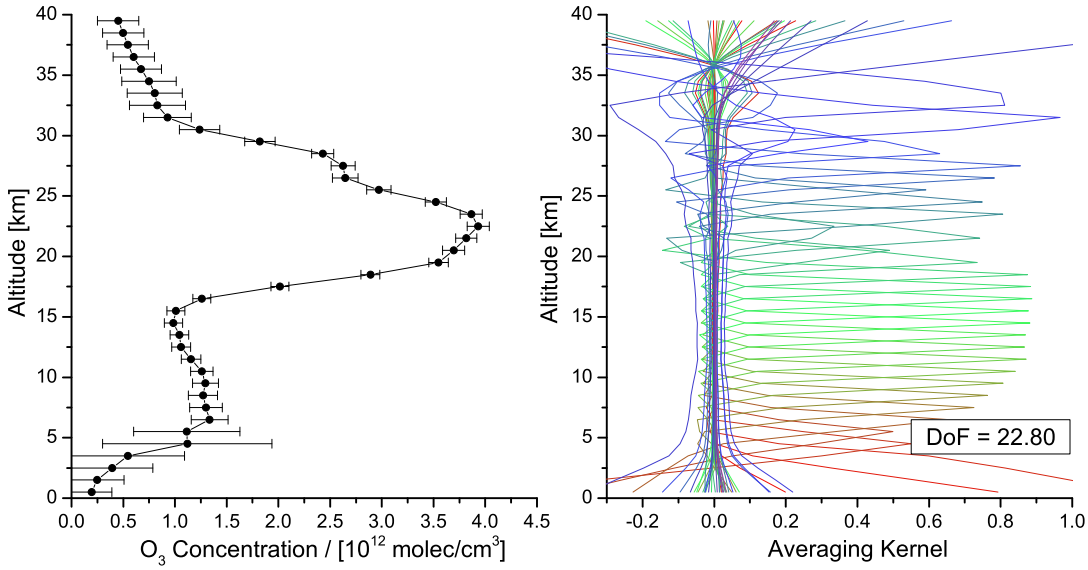

Figure 12.48.: *The O_3 ascent profile is plotted in the left panel. The right panel shows the corresponding AK matrix of the SVD retrieval. The colour coding of the AK matrix plot is used only to make the lines distinguishable.*

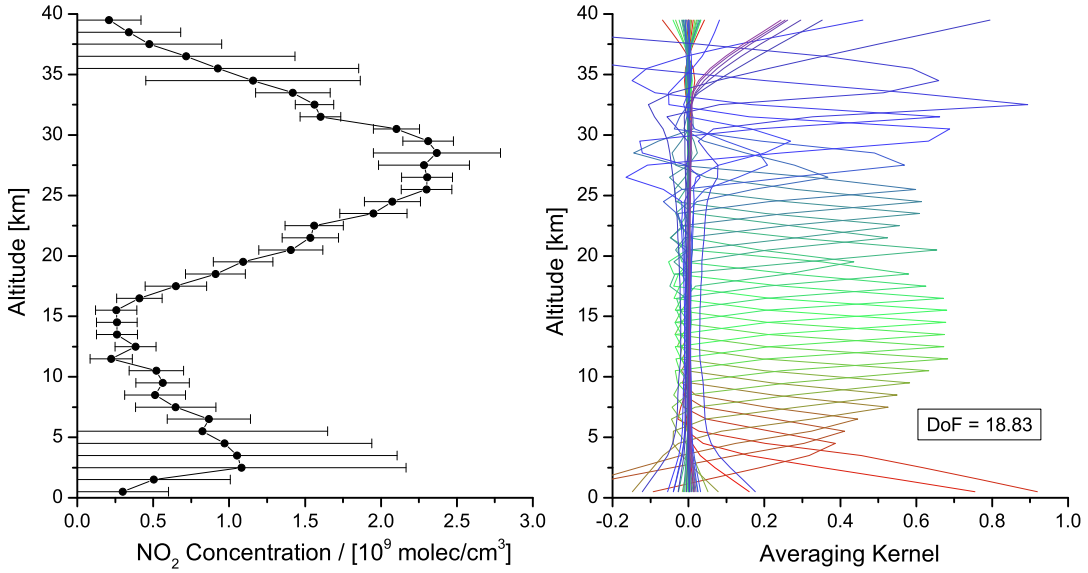

Figure 12.49.: *The NO_2 ascent profile is plotted in the left panel. The right panel shows the corresponding AK matrix of the SVD retrieval. The colour coding of the AK matrix plot is used only to make the lines distinguishable.*

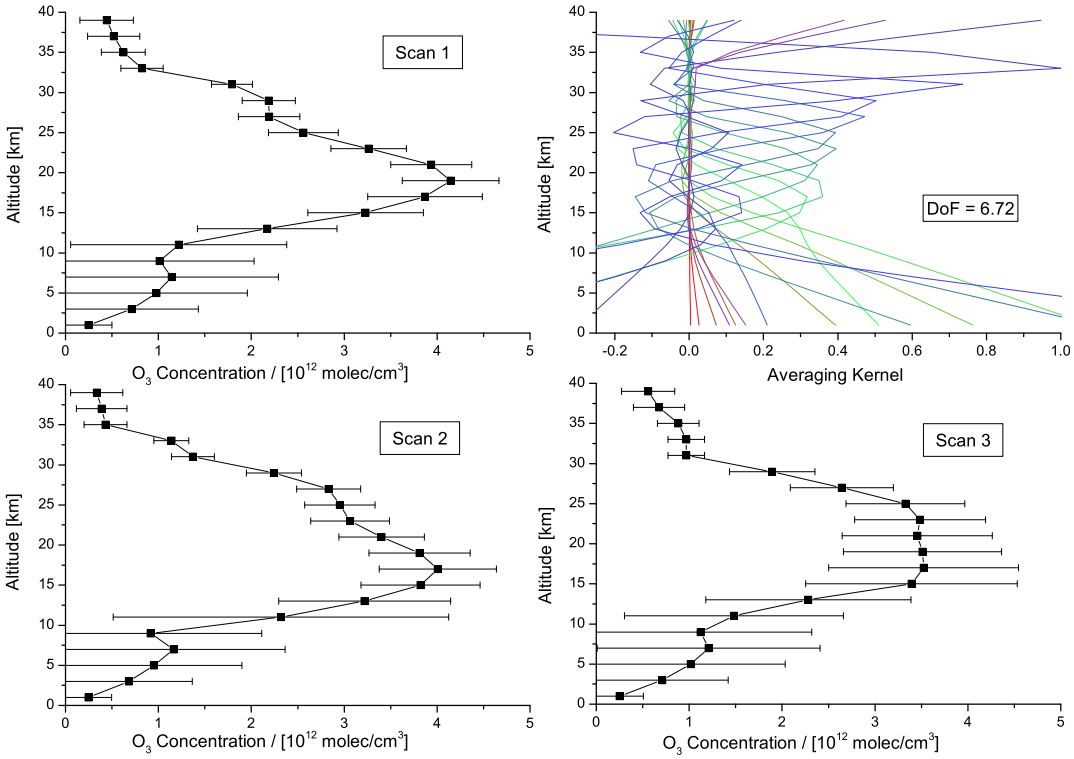

Figure 12.50.: *O_3 sunset profiles. In the upper right plot the AK matrix of the SVD retrieval of the first scan is plotted as an example.*

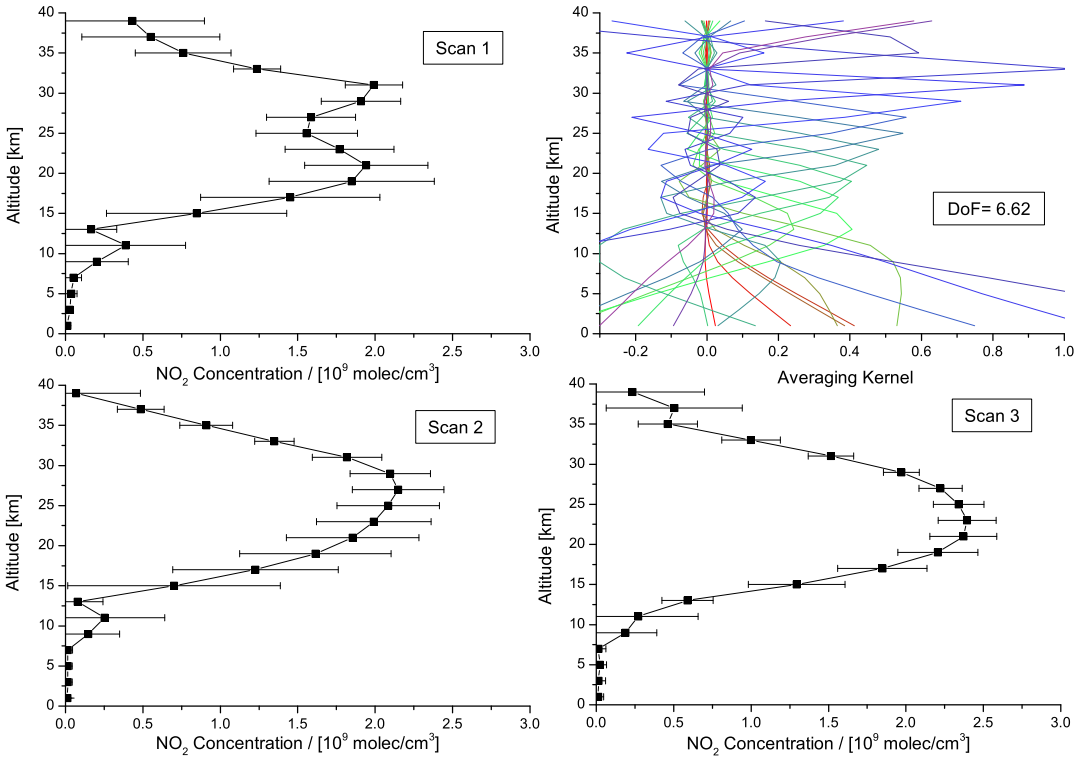

Figure 12.51.: *NO_2 sunset profiles. In the upper right plot the AK matrix of the SVD retrieval of the first scan is plotted as an example.*

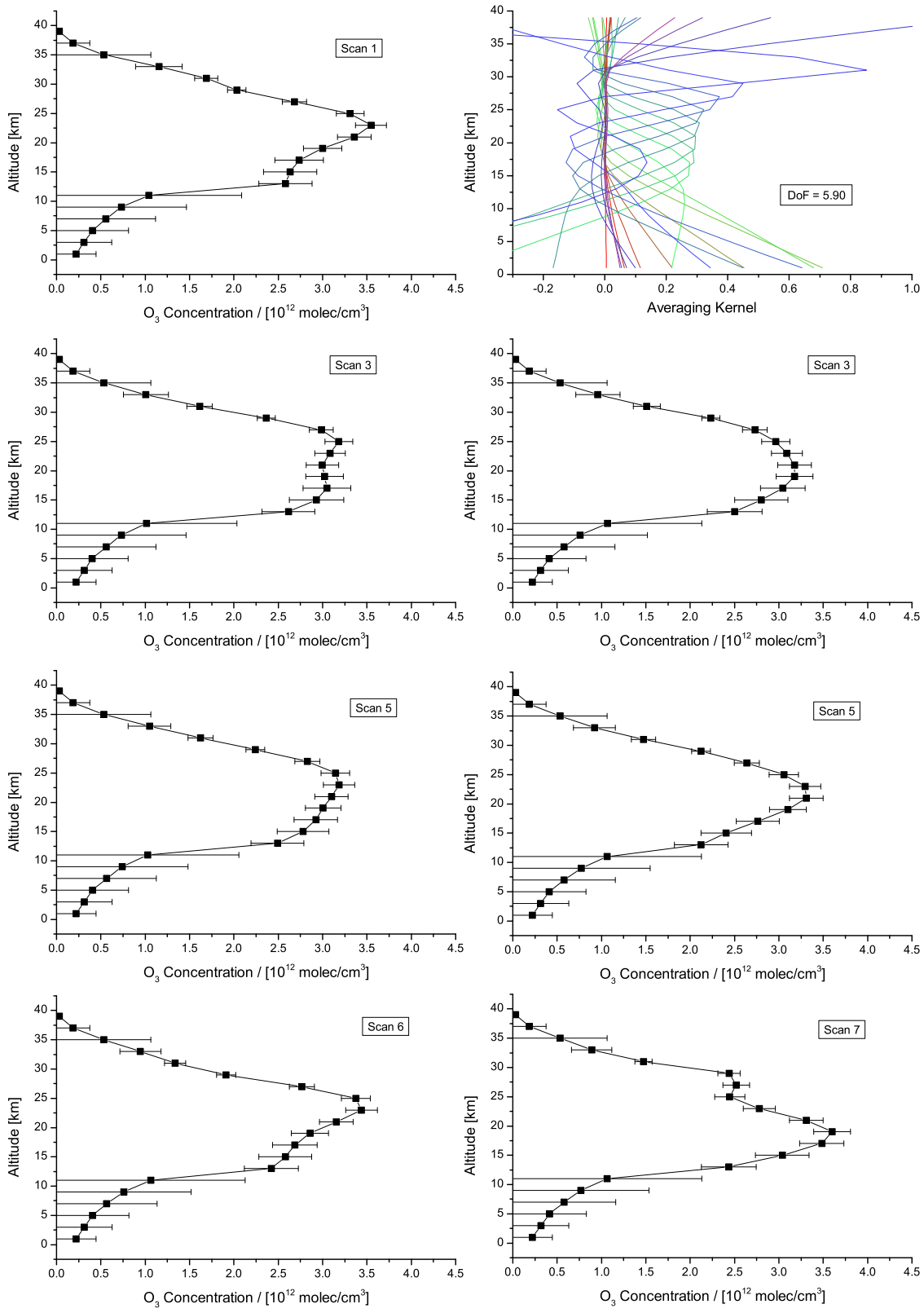

Figure 12.52.: *O_3 sunrise profiles. In the upper right plot the AK matrix of the SVD retrieval of the last scan is plotted as an example.*

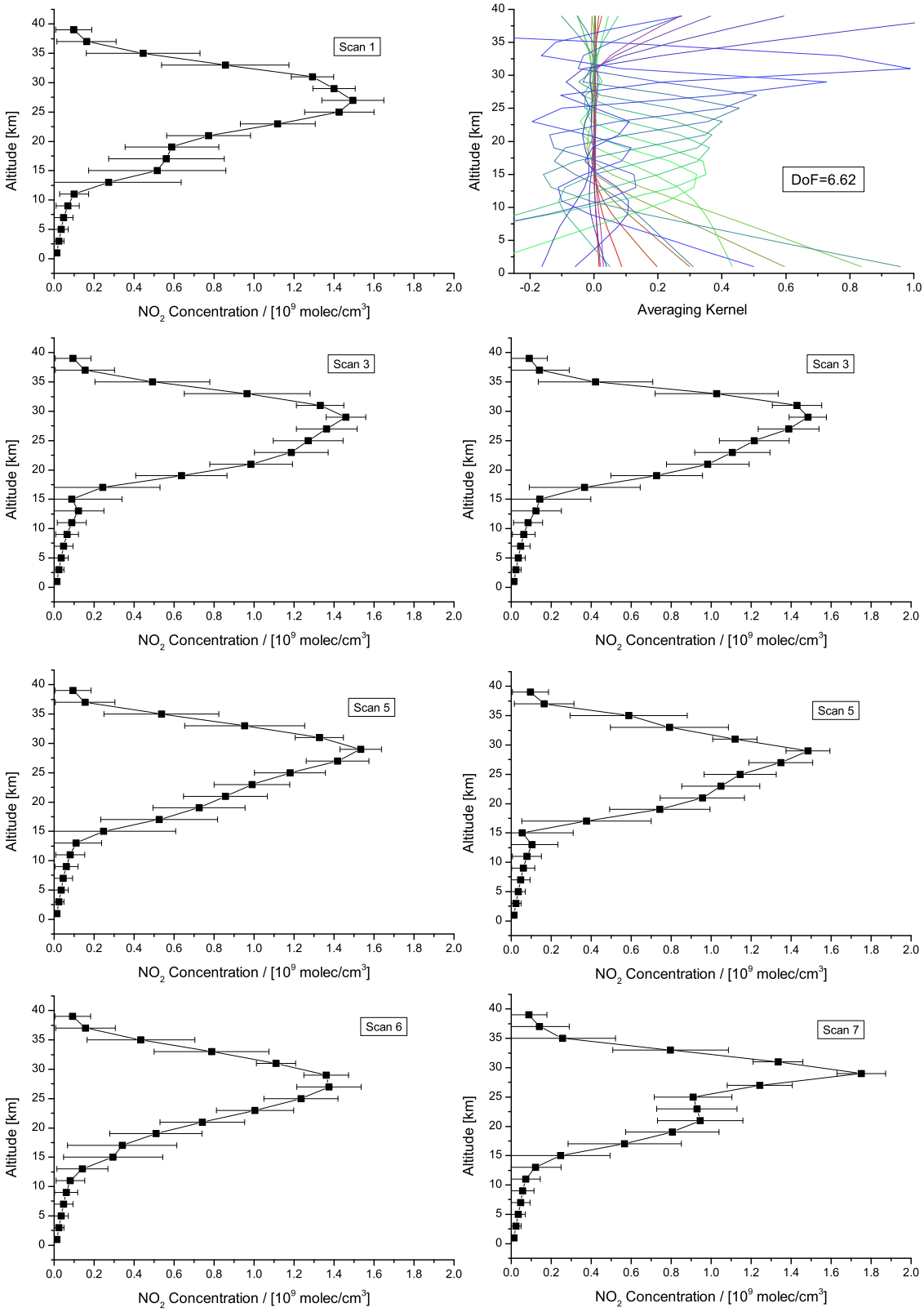

Figure 12.53.: *NO_2 sunrise profiles. In the upper right plot the AK matrix of the SVD retrieval of the last scan is plotted as an example.*

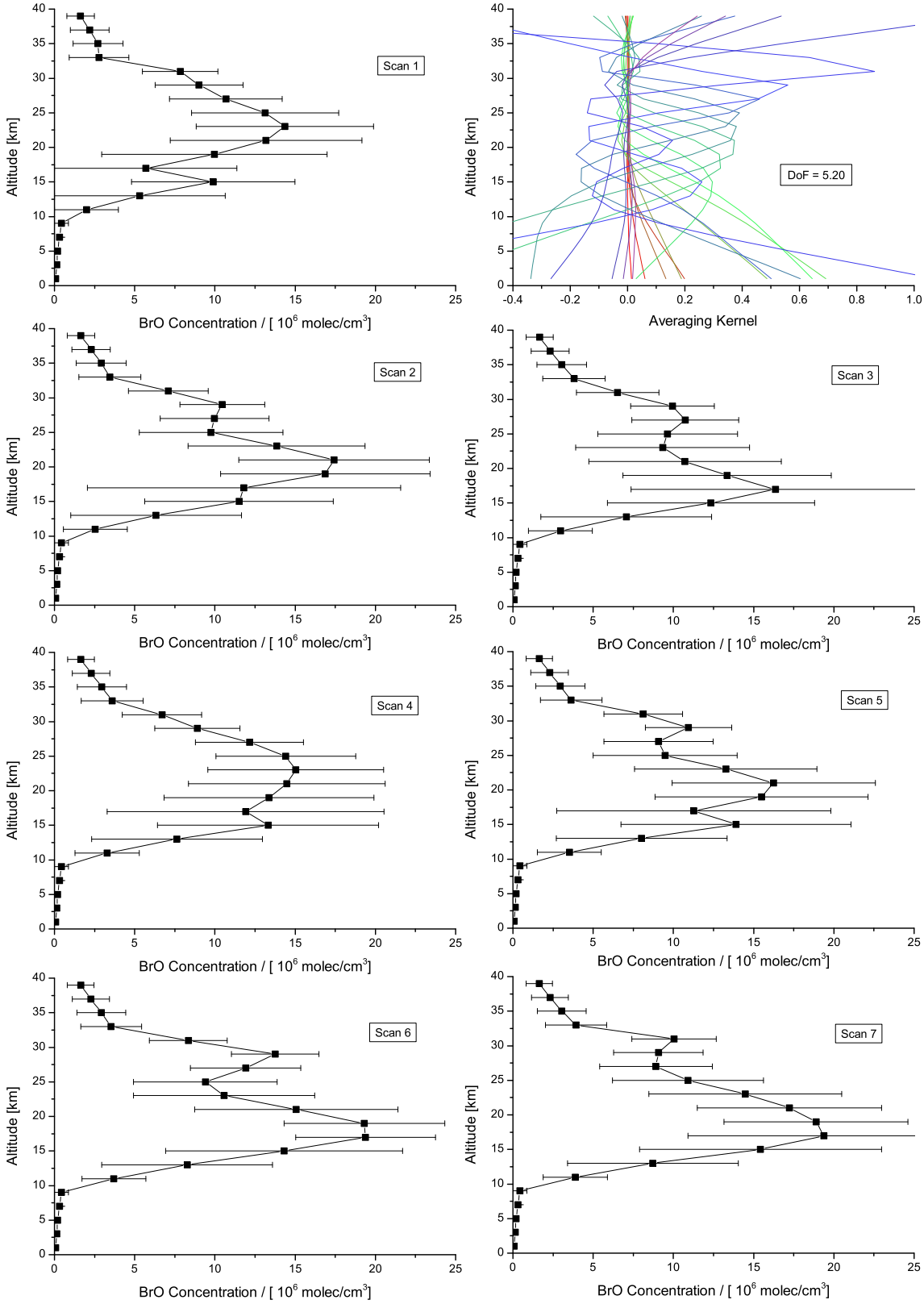

Figure 12.54.: *BrO sunrise profiles inferred from the seven limb scans recorded after sunrise on September 8th 2009. The upper right plot shows the Averaging Kernel Matrix of the SVD retrieval of the last scan. The degrees of freedom for this observation geometry are noted in the Averaging Kernel Matrix plot.*

Part IV.

Results

13. Investigation of the Stratospheric Bromine Chemistry

Figure 12.47 in the previous chapter showed that there is a discrepancy between the measured and modelled BrO SCDs inferred from the miniDOAS limb observations of scattered skylight during sunset and sunrise. Since the first SCDs of each elevation scan are in agreement, the difference must arise from incorrectly modelled BrO concentrations below balloon float altitude. The a priori profiles used to derive the modelled SCDs were calculated using the photochemical model Labmos.

Figure 13.1 shows the modelled diurnal evolution of the three bromine species for the atmospheric conditions of the balloon flight on September 7^{th} 2009: BrO, $BrONO_2$ and HOBr. During daytime BrO is the most abundant species. BrO and NO_2 produce $BrONO_2$ via Reaction 3.46. During the night the $BrONO_2$ concentration increases in the absence of sunlight driving the photolysis of $BrONO_2$ (Reaction 3.54). HOBr is produced during the night through hydrolysis of $BrONO_2$ (Reaction 3.47). Both night-time reservoirs $BrONO_2$ and HOBr are photolysed during sunrise. The subsequent increase in BrO in the morning is observed in both the direct sunlight measurements and the limb measurements of scattered skylight. The dashed red lines in Figure 13.1 indicate the time when the direct sunlight measurements probe the stratosphere below balloon float altitude for an SZA 95° - 90° in the morning and 90° - 95° in the evening. The solid red lines indicate the time when the limb measurements of scattered skylight are recorded (SZA = 86° - 75° in the morning and 85° - 95° in the evening).

HOBr concentrations are negligible for the duration of the limb measurements of scattered skylight in the evening, since the increase in HOBr starts after sunset following the bould up of $BrONO_2$. In the morning HOBr is quickly photolysed before the limb measurements of scattered skylight are recorded (SZA = 86°). Therefore, the decrease of BrO in the evening and subsequent increase of BrO in the morning observed by the limb measurements (SZA = 86° - 75°) must be due to the formation and photolysis of $BrONO_2$.

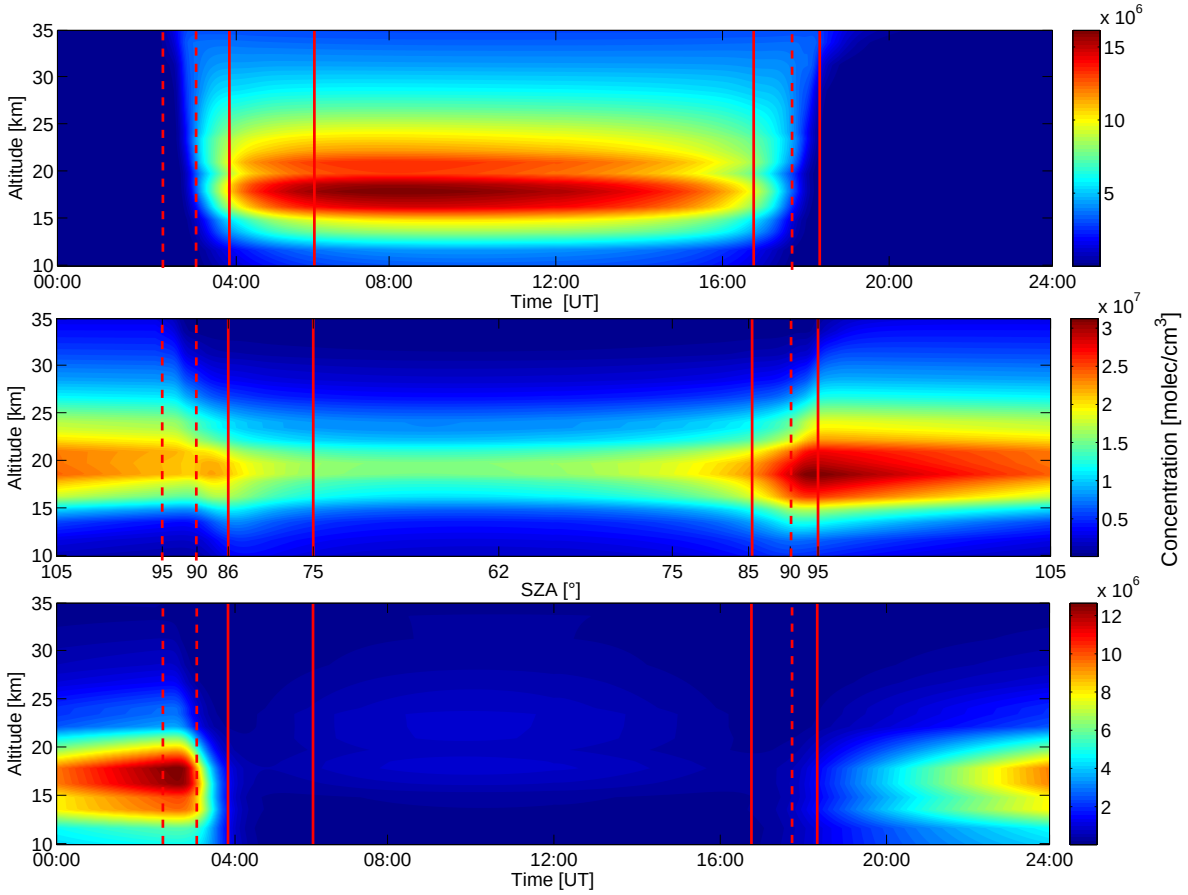

Figure 13.1.: *Labmos model output for a 24 hour window and the atmospheric conditions of the balloon flight on September 7th 2009. The upper panel shows the diurnal evolution of BrO. The middle panel shows the diurnal evolution of $BrONO_2$. The lowest panel shows the concentration evolution of HOBr. The red lines indicate the time during which limb measurements of scattered skylight were performed for an SZA of 86° - 75° in the morning and 85° - 95° in the evening. The dashed red lines indicate the time frame when the direct sunlight measurements were recorded during solar occultation in the morning (SZA = 95° - 90°) and the evening (SZA = 90° - 95°). All three plots show the same time and altitude range. In the upper and lower plot the time is represented by the UT time, in the middle plot by the SZA in degrees. The colour codes denote the respective concentrations.*

13.1. Sensitivity Study

The simulations of the photochemical model Labmos are analysed with the focus on these reactions:

1. The formation process of $BrONO_2$ (Reaction 3.46) depending on the rate coefficient $k_{[BrO][NO_2]}$

2. The photolysis of $BrONO_2$ (Reaction 3.54) depending on J_{BrONO_2}

Several simulations are made to gauge the effect and sensitivity of the model for the following parameters:

- The rate coefficient $k_{[\mathrm{BrO}][\mathrm{NO_2}]}$ of the formation process of $\mathrm{BrONO_2}$. *Sander et al.* (2011) lists the low-pressure rate coefficient as $1.4{\cdot}10^{-30}\frac{\mathrm{cm^6}}{\mathrm{molec^2\,s}}$ at 220 K. The 1σ uncertainty is stated to be a factor of 1.465 at 220 K.

- The photolysis rate $J_{\mathrm{BrONO_2}}$, which is calculated using the $\mathrm{BrONO_2}$ absorption cross section, the actinic flux and the quantum yield (see Reaction 8.10). *Sander et al.* (2011) lists the uncertainty of the photolysis rate as a factor of 1.4.

- The total bromine load of the stratosphere of 20.3 ppt with an uncertainty of 2.5 ppt (*WMO* 2011).

The comparison between measured and modelled SCDs in Figure 12.47 shows that the concentrations calculated from the photochemical model Labmos are too low. Therefore, either the rate coefficient of the formation $k_{[BrO][NO_2]}$ is too high or the photolysis rate J_{BrONO_2} is too low.

Given the uncertainty factors of the two parameters $k_{[\mathrm{BrO}][\mathrm{NO_2}]}$ and $J_{\mathrm{BrONO_2}}$, simulations are made for the following range:

- $k_{\mathrm{mod}}/k_{\mathrm{JPL}} = [0.60\ ..\ 1.10]$ in steps of 0.05

- $J_{\mathrm{mod}}/J_{\mathrm{JPL}} = [0.90\ ..\ 1.50]$ in steps of 0.10

k_{mod} denotes the rate coefficient used in the model. k_{JPL} denotes the value recommended by *Sander et al.* (2011). J_{mod} denotes the photolysis rate used in the model and J_{JPL} is the recommendation of *Sander et al.* (2011).

Additional tests are performed on the direct sunlight measurements recorded during sunrise to determine their sensitivity to HOBr photochemistry. Figure 13.1 shows that only the direct sunlight measurements are sensitive to changes in HOBr photochemistry, since all HOBr is photolysed before the limb observations of scattered skylight start at 03:50 UT (SZA = 86°). The two parameters used to test the HOBr photochemistry are:

- The formation of HOBr, based on the hydrolysis of $\mathrm{BrONO_2}$ during the night. The rate coefficient of the heterogeneous reaction is based on the uptake coefficient γ, which *Sander et al.* (2011) states to be 0.8 with an uncertainty factor of 1.5.

- The photolysis rate J_{HOBr}, which is calculated using the HOBr absorption cross section. The HOBr absorption cross section is also subject to large uncertainties (*Ingham et al.* 1998). *Sander et al.* (2011) states the uncertainty of the HOBr photolysis for wavelengths larger than 350 nm to be a factor of 10.

Using the miniDOAS limb measurements of scattered skylight to monitor BrO only allows for conclusions regarding the ratio $J_{BrONO_2}/k_{[BrO][NO_2]}$. This is because formation and photolysis of $\mathrm{BrONO_2}$ occur at the same time and cannot be independently analysed. In order to test different reaction rates for the formation of $\mathrm{BrONO_2}$, only the rate coefficient $k_{[\mathrm{BrO}][\mathrm{NO_2}]}$ needs to be varied. Changing the photolysis rate requires a further step.

The photolysis rate J is defined in Equation 8.10 as the integral of the product of the actinic flux $F(\lambda)$, the absorption cross section $\sigma(\lambda)$ and the quantum yield $q(\lambda)$.
However, the comparison between the measured and modelled radiances, showed that $F(\lambda)$ is correctly calculated (see Figure 12.28). The quantum yield $q(\lambda)$ can be assumed to be 1 (*Soller et al.* (2002), *Sander et al.* (2011)). As already stated in Section 3.3.1, when $BrONO_2$ is photolysed (Reactions 3.54 - 3.56) BrO and NO_2 are produced either directly or almost immediately via secondary reactions. Therefore, the $BrONO_2$ absorption cross section $\sigma(\lambda)$ is the parameter to focus on. The importance of exactly determined photolysis and reaction rates are already outlined by *Trentmann et al.* (2003) and *Kawa et al.* (2009).

13.1.1. The $BrONO_2$ Absorption Cross Section

The $BrONO_2$ absorption cross section was measured by *Spencer and Rowland* (1998), *Burkholder et al.* (1995) and *Deters et al.* (1998). It should be noted that the absorption cross section decreases over four orders of magnitude from 200 to 500 nm, see Figure 13.2.
Figure 13.2 shows the absorption cross section of $BrONO_2$ measured by *Burkholder et al.* (1995) on which the recommendation of *Sander et al.* (2011) is based. Figure 10.7 shows that the temperature in the entire lower stratosphere was 220 K for the time of the balloon flight on September 7^{th} 2009. Therefore, the absorption cross section is corrected for 220 K following the recommendations of *Burkholder et al.* (1995). The temperature corrected absorption cross section of $BrONO_2$ is used for all calculations shown here.
On the right side of Figure 13.2 the absorption cross section is multiplied with the actinic flux. The product can be divided into two parts: the UV part s_1 from 200 - 268 nm and the visible range part s_2 from 268 - 500 nm. The actinic flux is simulated for the atmospheric condition of the balloon flight on September 7^{th} 2009 and an altitude of 18 km using the RT model McArtim. At this altitude the $BrONO_2$ concentration profile is at its maximum.
Figure 13.3 shows the product of the actinic flux and the $BrONO_2$ absorption cross section. The product is calculated for an SZA of 86°, the time when the first miniDOAS limb measurements of scattered skylight are evaluated during sunrise on September 8^{th} 2009. The final miniDOAS limb measurements of scattered skylight during the sunrise are recorded at an SZA of 75°, for which the second curve in Figure 13.3 is calculated.

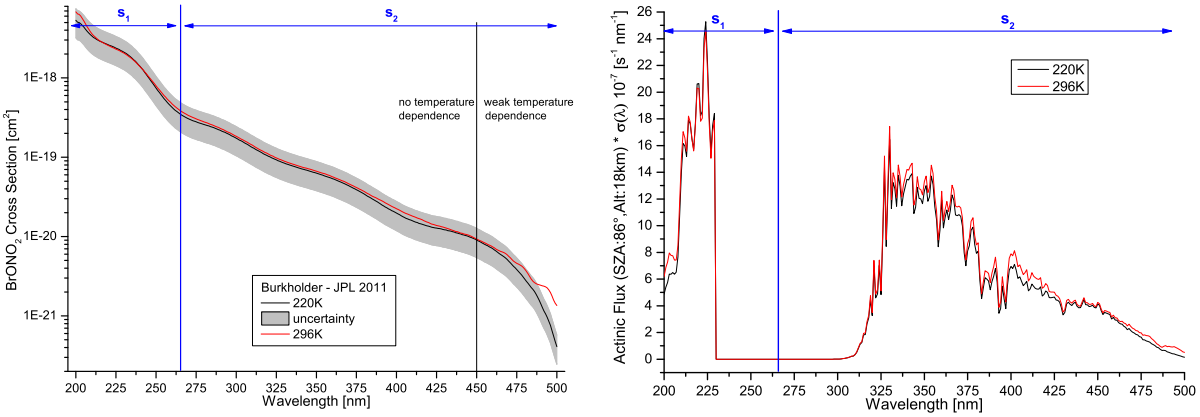

Figure 13.2.: *The left panel shows the $BrONO_2$ absorption cross section measured by Burkholder et al. (1995) at 296 K and the temperature corrected (220 K) absorption cross section. The uncertainty is plotted in grey and the distinction between the two parts s_1 and s_2 is indicated. The product of the actinic flux and the cross section is plotted for both 296 K and 220 K in the right panel*

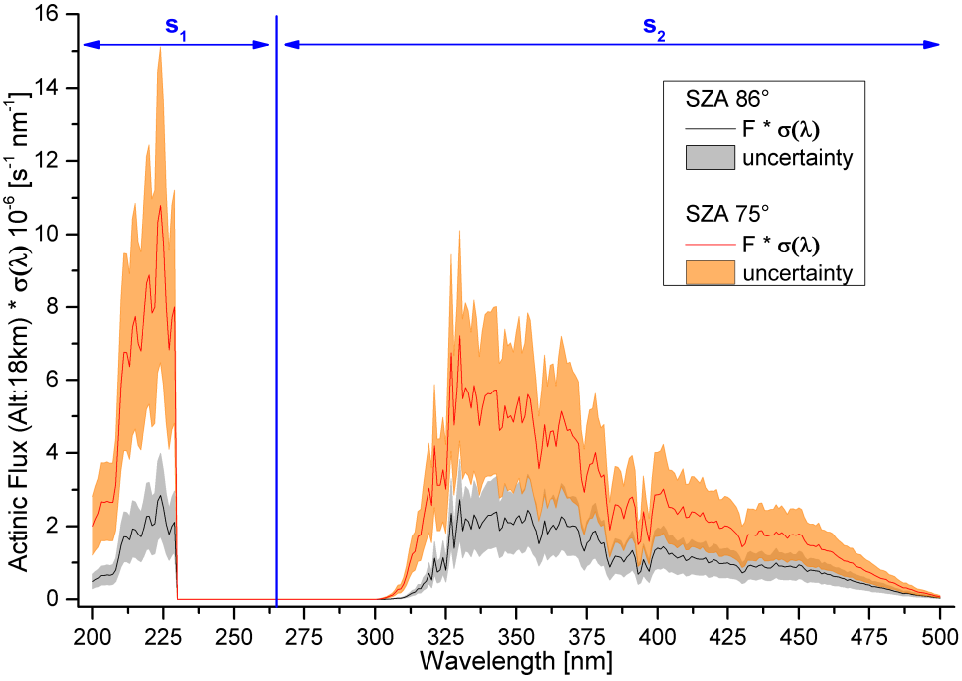

Figure 13.3.: *Product of the actinic flux and the $BrONO_2$ cross section. The actinic flux is calculated for two SZAs and the atmospheric condition of the flight on September 7^{th} 2009. Both fluxes are simulated using the RT model McArtim for an altitude of 18 km. At this altitude the $BrONO_2$ concentration profile is at its maximum.*

13.2. Labmos Model Initialisation

As stated in Chapter 8, the Labmos model is initialised using the output of the SLIMCAT model. The balloon ascent profiles from the direct sunlight instrument are used to further constrain the Labmos input for the model initialisation. CH_4 and N_2O profiles measured by the LPMA instrument are compared with the output of SLIMCAT before the data is implemented in the Labmos model. The comparison between SLIMCAT model data and the long-lived tracer profiles measured by the LPMA instrument is used to test the dynamic of the SLIMCAT model. The comparison is shown in Figure 13.4. Due to the difference between the two datasets, the SLIMCAT output is shifted 2 km upwards. This difference between measured and modelled data is most likely due to diabatic heating. Several test runs are made applying an offset of between 1 and 3 km in steps of 0.5 km. An offset of 2 km provided the best agreement.

The SLIMCAT output also shows a discontinuity at an altitude of approximately 12

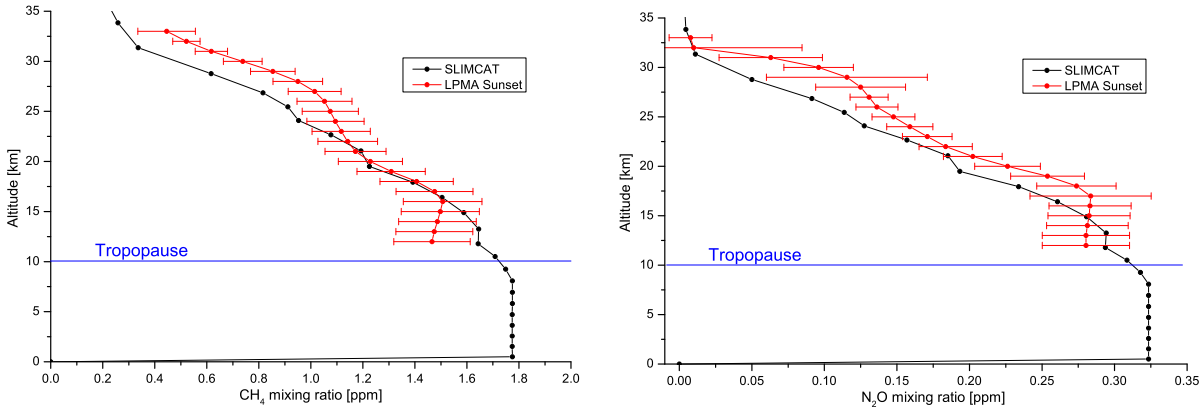

Figure 13.4.: *The left panel shows the CH_4 mixing ratio profile measured by the LPMA instrument. The right panel shows the comparison between SLIMCAT and the LPMA profile for N_2O. LPMA Profiles Courtesy of Sebastien Payan.*

km, which is a known boundary problem of the SLIMCAT model near the tropopause. Figure 13.5 shows how this is handled in the Labmos input: the Br_Y mixing ratio is shifted upwards by two kilometres and the discontinuity is smoothed.

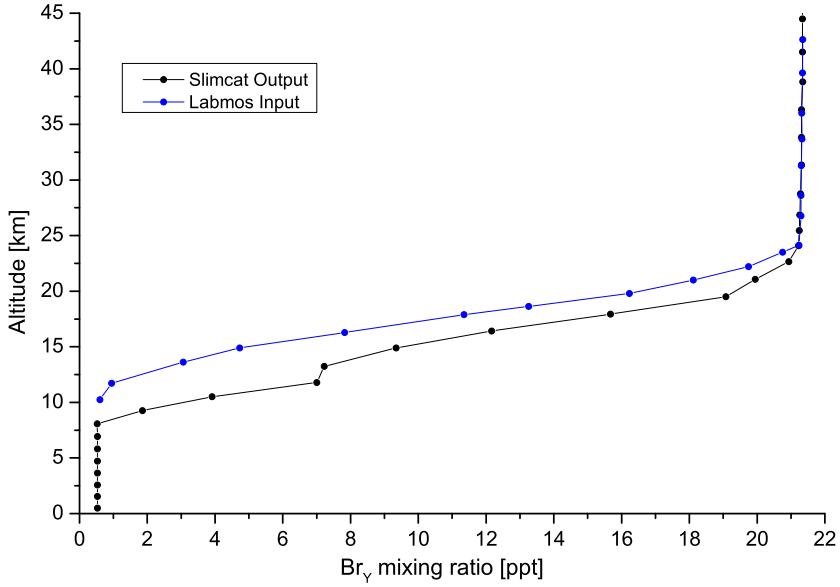

Figure 13.5.: *This graph shows the SLIMCAT output for the total Br_Y in black and the corrected version for the Labmos input in blue. The SLIMCAT model makes calculations on 32 altitude levels, while the Labmos uses only 19 altitude levels, starting above the tropopause.*

13.2.1. Sunrise Initialisation

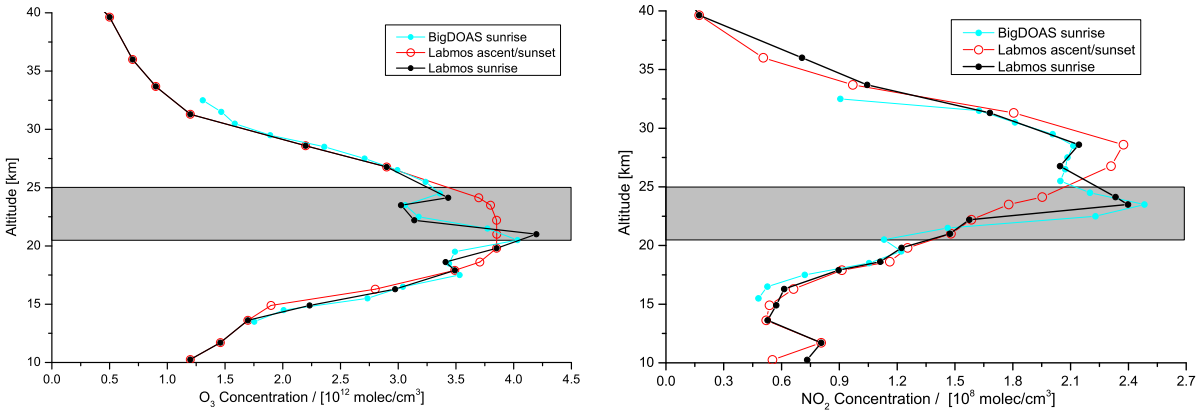

Figure 13.6.: *Comparison between the O_3 sunrise profile of the direct sunlight measurements (cyan) and the Labmos model output (SZA = 90°irc) for the sunrise initialisation (black). The Labmos profile of the ascent/sunset initialisation is plotted in red as a reference. The grey area indicates the altitude range of the mid-latitude intrusion based on the MIMOSA calculations and the deviations of the direct sunlight profiles. The right panel shows the same comparison for the NO_2 profiles.*

During the balloon ascent and sunset measurements the direct sunlight instrument faced north-west towards the setting Sun. The next morning the gondola turned eastwards towards the sunrise. Therefore, it is likely that the evening and morning measurements probed different air masses. With this eastwards viewing direction the instruments apparently probed a mid-latitude air mass intrusion near the Finnish-Russian border (see

Figure 10.5). This can also be seen in the direct sunlight profiles retrieved from the sunrise measurements, shown in Figure 13.6. Therefore, a separate Labmos initialisation for the sunrise measurements was used. The O_3 and NO_2 initialisation profiles of the Labmos model are adapted to match the concentrations during sunrise. Figure 13.6 shows a comparison between the measured direct sunlight profiles retrieved from the solar occultation observations during sunrise and the Labmos model output for the separate initialisations for ascent/sunset and sunrise.

13.3. Comparison between Measured and Modelled Limb Observations of Scattered Skylight

For a direct comparison between the measured and modelled data, the SCDs are plotted on the x- and y-axis. In the case of a good agreement, the resulting points should scatter around the 1:1 axis.

Changes in the photolysis rate are realised with changes in the absorption cross section of $BrONO_2$. The two parts of the absorption cross section s_1 and s_2 are increased in steps of 10% (see Section 13.1.1). However, changes of the absorption cross section in the UV range s_1 had no impact on the concentration evolution over the modelled period. The BrO and $BrONO_2$ concentration maxima are below the O_3 concentration maximum. Since the overhead O_3 absorbs the photons in the relevant wavelength range (< 320 nm), the intensity of UV radiation is rather low and the photolysis of $BrONO_2$ is predominantly driven by the radiation in the visible wavelength range. The rate coefficient $k_{[BrO][NO_2]}$ is changed in steps of 5%.

Figure 13.7 shows the comparison between the measured and modelled SCDs for the O_3 limb measurements of scattered skylight. Figure 13.8 shows the comparison between the modelled and measured SCDs for the NO_2 limb measurements of scattered skylight. The good agreement between measured and modelled SCDs shows that the model is correctly initialised for the dynamics, for which O_3 is a proxy and the NO_X photochemistry.

Figure 13.9 shows an increase of the measured SCDs compared to the modelled SCDs for the lower observation angles. However, if the photolysis rate is increased, more Br_Y exists in the form of BrO, since more $BrONO_2$ is photolysed.

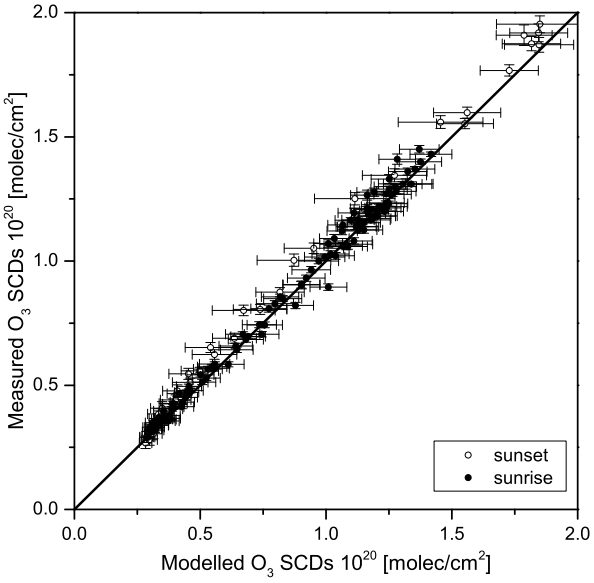

Figure 13.7.: *Comparison between the measured O_3 SCDs from the sunset and sunrise limb scans and SCDs calculated from the Labmos model.*

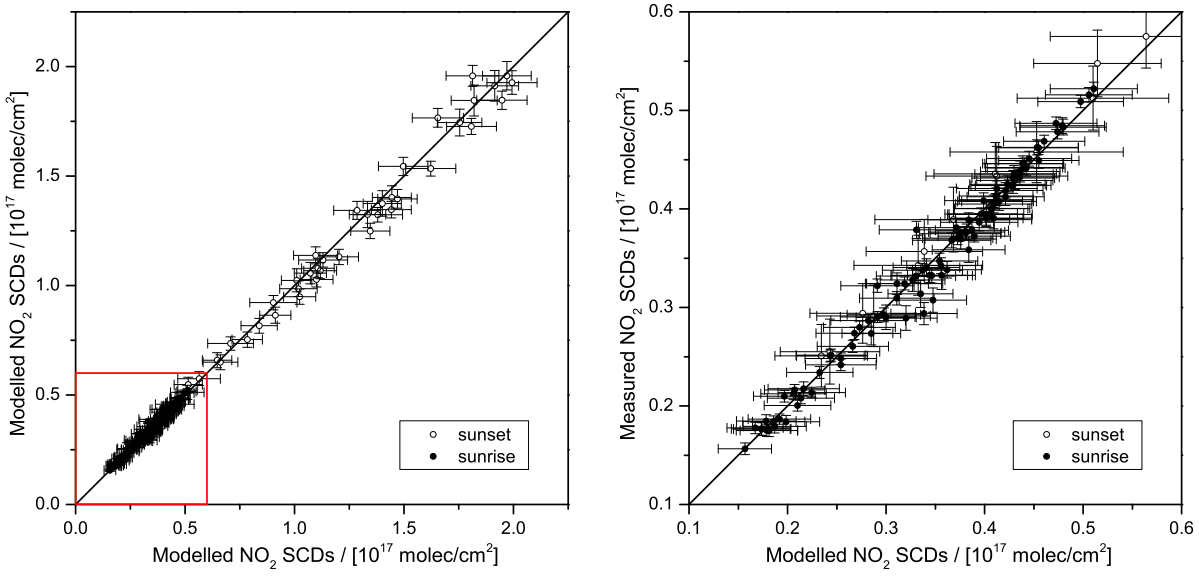

Figure 13.8.: *The left panel shows the comparison between measured and modelled NO_2 SCDs. The right panel is a zoom into the area indicated by the red square in the left plot, showing the SCDs retrieved from the sunrise limb measurements of scattered skylight.*

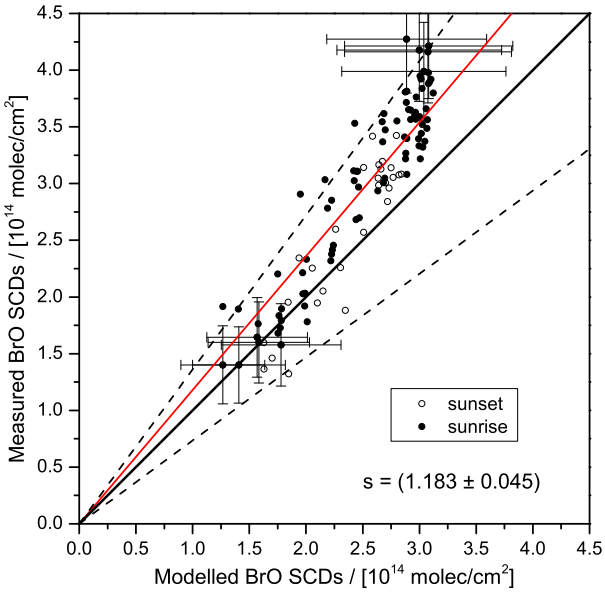

Figure 13.9.: *Comparison between the measured and calculated SCDs from the concentration profiles of the Labmos model. For reasons of clarity only the error bars of the five smallest and largest SCDs are plotted. The dashed lines indicate the uncertainty range resulting from the model parameters given by Sander et al. (2011). The ratio of measured SCDs / modelled SCDs = 1.183 ± 0.045, which is still within the uncertainty range given by Sander et al. (2011).*

13.3.1. J - k Dependence

The sensitivity of the Labmos model is first tested in respect to two parameters. As stated before, an increase in the photolysis rate J_{BrONO_2} is not the only explanation for the measured BrO SCDs; a decreased formation rate of $BrONO_2$ could also be responsible. The model runs, which resulted in the best agreement are shown in Figure 13.10.
For each model run, the measured SCDs are plotted against the SCDs calculated with the photochemical Labmos model and a linear fit through zero is performed. The slope of the fit is indicated in each panel in Figure 13.10. The results of the comparisons are discussed in Section 13.5 following in the analysis of the Br_Y parameter and the comparison of the direct sunlight measurements recorded during sunset.

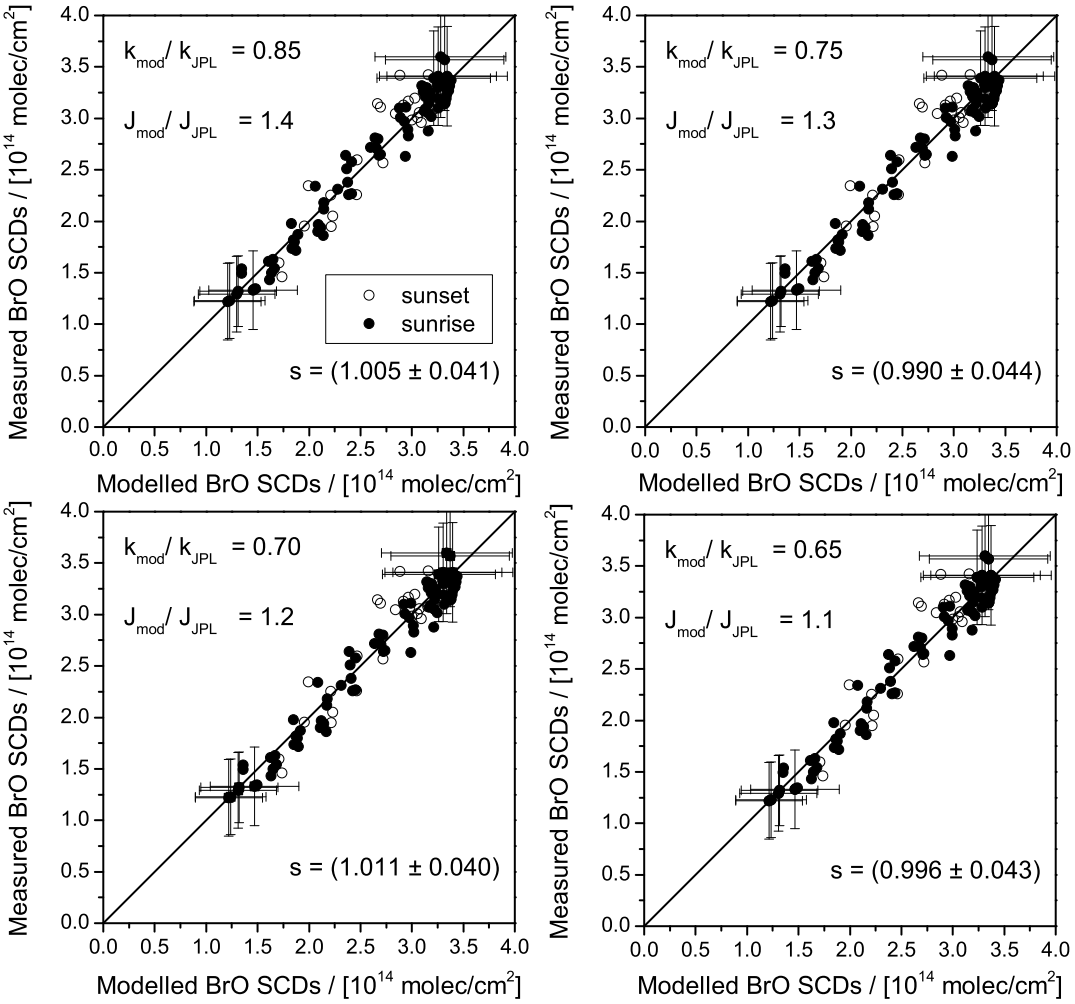

Figure 13.10.: *Comparison of several model runs using different sets of* $J_{\mathrm{BrONO_2}}$ *and* $k_{[\mathrm{BrO}][\mathrm{NO_2}]}$*, indicated in each panel in the upper left corner. The slope of the linear fit is listed in the lower right corner of each panel. For reasons of clarity only the error bars of the five smallest and largest SCDs are plotted.*

13.3.2. Br_Y Dependence

The mixing ratio of Br_Y is the third parameter tested. A Br_Y mixing ratio of (20.3 ± 2.5) ppt was inferred from the direct sunlight measurements of the LPMA/DOAS flight on September 7^{th} 2009 (*WMO* 2011). Two test runs for mixing ratios of 18 ppt and 23 ppt are performed. These are the uncertainty limits of the mixing ratio. The results from both runs, shown in Figure 13.11, deviate from the expected 1:1 line and the simulations using these Br_Y parameters cannot explain the measurements.

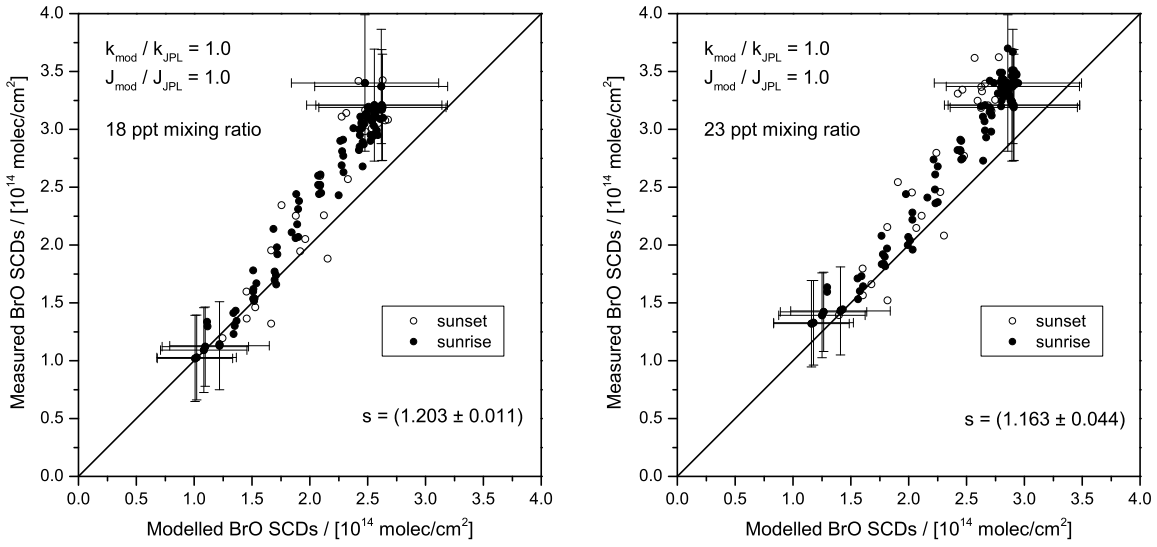

Figure 13.11.: *Different model runs with 18 ppt and 23 ppt mixing ratio above 24 km.*

13.4. Comparison between Measured and Modelled Direct Sunlight Observations

As already stated only the balloon ascent and sunset BrO measurements of the direct sunlight instrument can be compared to the limb observations of scattered skylight. The direct sunlight measurements recorded during sunrise are sensitive to HOBr photolysis and are discussed separately. In Figure 13.12, the BrO concentration profile inferred from the balloon ascent measurements is compared with the output of several Labmos model runs. A comparison between the inferred balloon ascent profile with the direct sunlight instrument indicates a better agreement for BrO with a profile calculated with a $J_{\mathrm{mod}}/J_{\mathrm{JPL}}$ = 1.4 than the standard photolysis rate $J_{\mathrm{mod}}/J_{\mathrm{JPL}} = 1$.

BrO SCDs are retrieved for all three datasets of the direct sunlight measurements: ascent, sunset and sunrise. However, the profiles are only inverted for the balloon ascent measurements. During solar occultation the BrO concentration changes very quickly (see Figure 13.13). Thus, an additional concentration profile would not generate more information than the ascent profile, because the values would be based to a large degree on

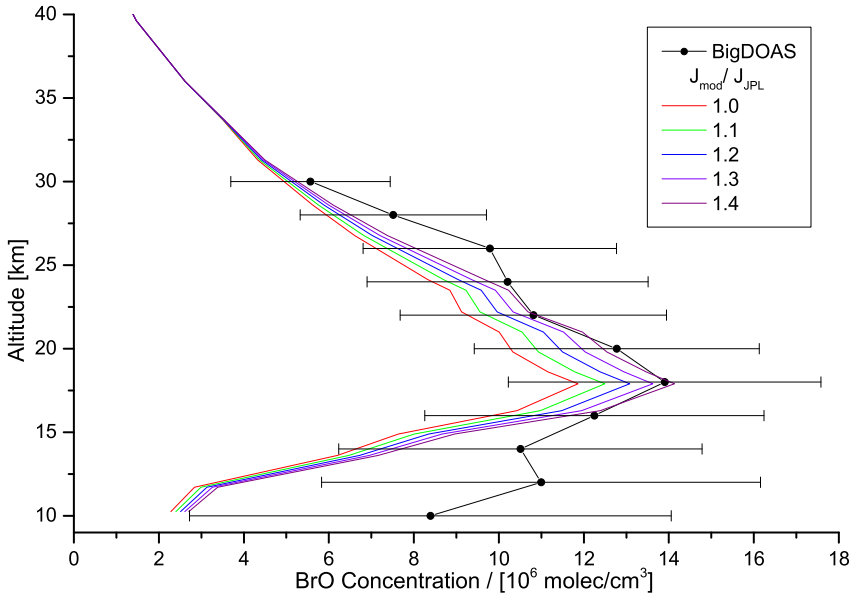

Figure 13.12.: *Comparison between the retrieved BrO balloon ascent profile with the direct sunlight measurements for different photolysis rates. The $BrONO_2$ absorption cross section is increased stepwise from 1.0 to 1.4 in steps of 0.1.*

the photochemical correction (*Dorf* 2005).

However, it is possible to compare the measured SCDs of the direct sunlight instrument directly with modelled SCDs from the chemical model. *Harder et al.* (2000) and *Dorf* (2005) used direct sunlight measurements recorded during solar occultation to analyse the bromine photochemistry of the stratosphere.

An important aspect of the direct sunlight measurements is indicated in Figure 13.13. In principle, each point along the light path of a direct sunlight viewing geometry can be identified by a unique local SZA and hence unique insolation and local photochemical conditions. The observed spectrum is a composite of all photochemical conditions along the light path. Figure 13.13 is a sort of folded perspective of the light path. The black lines indicate the light path of the direct sunlight measurements for observations during sunset. Normally the Earth would be plotted as a sphere and the light path as a straight line. Here the Earth's atmosphere (or the concentration distribution of BrO to be precise) is plotted on a straight altitude grid and the light paths travelling from the Sun towards the instrument as a curve.

This is important for photochemically active species. If the BrO SCDs are calculated for given viewing geometries, the local SZAs of each point along the light path have to be taken into account in order to determine the BrO concentration at that point. These calculations are done by the DAMF programme using the Labmos model output.

Figure 13.13 also illustrates one failing of the direct sunlight measurements of BrO recorded during solar occultation events. Altitude levels below the balloon float altitude are only probed for SZAs (at the location of the balloon gondola) larger than 90°. For these time frames, the concentrations of BrO are already significantly decreased in the case of sunset observations, or still significantly decreased in the case of sunrise observa-

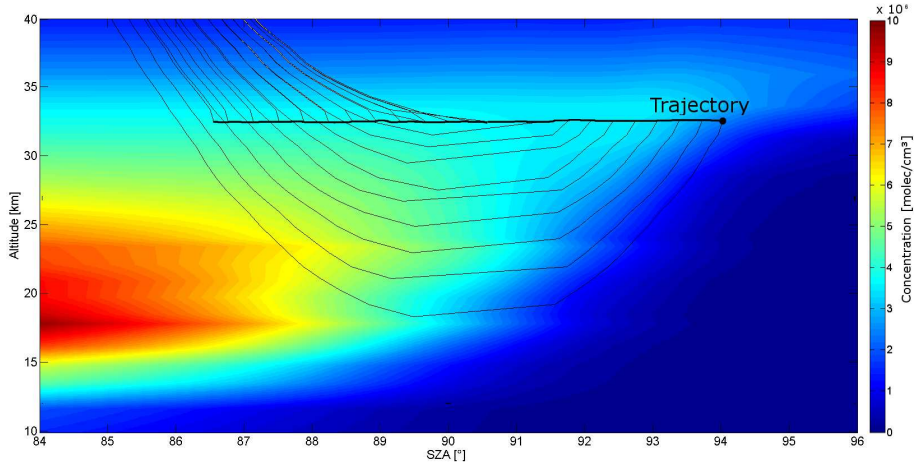

Figure 13.13.: *The BrO concentration is plotted against the altitude during solar occultation in the evening. For SZAs larger than 90° the light path probes altitudes below the balloon altitude at a tangent point around a local SZA of 90°. The black lines indicate the light path of a single direct sunlight spectrum through the atmosphere, starting at the corresponding point of the trajectory towards the Sun.*

tions, when compared with the concentration during the balloon ascent measurements. Therefore, they are less sensitive to changes in the BrO concentrations than the limb measurements of scattered skylight. In addition to that the light path probes altitudes below the balloon altitude per definition at a tangent point around a local SZA of 90°, which means every viewing geometry resembles the same photochemical condition. This makes the direct sunlight observations less suited for monitoring the concentration changes of BrO. The limb measurements continue to probe the altitude below balloon float level with elevation scans for SZAs from 86° - 95° during sunset and 86° - 75° during sunrise.
The concentration profiles of O_3 and NO_2 are used to constrain the Labmos model input. Therefore, modelled SCDs will return only the used measured SCDs. However, the comparison can be used to test the sensitivity and check for discrepancies. The comparison between the measured and modelled SCDs for the O_3 and NO_2 solar occultation measurements of the direct sunlight observations show a good agreement (see Figure 13.14).

Figure 13.15 shows the comparison between measured and modelled BrO SCDs for the direct sunlight measurements recorded during sunset. The standard model run uses a $k_{\mathrm{mod}}/k_{\mathrm{JPL}} = 1$ and $J_{\mathrm{mod}}/J_{\mathrm{JPL}} = 1$. Unlike the limb measurements of the miniDOAS instrument, only one scan through the atmosphere is performed for direct sunlight measurements.

Several simulations are performed using different parameters for the photolysis $J_{\mathrm{BrONO_2}}$ and rate coefficient $k_{[\mathrm{BrO}][\mathrm{NO_2}]}$. This is done to find pairs of the parameters that result in a good agreement between measured and modelled SCDs. Figure 13.16 shows the results for the comparison with the best agreement.

Figure 13.17 shows the measured and modelled BrO direct sunlight SCDs over time for the sunset observations.

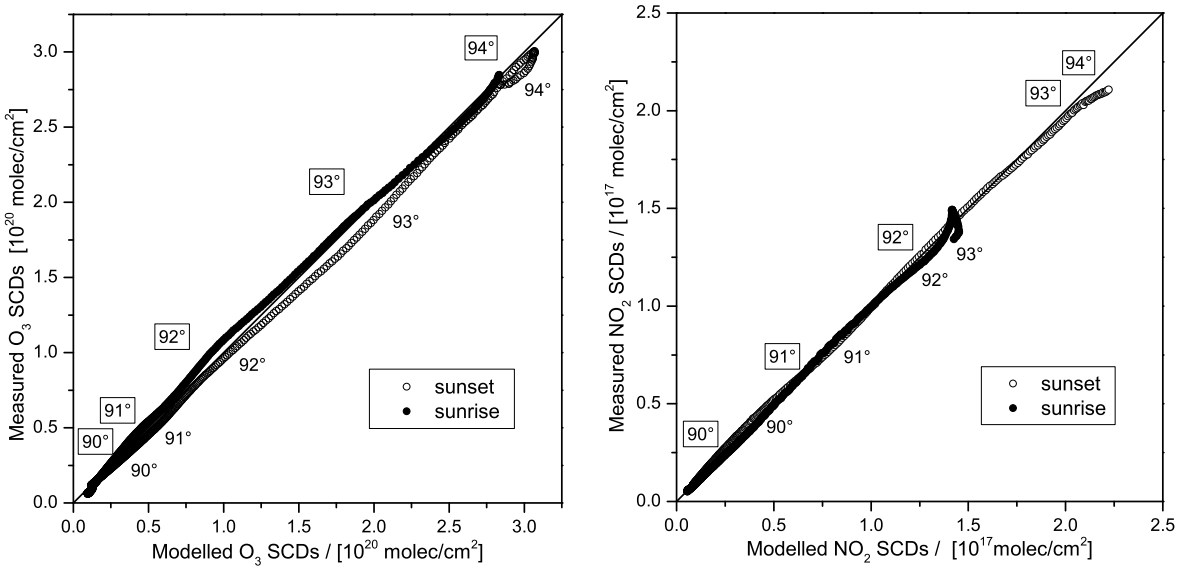

Figure 13.14.: *The comparison between measured and modelled direct sunlight O_3 SCDs for the sunset and sunrise measurements is shown in the left panel. The right panel shows the comparison between measured and modelled direct sunlight NO_2 SCDs. The local SZA is indicated on the left side of the corresponding SCD. The values above the 1:1 line with a frame denote the local SZA for the sunset measurements. The values below the 1:1 line without a frame are the corresponding SZAs of the sunrise SCDs.*

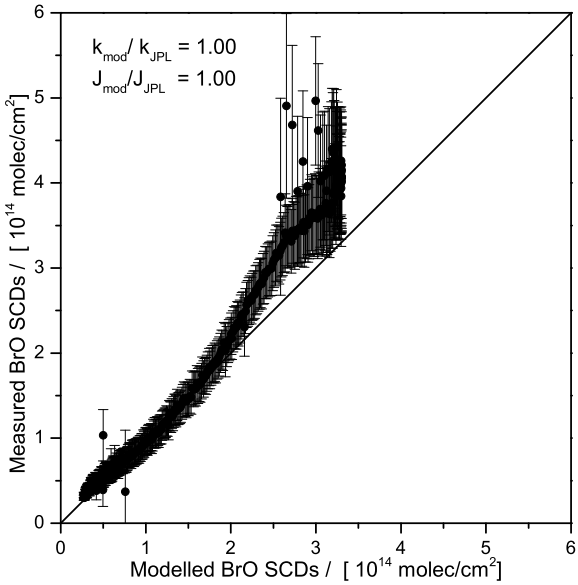

Figure 13.15.: *Comparison between BrO SCDs calculated using the standard model ($k_{\mathrm{mod}}/k_{\mathrm{JPL}} = 1$ and $J_{\mathrm{mod}}/J_{\mathrm{JPL}} = 1$) and the measured SCDs of the direct sunlight sunset observations.*

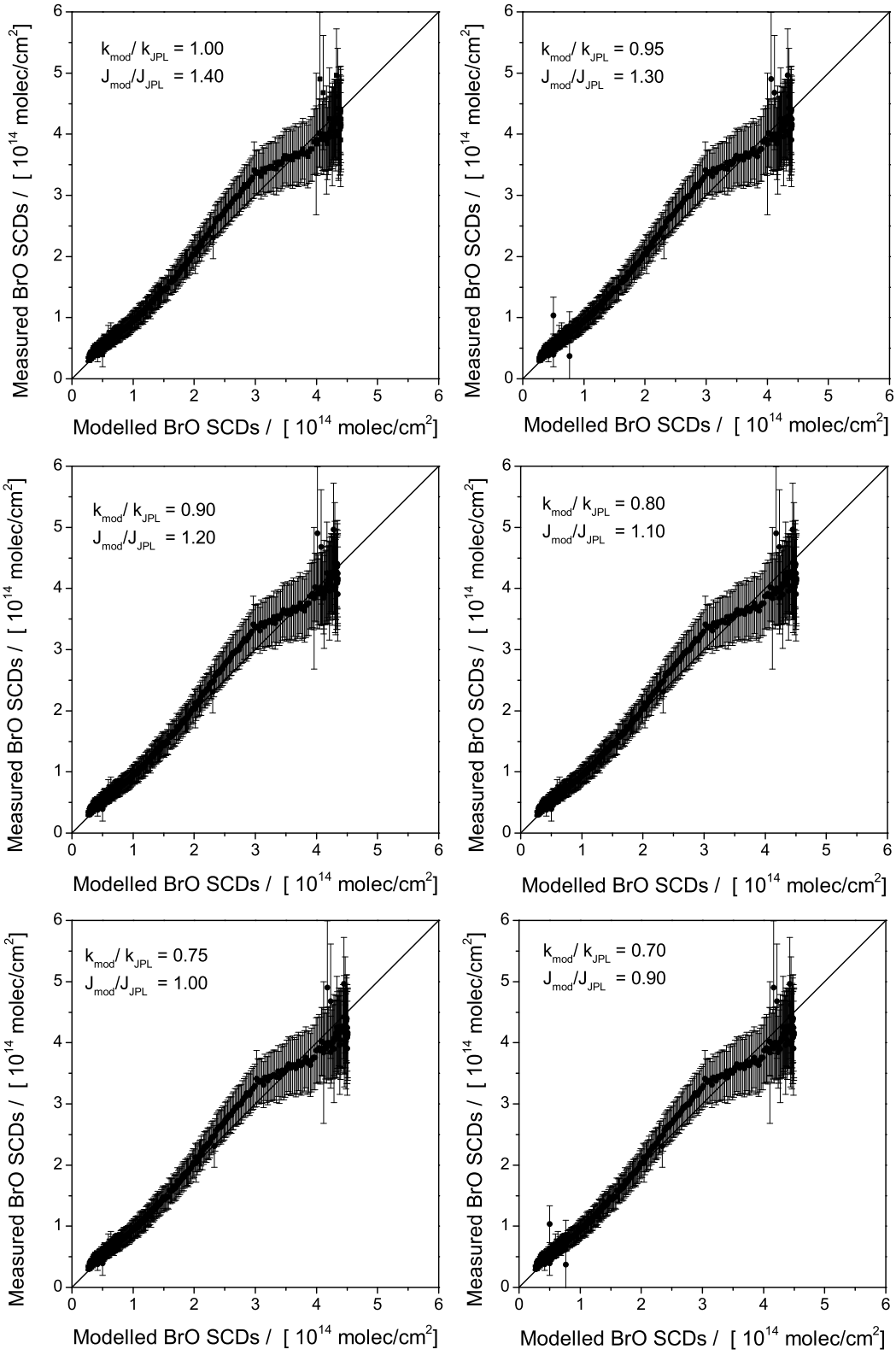

Figure 13.16.: *Comparison between different sets of* $J_{\mathrm{BrONO_2}}$ *and* $k_{[\mathrm{BrO}][\mathrm{NO_2}]}$ *for direct sunlight measurements made during sunset. The specific parameters are listed in the upper left corner of each panel.*

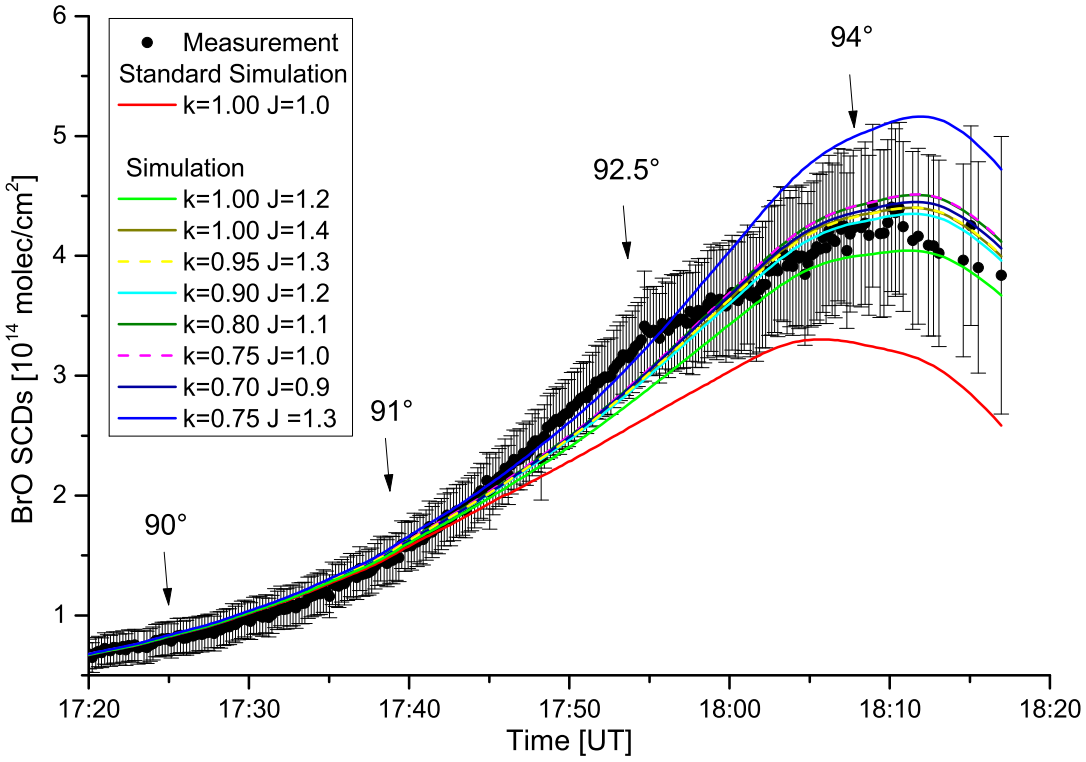

Figure 13.17.: *Comparison between the measured direct sunlight BrO SCDs and SCDs calculated from several different model runs. The values for the two parameters* $J_{\mathrm{mod}}/J_{\mathrm{JPL}}$ *and* $k_{\mathrm{mod}}/k_{\mathrm{JPL}}$ *used in the calculations for each model run are indicated in the legend as* J *and* k.

13.4.1. Sunrise Observations

As shown in Figure 13.1, the photolysis of HOBr is a dominant factor of the increase in BrO for the time of the direct sunlight measurements during sunrise (SZA = 95° - 90°). Figure 13.18 shows a comparison between the measured and modelled BrO SCDs for the JPL-2011 recommendations (*Sander et al.* 2011) and a model run with adapted parameters. Specifically, the hydrolysis of $BrONO_2$ is increased to produce more HOBr during the night for the adapted model run. The uptake coefficient γ of the heterogeneous rate coefficient k_{het} of the $BrONO_2$ hydrolysis, is increased by a factor of 1.25 (resulting in a $\gamma = 1$). The absorption cross section of HOBr was reduced by a factor of 10 in accordance with the uncertainty estimate of the photolysis rate (*Sander et al.* 2011). This corresponds with the modification of the photolysis rate of $BrONO_2$.
The increase of the rate coefficient of the direct production of HOBr through BrO and HO_2 (Reaction 3.47) is also tested (*Bedjanian et al.* 2001). The rate coefficient $k_{[BrO][HO_2]}$ was increased by a factor of 1.15 in accordance with the uncertainty stated by *Sander et al.* (2011). However, this modification only had a marginal effect on the change in BrO SCDs. Figure 13.18 shows that the measured BrO SCDs can be reproduced by the model within the uncertainty range given by the JPL-2011 recommendations (*Sander et al.* 2011).

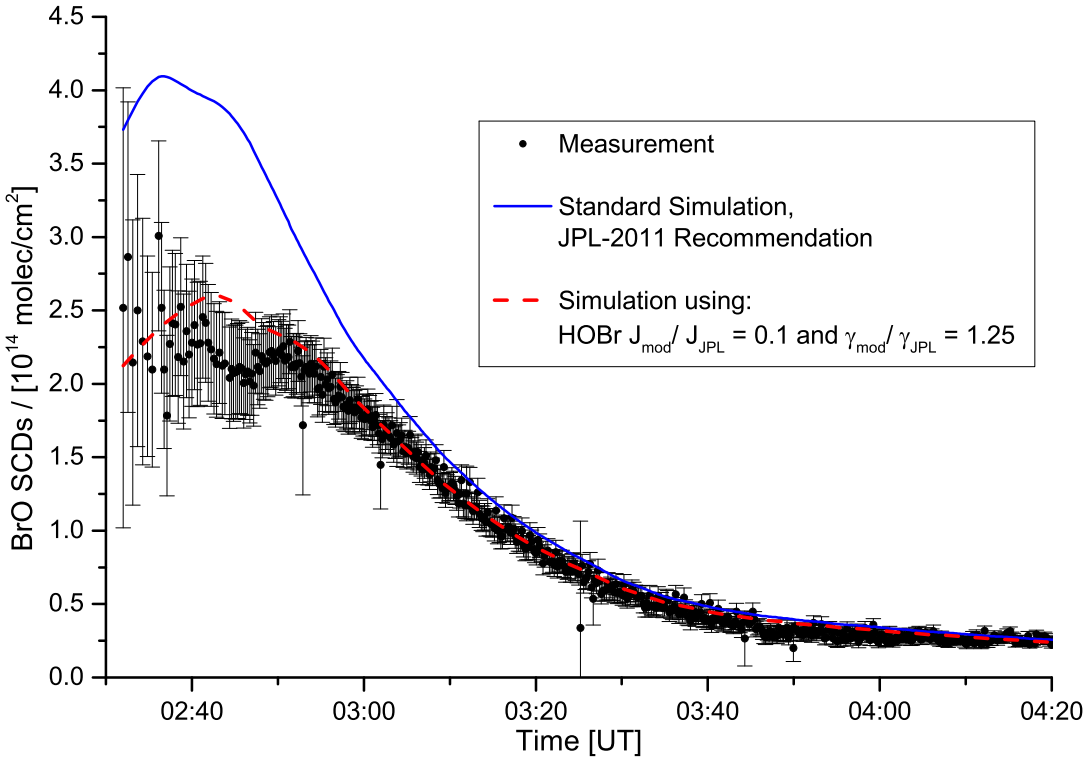

Figure 13.18.: *Comparison between measured and modelled BrO SCDs of the direct sunlight measurements during sunrise on September 8th 2009 for a model run with the JPL-2011 recommendations and a model with reduced absorption cross section of HOBr (factor of 10) and an increased uptake coefficient (factor of 1.25) of the $BrONO_2$ hydrolysis.*

13.5. Discussion of Results

As stated in Section 13.1, model runs are performed for the $k_{\mathrm{mod}}/k_{\mathrm{JPL}} = [0.60 .. 1.10]$ and $J_{\mathrm{mod}}/J_{\mathrm{JPL}} = [0.90 .. 1.50]$ range. The SCDs of the limb measurements of scattered skylight are plotted against the SCDs calculated with the photochemical Labmos model and a linear fit through zero is performed. The resulting slope of this fit is plotted in Figure 13.19 using the colour code indicated on the right side of the plot. A value of 1.00 indicates a good agreement between measured and modelled SCDs. Different $J_{\mathrm{BrONO_2}}$ and $k_{[\mathrm{BrO}][\mathrm{NO_2}]}$ values are tested until a good agreement with the measured BrO SCDs of the limb measurements of scattered skylight is found.
The four examples for a good agreement between measured and modelled BrO SCDs shown in Figure 13.10 are indicated by the black dots in Figure 13.19. The black stars indicate the best agreement for direct sunlight measurements recorded during sunset (see Section 13.4).
Figure 13.19 shows that a good agreement between measured and modelled SCDs can

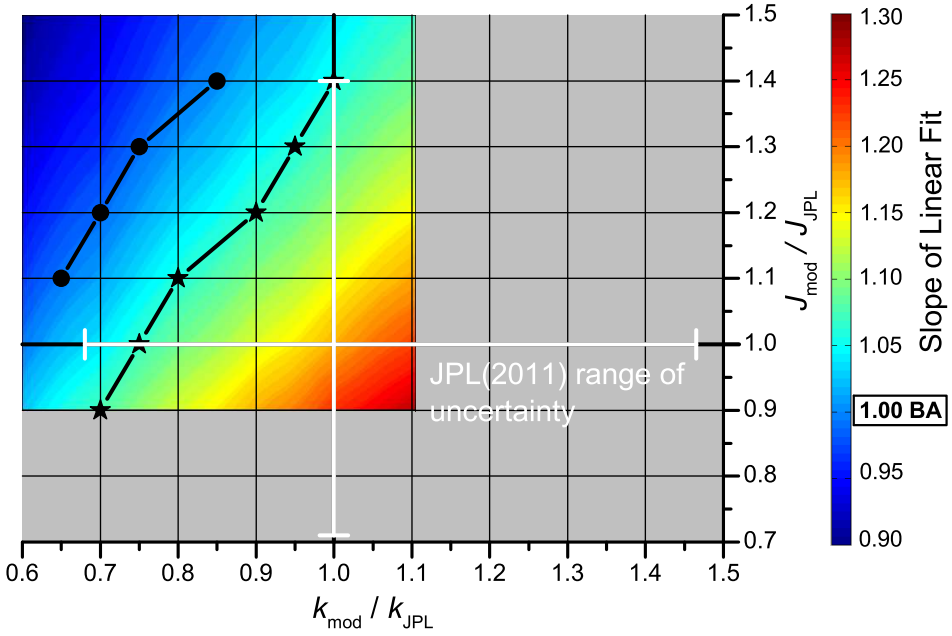

Figure 13.19.: *Agreement of measured and modelled BrO SCDs. The x-axis represents a multiplicative factor for the rate coefficient $k_{\mathrm{mod}}/k_{\mathrm{JPL}}$ and the y-axis for the photolysis $J_{\mathrm{mod}}/J_{\mathrm{JPL}}$. The 1σ-uncertainty range of Sander et al. (2011) is indicated in white. The black dots indicate the best agreement for the miniDOAS limb measurements. The black stars indicate the best agreement for sunlight measurements recorded during sunset (see Section 13.4). The colour code indicates the slope of the linear fit of the correlation plot (sunset and sunrise). A value of 1.00 indicates best results for the agreement of measured of modelled SCDs. The value is highlighted by the black box (BA).*

only be reached with a combination of a decreased $k_{[\mathrm{BrO}][\mathrm{NO_2}]}$ and an increased $J_{\mathrm{BrONO_2}}$ (e.g., $k_{\mathrm{mod}}/k_{\mathrm{JPL}} = 0.85$ and $J_{\mathrm{mod}}/J_{\mathrm{JPL}} = 1.4$).
Averaging the $J_{\mathrm{mod}}/J_{\mathrm{JPL}}$ and $k_{\mathrm{mod}}/k_{\mathrm{JPL}}$ pairs that result in the best agreement between the measured and modelled BrO SCDs of the limb measurements of scattered skylight

(black dots in Figure 13.19) results in a mean value:

$$\frac{J_{\mathrm{mod}}/J_{\mathrm{JPL}}}{k_{\mathrm{mod}}/k_{\mathrm{JPL}}} = 1.69 \pm 0.04 \tag{13.1}$$

The direct sunlight measurements recorded during balloon ascent and sunset support the need for an offset of the $J_{\mathrm{BrONO_2}}/k_{[\mathrm{BrO}][\mathrm{NO_2}]}$ ratio. However, the mean value for the direct sunlight measurements which provide the best agreement between measured and modelled BrO SCDs (black stars in figure 13.19) $[J_{\mathrm{mod}}/J_{\mathrm{JPL}}]\,/\,[k_{\mathrm{mod}}/k_{\mathrm{JPL}}]$ is lower. The determined value for the direct sunlight measurements is (1.35 ± 0.04). However, as already mentioned in Section 13.4, the direct sunlight measurements are less sensitive to the targeted change in BrO concentrations.

The change in the $J_{\mathrm{BrONO_2}}/k_{[\mathrm{BrO}][\mathrm{NO_2}]}$ ratio inherently leads to a change in the $\mathrm{BrO/BrONO_2}$ and $\mathrm{BrO/Br_Y}$ ratio.
Figure 13.20 shows the change in concentration at 28 km for the time of the miniDOAS

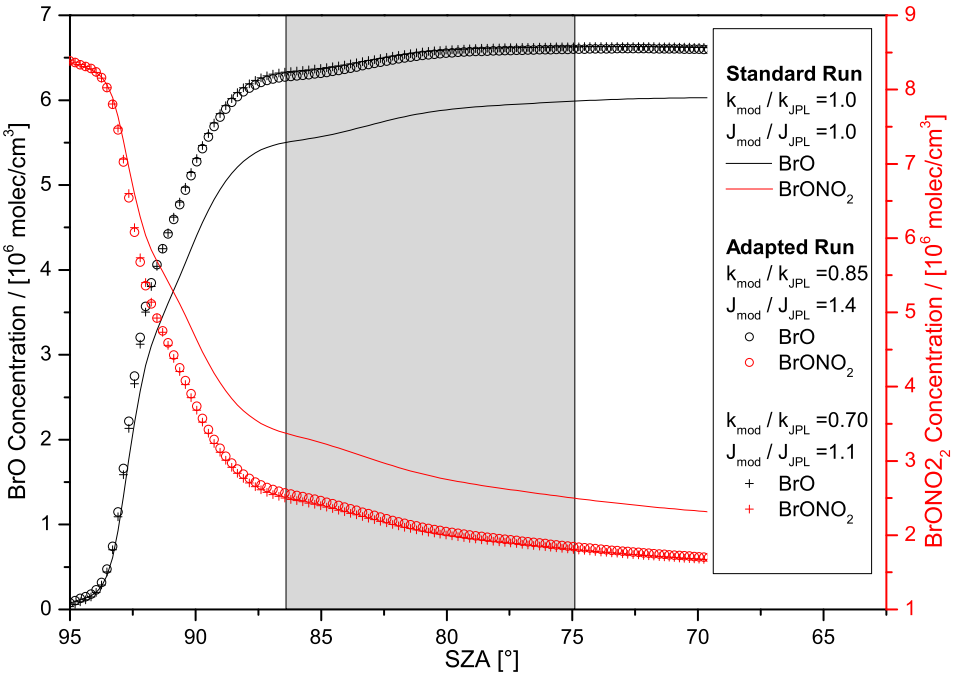

Figure 13.20.: *Modelled temporal evolution of BrO and $BrONO_2$ concentrations at 28 km for three different model runs. The time frame during which the miniDOAS measurements were taken is indicated in grey. The temporal evolution of BrO and $BrONO_2$ using the standard run is plotted as a line. The two exemplary model runs that resulted in the best agreement between measured and modelled SCDs are plotted as circles and crosses respectively. The parameters of the two adapted runs are indicated in the legend.*

limb measurements of scattered skylight during sunrise. For the $J_{\mathrm{BrONO_2}}$ and $k_{[\mathrm{BrO}][\mathrm{NO_2}]}$ values determined in Figure 13.10 at an SZA = 80°, the ratios of both BrO and $\mathrm{BrONO_2}$

are changed from:

$$\left[\frac{\mathrm{BrO}}{\mathrm{Br_Y}} = 0.59\ \frac{\mathrm{BrONO_2}}{\mathrm{Br_Y}} = 0.28\right]_{\mathrm{JPL}} \Longleftrightarrow \left[\frac{\mathrm{BrO}}{\mathrm{Br_Y}} = 0.66\ \frac{\mathrm{BrONO_2}}{\mathrm{Br_Y}} = 0.21\right]_{\mathrm{Observations}}$$

with respect to the total stratospheric $\mathrm{Br_Y}$. From the comparison between measurements and model the following conclusions regarding stratospheric $\mathrm{Br_Y}$ budget and photochemistry can be made:

- Using the revised $J_{\mathrm{BrONO_2}}/k_{[\mathrm{BrO}][\mathrm{NO_2}]}$ ratio and the changed $\mathrm{BrO/Br_Y}$ ratio, the total stratospheric $\mathrm{Br_Y}$ is likely to be 1.4 ppt smaller than previously estimated. This would bring the total stratospheric bromine inferred from ground-based measurements of organic source gases ($\mathrm{CH_3Br}$, $\mathrm{CH_2Br_2}$, $\mathrm{CHBr_3}$, halons, etc.) into closer agreement with estimates based on balloon-borne measurements of BrO (update of *Dorf et al.* 2006, (*Dorf et al.* 2008), *Hossaini et al.* 2012, *Brinckmann et al.* 2012).

- The consequences for stratospheric ozone as a result of this revision of $J_{(\mathrm{BrONO_2})}/k_{[BrO][NO_2]}$ are minor to negligible. A corrected $J_{\mathrm{BrONO_2}}/k_{[\mathrm{BrO}][\mathrm{NO_2}]}$ may cause a somewhat small, but close to negligible, increase in the bromine mediated ozone loss in the stratosphere, because ozone loss by $\mathrm{BrONO_2}$ and its product is small. An overestimated stratospheric $\mathrm{Br_Y}$ due to an incorrect $J_{BrONO_2}/k_{[BrO][NO_2]}$ ratio would be compensated for in the photochemical models when active bromine is calculated (*Salawitch et al.* 2005, *Sinnhuber et al.* 2009).

- In the troposphere, where high $\mathrm{NO_X}$ meets reactive bromine released by the degradation of organic bromine compounds, a diminished formation of $\mathrm{BrONO_2}$ may lead to a longer life-time of ozone destroying BrO (*Yang et al.* 2005). As a consequence, the revised $J_{\mathrm{BrONO_2}}/k_{[\mathrm{BrO}][\mathrm{NO_2}]}$ ratio may cause more ozone destruction and a more efficient degradation of organic molecules by their reaction with Br. At the same time, the change in reaction speed may hinder the activation of reactive bromine tied to the aerosol or in salt deposits (*von Glasow et al.* 2004, *Salawitch* 2006). Accordingly, the consequences of our findings for ozone, and the atmospheric oxidation capacity, may largely depend on the specific conditions.

- The rapid increase of BrO for a local SZA $> 90°$ is apparently due to the photolysis of HOBr. This can be seen in Figure 13.1. The measured BrO SCDs can be modelled if the photolysis rate of HOBr is reduced by a factor of 10 ($J_{\mathrm{mod}}/J_{\mathrm{JPL}}$) and the preceding hydrolysis of $\mathrm{BrONO_2}$ is enhanced via an increase of the uptake coefficient γ (by a factor of 1.25). The analysis of the direct sunlight measurements of BrO recorded during sunrise, the HOBr photolysis rate and the night-time build up via the hydrolysis of $\mathrm{BrONO_2}$ will be the focus of a future study including a more detailed analysis of the HOBr photochemistry (*Hanson and Ravishankara* 1995, *Erle et al.* 1998, *Hanson* 2003). A similar difference between modelled and measured BrO SCDs immediately after sunrise (SZA $> 90°$) was also observed in 2008 during a balloon deployment in the tropics in Teresina, northern Brazil. The details of this

LPMA/DOAS balloon deployment are listed in Figure 14.3. The atmospheric conditions of this balloon flight in the tropics in June 2008 make the dataset much more suited, since in the tropical lower stratosphere (below 25 km) the bromine photochemistry is likely to be dominated by cross reactions of the HO_X and Br_X families, leading to a predominant formation of HOBr (*Bedjanian et al.* 2001). Hence, the photolysis of HOBr during early dawn (SZA $> 90°$) can be studied in detail. The HOBr absorption cross section is subject to large uncertainties (*Ingham et al.* 1998). *Sander et al.* (2011) states the uncertainty of the HOBr photolysis for wavelengths larger then 350 nm to be a factor of 10. A changed hydrolysis of $BrONO_2$ (Reaction 3.50) during the night would increase the HOBr concentrations in the morning (*Hanson and Ravishankara* 1995, *Hanson* 2003) and thereby influence the rapid release of BrO via the photolysis of HOBr for SZAs $> 90°$. An analysis of the impact of a reduced HOBr photolysis is shown in Figure 13.18.

14. Satellite Validation

The high accuracy balloon-borne direct sunlight measurements are also used to validate satellite measurements of the SCIAMACHY[1] instrument on board the Envisat satellite (*Dehn* 2010).

14.1. The SCIAMACHY Instrument

SCIAMACHY was a passive remote sensing spectrometer observing backscattered, reflected, transmitted or emitted radiation from the atmosphere and Earth's surface. The SCIAMACHY viewing geometry is shown in Figure 14.1. SCIAMACHY covered a wavelength range between 240 and 2380 nm. This large wavelength range not only allowed the instrument to cover a larger number of trace gases, but it also enabled the determination of aerosol extinction profiles (Section 12.2.2) and cloud coverage. A detailed description of the instrument and the retrieved products is given in *Bovensmann et al.* (1999) and *Gottwald* (2010). The instrument is on board the Envisat satellite which was launched on March 1^{st} 2002 and was operated until April 8^{th} 2012, when contact with the satellite was lost. The SCIAMACHY instrument was able to observe the entire Earth within three days. However, the use of a high altitude, fast moving instrument means a loss in altitude resolution and accuracy of the measurements.

The ENVIVAL-LIFE (ENVIsat VALidation) project was founded to validate the satellite

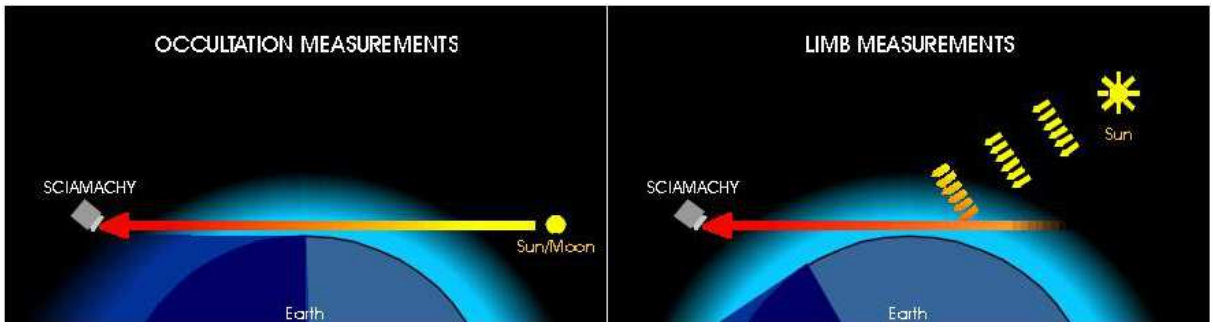

Figure 14.1.: *Viewing geometries of the SCIAMACHY instrument. Adopted from Bremen (2012).*

measurements and make improvements of the retrieval algorithms possible. During this project high accuracy balloon-borne measurements were compared to satellite measurements. The balloon-borne measurements are only point measurements compared to the

[1]SCIAMACHY stands for SCanning Imaging Absorption spectroMeter for Atmospheric CartograpHY

global coverage of a satellite instrument. However, approximately 50 times more spectra with a better signal-to-noise ratio are used to retrieve a profile from a balloon ascent compared to a satellite overpass. Combined with the simple geometric considerations for balloon-borne observations, this explains why the balloon-borne profiles are of much higher accuracy. This is confirmed by a comparison of the SCIAMACHY averaging kernel matrix for limb observations with the balloon direct sunlight observations in Figure 11.4 and 14.2. Balloon-borne measurements are inherently restricted by different operational

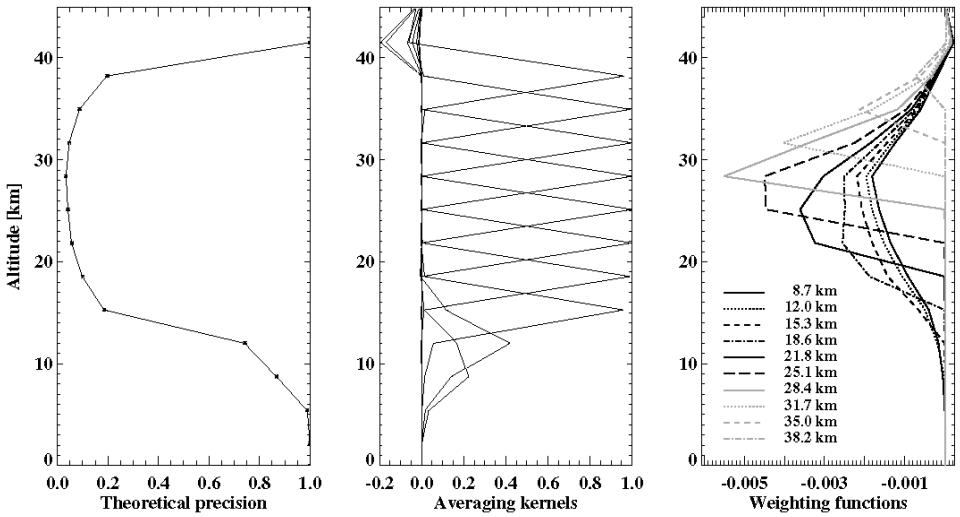

Figure 14.2.: *The left panel shows the theoretical precision, the middle panel the averaging kernels and the right panel differential weighting functions at 439.4 nm for a NO_2 vertical profile retrieval from SCIAMACHY limb measurements. Adopted from Rozanov et al. (2005).*

constraints, limiting their flexibility in satellite validation. These operational constraints, such as higher altitude wind regimes, ground wind and other weather conditions, inevitably lead to a temporal and spatial mismatch between satellite and balloon-borne observations.

14.2. Validation Approach

A detailed description of the validation method of the measurements of the SCIAMACHY instrument is given in *Butz* (2006) and *Butz et al.* (2006), hence only a short outline based on that work is given here.

To find the best coincidences between air masses probed by the balloon and the satellite instrument, air mass trajectory calculations are used (*Grunow* 2009). Based on the operational analysis of the ECMWF, the movement of air parcels probed by the balloon instrument is calculated on 25 isentropic levels by Katja Grunow. The movement of these parcels is calculated in 10 minute time steps and the resulting trajectory is stored in one hour time steps for a 48 hour time frame. These 48 hours of time calculations are then used to find the best satellite coincidence for comparison.

The actual geo-locations of SCIAMACHY observations are taken from the SCIAMACHY Operational Support Team (SOST) on their website[2]. The overpass time, the geo-location and detailed measurement specifications (e.g., swath, measurement duration, ground pixel size) are downloaded for the SCIAMACHY limb and for the SCIAMACHY nadir mode for each Envisat orbit.

This information is used to find satellite measurements which probed the same air masses

Date	Location	Geophysical condition	Available datasets	Satellite coincidence orbit, date, time/UT	Altitude range/ km	Time delay /h	Spatial distance/ km
04 Mar. 2003 13:20–16:17	Kiruna 67.9°N, 21.1°E	High-lat. spring SZA: 71.1°–94.1°	SO: LPMA	5273, 4 Mar., 11:05 5285, 5 Mar., 07:17	20–30 23–24	−5.1 +15.3	369–496 498–499
23 Mar. 2003 14.47–17:28	Kiruna 67.9°N, 21.1°E	High-lat. spring SZA: 78.9°–94.7°	BA: LPMA, DOAS SO: LPMA, DOAS	5545, 23 Mar., 11:07 5558, 24 Mar., 09:01 5545, 23 Mar., 11:07 5558, 24 Mar., 09:01	18–28 19–29 20–30 17–30	−5.2 +17.4 −6.2 +16.0	268–496 10–495 63–458 256–453
9 Oct. 2003 15:39–17:09	Aire sur l'Adour 43.7°N, 0.3°W	Mid-lat. fall SZA: 72.0°–87.8°	BA: DOAS	8407, 9 Oct., 09:51 8421, 10 Oct., 09:20	17–31 25–33	−6.5 +17.2	738–988 547–977
24 Mar. 2004 14:04–17:31	Kiruna 67.9°N, 21.1°E	High-lat. spring SZA: 74.5°–95.3°	BA: DOAS SO: DOAS	10798, 24 Mar., 10:35 10812, 25 Mar., 10:04 10798, 24 Mar., 10:35 10812, 25 Mar., 10:04	12–33 6–16 10–33 10–20	−5.4 +19.9 −6.9 +16.7	371–499 32–485 191–436 301–475
17 June 2005 18:32–21:13	Teresina 5.1°S, 42.9°W	Tropical winter SZA: 60.6°–95.8°	BA: DOAS SO: DOAS	17240, 17 June, 11:53 17255, 18 June, 13:02 17240, 17 June, 11:53 17255, 18 June, 13:02	25–30 5–33 23–32 8–33	−8.1 +18.4 −9.1 +16.2	382–491 6–490 519–971 12–496
27 June 2008 05:22 - 21:18	Teresina 5.1°S, 42.9°W	Tropical winter SZA: 60.4°–95.7°	SO: DOAS	33058, 26 June, 13:04 33072, 27 June, 12:32 33072, 27 June, 12:34	18-30 12-35 12-38	-19.9 +3.9 +3.9	416-989 540-991 160-543
7/8 Sep. 2009 14:53 – 06:05	Kiruna 67.9°N, 21.1°E	High-lat. summer SZA: 76.4° - 94.5°	LPMA/DOAS BA/SO	39326, 7 Sept., 09:57 39326, 7 Sept., 09:59 39340, 8 Sept., 09:25	21-34 9-34 10-34	-6.9 -6.8 +18.1	418-497 219-404 58-382
23 Apr. 2011	Kiruna 67.9°N, 21.1°E	High-lat. spring SZA: 85.4°-77.3°	BA: DOAS	To be determined			

Figure 14.3.: *The upper panel shows the list of deployments of the LPMA/DOAS gondola during the ENVIVAL project. The lower panel shows measurement sites of the LPMA/DOAS balloon flights. Based on Graphics (2012).*

[2](http://atmos.af.op.dlr.de/projects/scops)

as the balloon-borne instruments within a given match radius and time. The trajectory of the air parcels is then used to calculate the photochemical evolution of the probed air masses following the scheme outlined in Figure 14.4. The photochemically corrected

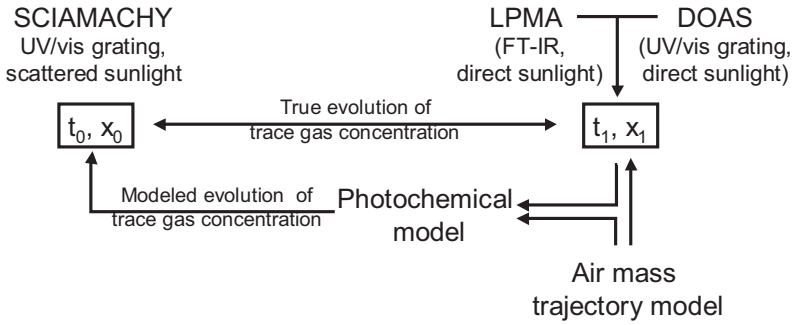

Figure 14.4.: *Schematic drawing of the balloon-satellite measurement comparison and validation strategy. SCIAMACHY observations are conducted at time t_0 and location x_0. Air mass trajectory calculations can be used before the flight to find the optimal launch time of the balloon. After the balloon flight, the trajectory model calculates the air mass history in order to identify satellite measurements which actually sampled the same air masses as the balloon borne instruments at the time t_1 and location x_1. The results of the calculations for the 2009 flight are shown in Figure 14.5. The modelled evolution of the trace gas history is used to appropriately scale the balloon-borne data to the photochemical conditions of the satellite measurements. Adopted from Butz (2006).*

concentration profiles are then compared to the retrieved profiles of that satellite orbit. The SCIAMACHY retrievals are provided by Alexei Rozanov from the IUP Bremen.
The table of the balloon validation flights performed during the ENVIVAL-LIFE project in Figure 14.3 also lists the coinciding satellite orbits. The retrieved profiles of the balloon flights in 2003 and 2004 were evaluated and compared to the satellite observations by *Butz et al.* (2006) for O_3 and NO_2 and by *Dorf et al.* (2006) for BrO. During the course of this thesis the balloon flights of 2008 and 2009 are analysed and the retrieved profiles compared with the corresponding satellite observations. While not shown here, the comparison of the retrieved profiles of the balloon flight in Teresina in 2008 and the coinciding satellite retrievals are published in *Dorf* (2009) and *Kreycy* (2009). The comparison of the balloon-borne O_3 measurements of the flight on September 7^{th} 2009 and the coinciding satellite observations is shown in Figures 14.6. The satellite profiles used for the comparison are based on the version 2.1 O_3 SCIAMACHY retrieval. The comparison of the balloon-borne measurements of the flight on September 7^{th} 2009 and coinciding satellite observations of NO_2 uses the version 3.1 NO_2 SCIAMACHY retrieval (Figure 14.7). The comparison of the balloon-borne measurements of the flight on September 7^{th} 2009 and coinciding satellite observations of BrO is shown in Figure 14.8. The version 3.2 BrO SCIAMACHY retrieval is used here.

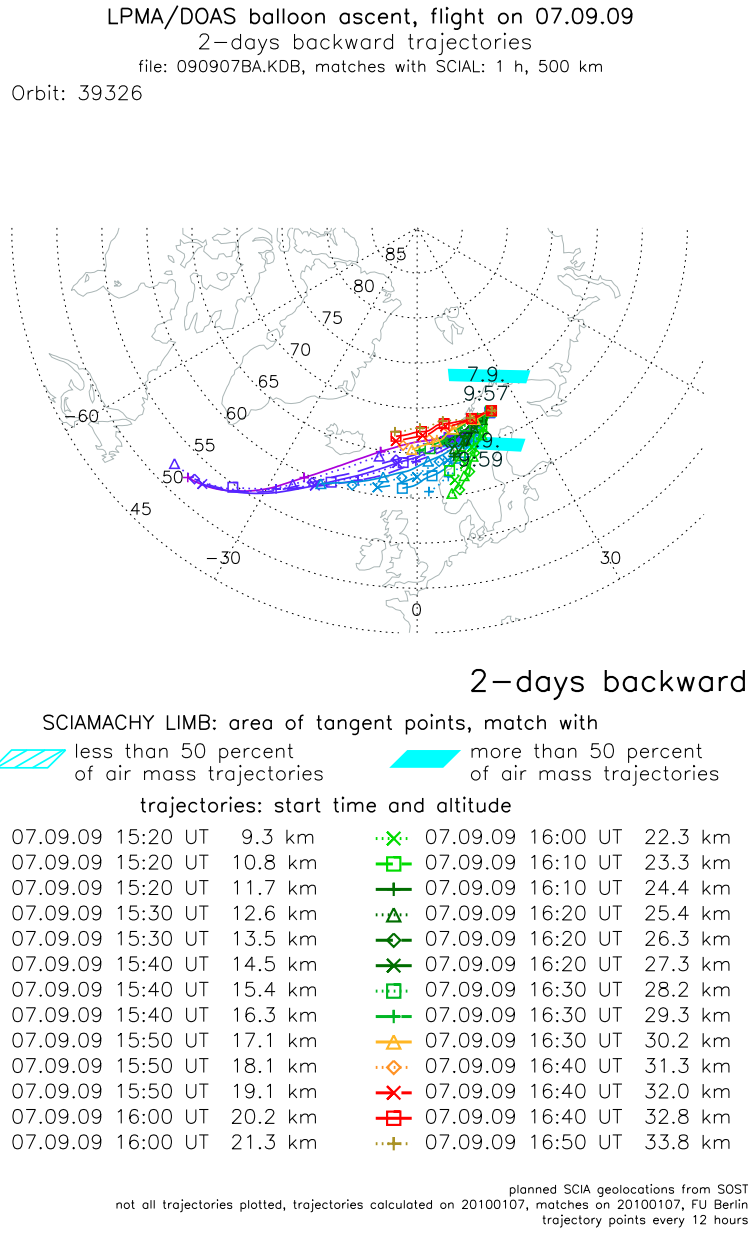

Figure 14.5.: *Two day backward trajectory calculations for the balloon ascent on September 7th 2009. There are two profiles measured by the SCIAMACHY instrument in range. The altitude of the air mass trajectories are identified below. Katja Grunow, 2009 (FU Berlin).*

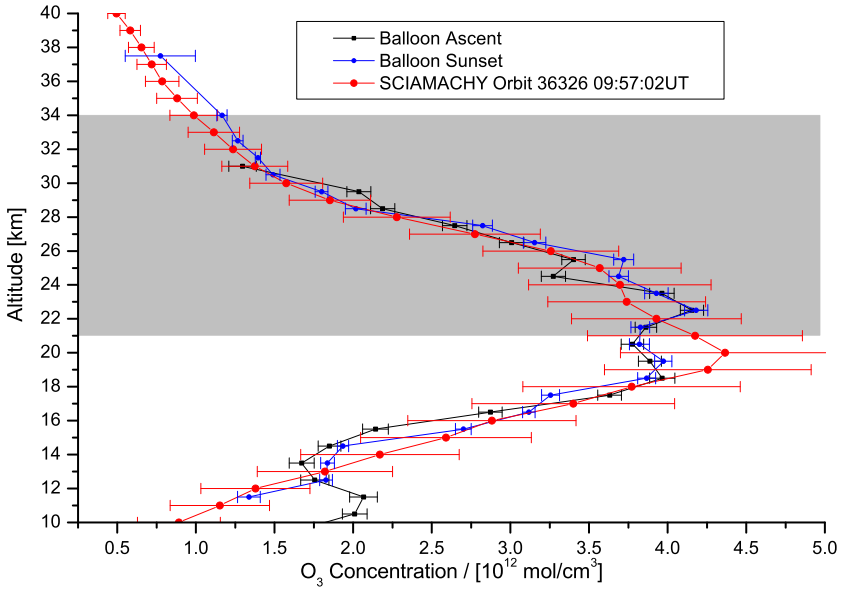

Figure 14.6.: *Comparison of the O_3 profile retrieved for the ascent and sunset measurements on September 7th 2009, with the satellite orbit indicated in Figure 14.5 at 09:57 UT that morning. The altitude range in which the same air masses are probed (21 - 34 km) is marked in grey. The satellite profiles used for the comparison are based on the version 2.1 O_3 SCIAMACHY retrieval.*

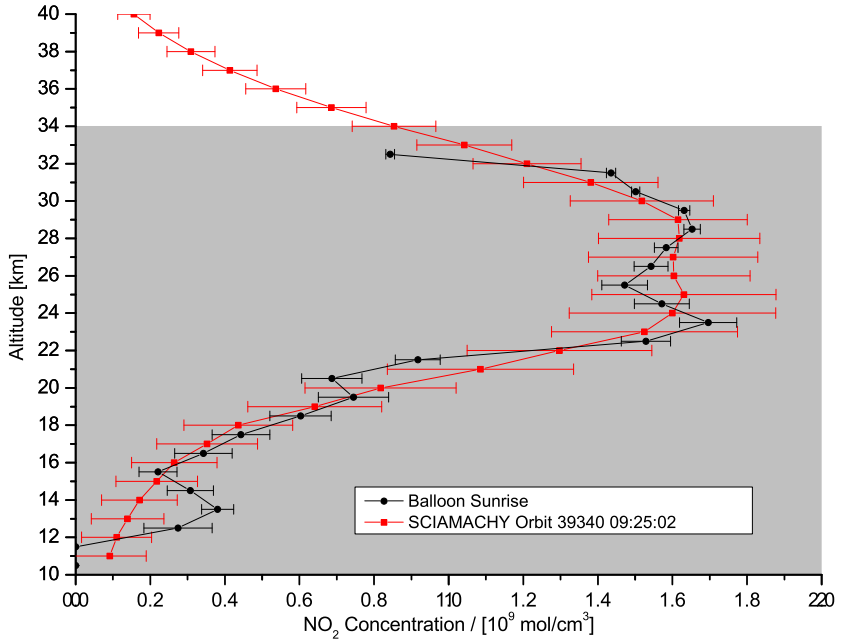

Figure 14.7.: *Comparison of the NO_2 profile retrieved from the direct sunlight measurements during sunrise on September 8th 2009 compared to the satellite orbit at 09:25 UT that morning. The altitude range in which the same air masses are probed (9 - 34 km) is marked in grey. The satellite profiles used for the comparison are based on the version 3.1 NO_2 SCIAMACHY retrieval.*

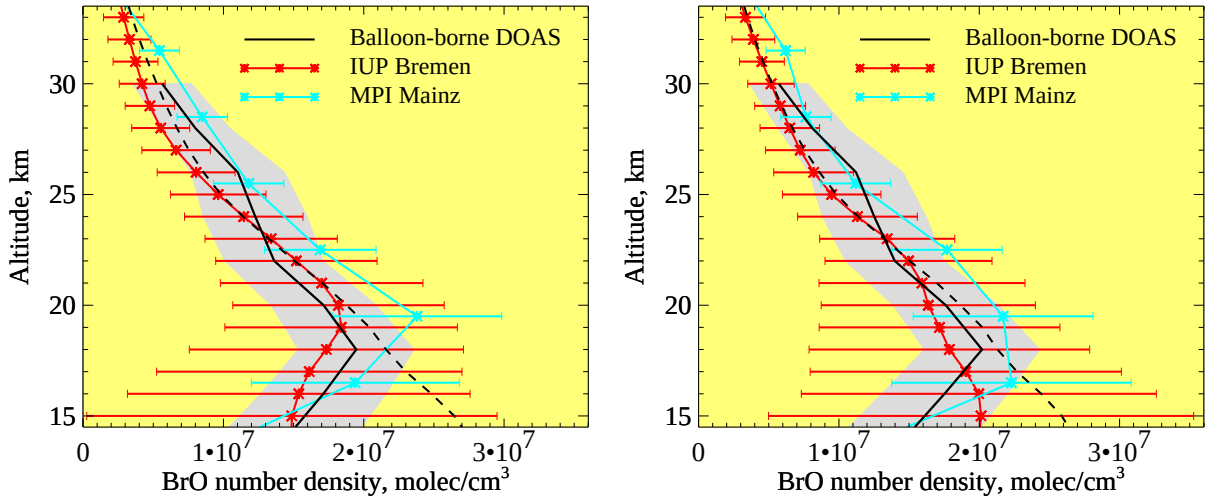

Figure 14.8.: *Comparison of the BrO profile retrieved from the balloon ascent and the satellite orbit at 09:57 UT that morning. The satellite data is evaluated by different institutes using different retrievals, currently at version 3.2, see color coding in the plot. The lower plot shows a comparison for the balloon ascent profile with the satellite orbit at 09:25 UT the next morning. Adopted from Rozanov et al. (2010).*

14.2.1. Summary

As stated above the goal of the ENVIVAL-LIFE project is an improvement of the satellite retrievals and a better agreement with the high accuracy balloon profiles. Therefore, all balloon-borne profiles listed in Figure 14.3 are compared to the newest satellite retrievals. Figures 14.9 and 14.10 are an update of the plots shown in *Butz et al.* (2006) using more recent versions of the satellite retrievals (see below).

The profiles used for the O_3 comparison are based on the version 2.1 O_3 SCIAMACHY retrieval. As shown in Figure 14.9 a good agreement between the balloon-borne O_3 measurements and the O_3 measurements of the SCIAMACHY instrument is reached within a 20% range. Below 18 km the sensitivity of the SCIAMACHY instrument is significantly reduced (see 14.2) and the SCIAMACHY O_3 profiles underestimate the balloon-borne data in most cases. This is due to the fact that the satellite retrievals cannot reproduce the frequently highly filamented O_3 profiles observed at high-latitudes during winter, as shown by *Butz et al.* (2006). With regard to the comparison shown in (*Butz et al.* 2006) a bias of +4.8% between the two data sets in the core altitude (20 - 31 km) has been removed. The mean devation is now 9.7% and has been improved by 1%.

The comparison of the balloon-borne NO_2 measurements and the coinciding satellite observations are based on the version 3.1 NO_2 SCIAMACHY retrieval. As shown in Figure 14.10 for the high- and mid-latitude measurements between 20 km to 30 km altitude the agreement between the balloon-borne NO_2 profiles and the satellite observations is on the order of 30%. However, there are still systematic discrepancies between the balloon and satellite-borne data for tropical latitudes in the core altitude range between 20 km and 31 km. Beyond that, the agreement between the entire two datasets below 20 km is still variable. With regard to the comparison shown in (*Butz et al.* 2006) a bias of +1.8% between the two data sets in the core altitude (20 - 31 km) has been removed. The mean devation has not changed.

The profiles for the BrO comparison are based on the SCIAMACHY retrieval version 3.2. As shown in Figure 14.11 an agreement between balloon and satellite-borne data is reached within a 30% range, while SCIAMACHY retrievals tend to underestimate the BrO concentrations in the altitude range between 22 - 30 km.

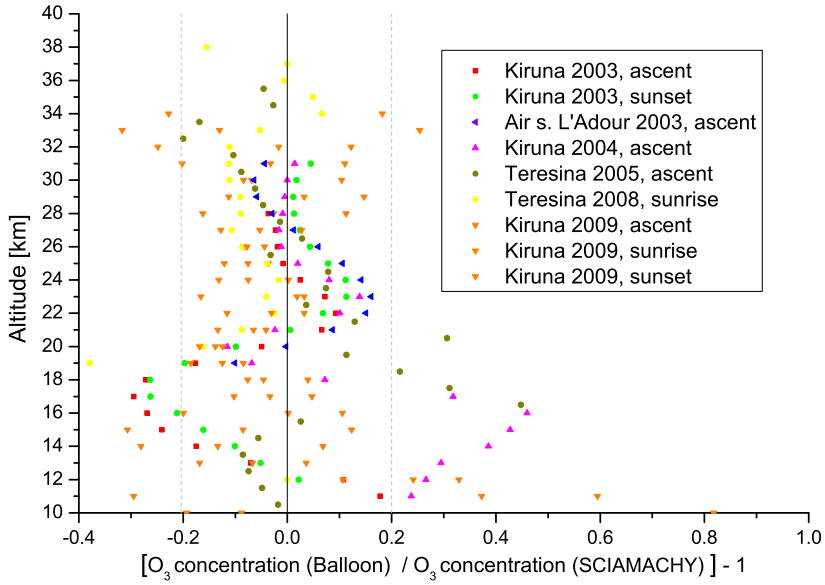

Figure 14.9.: *Comparison of O_3 measurements of the balloon-borne direct sunlight instrument and SCIAMACHY observations for the measurements listed in Figure 14.3. The (ratio - 1) is plotted against the altitude for the different flights listed in Figure 14.3. The plot shows a good agreement within 20% in an altitude range between 32 and 18 km. Below this altitude where satellite resolution and accuracy is significantly lower the values start to scatter.*

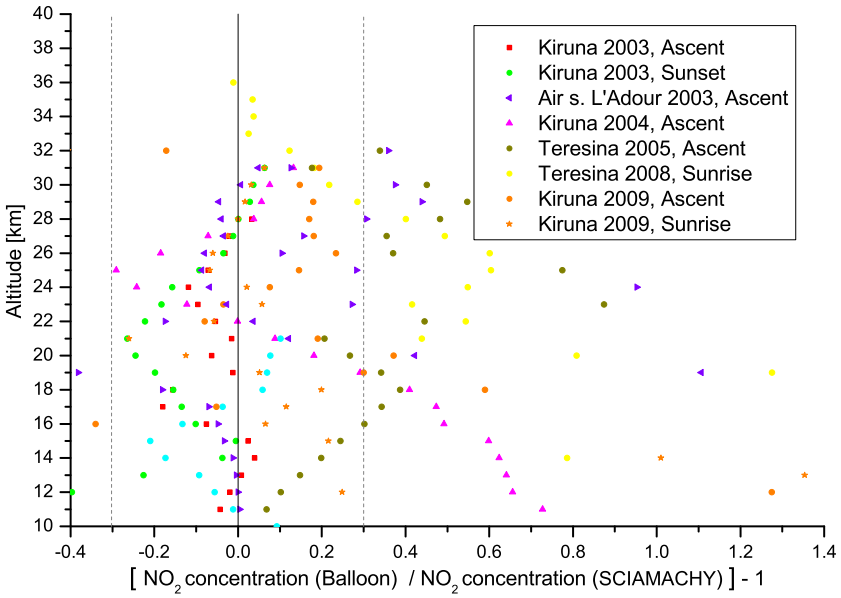

Figure 14.10.: *Comparison of NO_2 measurements from the BigDOAS instrument and SCIAMACHY observations for the measurements listed in Figure 14.3. The (ratio - 1) is plotted against the altitude for the different flights. The plot shows a good agreement within 30% in an altitude range between 32 and 18 km, except for the 2008 flight in Teresina. Below 18 km the satellite accuracy decreases and the values start to scatter.*

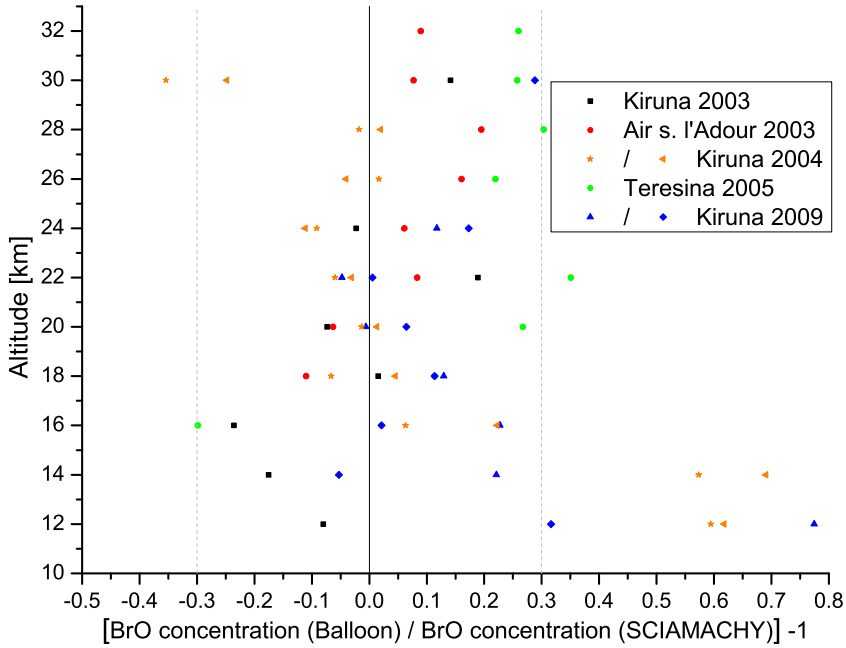

Figure 14.11.: *Comparison of balloon-borne and satellite-borne BrO profiles. The altitude is plotted against the (ratio - 1) for the different flights listed in Figure 14.3. The compared measurements agree within a 30% range down to an altitude of 15 km.*

15. Conclusion and Outlook

For the first time direct sunlight measurements and limb measurements of scattered skylight are combined to test the stratospheric bromine chemistry in high latitudes during fall circulation turn-over in a high NO_X environment. Within the StraPolÉté balloon campaign of 2009 the LPMA/DOAS balloon gondola was deployed, carrying the DOAS balloon instrument for direct sunlight measurements (*Ferlemann et al.* 2000) and the miniDOAS instrument for limb measurements of scattered skylight (*Weidner et al.* 2005). The recorded data is analysed using the DOAS technique introduced by *Platt et al.* (1979). A rigorous study is performed regarding the accuracy of the radiative transfer calculations of the RTM McArtim (*Deutschmann et al.* 2010) as well as their sensitivity towards aerosol extinction. The retrieved slant column densities of O_3, NO_2 and BrO are inverted into trace gas concentration profiles. Simulations of the 1-D chemical model Labmos are initialised with output of the 3-D chemical transport model SLIMCAT (*Chipperfield* 2006) and further constrained by the LPMA/DOAS direct sunlight observations of O_3, NO_2, N_2O, and CH_4. These simulations are compared with the measurements of the two DOAS instruments.
The following key results regarding the stratospheric photochemistry of bromine are obtained:

1. The comparison between measurements and model simulations showed that apparently the ratio of the photolysis rate J_{BrONO_2} and the rate coefficient $k_{[BrO][NO_2]}$ of the formation reaction of $BrONO_2$ deviates from the recommendation of (*Sander et al.* 2011). Such a discrepancy inherently changes the ratio between BrO and $BrONO_2$. The revised $J_{BrONO_2}/k_{[BrO][NO_2]}$ ratio is determined to be $[J_{mod}/J_{JPL}] \,/\, [k_{mod}/k_{JPL}] = (1.69 \pm 0.04)$. This value is larger, but still falls within the uncertainties given by *Sander et al.* (2011) for the two parameters.

2. The direct sunlight measurements recorded during sunrise are sensitive to the photolysis of HOBr, for which the best agreement between measurements and model simulations is found for $[J_{mod}/\, J_{JPL}] = 0.10$, a much slower rate than recommended by e.g., (*Ingham et al.* 1998). However, this values also falls within the uncertainty of the recommendations given by (*Sander et al.* 2011). Future studies should analyse the existing direct sunlight data recorded in the tropics in 2008 during sunrise, because the stratospheric bromine photochemistry system is even more sensitive to J_{HOBr} for this balloon flight.

The revised $J_{BrONO_2}/k_{[BrO][NO_2]}$ ratio has the following consequences for the budget of stratospheric bromine, stratospheric ozone loss and the oxidation capacity of the troposphere:

1. The revised $J_{BrONO_2}/k_{[BrO][NO_2]}$ ratio has adverse effects on the assessment of total stratospheric bromine using the inorganic method, since it largely determines the BrO/Br_Y ratio, where Br_Y is the total amount of stratospheric bromine. For late summer 2009, Br_Y was determined to be (20.3 ± 2.5) ppt (update of *Dorf et al.* (2006) in *WMO* (2011)), using the JPL-2011 recommendations (*Sander et al.* 2011) for J_{BrONO_2} and $k_{[BrO][NO_2]}$. Using the revised $J_{BrONO_2}/k_{[BrO][NO_2]}$ ratio, the total stratospheric Br_Y is 1.4 ppt smaller than previously estimated. However, this revised lower estimate of Br_Y is in better agreement with Br_Y estimates based on the organic method (e.g., *Montzka et al.* (2008), *WMO* (2011), *Brinckmann et al.* (2012)).

2. The consequences for stratospheric ozone due to the revised $J_{BrONO_2}/k_{[BrO][NO_2]}$ ratio is however minor or negligible, since (1) the overcorrection for the BrO/Br_Y ratio leads to an apparent overestimation of stratospheric Br_Y, which (2) is back-corrected when reactive bromine is calculated using the inorganic method (*Salawitch et al.* (2005), *Sinnhuber et al.* (2009)).

3. In the troposphere, where high NO_X meets reactive bromine released by the degradation of organic bromine compounds, a reduced formation of $BrONO_2$ may lead to a longer life-time of ozone-destroying BrO (*Yang et al.* 2005). As a consequence, the revised $J_{BrONO_2}/k_{[BrO][NO_2]}$ ratio may cause an elevated oxidation capacity, i.e. more efficient ozone destruction and a more efficient degradation of organic molecules by their reaction with Br. At the same time, the reduced formation of $BrONO_2$ may reduce the activation of reactive bromine tied to aerosols or in salt deposits (*von Glasow et al.* (2004), *Salawitch* (2006)). Accordingly, the consequences of these findings for ozone and the atmospheric oxidation capacity may largely depend on the specific conditions.

Outlook

Although within the present thesis major achievements have been made regarding the photochemistry and the budget of stratospheric bromine, it is highly recommended to further use existing spectroscopic data taken by our group during past balloon flights, in order to:

1. Rule out remaining uncertainties in the understanding of bromine photochemistry, in particular suspected for the ternary reaction of BrO with NO_2. For this, an important step might come through the analysis of the limb measurements data gathered during the ENRICHED campaign in 2011. During this balloon flight the miniDOAS instrument was deployed on board the MIPAS balloon gondola, which

is capable of measuring $BrONO_2$, and with the Limb measurement of BrO and NO_2 all three educts and products involved in the reaction were monitored.

2. Confirm the findings for J_{HOBr}. Here a detailed analysis of early sunrise (SZA > 90°) data obtained over Teresina, Brazil in June 2008 may help to unravel the HOBr photolysis rate, since in the tropical lower stratosphere (below 25 km) the bromine photochemistry is likely to be dominated by cross reactions of the HO_X and Br_X families, leading to a predominant formation of HOBr.

3. Improve the estimated total stratospheric Br_Y based on inorganic method (e.g., *Dorf et al.* (2006), *WMO* (2011), *McLinden* (2010), *Brinckmann et al.* (2012), *Millán et al.* (2012)).

Inferred from past experiences, the following technical improvements of the method are also highly recommended:

- Regarding McArtim, the previously used number of quadrature trajectories (NQT) should be increased to an NQT of 30,000 in order to improve the accuracy.

- The analysis of the UV limb measurements of the balloon ascent showed that a single pseudo-Ring-absorber might not be sufficient to account for the Ring effect during a balloon ascent. The investigation of limb scans in the UV also showed that a pseudo-Ring-absorber without absorption features from a low altitude might be better suited to account for Ring features in a DOAS fit for high altitude balloon-borne limb measurements of scattered skylight and should be used if available.

- The analysis of the radiance data of the limb scans of the miniDOAS instrument showed that they are well suited to put restrictions on an a priori aerosol extinction profile. Future versions of the retrieval should include a script for the automated retrieval of an aerosol extinction profile using McArtim.

References

Aliwell, S., M. Van Roozendael, P. Johnston, A. Richter, T. Wagner, D. Arlander, J. Burrows, D. Fish, R. Jones, K. Tornkvist, J.-C. Lambert, K. Pfeisticker, and I. Pundt (2002, January). Analysis for BrO in zenith-sky spectra: An intercomparison exercise for analysis improvement. *J. Geophys. Res.,* Vol. 107, No. D14.

Aschmann, J., B.-M. Sinnhuber, M. P. Chipperfield, and R. Hossaini (2011). Impact of deep convection and dehydration on bromine loading in the upper troposphere and lower stratosphere. *Atmospheric Chemistry and Physics,* Vol. 11, No. 6, 2671–2687.

Bates, D. R. and M. Nicolet (1950). Atmospheric hydrogen. *Pup. Astron. Soc. Pacific,* Vol. 62.

Bauer, N. (1997). *Charakterisierung des DOAS-Ballon-Spektrographen zur Bestimmung stratosphaerischer Spurenstoffe*. Diploma thesis, Institut für Umweltphysik, Universität Heidelberg.

Bedjanian, Y., V. Riffault, and G. Poulet (2001). Kinetic Study of the Reactions of BrO Radicals with HO2 and DO2. *The Journal of Physical Chemistry A,* Vol. 105, No. 13, 3167–3175.

Bergmann, L. und Schaefer C. und Raith, W. (2001). *Lehrbuch der Experimentalphysik, Bd.7, Erde und Planeten*. Berlin: Gruyter.

Birner, T. and H. Bönisch (2011). Residual circulation trajectories and transit times into the extratropical lowermost stratosphere. *Atmospheric Chemistry and Physics,* Vol. 11, No. 2, 817–827.

Bishop, F. S. (1979, August). Report on the Progress of Regulations to Protect Stratospheric Ozone. In D. Costle (Ed.), *Report to Congress*. Office of Toxic Substances, 401 M Street, S.W. Washington, D.C: United States Environmental Protection Agency.

Boenisch, H., A. Engel, T. Birner, P. Hoor, D. W. Tarasick, and E. a. Ray (2011). On the structural changes in the Brewer-Dobson circulation after 2000. *Atmos. Chem. Phys.,* Vol. 11, 3937–3948.

Bösch, H. (2002). *Studies of Stratospheric Nitrogen and Iodine Chemistry with Balloon Borne DOAS Measurements*. Phd thesis, Institut für Umweltphysik, Universität Heidelberg.

Bösch, H., C. Camy-Peyret, M. P. Chipperfield, R. Fitzenberger, H. Harder, U. Platt, and K. Pfeilsticker (2003). Upper limits of stratospheric IO and OIO inferred from center-to-limb-darkening-corrected balloon-borne solar occultation visible spectra: Implications for total gaseous iodine and stratospheric ozone. *J. Geophys. Res.,* Vol. 108, No. D15, 4455.

Bösch, H., C. Camy-Peyret, M. P. Chipperfield, R. Fitzenberger, H. Harder, C. Schiller, M. Schneider, T. Trautmann, and K. Pfeilsticker (2001). Comparison of measured and modeled startospheric UV/visible actinic fluxes at large solar zenith angles. *Geophys. Res. Lett.,* Vol. 28, No. 7, 1179–1182.

Bovensmann, H., J. P. Burrows, M. Buchwitz, J. Frerick, S. Nol, V. Rozanov, K. Chance, and A. Goede (1999). SCIAMACHY: Mission Objectives and Measurement Modes. *Journal of Atmospheric Science,* Vol. 56, 127–150.

Brasseur, G. and S. Solomon (2005). *Aeronomy of the middle atmosphere.* Dordrecht, Boston, Lancaster, Tokyo: Springer; Auflage: 3rd rev. and enlarged ed. ISBN-13: 978-1402032844.

Bremen, I. (2012, January). SCIAMACHY viewing geometries. http://www.iup.uni-bremen.de/sciamachy/instrument/modes/index.html.

Brewer, A. W. (1949). Evidence for a world circulation provided by the measurement of helium and water vapor distibution in the stratosphere. *Q. J. R. Meteorol. Soc.,* Vol. 75, 351–363.

Brinckmann, S., A. Engel, H. Bönisch, B. Quack, and E. Atlas (2012). Short-lived brominated hydrocarbons observations in the source regions and the tropical tropopause layer. *Atmospheric Chemistry and Physics,* Vol. 12, No. 3, 1213–1228.

Burkholder, J. B., A. R. Ravishankara, and S. Solomon (1995). UV/visible and IR absorption cross sections of BrONO2. *J. Geophys. Res.,* Vol. 100, No. D8, 16793–16800.

Burrows, J. P., A. Dehn, B. Deters, S. Himmelmann, A. Richter, S. Voigt, and J. Orphal (1999). Atmospheric remote-sensing reference data from GOME: temperature-dependent absorption cross section of ozone in the 231 - 794 nm range. *J. Quant. Spectroscopy and Rad. Transfer,* Vol. 61, 509–517.

Butz, A. (2006). *Case Studies of Stratospheric Nitrogen, Chlorine and Iodine Photochemistry Based on Balloon Borne UV/visible and IR Absorption Spectroscopy.* Phd thesis, Heidelberg University, Germany.

Butz, A., H. Bösch, C. Camy-Peyret, M. Chipperfield, M. Dorf, G. Dufour, K. Grunow, P. Jeseck, S. Kühl, S. Payan, I. Pepin, J. Pukite, A. Rozanov, C. von Savigny, C. Sioris, T. Wagner, F. Weidner, and K. Pfeilsticker (2006). Inter-comparison of stratospheric O_3 and NO_2 abundances retrieved from balloon borne direct sun observations and Envisat/SCIAMACHY limb measurements. *Atmospheric Chemistry and Physics,* Vol. 6, No. 5, 1293–1314.

Butz, A., H. Bösch, C. Camy-Peyret, M. P. Chipperfield, M. Dorf, S. Kreycy, L. Kritten, C. Prados-Román, J. Schwärzle, and K. Pfeilsticker (2009). Constraints on inorganic gaseous iodine in the tropical upper troposphere and stratosphere inferred from balloon-borne solar occultation observations. *Atmospheric Chemistry and Physics,* Vol. 9, No. 18, 7229–7242.

Calvetti, D., S. Morigi, L. Reichel, and F. Sgallari (2000). Tikhonov regularization and the L-curve for large discrete ill-posed problems. *Journal of Computational and Applied Mathematics,* Vol. 123, 423446. ISSN 0377-042.

Camy-Peyret, C., J.-M. Flaud, A. Perrin, C. Rinsland, and A. Goldman (1993). Stratospheric N_2O_5, CH_4 and N_2O profiles from IR solar occultation spectra. *J. Atmos. Chem.,* Vol. 16, 31–40.

Camy-Peyret, C., P. Jeseck, T. Hawat, G. Durry, G. Berubeé, L. Rochette, and D. Huguenin (1995). The LPMA balloon borne FTIR spectrometer for remote sensing of the atmospheric constituents. In *12th ESA Symposium on Rocket and Balloon Programmes and Related Research.*

Chance, K. and R. J. D. Spurr (1997). Ring effect studies; Rayleigh scattering, including molecular parameters for rotational Raman scattering and the Fraunhofer spectrum. *Appl. Opt.,* Vol. 36, 5224–5230.

Chapman, S. (1930). On ozone and atomic oxygen in the upper atmosphere. *Phil. Mag.,* Vol. 10.

Chipperfield, M. P. (2006). New Version of the TOMCAT/SLIMCAT Off-Line Chemical Transport Model: Intercomparison of Stratospheric Tracer Experiments. *Q. J. Roy. Meteorol. Society,* Vol. 132, No. 617, 1179–1203.

Chipperfield, M. P., W. Feng, and M. Rex (2005). Arctic ozone loss and climate sensitivity: Updated three-dimensional model study. *Geophys. Res. Lett.,* Vol. 32, No. doi:10.1029/2005GL022674, L11813.

Cobos, C. J. and J. Troe (1985). Theory of thermal unimolecular reactions at high pressures. II. Analysis of experimental results. *The Journal of Chemical Physics,* Vol. 83, No. 3, 1010–1015.

Crutzen, P. J. (1970). The influence of nitrogen oxides on the atmospheric ozone content. *Quart. J. Met. Soc.,* Vol. 96.

Dehn, A. (2010). The ENVISAT Atmospheric Chemistry mission (GOMOS, MIPAS and SCIAMACHY) -Instrument status and mission evolution. In *38th COSPAR Scientific Assembly*, Volume 38, pp. 126.

DeMore, W. B., S. P. Sander, D. M. Golden, R. F. Hampson, M. J. Kurylo, C. J. Howard, A. R. Ravishankara, C. E. Kolb, and M. J. Molina (1997). Chemical kinetics and photochemical data for use in statospheric modeling. *Technical Report, NASA/JPL Publication,* , No. 97-4.

Dessler, A. (2002). The effect of deep, tropical convection on the tropical tropopause layer. *Journal of Geophysical Research,* Vol. 107, No. 5, 4033.

Deters, B., J. P. Burrows, and J. Orphal (1998). UV-visible absorption cross sections of bromine nitrate determined by photolysis of BrONO2/Br2 mixtures. *J. Geophys. Res.,* Vol. 103, No. D3, 35633570.

Deutschman, T. (2011). Simulated radiances for wavelength dependent scattered skylight measurements. Personal Communication.

Deutschmann, T. (2008). *Atmospheric Radiative Transfer Modelling with Monte Carlo Methods*. Diploma thesis, Institut für Umweltphysik, Universität Heidelberg.

Deutschmann, T., S. Beirle, U. Frieß, M. Grzegorski, C. Kern, L. Kritten, U. Platt, J. Puķīte, T. Wagner, B. Werner, and K. Pfeilsticker (2010). The Monte Carlo Atmospheric Radiative Transfer Model McArtim: Introduction and Validation of Jacobians and 3D Features. *Journal of Quantitative Spectroscopy and Radiative Transfer,* Vol. 112, No. 6, 11191137.

Dobson, G. M. B. (1956). Origin and distribution of the polyatomic molecules in the atmosphere. *Proc. R. Soc. London A,* Vol. 236, 187–193.

Dorf, M. (2005). *Investigation of Inorganic Stratospheric Bromine using Balloon-Borne DOAS Measurements and Model Simulations*. Phd thesis, Institut fuer Umweltphysik, University of Heidelberg.

Dorf, M. (Ed.) (2009, June). *Update on Envisat/SCIMACHY Validation with Balloon-borne DOAS instruments: Comparison of O3, NO2 and BrO Profiles*, Number ESA SP-671. European Space Agency. Proceedings of the 19th ESA Symposium on European Rocket and Ballon Programmes and Related Research.

Dorf, M., H. Bösch, A. Butz, C. Camy-Peyret, M. P. Chipperfield, A. Engel, F. Goutail, K. Grunow, F. Hendrick, S. Hrechanyy, B. Naujokat, J.-P. Pommereau, M. Van Roozendael, C. Sioris, F. Stroh, F. Weidner, and K. Pfeilsticker (2006). Balloon-borne stratospheric BrO measurements: comparison with Envisat/SCIAMACHY BrO limb profiles. *Atmospheric Chemistry and Physics,* Vol. 6, No. 9, 2483–2501.

Dorf, M., J. Butler, A. Butz, C. Camy-Peyret, M. Chipperfield, L. Kritten, S. Montzka, B. Simmes, F. Weidner, and K. Pfeilsticker (2006). Long-term observations of stratospheric bromine reveal slow down in growth. *Geophys. Res. Lett,* Vol. 33, No. L24803.

Dorf, M., A. Butz, C. Camy-Peyret, M. P. Chipperfield, L. Kritten, and K. Pfeilsticker (2008). Bromine in the tropical troposphere and stratosphere as derived from balloon-borne BrO observations. *Atmospheric Chemistry and Physics,* Vol. 8, No. 23, 7265–7271.

Drouin, M. (2012, January). Strapolete Website. http://strapolete.cnrs-orleans.fr/.

Dufour, G., S. Payan, F. Lefèvre, G. Berthet, M. Eremenko, A. Butz, P. Jeseck, Y. Te, K. Pfeilsticker, and C. Camy-Peyret (2005). 4D comparison method to study NO_y partitioning in summer polar stratosphere. Influence of aerosol burden. *Atmos. Chem. Phys.,* Vol. 5, 919–926.

Erle, F., A. Grendel, D. Perner, U. Platt, and K. Pfeilsticker (1998). Evidence of heterogeneous bromine chemistry on cold stratospheric sulphate aerosols. *Geophys. Res. Lett.,* Vol. 25, No. 23, 4329PP.

Farman, J. C., B. G. Gardiner, and J. D. Shanklin (1985). Large losses of total ozone in Antarctica reveal seasonal ClO_x/NO_x interaction. *Nature,* Vol. 315, 207–210.

Ferlemann, F., N. Bauer, R. Fitzenberger, H. Harder, H. Osterkamp, D. Perner, U. Platt, M. Scheider, P. Vradelis, and K. Pfeilsticker (2000). Differential optical absorption spectroscopy instrument for stratospheric balloon-borne trace gas studies. *Appl. Opt.,* Vol. 39, 2377–2386.

Ferlemann, F., C. Camy-Peyret, R. Fitzenberger, H. Harder, T. Hawat, H. Osterkamp, M. Schneider, D. Perner, U. Platt, P. Vradelis, and K. Pfeilsticker (1998). Stratospheric BrO profiles measured at different latitudes and seasons: Instrument description, spectral analysis and profile retrieval. *Geophys. Res. Lett.,* Vol. 25, No. 20, 3847–3850.

Finlayson-Pitts, B. J. and J. J. N. Pitts (1999). *Chemistry of the Upper and Lower Atmosphere: Theory, Experiments, and Applications*. New York: Academic Press.

Finlayson-Pitts, B. J. and J. N. J. Pitts (1986). *Atmospheric chemistry : fundamentals and experimental techniques*. New York: Wiley and Sons.

Fish, D. J. and R. L. Jones (1995). Rotational Raman scattering and the Ring effect in zenith-sky spectra. *Geophys. Res. Lett.,* Vol. 22, No. 7, 811–814.

Fitzenberger, R., H. Bösch, C. Camy-Peyret, M. Chpperfield, H. Harder, U. Platt, J. Pyle, T. Wagner, and K. Pfeilsticker (2000). First profile measurement of tropospheric BrO. *Geophys. Res. Lett.,* Vol. 27, 2921–2924.

Frieß, U. (2009). The MS-DOAS software: A multi system DOAS Application. Personal Communication.

Fueglistaler, S., A. Dessler, T. Dunkerton, and I. Folkins (2009). Tropical tropopause layer. *Reviews of Geophysics,* Vol. 47, No. RG1004, 31pp.

Gettelman, A., P. Hoor, L. Pan, W. Randel, M. Hegglin, and T. Birner (2011). The Extratropical Upper Troposphere and Lower Stratosphere. *Reviews of Geophysics,* Vol. 49, No. RG3003, 31PP.

Gilbert, R. G., K. Luther, and J. Troe (1983). Theory of Thermal Unimolecular Reactions in the Fall-off Range. II. Weak Collision Rate Constants. *Berichte der Bunsengesellschaft für physikalische Chemie,* Vol. 87, No. 2, 169–177.

Gomer, T., F. Brauers, F. Heintz, J. Stutz, and U. Platt (1995). MFC, User Manual, Version 1.98. *Institut für Umweltphysik, Universität Heidelberg,.*

Gottwald, M. (2010). *SCIAMACHY - Exploring the Changing Earth's Atmosphere*. Springer. ISBN:978-9048198955.

Grainger, J. F. and J. Ring (1962). Anomalous Fraunhofer line profiles. *Nature,* Vol. 193, No. 762.

Graphics, P. (2012, January). PSD Graphics Worldmap Background. http://www.psdgraphics.com/backgrounds/world-map-background/.

Gray, D. F. (2008). *The Observation and Analysis of Stellar Photospheres*. Dordrecht, Boston, Lancaster, Tokyo: Cambridge University Press. 3rd Edition.

Grunow, K. (2009). *Anwendung von Trajektorien zur ENVISAT-Validierung und zur Untersuchung der Luftmassenherkunft in der Stratosphäre*. Phd thesis, FB Geowissenschaften, FU Berlin.

Gurlit, W., H. Bösch, H. Bovensmann, J. Burrows, A. Butz, C. Camy-Peyret, M. Dorf, K. Gerilowski, A. Lindner, S. Noel, U. Platt, F. Weidner, and K. Pfeilsticker (2005). The UV-A and visible solar irradiance spectrum: Inter-comparison of absolutely calibrated, spectrally medium resolved solar irradiance spectra from balloon- and satellite-borne measurements. *Atmos. Chem. Phys.,* Vol. 5, 1879–1890.

Hanke, M. (1996). Limitations of the L-curve method in ill-posed problems. *BIT Numerical Mathematics,* Vol. 36, 287–301. 10.1007/BF01731984.

Hansen, P. (1994). Regularization Tools: A Matlab package for analysis and solution of discrete ill-posed problems. *Numerical Algorithms,* Vol. 6, 1–35. 10.1007/BF02149761.

Hansen, P. C. (1992, December). Analysis of Discrete Ill-Posed Problems by Means of the L-Curve. *SIAM Review,* Vol. 34, No. 4, 561–580. URL: http://www.jstor.org/stable/2132628.

Hanson, D. (2003). Reactivity of $BrONO_2$ and HOBr on sulfuric acid solutions at low temperatures. *Jour. of Geophys. Res.,* Vol. 108, No. 4239, 11PP.

Hanson, D. and A. R. Ravishankara (1995). Heterogeneous chemistry of bromine species in sulfuric acid under stratospheric conditions. *Jour. of Geophys. Res.,* Vol. 22, No. 4, 385.

Harder, H., H. Bösch, C. Camy-Peyret, M. Chpperfield, R. Fitzenberger, S. Payan, D. Perner, U. Platt, B.-M. Sinnhuber, and K. Pfeilsticker (2000). Comparison of measured and mod-

eled Stratospheric BrO: implications for the total amount of stratospheric bromine. *Geophys. Res. Lett.,* Vol. 27, No. 22, 3695–3698.

Harder, H., C. Camy-Peyret, F. Ferlemann, R. Fitzenberger, T. Hawat, H. Osterkamp, M. Schneider, D. Perner, U. Platt, P. Vradelis, and K. Pfeilsticker (1998). Stratospheric BrO profiles measured at different latitudes and seasons: atmospheric observations. *Geophys. Res. Lett.,* Vol. 25, No. 20, 3843–3846.

Harder, J. W., J. W. Brault, P. V. Johnston, and G. H. Mount (1997). Temperature dependent NO_2 cross sections at high spectral resolution. *J. Geophys. Res.,* Vol. 102, No. D3, 3861–3879.

Hauchecorne, A., S. Godin, M. Marchand, S. Heese, and C. Souprayen (2002). Quantification of the transport of chemical constituents from the polar vortex to midlatitudes in the lower stratosphere using the high-resolution advection model MIMOSA and effective diffusivity. *J. Geophys. Res.s,* Vol. 107, No. 13PP., 2269–2286.

Herman, C., A. Vandaele, and M. Carleer (1999). update of: Absorption cross-sections of atmospheric constituents: NO2, O2, and H2O. *Environ Sci. Pollut. Res. Int.,* Vol. 6(3):151-8.

Holton, J. R., P. H. Haynes, M. E. McIntyre, A. R. Douglass, R. B. Rood, and L. Pfister (1995). Stratosphere-troposphere exchange. *Reviews of Geophysics,* Vol. 33, 403–439.

Hossaini, R., M. P. Chipperfield, W. Feng, T. J. Breider, E. Atlas, S. A. Montzka, B. R. Miller, F. Moore, and J. Elkins (2012). The contribution of natural and anthropogenic very short-lived species to stratospheric bromine. *Atmospheric Chemistry and Physics,* Vol. 12, No. 1, 371–380.

Hossaini, R., M. P. Chipperfield, B. M. Monge-Sanz, N. A. D. Richards, E. Atlas, and D. R. Blake (2010). Bromoform and dibromomethane in the tropics: a 3-D model study of chemistry and transport. *Atmospheric Chemistry and Physics,* Vol. 10, No. 2, 719–735.

Houghton, J., J. Ding, D. J. Griggs, M. Noguer, P. J. van der Linden, X. Dai, K. Maskell, and C. A. Johnson (2001). *Climate Change 2001: The Scientific Basis.* Cambridge University Press.

Ingham, T., D. Bauer, J. Landgraf, and J. N. Crowley (1998). Ultraviolet-Visible Absorption Cross Sections of Gaseous HOBr. *The Journal of Physical Chemistry A,* Vol. 102, No. 19, 3293–3298.

Jacobson, M. (2005). *Fundamentals of atmospheric modeling.* Cambridge Univ. Pr. ISBN:978-0521548656.

Jeseck, P. (1995). *Interfromtrie de Fourier, sous ballon stratosphrique, en vue de la mesure distance par spectroscopie infrarouge en absorption et haute rsolution spectrale, des constituants minoritaires de latmosphre terrestre.* Phd thesis, Universit Pierre et Marie Curie, Paris VII.

Johnston, H. S. (1971). Reduction of stratospheric ozone by nitrogen oxide catalysts from supersonic transport exhaust. *Science,* Vol. 173.

Jørgensen, J. H. (2009). *Knowledge-Based Tomography Algorithms.* Master thesis, Informatics and Mathematical Modelling, Technical University of Denmark. IMM-M.Sc.-2009-55.

Junge, C. E. (1961). Vertical profiles of condensation nuclei in the stratosphere. *J. Meterol,* Vol. 18, 501–509.

Kawa, S. R., R. S. Stolarski, P. A. Newman, A. R. Douglass, M. Rex, D. J. Hofmann, M. L. Santee, and K. Frieler (2009). Sensitivity of polar stratospheric ozone loss to uncertainties in chemical reaction kinetics. *Atmospheric Chemistry and Physics,* Vol. 9, No. 22, 8651–8660.

Kopp, G. and J. L. Lean (2011). A new, lower value of total solar irradiance: Evidence and climate significance. *Geophys. Res. Lett.,* Vol. 38, No. L01706, 7PP.

Kraus, S. (2006). *DOASIS - A Framework Design for DOAS*. Phd thesis, Heidelberg University, Germany.

Kreycy, S. (2007). *Vorbereitende Manahmen zur hochgenauen Vermessunge des BrO Absorptionsquerschnittes im Ultravioletten*. Diploma thesis, Institut für Umweltphysik, Universität Heidelberg.

Kreycy, S. (Ed.) (2009, November). *Envisat/SCIMACHY Validation with the LPMA/DOAS/miniDOAS Balloon Gondola: Comparison of O3, NO2 and BrO Profiles*, Number ESA SP-676. European Space Agency. Proceedings of Atmospheric Science Conference.

Kritten, L. (2009). *Time dependent profiling of UV/vis absorbing radicals by balloon-borne spectroscopic Limb measurements and implications for stratospheric photochemistry*. Phd thesis, Institut für Umweltphysik, Universität Heidelberg.

Kritten, L., A. Butz, M. Dorf, T. Deutschmann, S. Kühl, C. Prados-Roman, J. Pukite, A. Rozanov, R. Schofield, and K. Pfeilsticker (2010). Time dependent profile retrieval of UV/vis absorbing radicals from balloon-borne limb measurements a case study on NO_2 and O_3. *Atmospheric Measurement Techniques,* Vol. 3, No. 4, 933–946.

Krysztofiak, G. (2011, December). Detection in the summer polar stratosphere of air plume pollution from East Asia by balloon-borne in situ CO measurement. Poster, AGU Fall Meeting.

Lary, D. J. (1996). Gas phase atmospheric bromine chemistry. *Jour. of Geophys. Res.,* Vol. 101, 1505–1516.

Lary, D. J., M. P. Chipperfield, R. Toumi, and T. Lenton (1996). Heterogeneous atmospheric bromine chemistry. *Jour. of Geophys. Res.,* Vol. 101, 1489–1504.

Liang, Q., R. S. Stolarski, S. R. Kawa, J. E. Nielsen, A. R. Douglass, J. M. Rodriguez, D. R. Blake, E. L. Atlas, and L. E. Ott (2010). Finding the missing stratospheric Br_y: a global modeling study of $CHBr_3$ and CH_2Br_2. *Atmospheric Chemistry and Physics,* Vol. 10, No. 5, 2269–2286.

Marshak, A. and A. Davis (2010). *3D Radiative Transfer in Cloudy Atmospheres (Physics of Earth and Space Environments*. Springer. ISBN:978-3642063039.

McLinden, C. A., e. a. (2010). Odin/OSIRIS observations of stratospheric BrO: Retrieval methodology, climatology, and inferred Br_y. *J. Geophys. Res.,* Vol. 115, No. D15308, 19PP.

Meister, A. and C. Voemel (2011). *Numerik linearer Gleichungssysteme: Eine Einfuehrung in moderne Verfahren. Mit MATLAB-Implementierungen*. Vieweg und Teubner Verlag. ISBN:978-3834815507.

Mie, G. (1908). Beiträge zur Optik trüber Medien, speziell kolloidaler Metallösungen. *Annalen der Physik,* Vol. 25, 377–445.

Millán, L., N. Livesey, W. Read, L. Froidevaux, D. Kinnison, R. Harwood, I. A. MacKenzie, and M. P. Chipperfield (2012). New Aura Microwave Limb Sounder observations of BrO and implications for Br_y. *Atmospheric Measurement Techniques Discussions,* Vol. 5, No. 1, 325–350.

Molina, M. J. and F. S. Rowland (1974). Stratospheric sink for chlororflourmethanes: chlorine atom-catalysed destruction of ozone. *Nature,* Vol. 249, 810–812.

Montzka, S., J. Butler, B. Hall, D. Mondell, and J. Elkins (2003). A decline in tropospheric organic bromine. *J.Geophys.Res.,* Vol. 30, No. 15, 1826–1829.

Montzka, S., J. Daniel, J. Cohen, and K. Vick (2008). Current trends, mixing ratios, and emissions of ozone-depleting substances and their substitutes. In *Trends in Emissions of Ozone-Depleting Substances, Ozone Layer Recovery, and Implications for Ultraviolet Radiation Exposure*, Number 29-78, NOAA National Climatic Data Center, Asheville, NC. Synthesis and Assessment Product 2.4, report by the U.S. Climate Change Science Program and the Subcommittee on Global Change Research, edited by A.R. Ravishankara, M.J. Kurylo, and C.A. Ennis, 29-78, Department of Commerce.

NASA (2012a, January). Nasa Image Catalog. http://www.nasa.gov/multimedia/imagegallery.html.

NASA (2012b, January). SAGE III Database. http://www.eosweb.larc.nasa.gov/PRODOCS/sage3/table/sage3.html.

NIST (2012, January). NIST Atomic Spectra Database. http://www.nist.gov/pml/data/asd.cfm.

NOAA and NWS (2010, August). National Oceanic and Atmospheric Administration (NOAA). National Weather Service: Jet Stream. http://www.srh.noaa.gov/jetstream/global/jet.htm.

OceanOptics (2012, January). OceanOptics. http://www.oceanoptics.com/Products/benchoptions-qe.asp.

Petty, A. (2012, January). The Periodic Table of the Light. http://www.alexpetty.com/2011/07/20/the-periodic-table-of-the-light.

Pfeilsticker, K., H. Bösch, C. Camy-Peyret, R. Fitzenberger, H. Harder, and H. Osterkamp (2000). First atmospheric profile measurements of the atmospheric UV/vis O_4 absorption bands strength: Implications for the spectroscopy and the formation enthalpy of the O_2–O_2 dimer. *Geophys. Res. Lett.,* Vol. 24, No. 28, 45954598.

Platt, U., D. Perner, and H. Pätz (1979). Simultaneous measurement of atmospheric CH_2O, O_3 and NO_2 by differential optical absorption. *J. Geophys. Res.,* Vol. 84, 6329–6335.

Platt, U., D. Perner, and H. W. Pätz (1979). Simultaneous Measurement of Atmospheric CH_2O, O_3 and NO_2 by Differential Optical Absorption. *J. Geophys. Res.,* Vol. 84, 6329–6335.

Platt, U. and J. Stutz (2008). *Differential Optical Absorption Spectroscopy (DOAS), Principle and Applications*. Number ISBN 3-340-21193-4. Heidelberg: Springer Verlag.

Polvani, L. M., A. H. Sobel, and D. W. Waugh (2010). *The Stratosphere: Dynamics, Transport, and Chemistry*, Volume 190. Amer. Geophys. Union.

Poulet, N. and N. Huret (2011, August). MIMOSA Model: Potential Vortitcity and Temperature Maps. http://ether.ipsl.jussieu.fr/ether/pubipsl/mimosa_uk.jsp.

Prados-Roman, C. (2010). *Aircraft-borne spectroscopic limb measurements of trace gases absorbing in the UV-A spectral range. - Investigations of bromine monoxide in the Arctic troposphere.* Phd thesis, Institut fuer Umweltphysik, University of Heidelberg.

Pundt, I., J.-P. Pommereau, C. Phillips, and E. Latelin (1998). Upper limit of iodine oxide in the stratosphere. *J. Atmos. Chem.,* Vol. 30, 173–185.

Reeves, C., W. Sturges, G. Sturrock, K. Preston, D. Oram, J. Schwander, R. Mulvaney, J.-M. Barnola, and J. Chappellaz (2005). Trends of halon gases in polar firn air: implications for their emission distributions. *Atmos. Chem. Phys.,* Vol. 5, No. SRef-ID: 1680-7324/acp/2005-5-2055, 2055–2064.

Renard, J. (2008). Vertical distribution of the different types of aerosols in the stratosphere: Detection of solid particles and analysis of their spatial variability. *Journal of Geophyical Research,* Vol. 113, 17pp.

Renard, J.-B., C. Thaury, J.-L. Mineau, and B. Gaubicher (2010). Small-angle light scattering by airborne particulates: Environnement S.A. continuous particulate monitor. *Measurement Science and Technology,* Vol. 21, No. 8, 085901.

Rodgers, C. (2000). *Inverse methods for atmospheric sounding*. Singapore, New Jersey, London, Hongkong: World Scientific.

Roedel, W. (2011). Physik unserer Umwelt: Die Atmoshäre. *Springer-Verlag, Berlin, Heidelberg, Tokyo,* , No. 4. Auflage.

Roscoe, H. K., D. J. Fish, and R. L. Jones (1996). Interpolation errors in the UV-visible spectroscopy for stratospheric sensing: implications for sensitivity, spectral resolution, and spectral range. *Appl. Opt.,* Vol. 35, 427–432.

Rothman, L., A. Barbe, D. Benner, L. Brown, C. Camy-Peyret, M. Carleer, K. Chance, C. Clerbaux, V. Dana, V. Devi, A. Fayt, J.-M. Flaud, R. Gamache, A. Goldman, D. Jacquemart, K. Jucks, W. Lafferty, J.-Y. Mandin, S. Massie, V. Nemtchinov, D. Newnham, A. Perrin, C. Rinsland, J. Schroeder, K. Smith, M. Smith, K. Tang, R. Toth, J. Vander Auwera, P. Varanasi, and K. Yoshino (2003). The HITRAN Molecular Spectroscopic Database: Edition of 2000 Including Updates through. *J. Quant. Spec. and Rad. Transf.,* Vol. 82, 1–4.

Rozanov, A., H. Bovensmann, A. Bracher, S. Hrechanyy, V. Rozanov, M. Sinnhuber, F. Stroh, and J. Burrows (2005). NO2 and BrO vertical profile retrieval from SCIAMACHY limb measurements: Sensitivity studies. *Advances in Space Research,* Vol. 36, No. 5, 846 – 854. Atmospheric Remote Sensing: Earths Surface, Troposphere, Stratosphere and Mesosphere - I.

Rozanov, A., S. Kühl, A. Doicu, C. McLinden, J. Pukite, H. Bovensmann, J. Burrows, T. Deutschmann, M. Dorf, F. Goutail, K. Grunow, F. Hendrick, M. von Hobe,

S. Hrechanyy, G. Lichtenberg, K. Pfeilsticker, J. P. Pommereau, M. Van Roozendael, F. Stroh, and T. Wagner (2010). BrO vertical distributions from SCIAMACHY limb measurements: comparison of algorithms and retrieval results. *Atmospheric Measurement Techniques Discussions,* Vol. 3, No. 6, 5079–5178.

Salawitch, R. (2006). Atmospheric chemistry: Biogenic bromine. *Nature,* Vol. 439, No. 5, 275–277.

Salawitch, R. J., D. K. Weisenstein, L. J. Kovalenko, C. E. Sioris, P. O. Wennberg, K. Chance, M. K. W. Ko, and C. A. McLinden (2005). Sensitivity of ozone to bromine in the lower stratosphere. *Geophys. Res. Lett.,* Vol. 32, No. L05811.

Saltzman, E., M. Aydin, W. J. D. Bruyn, D. B. King, and S. Yvon-Lewis (2004). Methyl bromide in preindustrial air: Measurements from an Antartic ice core. *J. Geophys. Res.,* Vol. 109, No. D05301, doi:10.1029.

Sander, S., R. R. Friedl, J. Barkern, D. Golden, M. Kurylo, P. Wine, J. Abbat, J. Burkholder, C. Moortgaart, R. Huie, and O. R. E. (2011). Chemical kinetics and photochemical data for use in atmospheric studies. *Technical Report, NASA/JPL Publication,* Vol. 17, No. 10-06.

Sanghavi, S. (2003). *An effcient Mie theory implementation to investigate the influence of aerosols on radiative transfer*. Diploma thesis, Institut für Umweltphysik, Universität Heidelberg.

Schofield, R., S. Fueglistaler, I. Wohltmann, and M. Rex (2011). Sensitivity of stratospheric Br_y to uncertainties in very short lived substance emissions and atmospheric transport. *Atmospheric Chemistry and Physics,* Vol. 11, No. 4, 1379–1392.

Schulte, M. (1996). DAMF V1.22 direct light airmass factors. *Internal paper, Institut für Umweltphysik, Universität Heidelberg,*.

Shindell, D. T., S. Wong, and D. Rind (1997). Interannual Variability of the Antarctic Ozone Hole in a GCM. Part I: The Influence of Tropospheric Wave Variability. *J. Atmos. Sci.,* Vol. 54, 2308–2319.

Short, N. M. (2010, August). NASA: The remote sensing tutorial. http://rst.gsfc.nasa.gov/Sect14/Sect14-1c.html.

Simmes, B. (2007). *Development of a Novel Aircraft-borne DOAS Instrument for UV/visible Limb Observations*. Diploma thesis, Institut für Umweltphysik, Universität Heidelberg.

Sinnhuber, B.-M., N. Sheode, M. Sinnhuber, M. P. Chipperfield, and W. Feng (2009). The contribution of anthropogenic bromine emissions to past stratospheric ozone trends: a modelling study. *Atmospheric Chemistry and Physics,* Vol. 9, No. 8, 2863–2871.

Sioris, C. E., T. Kurosu, R. Martin, and K. Chance (2004). Stratospheric and tropospheric NO_2 observed by SCIAMACHY: first results. *Adv. Space Res.,* Vol. 34, 780–785.

Soller, R., J. M. Nicovich, and P. H. Wine (2002). Bromine Nitrate Photochemistry: Quantum Yields for O, Br, and BrO Over the Wavelength Range 248-355 nm. *The Journal of Physical Chemistry A,* Vol. 106, No. 36, 8378–8385.

Solomon, S., R. R. Garcia, and A. R. Ravishankara (1994). On the role of iodine in ozone depletion. *J. Geophys. Res.,* Vol. 99, No. D10, 20491–20499.

Spencer, J. E. and F. S. Rowland (1998). Bromine nitrate and its stratospheric significance. *J. Phys. Chem.,* Vol. 82, No. 1, 7–10.

Stohl, A., C. Forster, A. Frank, P. Seibert, and G. Wotawa (2005). Technical note: The Lagrangian particle dispersion model FLEXPART version 6.2. *Atmospheric Chemistry and Physics,* Vol. 5, No. 9, 2461–2474.

Stolarski, R. S. and R. D. Rundel (1975). Fluorine Photochemistry in the Stratosphere. *Geophys. Res. Lett.,* Vol. 2, No. 10, 443–444.

Stutz, J. (1996). *Messung der Konzentration troposhärischer Spurenstoffe mittels Differentieller-Optischer-Absorptionsspektroskopie: Eine neue Generation von Geräten und Algorithmen*. Phd thesis, Institut für Umweltphysik, Universität Heidelberg.

Stutz, J. and U. Platt (1996). Numerical analysis and error estimation of Differential Optical Absorption Spectroscopy measurements with least square fits. *Appl. Opt.,* Vol. 30, No. 30, 6041–6053.

Thieblemont, R., N. Huret, Y. Orsolini, and A. a. M.-A. D. Hauchecorne (2010, May). On the dynamical evolution of the polar stratosphere after the vortex breakdown. http://strapolete.cnrs-orleans.fr/bibliography/posters/Thieblemont_Poster_EGU.pdf.

Thomason, L. W. and G. Taha (2003). SAGE III aerosol extinction measurements: Initial results. *Geophys. Res. Lett.,* Vol. 30, No. 1631, 4PP.

Tikhonov, A., V. Arsenin, and F. John (1977). *Solutions of ill-posed problems*. Vh Winston Washington, DC.

Trentmann, J., H. Bovensmann, V. Eyring, R. Mller, and J. P. Burrows (2003). Impact of Accurate Photolysis Calculations on the Simulation of Stratospheric Chemistry. *Journal of Atmospheric Chemistry,* Vol. 44, 225–240.

Troe, J. (1977). Theory of thermal unimolecular reactions at low pressures. I. Solutions of the master equation. *The Journal of Chemical Physics,* Vol. 66, No. 11, 4745–4757.

Troe, J. (1979). Predictive possibilities of unimolecular rate theory. *The Journal of Physical Chemistry,* Vol. 83, No. 1, 114–126.

Uppala, S. e. a. (2005). The ERA-40 re-analysis. *Quartely Journal of the Royal Meterological Society,* Vol. 131, 2961–3012.

Van De Hulst, H. C. (1980). Multiple light scattering. *Academic Press, New York, London, Toronto, Sydney, San Francisco,*.

Van Hulst, H. (1957). *Light scattering by small particles*. Dover Publications, New York.

Van Roozendael, M. and C. Fayt (2000). WinDOAS 2.1. Software user manual. *Belgium Institute for Space Aeronomie (BIRA/IASB),*.

Vandaele, A., C., C. Hermanns, C. Simon, P., M. Carleer, R. Colin, S. Fally, F. Mrienne, M., A. Jenouvrier, and B. Coquart (1998). Measurements of the NO_2 absorption cross section from 42,000–10,000 cm^{-1} (238–1000 nm) at 220 and 294 K. *J. Quant. Spec. and Rad. Transf.,* Vol. 59, 171–184.

Vitt, F. M. and C. H. Jackman (1996). A comparison of sources of odd nitrogen production from 1974 through 1993 in the Earth's middle atmosphere as calculated using a two-dimensional model. *J. Geophys. Res.,* Vol. 101, No. D3, 6729–6739.

Vogel, L. (2011). *Volcanic plumes: Evaluation of spectroscopic measurements, early detection, and bromine chemistry*. Phd thesis, Institut für Umweltphysik, Universität Heidelberg.

Voigt, S., J. Orphal, K. Bogumil, and J. P. Burrows (2001). The temperature dependence (203-293 K) of the absorption cross-sections of O_3 in the 230 - 850 nm region measured by Fourier-transform spectroscopy. *J. of Photochemistry and Photobiology A: Chemistry,* Vol. 143, 1–9.

Voigt, S., J. Orphal, and J. P. Burrows (2002). The Temperature- and Pressure-Dependence of the Absorption Cross-section of NO_2 in the 250-800 nm Region measured by Fourier-Transform Spectroscopy). *J. Photochem. Photobiol. A,* Vol. 149, 1–7.

von Glasow, R., R. von Kuhlmann, M. G. Lawrence, U. Platt, and P. J. Crutzen (2004). Impact of reactive bromine chemistry in the troposphere. *Atmospheric Chemistry and Physics,* Vol. 4, No. 11/12, 2481–2497.

Wagner, T., S. Beirle, and T. Deutschmann (2009). Three-dimensional simulation of the Ring effect in observations of scattered sun light using Monte Carlo radiative transfer models. *Atm. Meas. Tech,* Vol. 2, 113–124.

Wagner, T., J. P. Burrows, T. Deutschmann, B. Dix, C. von Friedeburg, U. Frie, F. Hendrick, K.-P. Heue, H. Irie, H. Iwabuchi, Y. Kanaya, J. Keller, C. A. McLinden, H. Oetjen, E. Palazzi, A. Petritoli, U. Platt, O. Postylyakov, J. Pukite, A. Richter, M. van Roozendael, A. Rozanov, V. Rozanov, R. Sinreich, S. Sanghavi, and F. Wittrock (2007). Comparison of box-air-mass-factors and radiances for Multiple-Axis Differential Optical Absorption Spectroscopy (MAX-DOAS) geometries calculated from different UV/visible radiative transfer models. *Atmospheric Chemistry and Physics,* Vol. 7, No. 7, 1809–1833.

Wahner, A., A. Ravishankara, S. Sander, and R. Friedl (1988, November). Absorption cross section of BrO between 312 and 385 nm at 298 and 223 K. *Chem. Phys. Lett.,* Vol. 152, No. 6, 507–512.

Weidner, F. (2005). *Development and Application of a Versatile Balloon-Borne DOAS Instrument for Skylight Radiance and Atmospheric Trace Gas Profile Measurements*. Phd thesis, Institut für Umweltphysik, Universität Heidelberg.

Weidner, F., H. Bösch, H. Bovensmann, J. Burrows, A. Butz, C. Camy-Peyret, M. Dorf, K. Gerilowski, W. Gurlit, U. Platt, C. von Friedeburg, T. Wagner, and K. Pfeilsticker (2005). Balloon-borne limb profiling of UV/vis skylight radiances, O_3, NO_2, and BrO: technical set-up and validation of the method. *Atmos. Chem. Phys.,* Vol. 5, 1409–1422.

Werner, B. (2009). *Case study of stratospheric limb measurements of O_3, NO_2 and BrO in the polar summer*. Diploma thesis, Institut für Umweltphysik, Universität Heidelberg.

Wilmouth, D. M., T. F. Janisco, N. M. Donahue, and J. G. Anderson (1999). Fourier Transform Ultraviolet Spectroscopy of the $A\,^2\Pi_{3/2} \longleftarrow X\,^2\Pi_{3/2}$ Transition of BrO. *J.Phys.Chem.,A,* Vol. 103, 8935–8945.

WMO (2011). Scientific Assessment of Ozone depletion: 2010, *World Meteorological Organization Global Ozone Research and Monitoring Project, Report 52*. pp. 516PP. World Meteorological Organization: Scientific Assessment Panel of the Montreal Protocol on Substances that Deplete the Ozone Layer.

Wofsy, S. C., M. B. McElroy, and Y. L. Yung (1975). The chemistry of atmospheric bromine. *Geophys. Res. Lett.,* Vol. 2, 215–218.

Yang, X., R. A. Cox, N. J. Warwick, J. A. Pyle, G. D. Carver, F. M. O'Connor, and N. H. Savage (2005). Tropospheric bromine chemistry and its impacts on ozone: A model study. *Jour. of Geophys. Res.,* Vol. 110, No. D23311, 18PP.

Yilmaz, S. (2011). *Retrieval of Atmospheric Aerosol and Trace Gas Vertical Profiles using Multi-Axis Differential Optical Absorption Spectroscopy.* Phd thesis, Institut für Umweltphysik, Universität Heidelberg.

Zellner, Penkett, and Stuart (2001). Global Aspects of Atmospheric Chemistry. *Journal of Atmospheric Chemistry,* Vol. 38, 111–114. 10.1023/A:1026567705031.

A. J-k Plots

Here are all the plots listed, which are used to calculated the slope of the linear fit plotted in Figure 13.19.

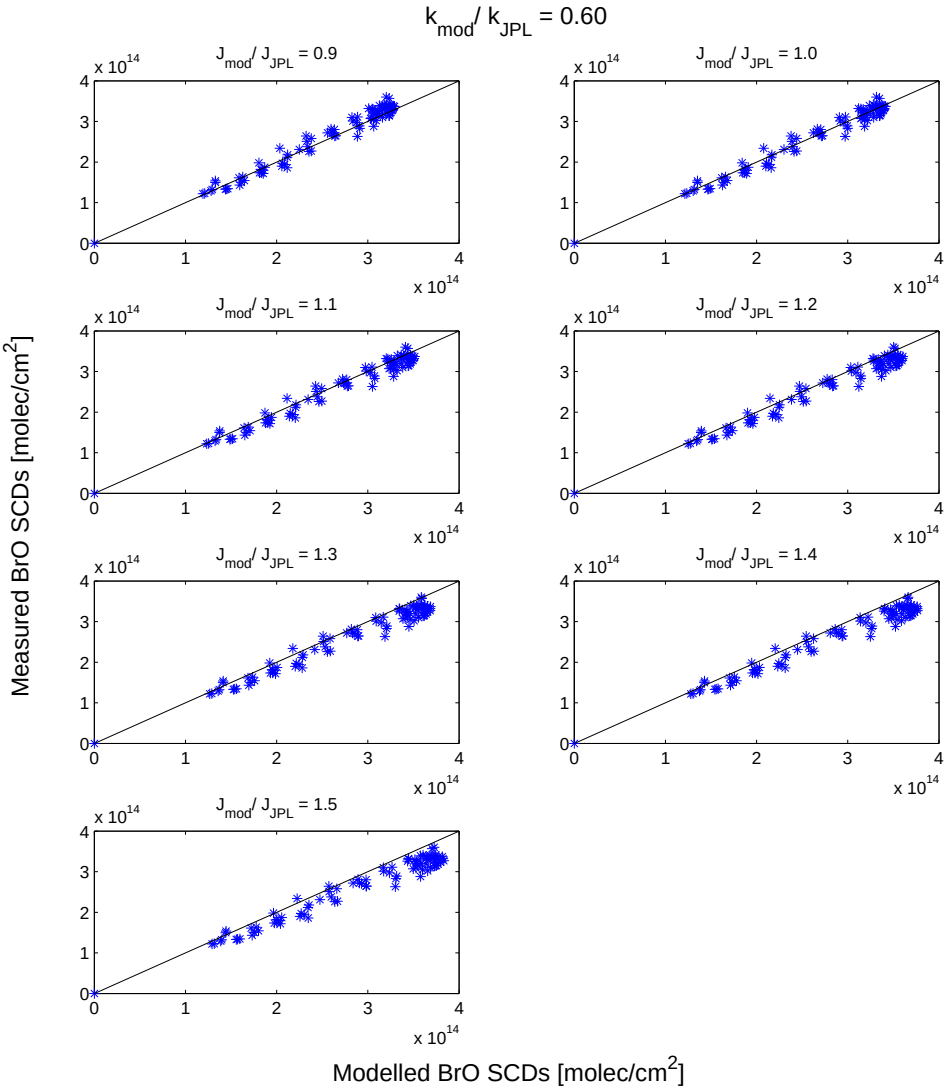

Figure A.1.: *J-k Plots for a* $k_{\mathrm{mod}}/k_{\mathrm{JPL}} = 0.60$

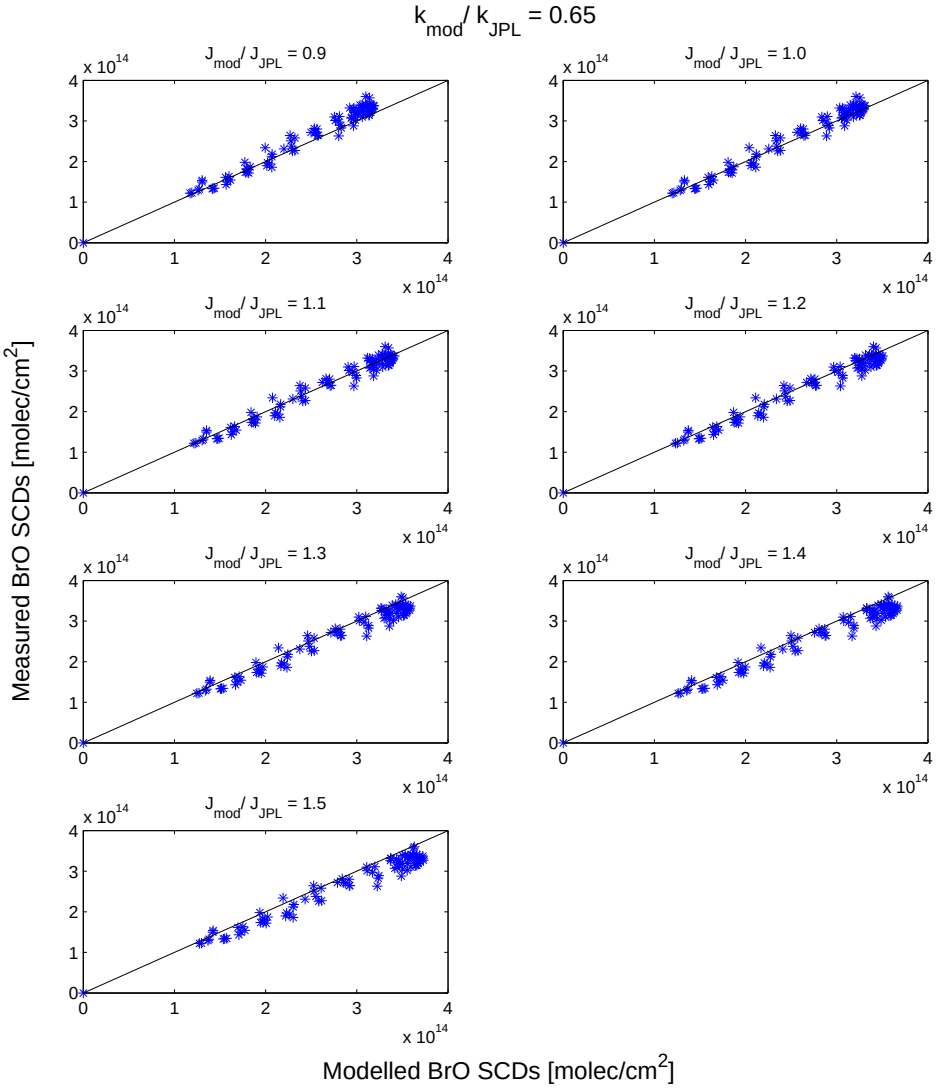

Figure A.2.: *J-k Plots for a* $k_{\mathrm{mod}}/k_{\mathrm{JPL}} = 0.65$

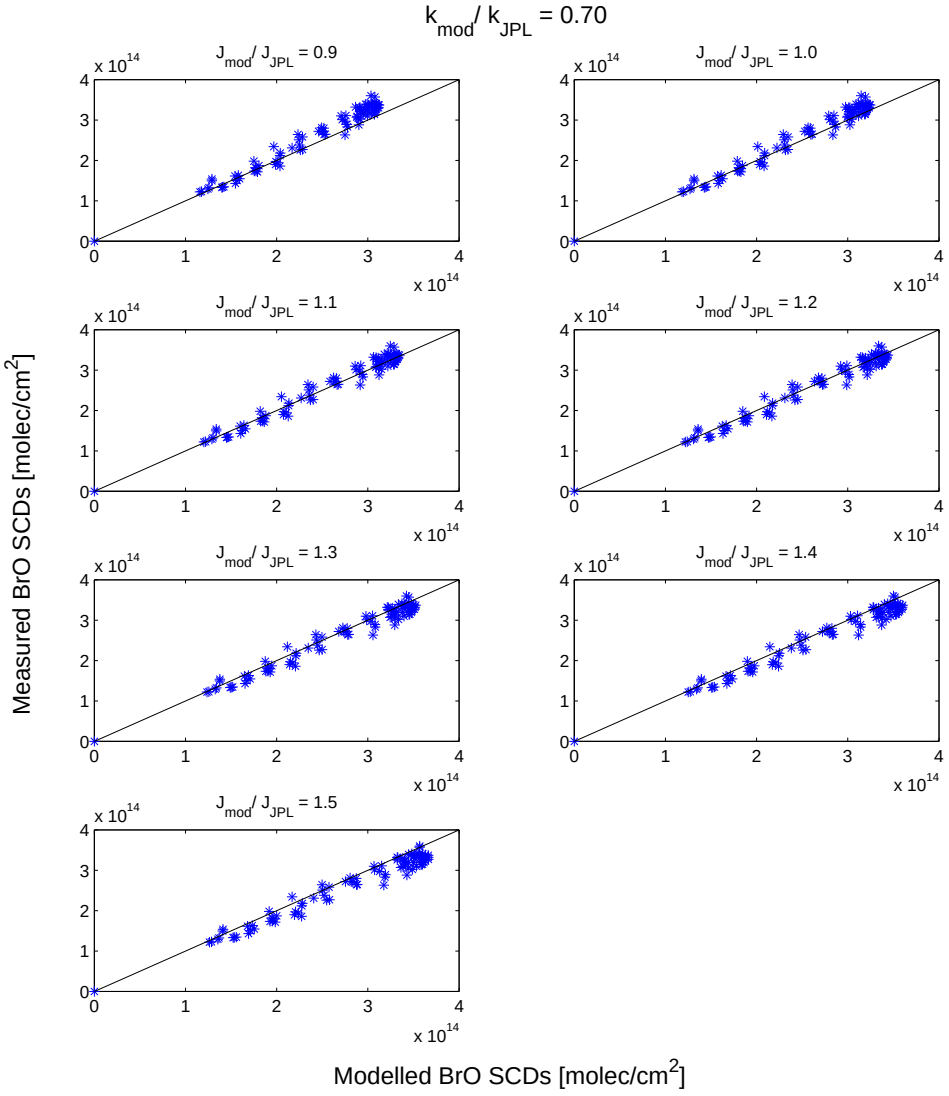

Figure A.3.: *J-k Plots for a* $k_{\mathrm{mod}}/k_{\mathrm{JPL}} = 0.70$

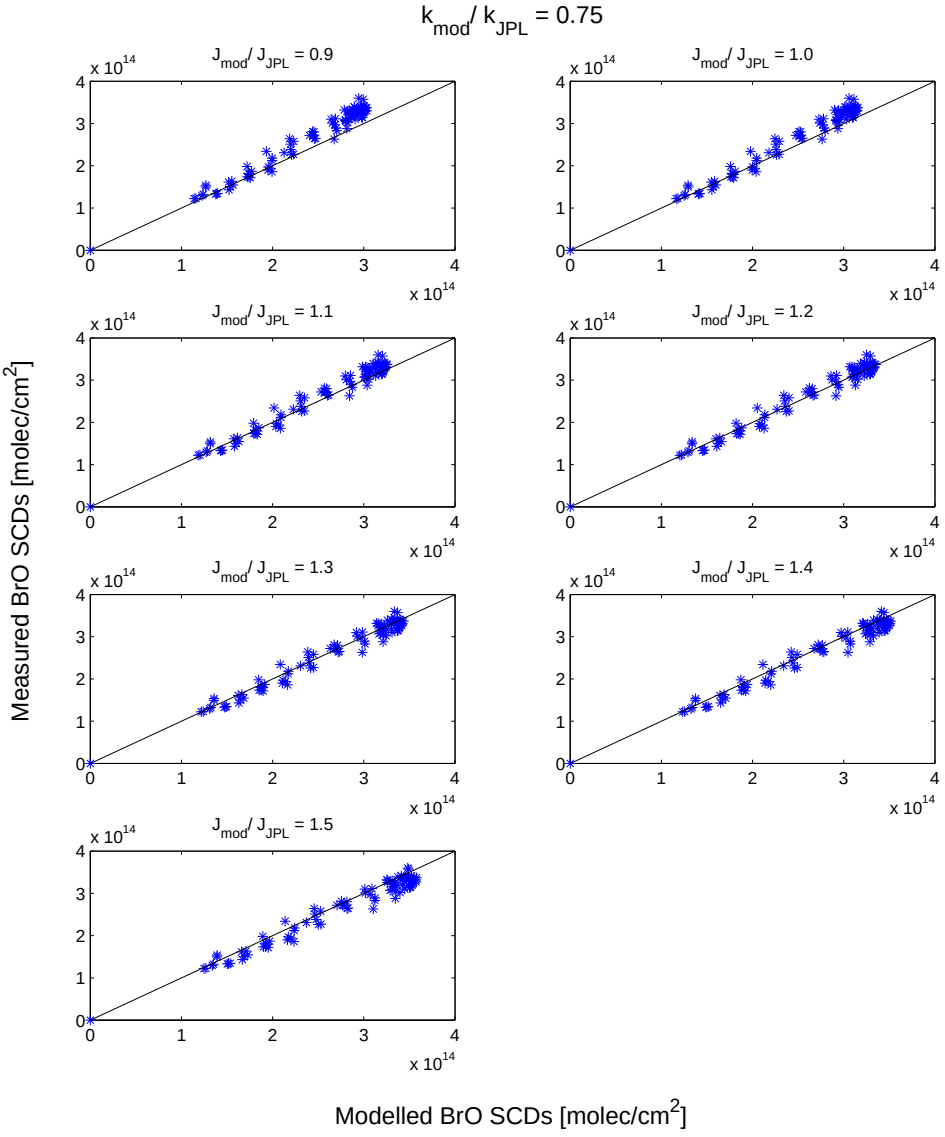

Figure A.4.: *J-k Plots for a* $k_{\mathrm{mod}}/k_{\mathrm{JPL}} = 0.75$

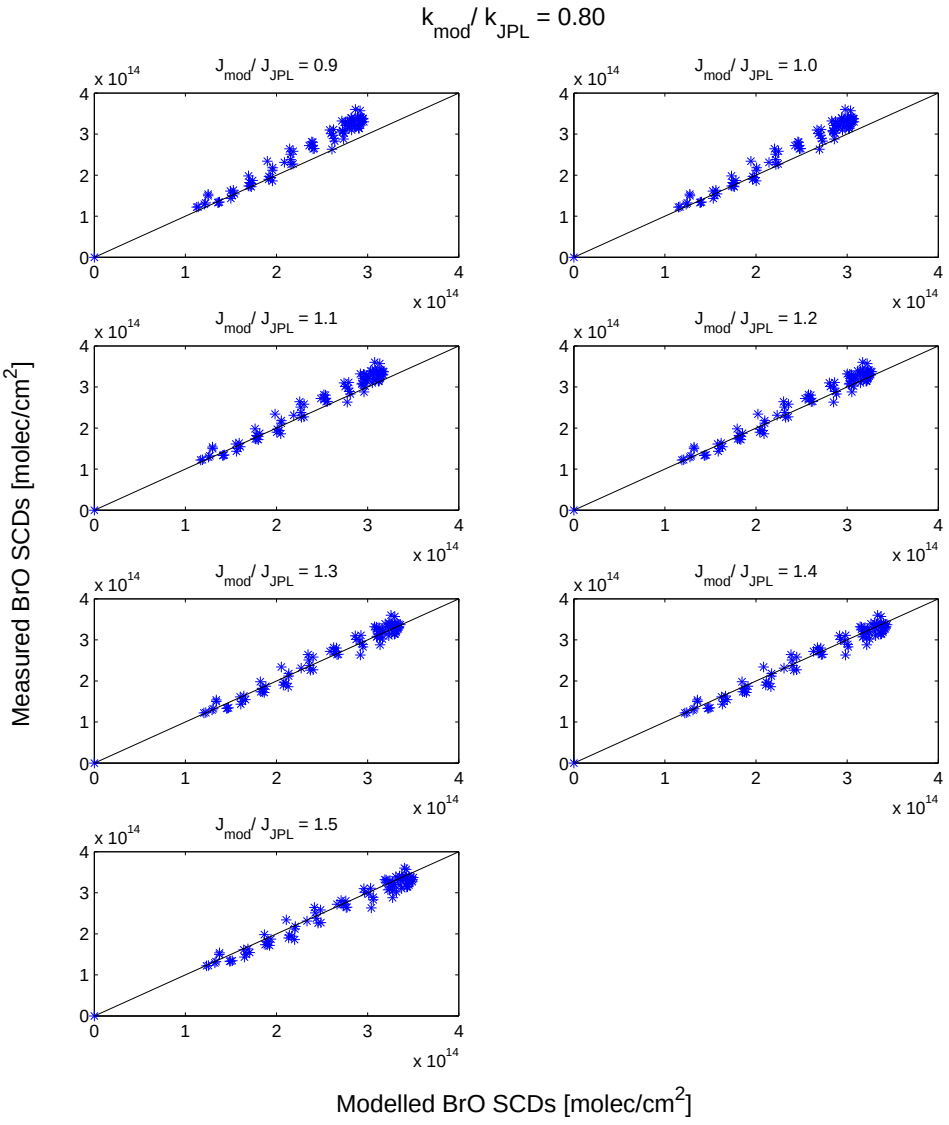

Figure A.5.: *J-k Plots for a* $k_{\mathrm{mod}}/k_{\mathrm{JPL}} = 0.80$

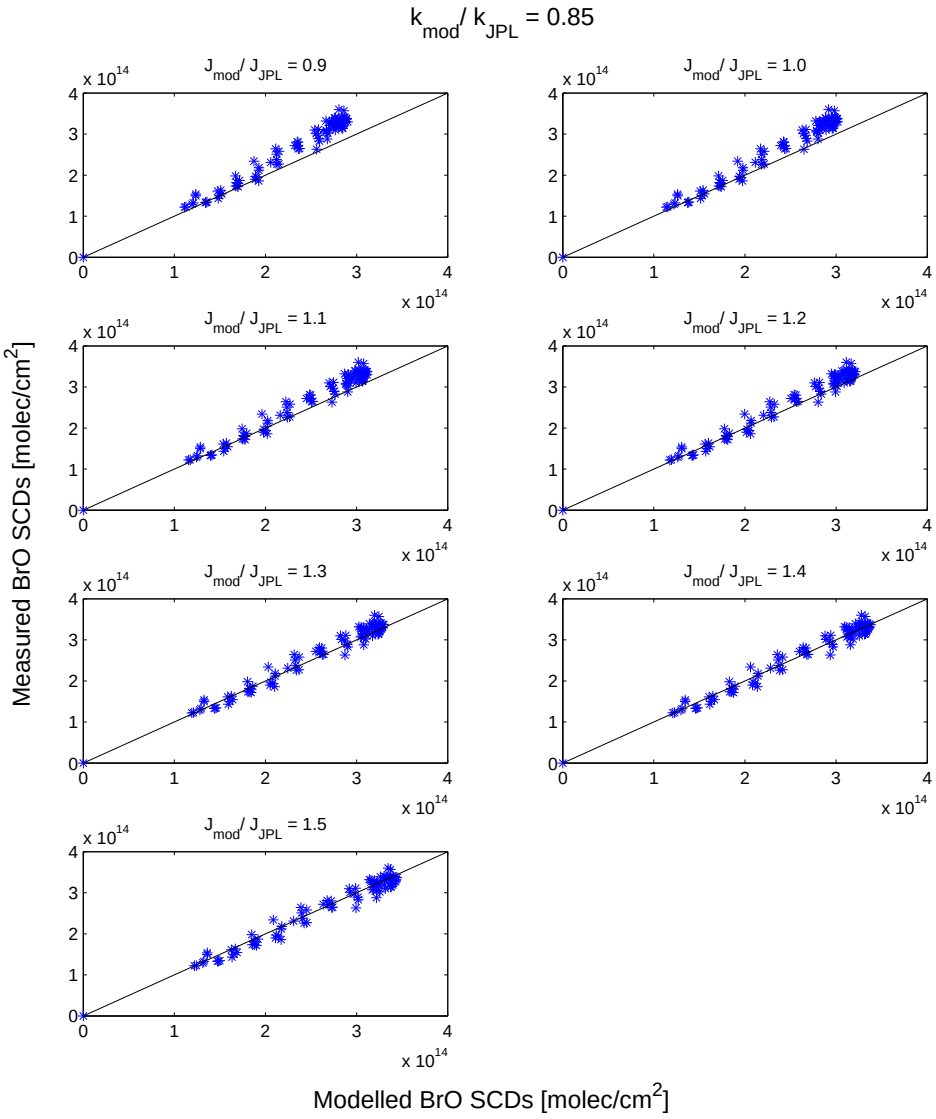

Figure A.6.: *J-k Plots for a* $k_{\mathrm{mod}}/k_{\mathrm{JPL}} = 0.85$

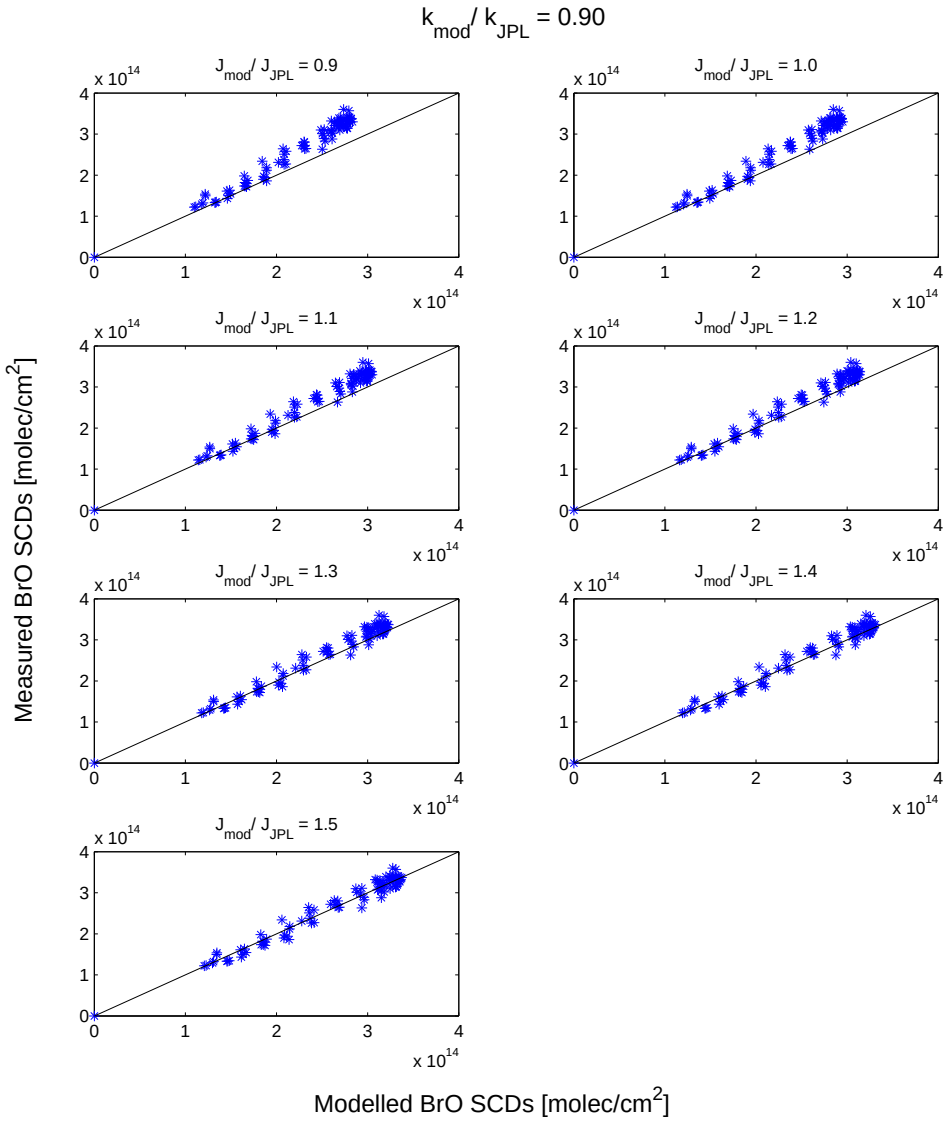

Figure A.7.: *J-k Plots for a* $k_{\mathrm{mod}}/k_{\mathrm{JPL}} = 0.90$

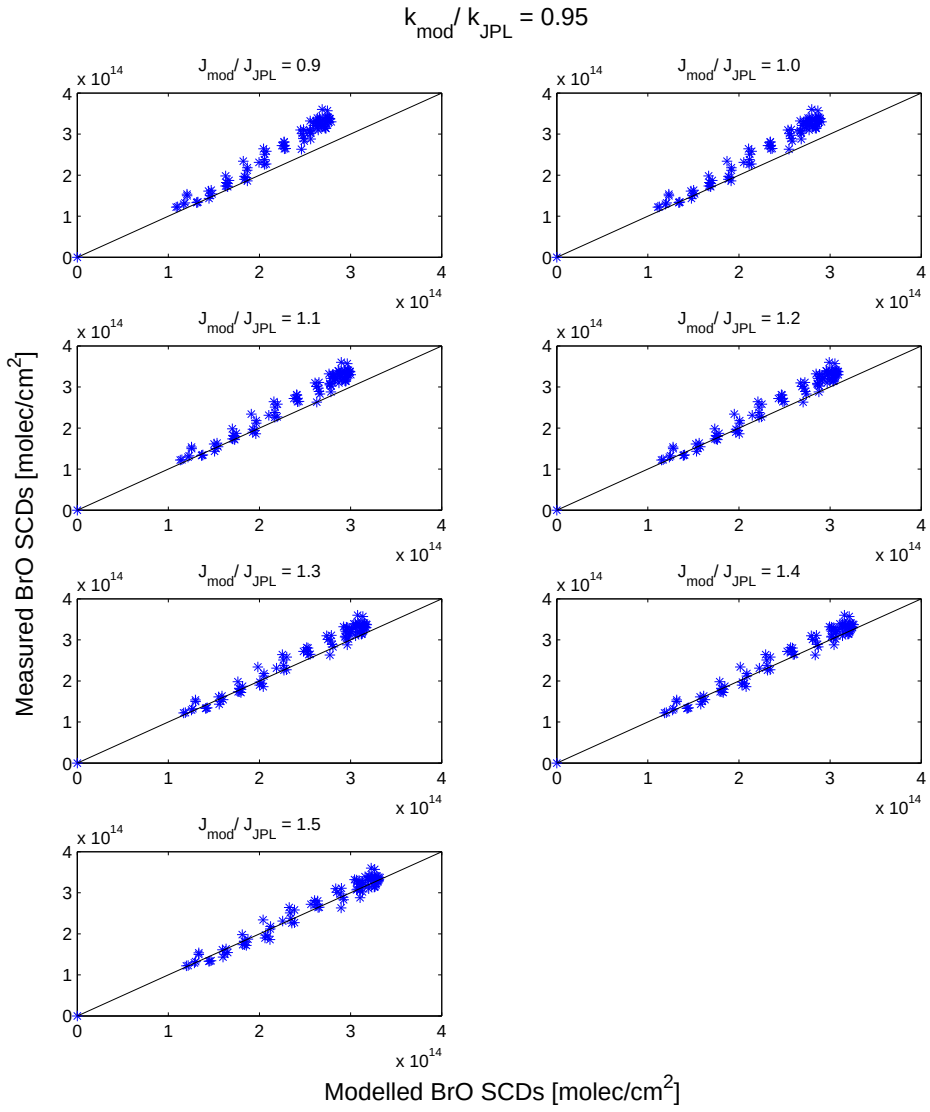

Figure A.8.: *J-k Plots for a* $k_{\mathrm{mod}}/k_{\mathrm{JPL}} = 0.95$

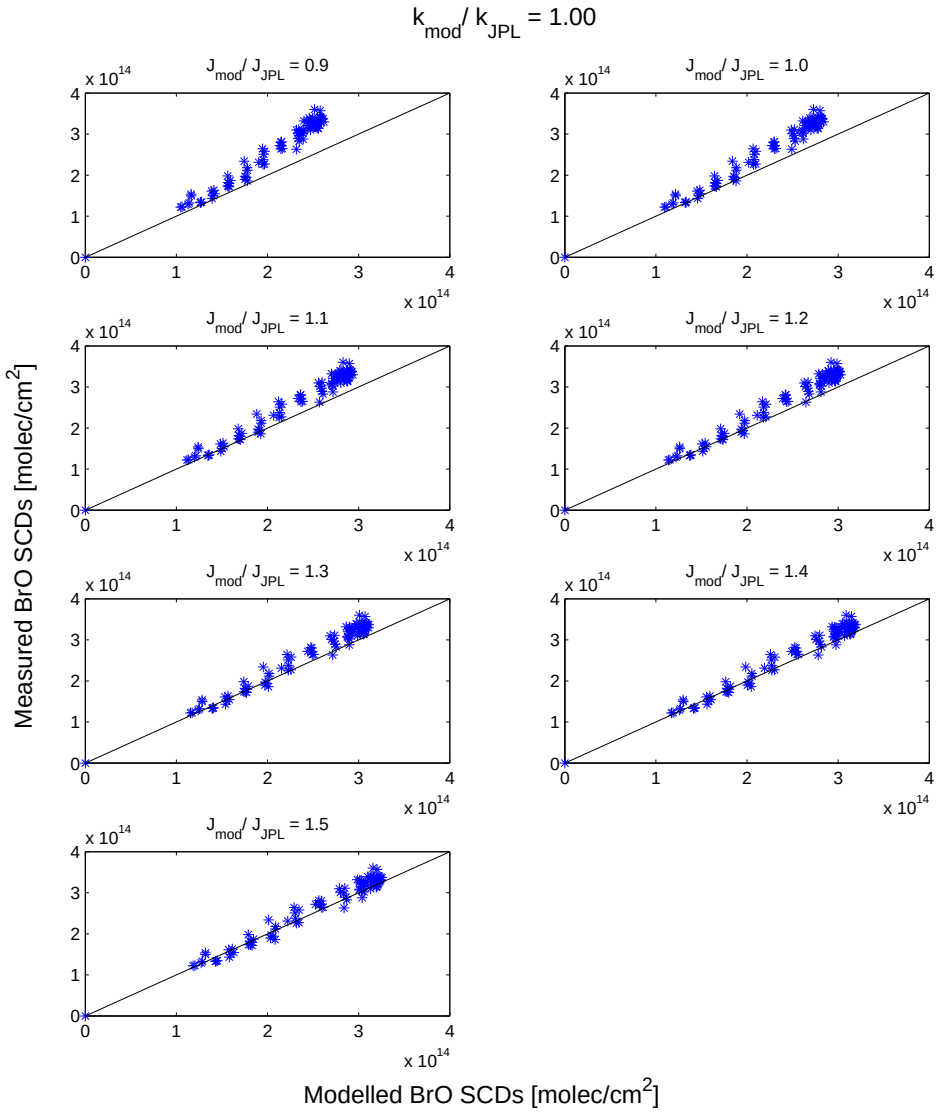

Figure A.9.: *J-k Plots for a* $k_{\mathrm{mod}}/k_{\mathrm{JPL}} = 1.00$

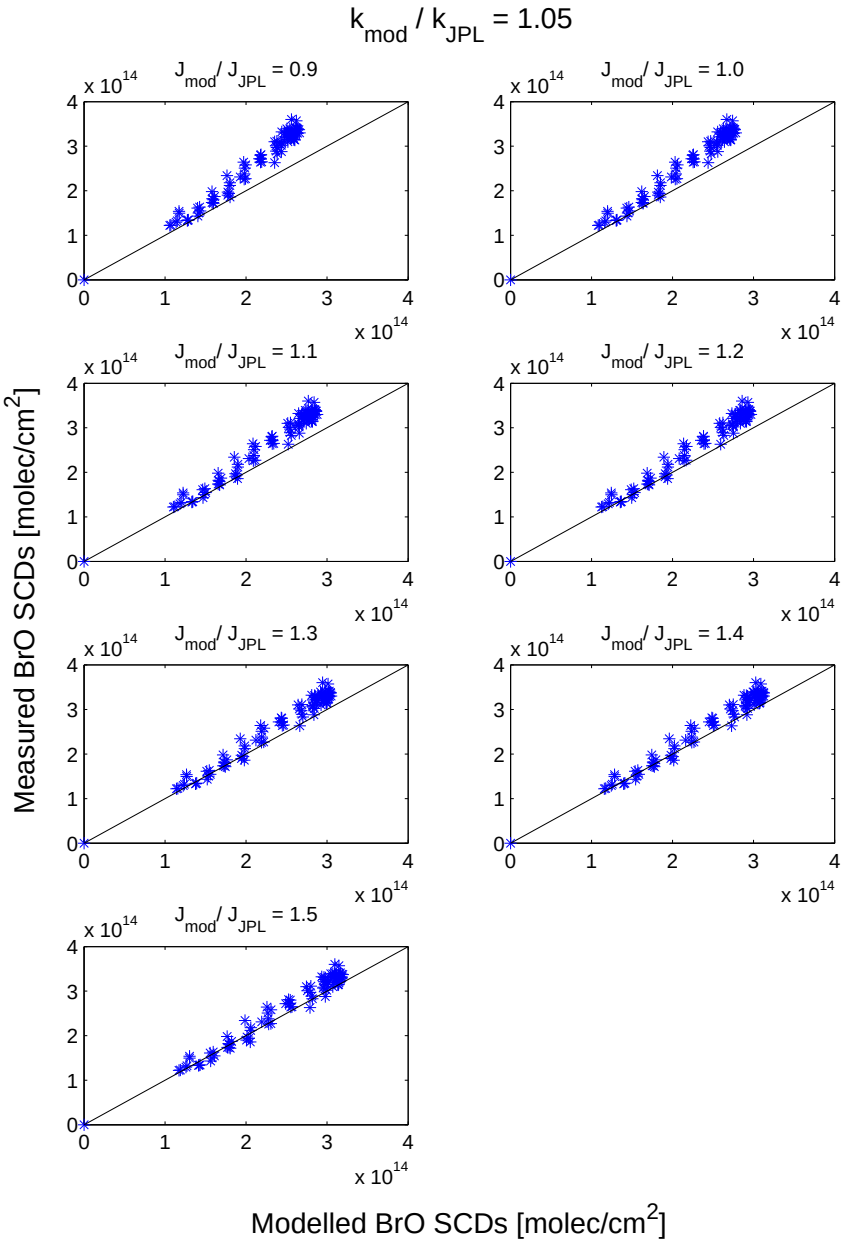

Figure A.10.: *J-k Plots for a* $k_{\mathrm{mod}}/k_{\mathrm{JPL}} = 1.05$

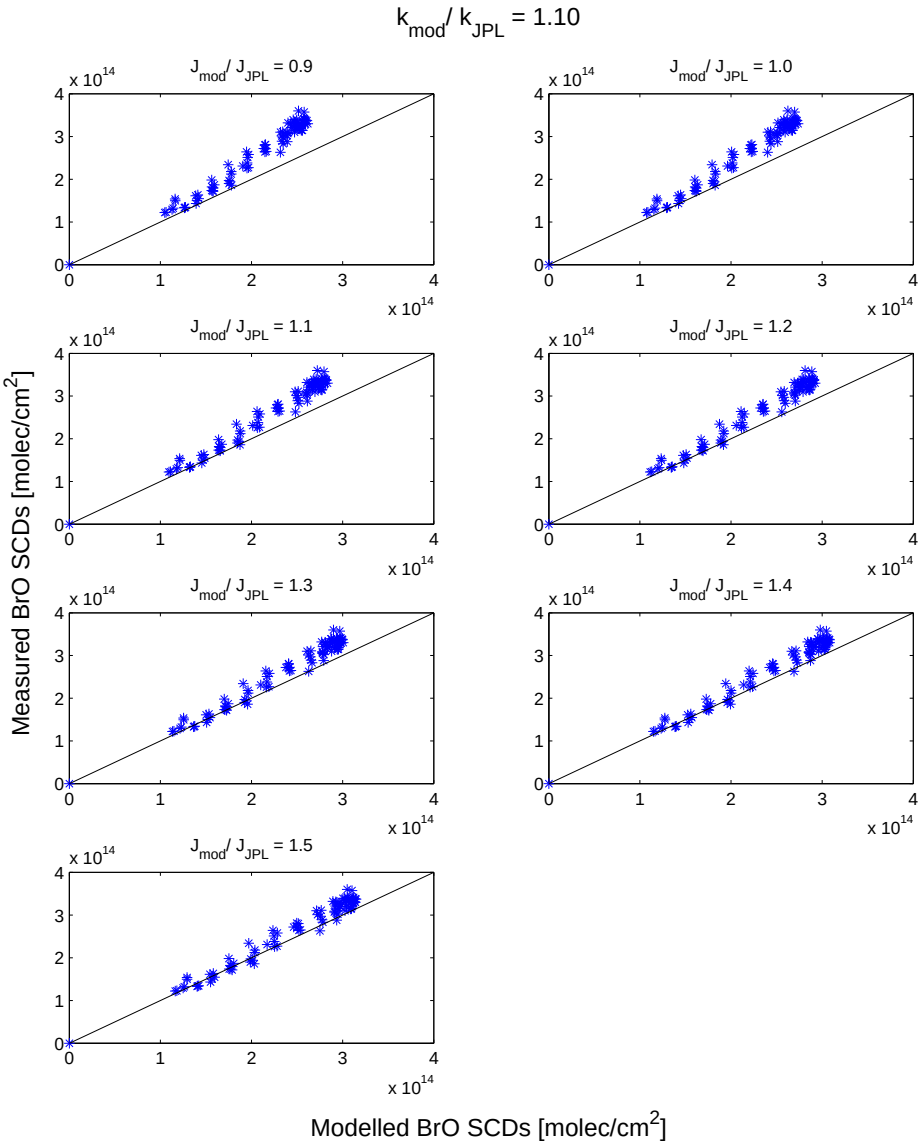

Figure A.11.: *J-k Plots for a* $k_{\mathrm{mod}}/k_{\mathrm{JPL}} = 1.10$

Acknowledgements

Finally I would like to express my gratitude to the following people for their support and assistance in making this work a success:

- Prof. Dr. Klaus Pfeilsticker, under whose scientific guidance this work was made possible, for his specialist knowledge and willingness to give so freely of his expertise. He also created a unique and enjoyable working environment.
- Dr. Christoph Garbe for agreeing to take part in the assessment of this work.
- Prof. Dr. Ulrich Platt who gave me the opportunity to carry out the necesarry research with academic freedom at the Institut für Umweltphysik.
- My colleagues from the DOAS balloon team André Butz and Bodo Werner, Lena Kritten, Sabrina Ludmann, Katja Großmann, Tilman Hüneke, Udo Tricoli, Cristina Prados-Roman and especially Marcel Dorf for their valued support and company during balloon campaigns, proof reading my work and willingness to discuss and solve problems together.
- Special thanks also to the 'glue girls' and the 'the hammer'
- All colleagues from the atmospheric chemistry group at the Institut für Umweltphysik for frequent Mensa visits at high-noon, coffee breaks, biscuit discussions and the cooperative atmosphere.
- The LPMA balloon team - Claude Camy-Peyret, Pascal Jeseck, Isabelle Pepin, Christian Rouillé , Sebastian Payan and Yao Té - for the successful cooperation, their support in preparing the LPMA / DOAS payload (especially the sun-tracker) and for processing the LPMA spectra.
- Our colleagues from the other balloon teams. Especially Fred Stroh, Andreas Engel (Triple), Hermann Oelhaf, Felix Friedl-Vallon and Hans Nordmeyer (MIPAS) for their cooperation and for making their equipment, measurements and results available to us.
- Pierre Chadoutaud who finally saw "an opportunity to fly today" and of course the entire CNES balloon division
- Katja Grunow and Jana Abalichin for her meterological support and the calculations of the air mass trajectories
- Alexei Rozanov for providing SCIAMACHY O_3, NO_2 and BrO limb profiles.
- The IUP Workshop Team for the always quick help and cooperative work
- My family who accompanied me and always gave me their unconditional support
- Susanne Weißert, who with her love and calm gave me the necessary energy during the last year.